University of Basel

Swiss Nanoscience Institute

SNI SWISS NANOSCIENCE INSTITUTE

EINE INITIATIVE DER UNIVERSITÄT BASEL UND DES KANTONS AARGAU

Annual Report 2016 Supplement

Swiss Nanoscience Institute University of Basel

The Swiss Nanoscience Institute (SNI) is a research initiative of the Canton of Aargau and the University of Basel.

This report summarizes work conducted at the Swiss Nanoscience Institute (SNI) in 2016.

Swiss Nanoscience Institute
Klingelbergstrasse 82
4056 Basel
Switzerland
www.nanoscience.ch

Cover illustration: Winter landscape: Diamond surface after etching with a plasma. The rectangular paddles can be broken out and used as samples.
Marietta Batzer, Dominik Rohner, Physics Department, University of Basel

Contents

Sample preparation of nanoliter sized volumes for electron microscopy and diffraction experiments

Project P1201 Microfluidics to study nano-crystallization of proteins
Project Leader: T. Braun and H. Stahlberg
Collaborators: S. Arnold (SNI PhD Student), N. Opara, C. Padeste, K. Goldie, A. Syntychaki, S. Albiez, A. Bieri, M. Chami, M.-A. Mahi, and T. Schwede

Introduction

Two recent developments pushed fast and lasting changes to the field of structural biology: (i) the advent of free electron X-ray lasers (X-FEL) and, (ii), direct electron detector cameras (DEDC) now used in electron microscopy (EM). Whereas the X-FEL promises to solve the structure of proteins assembled in nanometre-sized 3D/2D crystals, cryo-electron microscopy (cryo-EM) allows the structural investigation of protein complexes without crystallization by a so called "single particle approach".

However, sample preparation techniques did not progress significantly over the last 20 years. Here we report on new conditioning and preparation methods using nanoliter sized samples for 3D nanocrystals (diffraction experiments) and cryo-EM (single particle analysis).

Preparation of nanoliter sized samples of nanocrystals for diffraction experiments

For serial crystallography of 3D nanocrystals or 2D crystals by the X-FEL or EM, diffraction pattern from many individual crystals must be recorded. For 3D nanocrystals in X-FEL, liquid-jet injectors are commonly used. However, this form of sample delivery consumes a lot valuable biological sample. An alternative is the adsorption of the crystals on an x-ray or electron transparent solid support. This also means that the crystals are exposed to harsh conditions [1]: the crystals must be protected from drying out, especially in the ultra-high vacuum in the EM. This can be performed by cryo-conservation of the sample (see next section) or an embedding using a protecting agent, e.g., trehalose.

We developed a sample conditioning and deposition method for electron diffraction of nanocrystals [2]. To this end, approx. 3 nl of sample containing nanocrystals are aspirated in a microcapillary (Fig. 1A) and conditioned using trehalose by a diffusion controlled process (Fig. 1B). Subsequently, the solution is spread on a support, here a glow-discharged carbon surface of an EM grid (Fig. 1C). The results show, that nanocrystals indeed can be prepared from nanoliter sized volumes and that trehalose embedding protects the crystal from the harsh ultrahigh vacuum in the EM: Figure 2A shows an overview image of a nanocrystal prepared using the method shown in figure 1. Figure 2B shows a diffraction pattern. Diffraction spots below 1/(1 Å) are visible (arrows).

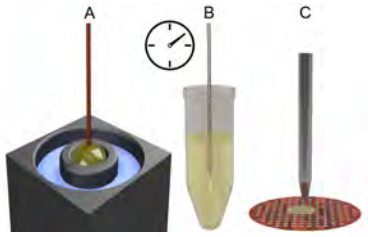

Fig. 1 Conditioning of nanocrystals with trehalose and deposition on an EM grid. A) Aspiration of nanocrystals from a sitting-drop crystallization assay by a micro-capillary (3 nl). B) Conditioning by a diffusion driven process: the capillary is dipped into a trehalose solution to remove salts, precipitants and to introduce trehalose. This method exploits the much larger diffusion constants of salts and trehalose compared to nanocrystals. C) Deposition of 3 nl sample on an EM grid.

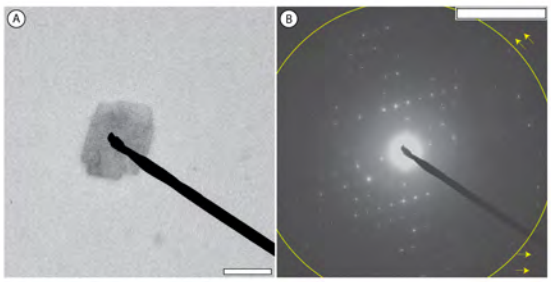

Fig. 2 Nanocrystals conditioned in 2.5% (w/v) trehalose for embedding. A) Overview image showing a lysozyme protein crystal. B) Electron diffraction of the nanocrystal depicted in A. The yellow circle marks the resolution of 1/1 Å. Higher resolution diffraction spots are visible (yellow arrows). The scale bar represents 1 µm in A and 1/1.7 Å in B. (Figure and legend adapted from [2]).

Preparation of nanoliter sized samples for cryo-EM

Cryo-EM sample preparation techniques ensure that biological specimens can be investigated at physiological conditions in the electron microscope. However, conventional preparation methods suffer from extensive blotting steps leading to a massive loss of sample [3] and sometimes to partial denaturation of sensitive protein complexes. We have developed a simple but versatile method for the almost lossless conditioning and preparation of nanolitre-volumes of biological samples for EM [2, 4]. The method does not involve any paper blotting steps. A microcapillary is used to aspirate 3 to 20 nanoliters of sample, depending on the experiment. The sample is applied and spread on the EM-grid.

Real-time monitoring allows the thickness of the water film to be assessed and decreased to the optimum value prior to vitrification. The principles of the cryoWriter device are depicted in figure 3. We prepared cryo-EM grids of various samples, e.g., bacteriophages and soluble proteins as shown in figure 4.

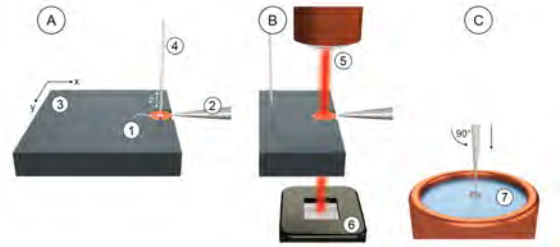

Fig. 3 Working principle of the cryoWriter device (adapted from [3]). (A) A standard holey carbon film EM grid (1) is mounted between the tips of tweezers (2) and positioned flat in a slot in a temperature-controlled stage (3). The stage temperature is set close to the dew point temperature and can be regulated using a PID controller. The dew point stage (3) is mounted on a motorized xy axis to move the grid relative to a microcapillary (4), which can be lowered to a few micrometers above the grid. This microcapillary deposits a few nanoliters of sample while the stage is moving in a sinuous pattern. (B) After sample deposition, the microcapillary is withdrawn and the stage (3) moves to position the grid (1) between an IR laser (λ=780 nm; 5) and a photodiode (6). Interference effects from the thin aqueous sample film on the grid cause a change in signal intensity as water evaporates. (C) A trigger automatically initiates plunge-freezing when the photodiode signal reaches a defined threshold level. The tweezers and grid are rapidly withdrawn from the stage, flipped by 90 degrees into the vertical position and plunged into a cryogen (7).

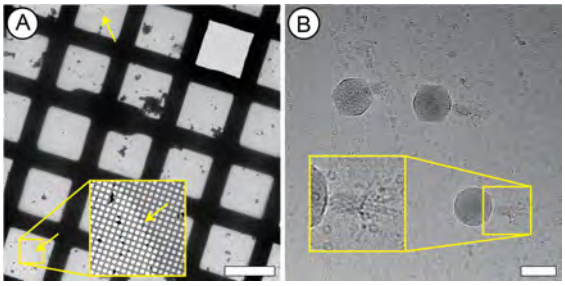

Fig. 4 Proof-of-concept data for cryo-grid preparation using the cryoWriter device (figure adapted from [3]). (A) Typical overview of a prepared grid showing a thin film of vitreous ice. Yellow arrows indicate sample borders. Inset: four-fold enlargement of a border region after contrast adjustment to improve visibility. Note the homogenous layer of vitreous sample. Scale bar: 100 µm. (B) Apoferritin particles and bacteriophages in Tris-HCl buffer prepared by this method and imaged at high magnification and defocus to increase contrast. Inset: two-fold enlargement of the indicated region showing a bacteriophage tail and a few ring-shaped apoferritin complexes. Scale bar: 80 nm.

In order to demonstrate the usefulness of the cryoWriter method for high-resolution structural analysis, urease from *Yersinia enterocolitica* bacteria was prepared for cryo-EM, and imaged with a Titan Krios microscope equipped with a DEDC. Figure 5A documents the high quality of the sample grid. Class averages selected from an initial 2D classification are shown in figure 5B. Particle refinement yielded a 3D reconstruction (Fig. 5C) of the tetrameric complex at a resolution of 5.03 Å.

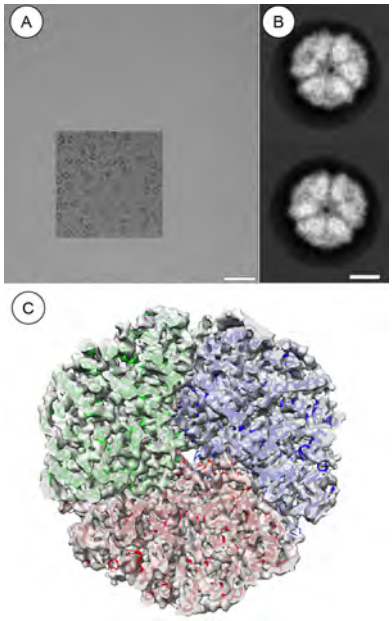

Fig. 5 Use of the cryoWriter to prepare samples for high-resolution structural analysis; proof-of-concept (figure adapted from [3]). (A) Drift-corrected cryo-EM image of urease particles embedded in vitreous ice. Inset: the particles with increased contrast. Scale bar, 50 nm. (B) 2D class averages including ~3'400 of the 10,000 particles initially selected. Scale bar, 5 nm. (C) Urease density map at 5.03 Å resolution.

References

[1] N. Opara, S.A. Arnold, T. Braun, H. Stahlberg, M. Makita, C. David, and C. Padeste. *Direct protein crystallization on ultrathin mem-branes for diffraction measurements at X-ray free electron lasers*, to be submitted (2016)

[2] S.A. Arnold, S. Albiez, N. Opara, M. Chami, C. Schmidli, A. Bieri, H. Stahlberg, C. Padeste and T. Braun, *Total sample conditioning and preparation of nanoliter volumes for electron microscopy*. ACS Nano, 10(5), pp. 4981-4988, 2016

[3] S. Kemmerling, J. Ziegler, G. Schweighauser, S.A. Arnold, D. Gisz, S.A. Mueller, R. Ringler, K.N. Goldie, N Goedecke, A. Hierlemann, H. Stahlberg and T. Braun, *Connecting mu-fluidics to electron microscopy*. J Struct Biol., 177(1), pp. 128–34, 2012

[4] S.A. Arnold, S. Albiez, A. Bieri, A. Syntychaki, R. Adaixo, R.A. McLeod, K.N. Goldie, H. Stahlberg and T. Braun. *Blotting-Free and Lossless Cryo-Electron Microscopy Grid Preparation from Nanoliter-Sized Protein Samples and Single-Cell Extracts*. J Struct Biol, 2017, in press

PDMS-based nanofluidic trapping devices for high-throughput fabrication and screening of nano-objects

Project P1202 Electrostatic Nanotrapping for Single-Macromolecule Analysis
Project Leader: Y. Ekinci and T. Pfohl
Collaborators: M. Gerspach (SNI PhD Student) and N. Mojarad

Introduction

Monitoring the motion and interactions of single particles in solution is of great scientific and industrial interest since it provides information on local dynamics and reactions. However, stable trapping of nano-objects smaller than 100 nm without changing their properties remains challenging. In the last years, especially one method has attracted the attention that enables contact-free and passively trapping and detecting nano-objects, the so-called geometry induced electrostatic (GIE) trapping [1]. In GIE trapping, single charged nano-objects are trapped by electrostatic repulsion from charged walls of nanometer height fluidic channels (see sketch in Fig 1).

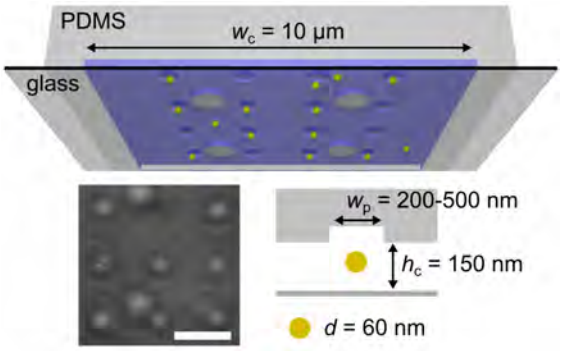

Fig. 1 3D schematic and dimensions of a geometry-induced electrostatic (GIE) trapping device made from the soft material PDMS. Nano-objects are trapped within the pockets of the nanochannels by electrostatic repulsion. Supporting pillars prevent the PDMS nanochannel from sagging and collapsing to the glass surface. Eight trapped particles with a diameter of 60 nm and one empty pocket are shown in the optical image (bottom left). The bigger white circles are the supporting pillars. Scale bar: 3 µm.

Tailoring the surface topology of the nanochannels creates local energy potential wells in which nano-objects have been reliably trapped from milliseconds to hours depending on the potential depth. Various trapping geometries (pockets, channels or grids) can be realized using nanolithography. The trap stiffness and trapping time can be controlled by altering the trap dimensions, charge density of the trapped object and the device surface, and by the salt concentration of the buffer solution. Since the trapping depends only on the electrostatic potential created by the channel walls and the charged objects, GIE-trapping is getting along without any externally applied forces, making its integration into many other systems and materials straightforward [2].

Current GIE trapping devices are fabricated from silicon or glass substrates using state-of-the-art top-down nanofabrication, such as reactive ion etching (RIE) and electron beam (e-beam) lithography. However, beside the high costs and time-consuming nanofabrication of glass or silicon-based devices, cleanroom facility access is limited for many researchers and manufacturers, making development and usage of GIE trapping devices difficult.

Polydimethylsiloxane (PDMS)-based soft lithography uses replica molding, which simplifies fabrication and results in high-throughput and low cost production. In addition, PDMS is biocompatible and integrated with established microfluidic techniques and infrastructures, which opens the realization of combining GIE trapping with more complex fluidic systems such as particle sorting or trapping along concentration gradients [2]. The ease and fast production would make them equally available for research and commercial applications. However, fabricating nanometer height PDMS channels and high-resolution nanostructures down to 200 nm require advanced designs and material processing techniques.

Fabrication of PDMS-based GIE-trapping devices

The fabrication steps of PDMS-based GIE trapping devices are sketched in figure 2. The fabrication consists of three main steps. First, the production of a silicon master using top-down nanofabrication including e-beam lithography and RIE (I), followed by a straightforward two-step replica molding process using an inorganic-organic UV curable hybrid polymer (II, OrmoStamp®) and a silicon-based organic polymer (III, PDMS). The obtained OrmoStamp® masters can be repeatedly used as molding masks for the fabrication of PDMS devices. This production step is carried out without the need of cleanroom facilities. In each scanning electron microscopy (SEM) image of Fig. 2, pockets with diameters w_p of 200, 250 and 500 nm are seen. The pockets are transferred with high fidelity and resolution into the OrmoStamp® master and finally into the PDMS devices.

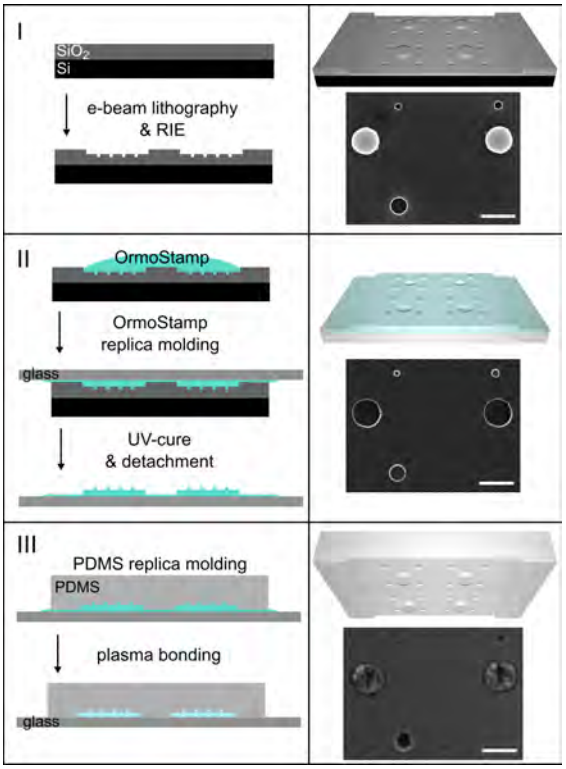

Fig. 2 Schematic of the fabrication steps of the PDMS-based GIE trapping device (left). Corresponding 3D-model and scanning electron microscopy (SEM) images (right). First, a silicon master is fabricated in the cleanroom using e-beam lithography and reactive ion etching (I), followed by a two step replica molding process using first a UV curable resin (II) and secondly PDMS (III). The high-throughput PDMS replica molding step is carried out without the need of cleanroom facilities. Scale bars of the SEM images: 1 µm.

Influence of pocket diameter on trapping stiffness and trapping time

The lateral motions of trapped gold nanoparticles (AuNP) with a diameter of d = 60 nm in circular pockets of w_p = 200 nm (green) and 500 nm (blue) were recorded as shown in figure 3b. As seen from the motion plots, particles trapped in a smaller trap size were confined stronger by the electrostatic repulsion from the channel walls compared to the particles in the larger pockets. To quantify the trapping strength, the mean square displacements (MSDs) $< [\Delta r(\Delta t)]^2 >$ were plotted as a function of lag time Δt (Fig. 3c). From the plateau of the MSDs the trapping stiffness k_r can be calculated as

$$< [\Delta r(\Delta t)]_p^2 > = \frac{4k_bT}{k_r},$$

were k_b is the Boltzmann constant and T is the absolute temperature. For the particles in the 500 nm pockets, a weaker trap stiffness of k_r = [0.22 ± 0.06] fN/nm was achieved, in comparison to k_r = [0.8 ± 0.3] fN/nm for the particles in the 200 nm pockets. To experimentally quantify the depth of the electrostatic potential of the 200 nm pockets, we measured the average time the particles dwell in the traps before escaping known as the Kramers time $\bar{\tau}_K$

$$\bar{\tau}_K \cong \tau_R \, e^{\frac{Q}{k_BT}},$$

where τ_R is the relaxation time within the potential well and Q is the potential depth. From the residence time probability distribution $p(\tau)$ of the escaping events (Fig. 3d), a Kramers time of $\bar{\tau}_{K,200}$ = 2.7 s was obtained, corresponding to a potential depth of Q_{200} = 6.3 k_bT. Since the particles in the 500 nm pockets were stably trapped for several minutes in the traps, a quantitative analysis of the Kramers time was not possible. However, estimating $\bar{\tau}_{K,500} \approx 120$ s from the experimental observations, suggests a potential depth of $Q_{500} \approx 8.7\ k_bT$.

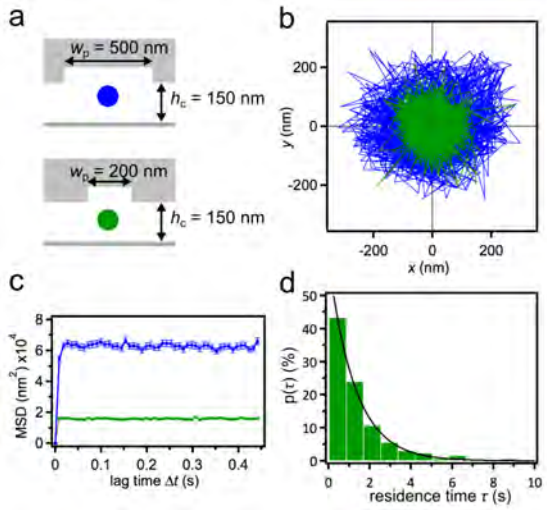

Fig. 3 Influence of the trap diameter on the lateral trap stiffness and residence time: a) sketch of the trap dimensions, b) lateral position plots of a 60 nm gold particle in a w_p = 500 nm (blue) and a w_p = 200 nm pocket (green), c) corresponding mean square displacement (MSD) plots, d) exponential decay of the residence time of 60 nm particles in d = 200 nm pockets.

In summary, we introduced nanofluidic devices made from the soft material PDMS for high-throughput fabrication and high performance contact-free and passive trapping of single charged gold particles down to 60 nm in diameter. These devices enable parallel trapping of single particles by fabricating trap lattices within the channels. Due to its ease of fabrication, our method opens the feasibility to carry out single and label-free research on colloidal particles using the GIE trapping method with little effort.

References

[1] M.A. Gerspach, N. Mojarad, T. Pfohl and Y. Ekinci, *Glass-based geometry-induced electro-static trapping devices for improved scattering contrast imaging of nano-objects*, MEE, 2015, 145, 43-48

[2] M.A. Gerspach, N. Mojarad, D. Sharma, T. Pfohl and Y. Ekinci, *Nanofluidic lab-on-a-chip trapping devices for screening electrostatics in concentration gradients*, Microelec.Eng., 2017, 175, 17 - 22

2D supramolecular chemistry with pyrimidine functionalized 4,2':6',4''-terpyridines

Project P1203 On surface covalent assembly of coordination polymers with integrated read and write functions
Project Leader: C.E. Housecroft and E.C. Constable
Collaborators: T. Nijs (SNI PhD Student), T.A. Jung, Y.M. Klein, A. Ahsan, S.F. Mousavi, and S. Nowakowska

Introduction

Here we investigate so-called SurfMONs (surface metal organic networks) towards implementing complex reactions. We aim at implementing light harvesting or site/shape selective chemical reactions [1] into the versatile configurable toolkit provided by 2D on-surface arrays. The arrangement of functional groups available for bonding, the different metals coordinated by the ligand frameworks or the size of the scaffold pockets will be used for the control of size and shape selective chemical reactions as well as catalysis.

Here we report the influence of the pyrimidine functionalization of 4,2':6',4''-terpyridine derivatives (Fig. 1) [2]. We have investigated the structures and the self-organization mechanisms of these surface-supported assemblies. 4,2':6',4''-terpyridines possess inherent design features to facilitate the formation of extended arrays via coordination through the **N** atoms in contrast to the chelating 2,2':6',2''-terpyridines [3]. In the second year, we have started the investigation of the pyrimidine functionalized **1** and the methylpyrimidine functionalized **2** on single crystal metallic substrates. In the third year, this study was extended by comparesons of assemblies formed using the ethylpyrimidine functionalized compound **3**.

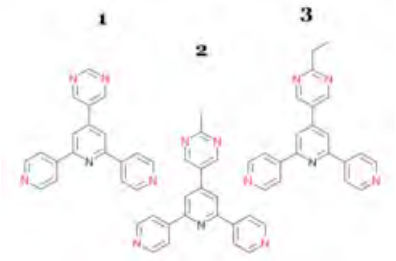

*Fig. 1 Pyrimidine **1**, methylpyrimidine **2** and ethylpyrimidine **3** functionalized 4,2':6',4''-terpyridines.*

In addition to the different physical, chemical and steric properties, the methyl and ethyl modifications act as 'imaging groups' in the STM (Scanning Tunnelling Microscope) measurements, allowing for the unambiguous identification of the molecular orientations and conformations.

Close-packed weakly bonded assemblies

The molecules' shape allows for an interdigitated packing motif and rather high 2D packing densities. This occurs for both **1** and **2** after deposition on the inert surface of Au(111) exhibiting extended close-packed phases (Fig. 2a,b). In addition to weak non-classical C-H...N H-bond interactions, attractive dipole forces are also of relevance in these assemblies to compensate the presence of repulsive H...H interactions. Compared to 1 and 2, 3 shows a significantly modified pattern. The packing density is reduced and a porous structure emerges. We attribute this transformation to the steric requirements of the longer ethyl tails. These point into the cavity along the three principal directions of the substrate, thereby effectively blocking the filling of the vacancy. The backbone of the network is formed by linear tail-alternating rows.

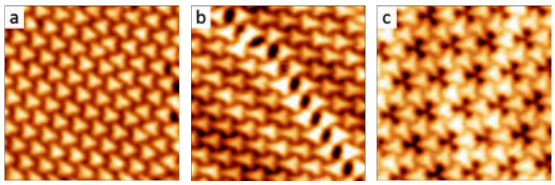

*Fig. 2 a,b,c) STM micrographs of terpyridines **1**,**2**,**3**/Au(111) taken at 5K with clearly distinguishable (m)ethyl 'corner' allowing for the unambiguous identification of the molecular orientation. (10 x 10 nm²)*

Metal coordination with multi-stage tuning

By addition of Cu-adatoms from a thermal evaporation source to the molecular adlayers formed on Au(111) samples, coordination occurs at the free electron pair present at the **N** atoms (see X-ray Photoelectron Spectroscopy (XPS) data in Table 1). Molecules orient themselves such that all the **N** atoms are preferentially linked by coordination to a neighboring molecule (Fig. 3). Interestingly, only 1D coordination polymers are formed in the form of ladder-like structures, with 3 of the 4 coordinated **N** atoms sharing their Cu adatom with a neighboring molecule. These results in 3 binding Cu-adatoms involved in the unit cell.

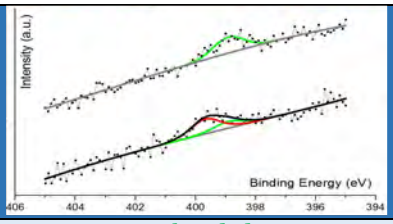

	-N= [eV]
H-bonded	398.8
Cu-coord.	399.6

*Table 1 N1s XPS data of **1** (representative for **1**, **2** and **3**) on Au(111) show a clear increase of the binding energy upon metal coordination (green to red line). The inner terpyridine N remains uncoordinated.*

The same ladder-like structures are obtained by deposition of the molecules on Cu(111) substrates, where sufficient adatoms are available by thermally activated emission from step and kink sites during the sample preparation at room temperature (Fig. 3a,b). Also, since all three molecules (**1**, **2** and **3**) result in the same ladder-like assembly, this provides evidence for the model shown in figure 3c in that the length of **R** points to the outside of the chains and hence does not influence the length of the ladder unit.

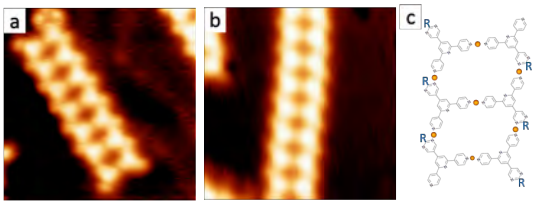

*Fig. 3 a,b) Comparison of metal coordinated ladder-like chains of **3** on Au(111) and Cu(111) (10x10nm²). The consistent morphology of these two, but also of all three functionalizations (not shown) is remarkable.*

Activation stage 1

These ladder-like assemblies can be further tuned by controlled annealing on Cu(111). Due the availability of more Cu adatoms, molecules feel less urge to share their adatoms with their neighbors, making the ladders dissociate into single tetramers (Fig. 4). Now per tetramer, four Cu adatoms are involved in binding, but only two out of four coordination atoms are shared per molecule (ladder: three out of four). Interestingly, the **N** atom close to the substituent does not share the coordinated Cu atom, which prevents further polymerization and leads to discrete metallocyclic assemblies.

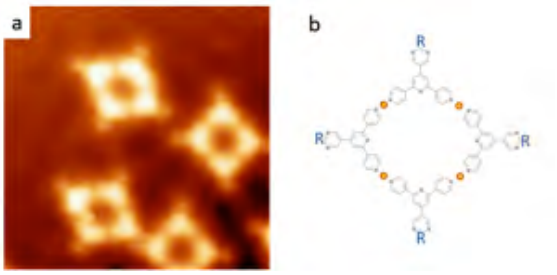

*Fig. 4 Left: 10x10 nm² STM visualization of **1**,**2**,**3**/ Cu(111) after slight annealing. Right: Schematic.*

The formation of the metallotetramer is not affected by the lengths of the different pyrimidine functionalizations **R**. This is in analogy to the case of the ladder-like chains. Note that the same result is also obtained by depositing molecules on a hot Cu(111) substrate. The strong interaction of the metallotetramers with the substrate enforces that only 3 orientations of the tetramers are observed (along the three fold symmetry of the 111 substrate) and the rhombohedral appearance (80°/100°).

Activation stage 2

Further annealing surprisingly results in a rearrangement of the rhombuses into a 2D-pattern (Fig. 5). Closer inspection reveals, in analogy to the case of the 2D close-packed phase presented above, only one of the molecules is forming this porous assembly, namely **2**. We attribute this observation to i) steric constraints of **1** to link to a binding partner in view of the repulsive forces from neighboring molecules and ii) the thermally activated mobility of the ethyl endgroup of **3** preventing a condensation of these molecules at this end. Notably, the repulsive action of mobile endgroups (random coil segments in biomolecular sciences) is an important factor in the assembly of biomacromolecules which has also been observed in the case of 2D supramolecular layers [4]. This assignment is summarized in our tentative model. This porous assembly is present in two chiral domains.

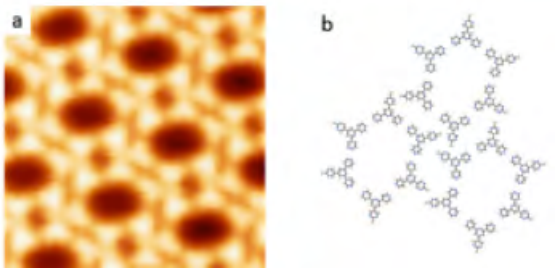

*Fig. 5 a) 10 x 10 nm² STM image of **2**/Cu(111) after extended annealing. b) Current model of the assembly.*

The complexity of the assembly of these three terpyridines make them an ideal study-case to investigate the role of different binding motifs in on-surface, planar supramolecular chemistry. Small changes in **R** decisively influence the structure of the on-surface assembly.

Outlook

We are able to change the intermolecular binding motifs from hydrogen-bonded to metal-coordinated by controlling the availability ('titration') of Cu atoms. In our ongoing work we shall investigate further specifically designed ligands in order to increase our understanding of on-surface molecular chemistry and the emergence of different structures from the different functionalization and activation of the functional linking groups onto specific architecture of on-surface assemblies and coordination polymers. Our aim is to try to understand the design rules for programmable metal-organic networks and get access to a larger portfolio of building blocks and assembled structures.

References

[1] A. Shchyrba, et al., *Controlling the dimensionality of on-surface coordination polymers via endo- or exoligation*, J. Am. Chem. Soc., 2014, 136, 9355-9363

[2] Y.M. Klein, E.C. Constable, C.E. Housecroft, J.A. Zampese, *4′-(Pyrimidin-5-yl)- and 4′-(2-methylpyrimidin-5-yl)-4,2′:6′,4″-terpyridines: Selective coordination to zinc(II) through the 4,2′:6′,4″-terpyridine domain,* Polyhedron, 2014, 81, 98 – 104

[3] T. Nijs, F.J. Malzner, S. Fatayer, A. Wäckerlin, S. Nowakowska, E.C. Constable, C.E. Housecroft, T.A. Jung, *Programmed assembly of 4,2′:6′,4″-terpyridine derivatives into porous, on-surface networks*, ChemComm., 2015, 51, 12297-13000

[4] M. Stöhr, et al., *Selbstorganisation und spontane 2D-Racematspaltung eines Dicyano-[7]helicens auf Cu(111)*, Chem. Eur. J., 2011, 14, 5794-5802

Magnetic properties of single transition metal atoms on a Bi(111) substrate exhibiting large Rashba splitting

Project P1204 Site-specific magnetic studies and control of large self-assembled spin systems
Project Leader: T.A. Jung and A. Kleibert
Collaborators: J. Nowakowski (SNI PhD Student) and M. Baljozovic

Magnetism in single atoms

This project has been so-far mainly focused on studying magnetic properties of assemblies built from spin-bearing molecules, which provide several advantages including diversity and tunability. However, in order to reach the ultimate limit of magnetic data storage, investigating the magnetic properties of systems made of single surface-supported atoms is also very interesting due to the significantly lower size of the building blocks.

Isolated single atoms cannot exhibit a stable magnetic moment due to their spherical symmetry: there is no preferential direction for the spin to align with, as long as there is no external magnetic field. When put on a surface, however, the atoms can gain a directional dependence of magnetic properties, called magnetic anisotropy (MA). MA is a pre-requisite to observe magnetic hysteresis in low-dimensional systems and it can be quantitatively studied by measuring the angle-dependent X-ray Magnetic Circular Dichroism (XMCD) [1]. Even if remanence is not observed in single atoms, the higher the magnetic anisotropy per atom, the lower the minimum amount of atoms required to build a stable magnet. Thus, magnetic adatom clusters are of potential interest towards future high-density storage.

Transition metal atoms on a Bi substrate

Our group focused on investigating magnetic properties of transition metal (TM) atoms on Bi/Si(111). The Bi substrate was chosen due to the fact that it exhibits a large Rashba splitting, *i.e.* a momentum-dependent splitting of spin bands at the surface [2]. Additionally, this system allows for a relatively high coverage of single paramagnetic atoms, *i.e.* without clustering; it is possible due to the fact that the TMs on Bi(111) penetrate the first layer of Bi and adsorb below the surface [3].

The magnetic moment preferentially aligns, depending on the anisotropy, along the surface plane (in-plane) or perpendicular to the surface (out-of-plane). The latter is the preferential type for magnetic data storage applications, as the spin flip in this case requires going through the hard magnetization plane, which is not the case for in-plane anisotropy. Interestingly, both of the studied atoms, *i.e.* Fe and Cr, exhibit a significant out-of-plane magnetic anisotropy when deposited on a Bi(111) substrate. This is visible in figure 1 as higher XMCD signal when measuring in normal incidence (Fig. 1a, c) in comparison to grazing incidence (Fig. 1b, d). This difference is particularly high for Cr atoms. The observation that the dichroism at the second absorption edge is very small (for Fe) / pointing into the same direction as the first one (for Cr) evidences a significant orbital magnetic moment present on these elements. High orbital magnetic moment is a prerequisite for large magnetic anisotropy.

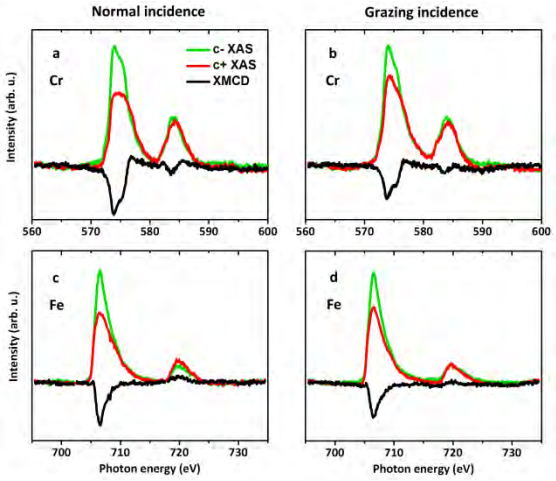

Fig. 1 Magnetic isotropy of Fe / Cr adatoms embedded into the first Bi layer: XMCD data of Cr (a, b) and Fe (c, d) $L_{3,2}$ edges measured in normal incidence (a, c) and grazing incidence of 60° (b, d) in the external magnetic field of 6.8 T. The shape of the XMCD signatures, in particular as observed for Cr, suggests a large orbital moment of the atoms (L_3 and L_2 edges pointing in the same direction). The spectra have been acquired at ~10 K.

Origin of magnetic anisotropy

In order to quantify the magnetic anisotropy observed by XMCD, *i.e.* to determine the magnetic anisotropy energy, magnetization curves at normal and grazing incidence need to be measured (data shown in Fig. 2). These curves can then be fitted using a model described in detail in [4]. In this classical model both magnetization curves are fitted simultaneously with three free parameters: magnetic moment m, magnetic anisotropy energy K and temperature T.

The magnetic anisotropy originates from the interaction between the spin and the orbital momentum of an atom; additionally, it requires the ligand field breaking the spherical symmetry of the

free ion. In the majority of magnetic materials, however, hybridization and ligand field effects result in quenching of the orbital magnetic moment, resulting in magnetic anisotropy energies significantly below 1 meV. Therefore, already the value of K=2.5 meV for Fe can be considered as high; the K for Cr, however, is much higher at ~30 meV.

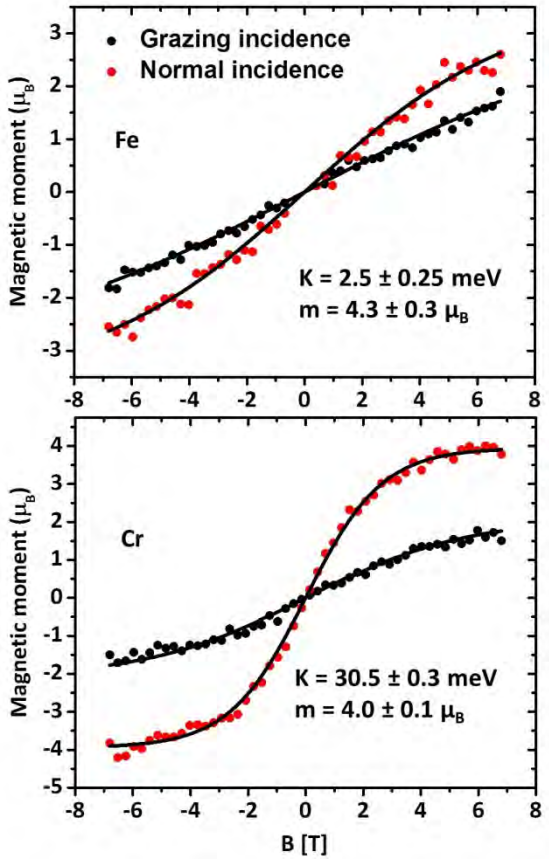

Fig. 2 Magnetization curves obtained in normal and grazing incidence geometry on ~3% of a ML of Fe (top) and Cr (bottom) deposited on Bi/Si(111). The black lines indicate the obtained fits, from which the given parameters were calculated: magnetic moment m and magnetic anisotropy energy K.

In order to put these values into perspective, it is interesting to consider what the physical limit of K is. It can be calculated as λL, where λ is the spin-orbit coupling constant and L is the atom's orbital angular momentum [5]. Taking into account the $3d^5$ occupancy of Cr and its spin state of S=3/2 it can be concluded that λ=10 meV and L=3, resulting in λL =30 meV. Therefore, the observed magnetic anisotropy of Cr atoms is nearly at its physical limit. Currently, DFT+U calculations are underway with the goal to gain a deep understanding of the processes leading to such high magnetic anisotropy energy. They will also allow investigating the role of the so-called T_z term influencing the XMCD spectra and possibly causing an uncertainty in the obtained values of K.

Summary

In this project, magnetic properties of single TM atoms adsorbed on a Bi(111) substrate have been studied using XMCD. Both of the studied Cr and Fe showed a out-of-plane magnetic anisotropy, which is interesting in the prospect of reaching the ultimate limit of magnetic data storage. The quantitative data analysis allowed for the observation of extremely high magnetic anisotropy energy of Cr atoms, which was determined to be close to the physical limit. To the best of our knowledge the physical limit of K has been nearly reached for Co atoms on a thin layer of an insulator [5], but so-far never for other 3d transition metal atoms or on a semi-metal like Bi. The currently running DFT+U calculations will allow us to better understand why TM atoms adsorbed on Bi(111) maintain their orbital moment and exhibit high magnetic anisotropy.

References

[1] Aharoni, A., *Introduction to the theory of ferromagnetism*, International series of mono-graphs on physics, Clarendon Press: Oxford, 1998

[2] Bihlmayer, G., Blügel, S., Chulkov, E.V., *Enhanced Rashba spin-orbit splitting in Bi/Ag(111) and Pb/Ag(111) surface alloys from first principles*, Phys. Rev. B, 2007, 75 (19)

[3] Klein, C., Vollmers, N.J., Gerstmann, U., Zahl, P., Lükermann, D., Jnawali, G., Pfnür, H., Tegenkamp, C., Sutter, P., Schmidt, W.G., Horn-von Hoegen, M., *Barrier-free subsurface incorporation of 3d metal atoms into Bi(111) films*, Phys. Rev. B, 2015, 91 (19)

[4] Gambardella, P., Rusponi, S, Veronese, M., Dhesi, SS., Grazioli, C., Dallmeyer, A., Cabria, I., Zeller, R., Dederichs, PH., Kern, K., Carbone, C., Brune, H., *Giant magnetic anisotropy of single cobalt atoms and nanoparticles,* Science, 2003, 300 (5622), 1130–1133

[5] Rau, I.G., Baumann, S., Rusponi, S., Donati, F., Stepanow, S., Gragnaniello, L., Dreiser, J., Piamonteze, C., Nolting, F., Gangopadhyay, S., Albertini, O.R., Macfarlane, R.M., Lutz, C.P., Jones, B.A., Gambardella, P., Heinrich, A.J., Brune, H. *Reaching the magnetic anisotropy limit of a 3d metal atom,* Science, 2014, 344 (6187), 988–992

Structural and functional dynamics of nuclear pore complexes

Project P1205 Watching the nanomachinery of the nuclear pore complex at work by high speed-AFM
Project Leader: R.Y.H. Lim and C. Gerber
Collaborators: Y. Sakiyama (SNI PhD Student)

Spatiotemporal dynamics of a molecular machine

Nuclear pore complexes (NPCs) are the sole gateways of nucleocytoplasmic transport in eukaryotic cells. Each vertebrate NPC has 50 nm-diameter channels and is made of 30 types of proteins called nucleoporins (Nups) arranged in an octagonal geometry [1]. Small solutes or ions can diffuse freely through the NPC, but macromolecules require soluble transport receptors (karyopherins or Kaps) to access the pore. Kaps interact specifically with a group of barrier-forming intrinsically disordered Nups that harbour phenylalanine-glycine repeats (FG Nups) [2]. Previously, we had implemented high-speed atomic force microscopy (HS-AFM) to visualize FG Nup behaviour in the NPC for the first time [3]. Our ongoing efforts seek to correlate how Kaps induce dynamic conformational states in the FG Nups and other NPC structures such as the nuclear basket (NB) that regulate transport.

FG Nup dynamics when binding Kaps

Previously, we found that the affinity and kinetics of Kapβ1-FG Nup binding depends on Kapβ1 concentration due to avidity [4]. This provides a means to slow Kapβ1 translocation to the point where HS-AFM can maximally capture (at ~150 ms per frame) dynamic FG Nup behavior when binding Kapβ1.

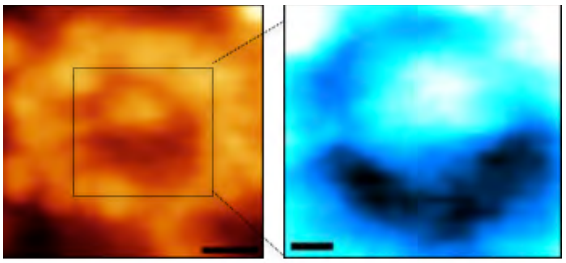

Fig. 1 Left: HS-AFM reveals a cargo trapped within the NPC channel. Scale bar = 30 nm. Right: Zooming into the region of interest reveals highly dynamic interactions between several FG Nups and the cargo. Scale bar = 10 nm.

Structural dynamics of the nuclear basket

NB structure consists of eight nuclear filaments that co-join into a distal ring and may act as a selective gate. Still, it is unknown if and under what conditions the distal ring opens and closes to facilitate the passage of large Kap-cargo complexes. By SEM, NBs were clearly visualized but required sample fixation and coating with metal [5]. Further, the NB is inaccessible to cryo-electron tomography (cryo-ET) studies, which depend on structural averaging [6-8]. By HS-AFM, we have directly resolved the eight nuclear filaments and the distal ring. Interestingly, we observe that the distal rings can exist in open and closed states, and are working towards ascertaining the functional basis for these changes without fixation in physiological environments.

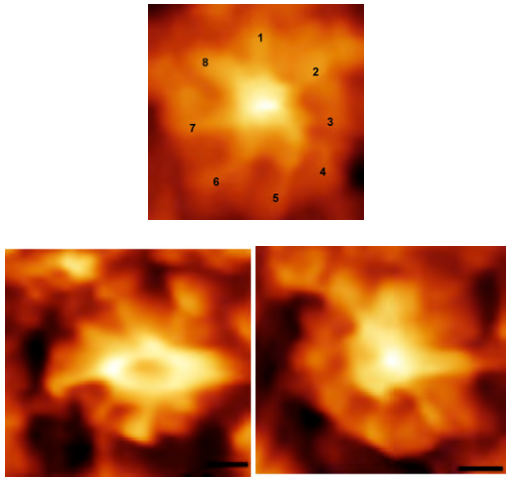

Fig. 2 Top: Zoom in of an individual nuclear basket revealing eight nuclear filaments that connect into a distal ring. Scale bar = 25 nm. Bottom: Nuclear basket in an open (left) and closed (right) configuration. Scale bar = 30 nm.

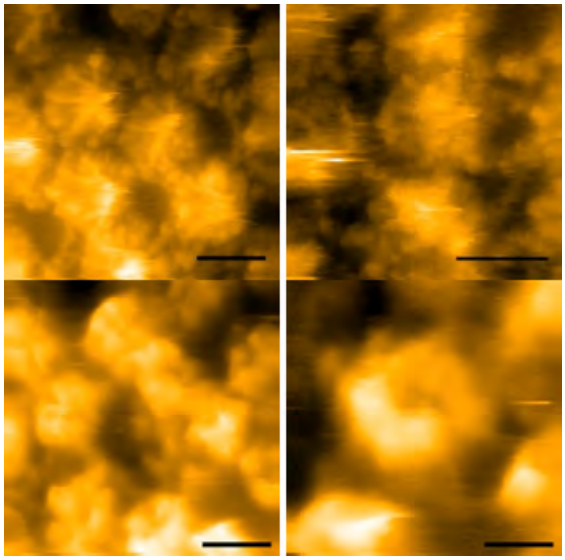

Fig. 3 Top: "Closed" nuclear baskets resolved by HS-AFM in the absence of calcium. Scale bar = 100 nm. Bottom: "Open" nuclear baskets resolved by HS-AFM in the presence of calcium. Scale bar is 100 nm (left) and 25 nm (right).

Ca^{2+} changes the nuclear basket structure

The nuclear basket has been shown previously by AFM [9] and SEM [10] to open in the presence of Ca^{2+} no doubt at low resolution. Using HS-AFM, we have now verified the structural dynamics of the distal ring under similar conditions.

Summary

Although we have resolved dynamic FG Nup behavior directly inside native NPCs at transport-relevant timescales, several questions remain as to how the NPC regulates Kap-cargo translocation. One key feature is the nuclear basket, which might act as a selective gate that opens and closes in a signal-dependent manner, but is too fragile in its native state to visualize. However, because HS-AFM exerts a very small impulse with every "tap" on the sample surface, it promises to visualize such biological surfaces without disturbance.

References

[1] Fahrenkrog, B. & Aebi, U., *The nuclear pore complex: nucleocytoplasmic transport and beyond*. Nat Rev Mol Cell Biol **4,** 757–766 (2003)

[2] Grünwald, D., Singer, R.H. & Rout, M., *Nuclear export dynamics of RNA – protein complexes*. Nature Review **31,** 28–31 (2011)

[3] Sakiyama, Y., Mazur, A., Kapinos, L.E. & Lim, R.Y.H., *Spatiotemporal dynamics of the nuclear pore complex transport barrier re-solved by high-speed atomic force microscopy*. Nat. Nanotechnol. 1–6 (2016)

[4] Kapinos, L.E., Schoch, R.L., Wagner, R.S., Schleicher, K.D. & Lim, R.Y.H., *Karyopherin-centric control of nuclear pores based on molecular occupancy and kinetic analysis of multivalent binding with FG nucleoporins*. Biophys. J. 106, 1751–1762 (2014)

[5] Kiseleva, E., Goldberg, M.W., Daneholt, B. & Allen, T.D., *RNP export is mediated by structural reorganization of the nuclear pore basket*. J. Mol. Biol. **260,** 304–11 (1996)

[6] von Appen, A. *et al. In situ structural analysis of the human nuclear pore complex*. Nature **526,** 140–143 (2015)

[7] Kosinski, J. *et al. Molecular architecture of the inner ring scaffold of the human nuclear pore complex*. Science **352,** 363–365 (2016)

[8] Lin, D.H. *et al., Architecture of the symmetric core of the nuclear pore*. Science, **352** (6283)**,** 1015-1015 (2016)

[9] Stoffler, D., Goldie, K.N., Feja, B. & Aebi, U., *Calcium-mediated structural changes of native nuclear pore complexes monitored by time-lapse atomic force microscopy*. J. Mol. Biol. **287,** 741–752 (1999)

[10] Perez-Terzic, C., Pyle, J., Jaconi, M., Stehno-bittel, L. & Claphamt, D.E., *Conformational States of the Nuclear Pore Complex Induced by Depletion of Nuclear Ca2+ Stores*. Science **273** (5283)**,** 1875–1877 (1996)

Hybrid spin-nanomechanics with diamond cantilevers

Project P1206 Nanomechanical oscillators for diamond spin-optomechanics
Project Leader: P. Maletinsky and R. Warburton
Collaborators: A. Barfuss (SNI PhD Student), J. Kölbl, M. Kasperczyk, J. Teissier, and P. Appel

Introduction and motivation

An individual electronic spin coupled to a nanomechanical oscillator constitutes a prototypical "hybrid quantum system". Such systems form highly valuable quantum resources for fundamental investigations of quantum mechanics and for potential high-performance nanoscale sensors [1]. Specifically, these systems are highly attractive candidates for studying the crossover from quantum to classical physics and they have the potential to yield novel types of high-performance sensing devices for diverse quantities such as mass, acceleration or pressure. Furthermore, such hybrid systems can be exploited for efficient, coherent manipulation of a quantum system by purely mechanical means [2] – an approach which could be highly advantageous over established methods due to its compactness and efficiency.

In this project, we exploit a particular, novel hybrid spin-mechanical system consisting of a single, electronic "Nitrogen-Vacancy" (NV) spin, embedded in a diamond mechanical oscillator (Fig. 1, inset). The individual sub-systems in our devices - the spin and the oscillator - are highly attractive for the experiments we envisage: Diamond nanomechanical resonators, have been shown to exhibit very high quality-factors up to Q~10^6 [3], and therefore form a well-isolated, high-quality nanomechanical system. NV center electronic spins are advantageous in this context for multiple reasons. They form a spin-1, three level system, which is highly quantum coherent, even at room temperature, with quantum coherence times approaching one second. The NV spin can be conveniently read out and initialized using optical means and coherently manipulated using microwave magnetic fields. Our NV-based hybrid spin-mechanical system is therefore ideally suited to study the subtle effects a single spin could have on the mechanical oscillator and vice versa.

Key experimental results

Our work this year focused on two activities related to such hybrid spin-mechanical quantum systems. On one hand, we explored coherent, parametric driving of the spin by a mechanical oscillator for coherence protection of the spin [4]. On the other hand, we extended our existing activities to cryogenic operation, where spin-oscillator coupling in the spin's excited state can be studied.

Parametric driving of a spin refers to the periodic modulation of the spin's energy splitting by an external control field, which in our case corresponds to the time-varying strain field along the NV axis, which is generated by the mechanical oscillator. In conjunction with conventional microwave driving of the spin transition, such parametric driving can lead to phenomena such as spin-locking or coherence protection by dynamical decoupling through "concatenated coherent driving" [5].

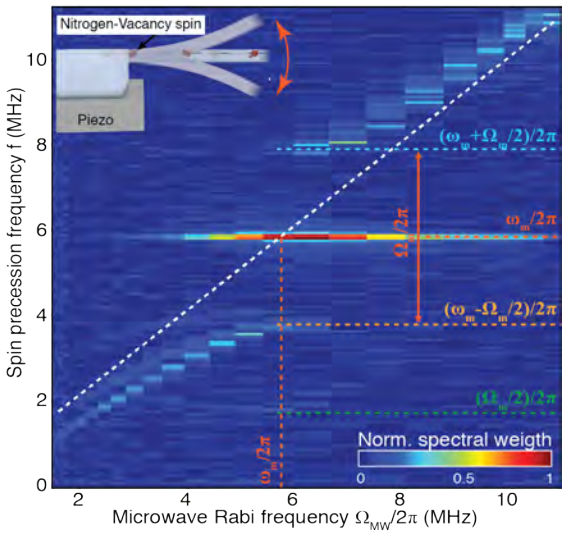

Fig. 1 Frequency-locking of a driven NV spin to a nanomechanical oscillator. Spin precession spectrum under combined microwave drive and parametric mechanical strain-driving, as a function of microwave Rabi frequency Ω_{MW}. The spectra were obtained by Fourier-transforming the experimentally acquired Rabi oscillation data for each Ω_{MW}. The white dashed line follows $f = \Omega_{MW}/2\pi$, i.e. the precession frequency expected for pure microwave driving within the rotating wave approximation. The additional spin frequency components in the spin precession spectrum (see colored dashed lines) are a result of parametric driving of the NV spin, which can be explained in a picture of a "double-dressed" spin. The inset illustrates the key parts of the sample investigated.

In our work, we have investigated the phenomenon of strain-induced spin-locking for the first time. Spin-locking can be observed in an experiment, where the NV is coherently driven into Rabi precession by an external microwave field of controlled amplitude Ω_{MW} and in the presence of a parametric drive of frequency ω_m. For varying Ω_{MW}, one observes a striking "locking" of the spin's Rabi precession frequency to ω_m, as soon as the condition $\Omega_{MW} \approx \omega_m$ is fulfilled. This behavior is demonstrated by the experimental data shown in figure 1 and is the main evidence that our hybrid quantum systems allow for such spin-locking phenomena to be observed.

This spin-locking can further be employed to protect the quantum coherence of the NV spin - a key resource for quantum sensing or quantum information processing applications of such spins. We have systematically studied such coherence protection phenomena in our nanomechanical system. For example, we have conducted Rabi nutation experiments with the NV spin, using a microwave driving field in presence of the coherent parametric strain drive. The time-trace of this signal (Fig. 2) shows sustained, coherent Rabi oscillations over a timescale of ~3 ms, i.e. approaching the fundamental "T_1-limit" imposed by energy relaxation of the spin. Our systematic studies [4] revealed how these findings can be interpreted in the context of "double-dressing" of the NV spin and suggested a route to harnessing this coherence protection for future quantum technologies.

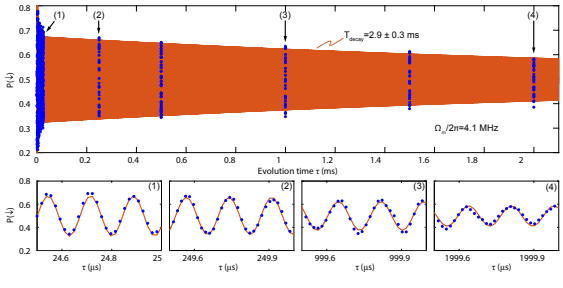

Fig. 2 Protection of NV spin coherence by parametric, mechanical driving. Single spin Rabi oscillations stabilised by parametric, mechanical driving with $\Omega_{MW}/2\pi$=4.1 MHz. Data (blue dots) are well fit by an exponentially damped oscillation (orange) with decay time T_{decay}=2.9 ms and a spin-precession (Rabi) frequency 5.83 MHz. The sub-panels show zoomed views over the measurement intervals labelled (1)- (4) and confirm that the slowly decaying signal indeed consists of monochromatic Rabi oscillations at the mechanical frequency $\omega_m/2\pi$.

In addition to these room temperature studies of coherence protection by parametric driving, we have extended our experiment to allow for investigations of our hybrid spin-mechanical systems under cryogenic conditions. In particular, we have constructed a brand-new setup based on a closed-cycle, "dry" cryostat (attoDRY800 from Attocube), which allows for long-time continuous measurements without the need to handle cryogenic liquids. Our activities in this direction are largely motivated by the prospect of studying spin-strain interactions in the NVs excited orbital states, where the interaction strength is predicted to be ~10^5 × stronger than in the ground state we investigated up until now. We have achieved preliminary results that demonstrate such enhanced strain interactions, by following up on our initial "beam-bending" experiments that forms the starting point of this project [6]. In particular, we have demonstrated narrow optical linewidths [7] in our diamond nanostructures [8], combined with tuning of the optical emission line through strain by tens of terahertz - an interesting future avenue for large range tuning of the emission frequency of a single quantum emitter.

Outlook

In the next year, we will further pursue the two lines of research highlighted in this report. We will on one hand further investigate room temperature coherent dynamics of the NV spin coupled to our nanomechanical oscillators, with a particular focus on coherence protection and quantum interference phenomena. On the other hand, we will further push control and understanding of our cryogenic experiments, where we expect highly interesting results regarding spectroscopy of the NV centers electronic states and their use in NV-cantilever coupling. These studies will bring significant advances towards our ultimate goal to use spins to cool [9] and quantum-control macroscopic mechanical objects.

References

[1] P. Treutlein, C. Genes, K. Hammerer, M. Poggio, and P. Rabl, *Hybrid Mechanical Systems* (Springer, 2014)

[2] A. Barfuss, J. Teissier, E. Neu, A. Nunnenkamp, and P. Maletinsky. *Strong mechanical driving of a single electron spin*, Nature Physics 11, 820 (2015)

[3] P. Ovartchaiyapong, L.M.A. Pascal, B.A. Myers, P. Lauria, A.C. Bleszynski-Jayich, *High quality factor single-crystal diamond mechanical resonators*, Appl. Phys. Lett. 101, 16, 163505

[4] J. Teissier, A. Barfuss P. Maletinsky, *Hybrid continuous dynamical decoupling: a photon-phonon doubly dressed spin, ArXiv:*1611.01515 (2016)

[5] J.M. Cai, B. Naydenov, R. Pfeiffer, L. McGuinness, K. Jahnke, F. Jelezko, M. Plenio, A. Retzker. *Robust dynamical decoupling with concatenated continuous driving,* New J. Phys. 14, 11, 113023 (2012)

[6] J. Teissier, A. Barfuss, P. Appel, E. Neu, and P. Maletinsky. *Strain Coupling of a Nitrogen-Vacancy Center Spin to a Diamond Mechanical Oscillator*, Phys. Rev. Lett. 113, 020503 (2014)

[7] Y. Chu, N.P. de Leon, B.J. Shields, B. Hausmann, R. Evans, E. Togan, M.J. Burek, M. Markham, A. Stacey, A.S. Zibrov, A. Yacoby, D. J. Twitchen, M. Loncar, H. Park, P. Maletinsky, and M. D. Lukin. *Coherent Optical Transitions in Implanted Nitrogen Vacancy Centers*, Nano letters 14, 4, 1982 (2014)

[8] P. Appel, E. Neu, M. Ganzhorn, A. Barfuss, M. Batzer, M. Gratz, A. Tschoepe, P. Maletinsky, *Fabrication of all diamond scanning probes for nanoscale magnetometry*, Rev. Sci. Instrum. 87, 063703 (2016)

[9] I. Wilson-Rae, P. Zoller, and A. Imamoglu, *Laser Cooling of a Nanomechanical Reso-nator Mode to its Quantum Ground State*, PRL 92, 075507 (2004)

Using proteorhodopsin to drive a molecular hoover

Project P1207 Design of a polymer membrane-based molecular “hoover”
Project Leader: W. Meier and D.J. Müller
Collaborators: R. Goers (SNI PhD Student), J. Thoma, and N. Ritzmann

Introduction

The creation of nanocells, which resemble a light-driven molecular hoover, requires the functional assembly of synthetic membranes and certain membrane proteins, which provide the function-ality. The reconstitution process of membrane proteins is still a challenge and requires separate optimization for every membrane protein [1, 2]. Especially in case of proteins with a directional function, such as transport, the final orientation is crucial for full functionality [4]. Furthermore, after the reconstitution of the membrane protein, it is necessary to evaluate its functionality and to characterize it’s localization in the structure.

Materials & Methods

In order to bypass the need for additional labeling and to influence the orientation after reconstitution, fusion proteins (PR-GFP/PR-mCh) of the transmembrane proton pump proteorhodopsin (PR) and the water-soluble green and red fluorescent protein (GFP/mCh) were created and fused to PR’s C- or N-terminus (Fig. 1a). The hydrophilic nature of GFP should influence the orientation of PR during reconstitution. The inner hydrophobic domain of the membrane should prevent GFP from passing through and thus, PR’s corresponding terminus should always be facing outwards of the vesicle. This should lead to proton transport into or out of the interior of the vesicle. The statistical modeling technique design of experiments (DoE) has gained considerable attention in industry and academic science, especially in engineering topics such as process optimization [3]. It allows an efficient screening of relevant factors and their inter-actions and is thus an ideal candidate for optimi-zation of membrane protein reconstitutions (Fig. 1b)[3]. A definitive screening design was emp-loyed to analyze the influence of the detergent n-octyl-β-D-glucoside (OG), the pH value and to find proper ratios of PR to the lipid 1,2-Dioleoyl-sn-glycero-3-phosphocholine (DOPC) or to the PMOXA17-PDMS65-PMOXA17 (ABA) block co-polymer, which were also used as parameters. The resulting structures were characterized via dynamic light scattering (DLS), transmission electron microscopy (TEM) and fluorescence correlation spectroscopy (FCS). In addition we further characterized the proton pumping activity by encapsulating the pH sensitive fluorescent dye pyranine and recording its intensity over time during illumination at 525 nm. The PdI, the size determined by FCS and DLS were defined as responses, as well as the relative change of pyranine’s fluorescence intensity. The results were used to construct a response surface (RS), which was then used to analyze the influence of these parameters and predict possible optimal conditions.

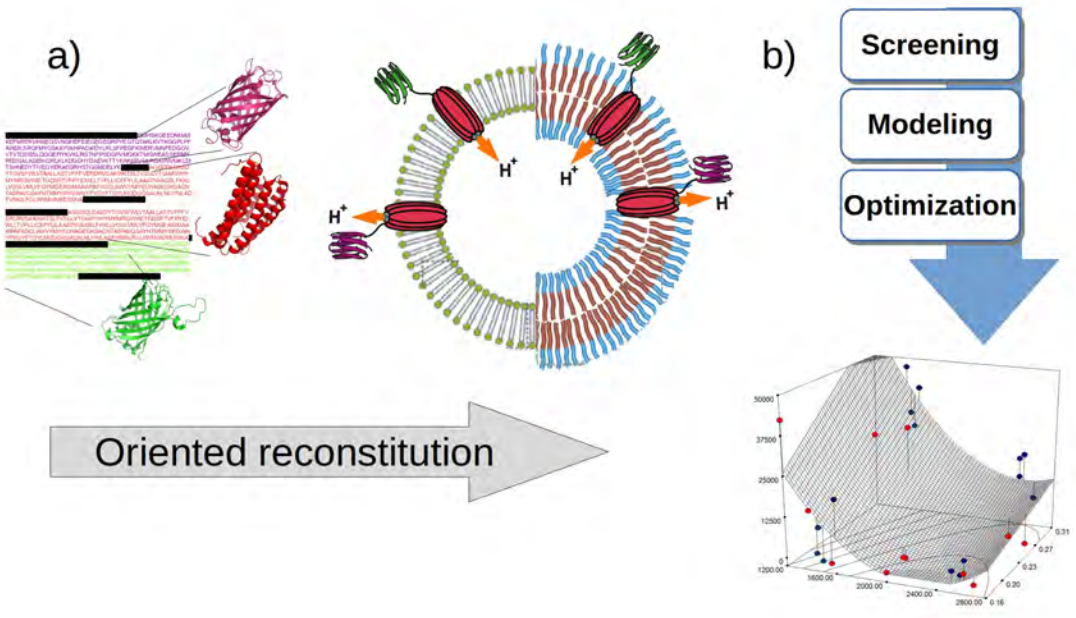

Fig. 1 Graphical overview of the creation and application of PR fusion proteins (a). GFP (green) and mCherry (violet) are fused to the corresponding C- or N-terminus. Due to the hydrophilic nature of GFP and mCherry, it orients itself such that the protons are transported inwards in case of GFP and outwards for mCherry. The protein’s behavior during reconstitution and the characterization of the resulting structures can be efficiently studied by applying design of experiments in order to detect significant parameters and their influence (b).

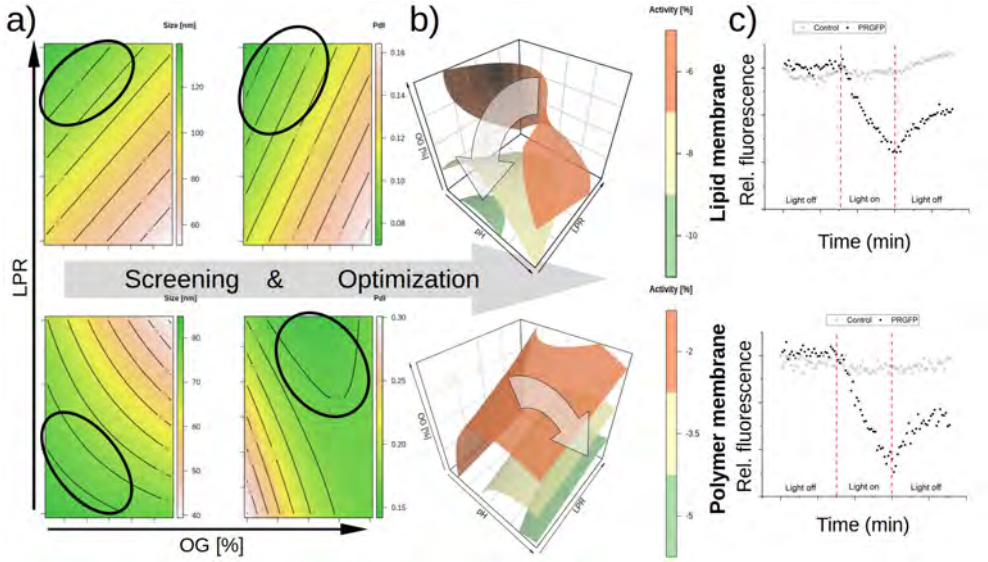

Fig. 2 a) The sizes data obtained from FCS show very different behavior of PR-GFP insertion. Formation of proteoliposomes appears to require a minimum amount of OG to obtain sizes in the range of 100 nm, whereas proteopolymersomes require low amounts to assemble in a similar size range. Using minimum requirements in terms of size and PdI, a region of interest can be identified. b) This parameter space was sampled and its results used for activity optimization. c) The performance in ABA polymersomes is comparable to the DOPC liposomes and reports found in liposomes literature [4].

Results & Discussion

The analysis of the experimental results was grouped in two steps: *i)* find conditions which yield proper vesicular structures (e.g. size >100nm, PdI < 0.15) and *ii)* investigate the activity of these vesicles and maximize their proton pumping activity (Fig. 2). Formation of proteo-liposomes worked best within a broad range of detergent and high amounts of protein, whereas proteopolymersomes required low amounts of protein and detergent, as well as a slightly basic environment (Fig. 2a). In general, the formed polymer vesicles exhibited a smaller diameter (around 60 nm compared to 110 nm) and a higher PdI (around 0.2 compared to 0.1), which is in agreement to results from literature [1, 2, 4]. Subsequent activity screening within this parameter space obtained the necessary data to optimize the response surface. Figure 2b illustrates the optimization process in which the possible parameter space converges towards an optimum. The found optima were remarkably different. Highest activity for the proteoliposomes was found when the reconstitution was carried out at pH 6, using 0.5 % (w/v) of OG and a LPR of 25. In contrast active proteopolymersomes require a basic pH of 7.8, 0.5 % (w/v) and a PPR of 125. Measuring the proton pumping activity of vesicles formed with the optimal conditions showed that a gradient was formed in both cases and its amplitude was according to the predictions made by the derived model (Fig. 2c).

Conclusion

In conclusion, this work demonstrates that *i.* DoE is a powerful tool to gain control over the assembly process and offers valuable insight, *ii.* PR-GFP fusion proteins allow influencing the orientation during reconstitution and furthermore *iii.* the predictions made by the model are accurate and the resulting proteoliposomes and –polymersomes were active in terms of proton transport.

References

[1] C.G. Palivan, R. Goers, A. Najer, X. Zhang, A. Car and W. Meier, *Bioinspired polymer vesicles and membranes for biological and medical applications*, Chem. Soc. Rev., 2016, 45, 377 - 411

[2] J.-L. Rigaud and D. Lévy, *Reconstitution of membrane proteins into liposomes*, Methods Enzymol., 2003, 372, 65-86

[3] S.A. Weissman and N.G. Anderson, *Design of experiments (DoE) and process optimization*, Org. Process Res. Dev., 2015, 19, 1605-1633

[4] D. Harder, S. Hirschi, Z. Ucurum, R. Goers, W. Meier, D.J. Müller and D. Fotiadis, *Engineering a Chemical Switch into the Light-driven Proton Pump Proteorhodopsin by Cysteine Mutagenesis and Thiol Modification*, Angew. Chem Int. Ed. Engl., 2016, 55 (31), 8846-8849

High resolution contact potential variations

Project P1208 Ultra-sensitive force detection and molecular manipulation
Project Leader: E. Meyer and M. Poggio
Collaborators: M. Schulzendorf (SNI PhD Student), S. Kawai, Th. Glatzel, A. Hinaut, R. Pawlak, U. Gysin, Y. Pellmont, and S. Decurtins

The project is within its last months. S. Kawai moved to Japan for a new position and M. Schulzendorf started writing his thesis. The new low-temperature Atomic Force Microscope (LT-AFM) has been moved to Japan during this summer. At this point we would like to review the four years that have past and show some new high resolution measurements on KBr/Cu(111).

Review

The new LT-AFM has been developed and constructed in-house. It allows for the use of standard silicon cantilevers at low temperatures down to 4K with the beam deflection method. The clear advantage to conventional tuning-fork microscopes is the use of higher harmonics of the cantilever at low temperatures, dramatically improving the force sensitivity [1].
While the new microscope has been built we investigated the intercalation of graphene islands by KBr thin-films on Cu(111) with a home-built AFM in ultra-high vacuum (UHV) at room temperature.
In our lab we employed noncontact Atomic Force Microscopy (nc-AFM) [2] with a multimodal setup for our measurements, simultaneously actuating the cantilever mechanically and electronically at different eigenmodes.
Our samples have been prepared *in situ*. Graphene nano-flakes have been prepared according to Gao et al. [3], Ethylene gas (CanGas) was directly dosed on a clean Cu(111) surface via a fine nozzle (outlet diameter 2 mm, distance 10 mm and 60° tilt in respect to surface).
By means of FM-KPFM [4], shown in figure 1, a shift of 400 mV in the work-function of graphene in presence of KBr was found. This strong change in the electronic properties was a first indication that graphene could have been intercalated.

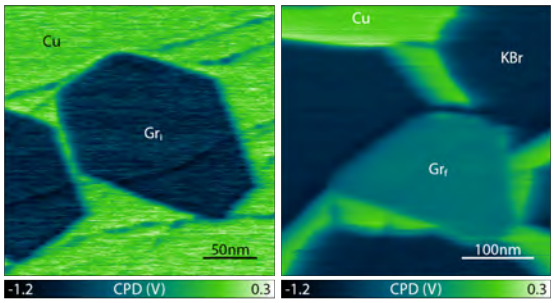

Fig. 1 Change in the work function of graphene upon KBr deposition. On bare copper the CPD of graphene (Gr$_i$) was 850 mV (left), in presence of KBr the CPD of graphene (Gr$_f$) was 450 mV (right) in respect to copper.

These experiments were complemented by X-Ray Photoelectron Spectroscopy at the Swiss Light Source (SLS). As shown in figure 2, a clear change upon co-adsorption of graphene and KBr occurred for both materials.

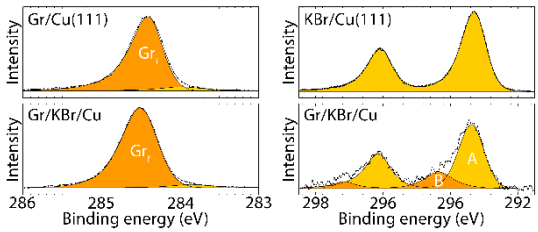

Fig. 2 Core level of C 1s and K 2p (right) before (top) and after the intercalation (bottom). The C 1s peak shifted towards a binding energy comparable to graphite. For K 2p a second species (B) was found, related to graphene.

While the core level (C 1s) for graphene became comparable to those of graphite. Angle resolved data, not shown here, showed that the intensity of the new species found for KBr (K 2p) has been attenuated by the graphene, further indicating intercalation.

High resolution of KBr on Cu(111)

Recently, we resolved the local contact potential difference (LCPD) on KBr/Cu(111) by means of frequency modulated Kelvin Probe Force Microscopy (FM-KPFM) [2] with the second flexural mode of a cantilever.

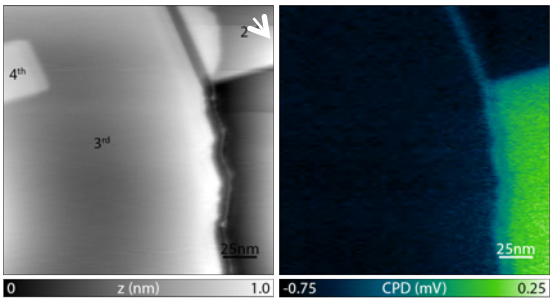

Fig. 3 Topography of KBr thin-films on Cu(111) (left side) and CPD (right side). In the left part of the topography a 3rd layer island with a square 4th layer on top can be seen, in the top corner is a 2nd layer. The CPD between the metal and the insulator is 1V.

A Cu(111) single-crystal (Mateck), has been cleaned by repeated Ar-sputtering and annealing. KBr (crushed single-crystal, Mateck) has been evaporated on the clean copper surface that was kept at 150 °C during the evaporation. As visible in figure 3 the most abundant island height was of 2nd and 3rd layer. Th. Glatzel *et al.* showed earlier that the CPD of different layers can be distinguished by AM-KFPM [5]. Here only the CPD between copper and the alkali halide has been resolved, as the variation between the layers compared to the signal to noise ratio was too small.

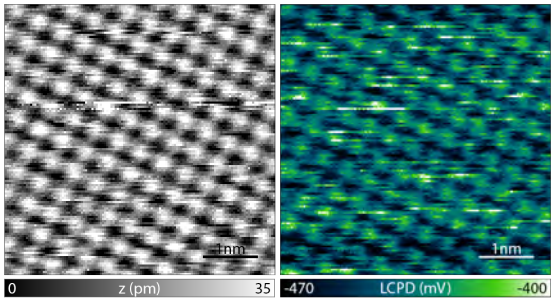

Fig. 4 Topography (left) showing atomic resolution on the second layer island. The local CPD variations (right) became visible on an atomic scale.

Atomic resolution in topography and CPD has been obtained on the third layer, not shown here, and the second layer islands, shown in figure 4. The contrast of the LCPD followed the topography. The origin of the CPD at the atomic level is not yet fully understood. In case of NaCl single crystals it could be attributed to short-range forces arising from moving ions [6]. The movement was induced by the ac-bias applied to the surface by KPFM, enhancing resolution [7]. This can also be expected for the KBr thin films.

Conclusion

Within this project a new LT-AFM was built that enables ultra-sensitive force measurements down to temperatures of 4K. Our studies on the co-adsorption of graphene and KBr thin-films on copper revealed strong changes for graphene and KBr, indicating intercalation of graphene by KBr. In addition, we showed high-resolution nc-AFM and FM-KPFM measurements at room temperature.

References

[1] F. Federici Canova, S. Kawai, C. de Capitani, K. Kan'no, T. Glatzel, B. Such, A.S. Foster and E. Meyer, *Energy Loss Triggered by Atomic-Scale Lateral Force*. Phys. Rev. Lett. 110, 203203 (2013)

[2] Morita, S., Giessibl, F.J., Meyer, E. & Wiesendanger, R. *Noncontact atomic force microscopy*. Vol. **3,** Springer Berlin Heidelberg, (2015)

[3] Gao, L., Guest, J.R. & Guisinger, N.P. Epitaxial graphene on Cu(111). *Nano Lett.* 10, 3512–6 (2010)

[4] Kitamura, S. & Iwatsuki, M. *High-resolution imaging of contact potential difference with ultrahigh vacuum noncontact atomic force microscope*. Appl. Phys. Lett. 72, 3154–3156 (1998)

[5] Glatzel, T. *et al. Determination of effective tip geometries in Kelvin probe force microscopy on thin insulating films on metals.* Nanotechnology, 20, 264016 (2009)

[6] Sadeghi, A., Baratoff, A. & Ghasemi, S. *Multiscale approach for simulations of Kelvin probe force microscopy with atomic resolution*. Phys. Rev. B 86, 75407 (2012)

[7] Nony, L., Foster, A., Bocquet, F. & Loppacher, C. *Understanding the Atomic-Scale Contrast in Kelvin Probe Force Microscopy*. Phys. Rev. Lett. 103, 36802 (2009)

Design of polymer nanoreactors with triggered activity

Project P1209 Design of polymer nanoreactors with triggered activity
Project Leader: C.G. Palivan and J. Huwyler
Collaborators: T. Einfalt (SNI PhD Student)

Introduction

Mimicking biological processes, by engineering biomimetic nanostructures, is a fundamental concept relevant to various scientific fields such as materials science, chemistry, electronics and medicine [1, 2]. By using the strategy of biomimicry at the molecular level it is possible to combine highly efficient and specific biological molecules (e.g. proteins, lipids, DNA) with robust synthetic materials (e.g. porous silica surfaces, block copolymers) [3]. In this respect, biomolecules combined with nanoassemblies that provide a high degree of architectural control can providebe used both for insights in the progression from non-living materials to a living system, and translational applications [4, 5].

Here, we extend the concept of nanoreactors with triggered activity by introducing nanocarriers for protein delivery, as a complementary strategy with medical potential. Asymmetric poly(ethylengycol)-b-poly(methylcaprolactone)-b-poly(2-(N,N diethylamino)ethylmethacrylate) (PEG-b-PMCL-b-PDMAEMA) copolymers were used to self-assemble into soft nanoparticles (NP) with a morphology serving for attachment of proteins (Scheme 1) [3]. The hydrophilic/hydrophobic ratio, nanoparticle size, and the nature of attached bio-molecules were key factors for modulating protein localization and attachment efficiency [4]. We have evaluated the efficacy of the polymer nanoparticles as protein carriers with both, a model protein – bovine serum albumin (BSA), and acid sphingomyelinase (ASM) - known for its role in catalyzing the breakdown of sphingomyelin to ceramide in the treatment of Niemann-Pick disease.

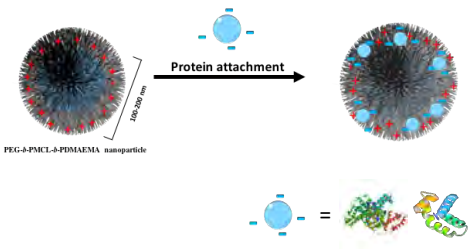

Scheme 1 Schematic illustration of the self-assembly of PEG-b-PMCL-b-PDMAEMA copolymers before and after interaction with a charged protein at pH 7.2.

Self-assembly of PEG-b-PMCL-b-PDMAEMA copolymers

Self-assembly of PEG-b-PMCL-b-PDMAEMA (PEG_{45}-b-$PMCL_{110}$-b-$PDMAEMA_{37}$ and PEG_{45}-b-$PMCL_{101}$-b-$PDMAEMA_{27}$) copolymers was performed at various pH values in the range 3.5 - 10 to analyze both the resulting 3D assemblies, and their pH responsiveness. Supramolecular architectures of the copolymers were characterized by a combination of light scattering (dynamic and static), and TEM. TEM micrographs of self-assembled nanostructures of copolymers show the coexistence of two populations of circular nanoparticles with different sizes (Fig. 1). Such nanoparticles had a morphology based on a core domain formed by PEG / PMCL blocks, and an outer corona mainly formed by the pH responsive PDMAEMA. This specific nanoarchitecture of NPs favors both the attachment of oppositely charged proteins, and their release in a pH-responsive manner.

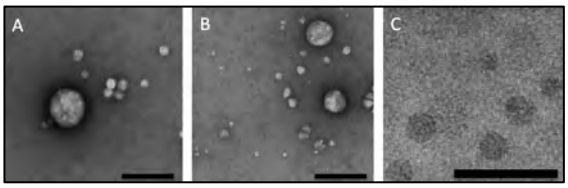

Fig. 1 TEM micrographs of 3D supramolecular assemblies generated by PEG-b-PMCL-b-PDMAEMA copolymers at physiological pH. A) $A_{45}B_{110}C_{37}$ copolymer, B) $A_{45}B_{101}C_{27}$ copolymer. C) Cryo-TEM micrograph of 3D supramolecular assemblies of A45B110C37 copolymer after 2 months. Scale bar: 200 nm.

pH sensitive behavior of PEG-b-PMCL-b-PDMAEMA soft nanoparticles

pH-sensitive behavior of PEG-b-PMCL-b-PDMAEMA soft nanoparticles indicates that indeed, the polymer domain exposed at the interface with the environment is mainly PDMAEMA, whilst PEG block is mainly confined in the soft core of nanoparticles. This privileged orientation of the hydrophilic domains supports attachment of charged biomolecules based on electrostatic interactions with the charged PDMAEMA, but no insertion inside the core due to the repellent property of PEG (Fig. 2).

Attachment of proteins to PEG-b-PMCL-b-PDMAEMA soft nanoparticles

A further step was to select model proteins and analyze how they interact with PEG-b-PMCL-b-PDMAEMA soft nanoparticles. Fluorescent labeled BSA and ASM were selected, due to their negatively charged backbone, which favors the interaction with positively charged nanoparticles. The attachment of proteins was monitored by fluorescence correlation spectroscopy, zeta-potential measurements and by following the enzymatic reaction of ASM – a key

parameter for the potential medical application of the nanoparticles. Since ASM is stable in acidic conditions, its activity was measured at pH 7.2 both for ASM attached-$A_{45}B_{110}C_{37}$ nanoparticles kept at this pH value, and for those previously exposed to acidic conditions for 60 min (pH = 5.5) (Fig. 3). The activity of ASM-$A_{45}B_{110}C_{37}$ kept at pH 7.2 was lower than that of ASM-particles previously exposed to acidic conditions due to the lower accessibility of ASM molecules at pH 7.2, being protected in the hydrophilic corona of the nanoparticles.

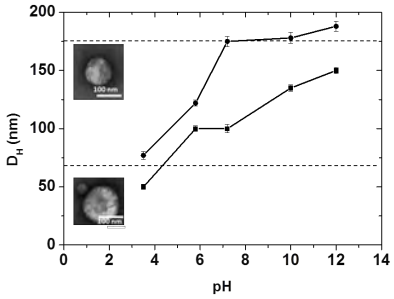

Fig. 2 Hydrodynamic diameter (DH) of PEG-b-PMCL-b-PDMAEMA NP. $A_{45}B_{110}C_{37}$ nanoparticles (circles), and $A_{45}B_{101}C_{27}$ nanoparticles (squares) at different pH values. Dashed lines represent a transition domain where both small and large nanoparticles co-exist.

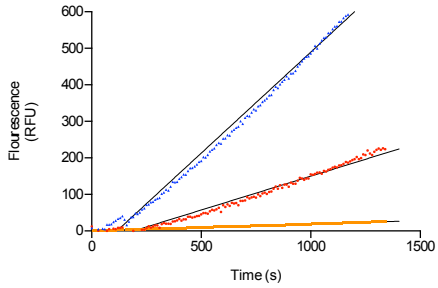

Fig. 3 Enzymatic activity of ASM measured at pH 7.2: ASM-$A_{45}B_{110}C_{37}$ nanoparticles kept at pH 7.2 (red), and ASM-$A_{45}B_{110}C_{37}$ nanoparticles exposed at pH 5.5 for 60 min (blue); $A_{45}B_{110}C_{37}$ nanoparticles (yellow).

Cellular integration of ASM-attached nanoparticles

To be applied as a therapeutic agent, cellular uptake of ASM-nanoparticles is essential, and therefore it was investigated in HeLa cells using confocal laser scanning microscopy (CLSM) and flow cytometry. In HeLa cells incubated with the Oregon green(o)-ASM/ABC nanoparticles for 24 h, the presence of a fluorescent signal for o-ASM/$A_{45}B_{110}C_{37}$ nanoparticles, and o-ASM/$A_{45}B_{101}C_{27}$ nanoparticles clearly indicated uptake of o-ASM loaded nanoparticles (Fig. 4).

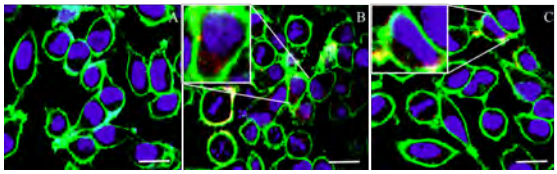

Fig. 4 Confocal laser scanning micrographs of HeLa cells. The cellular membrane was visualized by Cell Mask Deep Red (green), nuclei with Hoechst 33342 (violet), and o-ASM (red). A) Untreated cells, B) Cells treated with 50µg/ml o-ASM-A45B110C37 nanoparticles, C) cells treated with 50µg/ml o-ASM-A45B101C27 nanoparticles. Insets: zoomed regions of HeLa cells treated with 50µg/ml o-ASM-A45B110C37 and 50µg/ml o-ASM-A45B101C27 nanoparticles. Scale bar: 50 µm

Conclusion

Soft nanoparticles were produced using the copolymer poly(ethylenegycol)-b-poly(methyl caprolactone)-b-poly(2-(N,N-diethylamino) ethyl methacrylate) with two different ratios of the hydrophobic to hydrophilic blocks. Nanoparticles were modified with conjugated proteins to develop an efficient protein delivery platform. The asymmetry of the block copolymers favors attachment of proteins and small molecular mass molecules: the PDMAEMA block is predominantly present at the external interface and promotes attachment of proteins and small molecular mass molecules carrying an opposite charge, whilst PEG is mainly embedded inside the hydrophilic domain. PEG-b-PMCL-b-PDMAEMA nanoparticles can bind a variety of charged biomolecules and then release them in a pH-responsive manner. This mechanism supports their future use for potential therapeutic applications. Our study is the first one showing that it is possible to deliver proteins in a pH responsive manner by their controlled immobilization at the interface between the nanoparticle and its environment.

References

[1] G. Martina, T. Einfalt, M. Lomora, A. Car, C.G. Palivan, *Artificial Organelles: Reactions inside Protein–Polymer Supramolecular Assemblies,* CHIMIA International Journal of Chemistry, 70 (6), 424-427 (2016)

[2] T. Einfalt, R. Goers, A. Najer, I.A. Dinu, M. Spulber, O. Onaca-Fischer, C.G. Palivan, *Stimuli-triggered activity of nanoreactors by biomimetic engineering polymer membranes,* Nano Letters, 15 (11), 7596-7603 (2015)

[3] C.G. Palivan, R. Goers, A. Najer, X. Zhang, W. Meier, *Bioinspired polymer vesicles and membranes for biological and medical applications,* Chem. Soc. Rev, 45, 377-411 (2015)

[4] D. Vasquez, T. Einfalt, W. Meier, C.G. Palivan, *Asymmetric triblock copolymer nanocarriers for controlled localization and pH-sensitive release of proteins,* Langmuir, 32 (40), 10235-10243 (2016)

[5] L.H. Dieu, L.H., D. Wu, C.G. Palivan, V. Balasubramanian, J. Hüwyler, *Polymersomes conjugated to 83-14 monoclonal antibodies: In-vitro targeting of brain capillary endothelial cells,* Eur. J. Pharm. Biopharm. 88, 316 (2014)

Nanowires as sensitive scanning sensors

Project P1210 Bottom-up nanowires as ultra-sensitive force transducers
Project Leader: M. Poggio and R.J. Warburton
Collaborators: D. Cadeddu (SNI PhD Student)

Introduction

We have continued our focus on two novel applications of nanowires (NWs) as sensitive scanning sensors. In the first, we used as-grown GaAs/AlGaAs NWs as scanning vectorial force sensors. By virtue of slight asymmetries in geometry, a NW's flexural mechanical modes are split into doublets corresponding to two orthogonal directions. By monitoring the frequency shift of both modes as we scan the nanowire above a surface, we construct a vectorial map of the in-plane force gradients in non-contact mode. This capability, combined with the exquisite force sensitivity of nanowire sensors, allows for a type of atomic force microscopy specially suited to directional measurements of weak tip-sample interactions or small friction forces. In the second, we realize a quantum fiber-pigtail and have started proof-of-principle experiments demonstrating its use as a sensitive scanning sensor. The device consists of a semiconductor quantum-dot embedded into a conical photonic wire that is directly connected to the core of a fiber-pigtail. We demonstrate a photon collection efficiency at the output of the fiber of 5.8% and suggest realistic improvements for the implementation of a useful device in the context of quantum information. The approach is generic and transferable to other materials including diamond and silicon. Both of these experimental directions have relied on the unique experimental apparatus and infrastructure built up for this project, i.e. a low-temperature scanning probe microscope customized for use with NW cantilevers and emitters.

NWs as sensors in a new type of atomic force microscopy

Self-assembled NW crystals can be grown into nearly defect-free nanomechanical resonators with exceptional properties, including small motional mass, high resonant frequency and low dissipation. Furthermore, by virtue of slight asymmetries in geometry, a NW's flexural modes are split into doublets oscillating along orthogonal axes. These characteristics make bottom-up grown NWs extremely sensitive vectorial force sensors as recently demonstrated by the Arcizet group in Grenoble [1]. We extended this concept by taking advantage of a single NW's adaptability as a scanning probe and demonstrating its ability to image a sample surface [2]. By monitoring the frequency shift and direction of oscillation of both modes as we scanned above the surface, we constructed a map of all spatial tip-sample force derivatives in the plane. Essentially, we used a NW like tiny mechanical compasses to measure both the direction and size of the surrounding forces, thereby producing a full map of the tip-sample force fields in two-dimensions. A NW was also used to image AC electric force fields produced by voltages applied to tiny gates patterned on a surface. The team was able to distinguish between forces arising from the NW charge and polarizability.

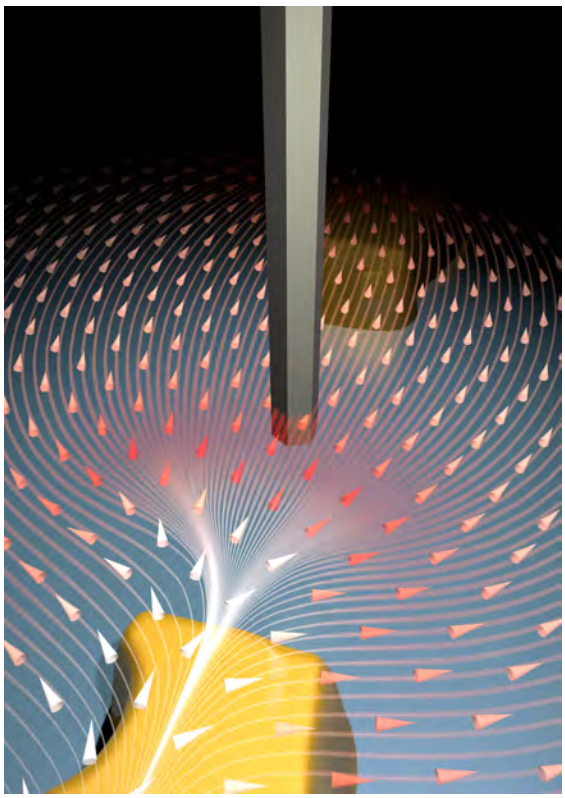

Fig. 1 An artist's representation of a NW force sensor immersed in a vector force field.

This universally applicable technique enables a form of atomic force microscopy particularly suited to mapping the size and direction of weak tip-sample forces. It could be used, for instance, to measure magnetic forces with proper functionalization of the NW tip or even in liquid for the study of batteries, water splitting or fuel cells. The same directional technique could be applied to NWs that are grown or processed to have sharp tips, presenting the possibility of atomic resolution. With such capabilities, one could imagine the use of vectorial NW-based AFM of tip-sample forces and non-contact friction to reveal, for example, the anisotropy of atomic bonding forces.

Scanning quantum fiber-pigtail

Semiconductor quantum-dots (QDs) are attractive single photon sources. They are robust, compact and provide on-demand single photons at rates in the GHz range. Their potential in the context of

quantum optics however relies on the fulfillment of several demanding criteria: high efficiency, high photon purity, and simple operation. Recent progress has nevertheless brought QDs close to such applications. Single-photon operation has been obtained in a compact, table-top Stirling machine, offering a low-cost and user-friendly solution.

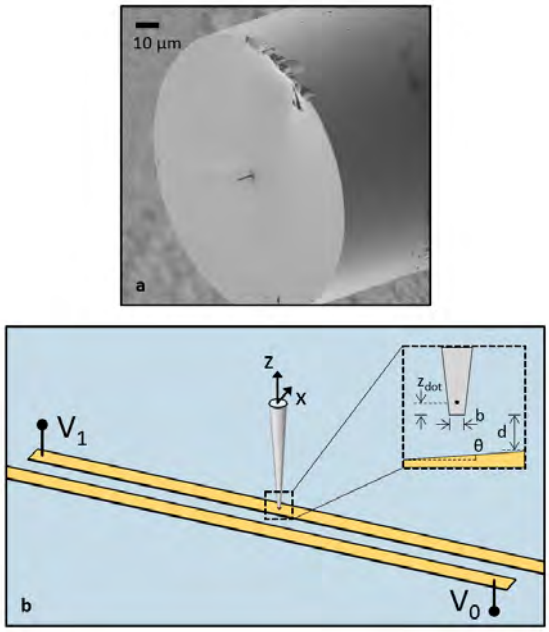

Fig. 2 a) SEM of a quantum fiber-pigtail. b) Schematic diagram of a quantum fiber-pigtail scanned above two patterned electrodes.

Thanks to the increasing quality of the epitaxial material, spectrally pure emission has been demonstrated. The last challenge that needs to be addressed is to efficiently couple the emitted light into a single mode fiber. Great progress in this direction has been made with the integration of QDs into micro and nanoscale photonic structures, such as cavities and waveguides, which allow the control of spontaneous emission. In the last few years, important efforts to position the QD in an optimal way and to minimize the diffraction of light at the output of photonic NWs have pushed the collection efficiencies to values > 75% while maintaining a Gaussian spatial profile. These impressive results require, however, the use of objective lenses with large numerical apertures. In parallel, different strategies to couple the emitted light directly into a single mode fiber have emerged.

In the past two years, we have realized the experimental realization of a quantum fiber-pigtail for convenient and efficient extraction of QD photons [3]. The device consists of a semiconductor quantum-dot embedded into a conical photonic wire that is directly connected to the core of a fiber-pigtail. We demonstrate a photon collection efficiency at the output of the fiber of 5.8% and suggest realistic improvements for the implementation of a useful device in the context of quantum information.

In the last year, we have focused on a proof-of-principle demonstration of this device as a scanning electric field sensor, with potential applications in scanning probe microscopy.

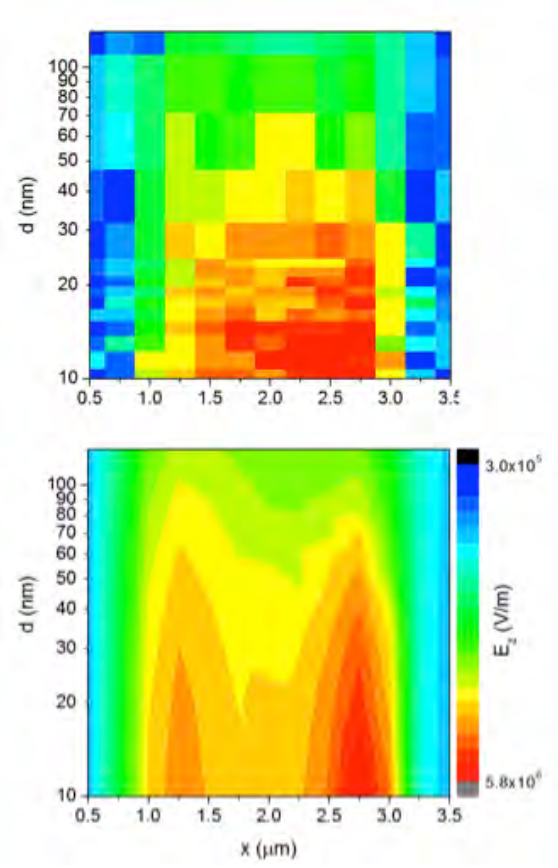

Fig. 3 Measured (top) and simulated (bottom) electric field in the z-direction above a patterned electrode. The data was measured by monitoring the quantum-confined Stark effect of a single QD at the tip of a scanning quantum fiber-pigtail.

In particular, use the tip-like geometry of the fiber-pigtail to scan and monitor a single optically active QD. We map the z-component of the electric field induced by a pair of electrodes patterned on a surface by measuring the quantum-confined Stark effect induced on the spectral line of the QD at the pigtail tip. Our results are in good agreement with finite element simu-lations of the experiment. Furthermore, these simulations point to realistic improvements of the device, which should allow us increase sensitivity to electric fields.

References

[1] A. Gloppe, P. Verlot, E. Dupont-Ferrier, A. Siria, P. Poncharal, G. Bachelier, P. Vincent, and O. Arcizet, *Bidimensional nano-optomechanics and topological backaction in a non-conservative radiation force field*, Nat. Nanotechnol. 2014, 9, 920.

[2] N. Rossi, F.R. Braakman, D. Cadeddu, D. Vasyukov, G. Tütüncüoglu, A. Fontcuberta, I. Morral, and M. Poggio, *Vectorial scanning force microscopy using a nanowire sensor*, Nat. Nanotechnol., 2016, 12, 150.

[3] D. Cadeddu, J. Teissier, F.R. Braakman, N. Gregersen, P. Stepanov, J.-M. Gérard, J. Claudon, R.J. Warburton, M. Poggio, and M. Munsch, *A fiber-coupled quantum-dot on a photonic tip*, Appl. Phys. Lett., 2016, 108, 01111.

Electron optics in encapsulated graphene

Project P1211 Electrical properties of ultraclean suspended graphene
Project Leader: C. Schönenberger and D. Zumbühl
Collaborators: C. Handschin (SNI PhD Student), P. Rickhaus, and P. Makk

Motivation

The rise of graphene during the last decade can be attributed to several unique features. To name only a few of them: the linear dispersion relation of the charge carriers, which makes electrons to behave as photons, the vanishing density of states at the Dirac point where conduction and valence bands touch, or the high mobility and ballistic electron transport with mean-free paths that can reach or even exceed several micrometers.

Research has shown, that in order to access the interesting physics of pristine graphene, the environmental influences (potential fluctuations from the substrate, unintentional chemical doping etc.) have to be reduced to a minimum. Currently the two most prominent techniques to obtain "clean" graphene are to either freely suspend the graphene or encapsulate it between hexagonal boron-nitride (hBN), which like graphene is a layered material but a non-conducting one. Even though suspended graphene yields the highest graphene quality, the device geometries which can be realized are rather limited [1]. This can be circumvented by encapsulating graphene in hBN. Encapsulation of graphene in hBN holds several additional advantages, such as e.g. the possibility to create a sharp *pn*-junctions (using electrostatic gates) which is desirable for the realization of several experiments, such as the Veselago lens or a Michelson-Morley interferometer. Another advantage is the ability to create a superlattice in graphene with hBN. The small lattice mismatch between graphene and hBN causes a periodic potential modulation leading to a Moiré pattern. These results in a band-reconstruction of graphene, including the emergence of so called satellite Dirac-peaks (DP), which can be resolved in transport measure-ments as shown in figure 1c.

Michelson Morley Interferometer

We continued our efforts towards the realization of a Michelson-Morley interferometer (MMI) in graphene, which works in analogy to the MMI known from optics. The MMI is a two-path interferometer, where a tilted *pn*-interface is used as the semi-transparent interface (beam-splitter) and the graphene edges as the mirror-analogues. For more details concerning the working principle please refer to the SNI report from 2015. Up to now we could not observe an interference signal. We spent considerable effort to improve the most reasonable limitations of the experiment. Those are i) the *pn*-interface and edge-roughness and ii) the lack of a collimated source of charge-carriers. The roughness of the *pn*-interface and the edges are responsible for scattering events, thus suppressing the observation of an interference signal. Even with using naturally torn graphene flakes, which we hoped would reduce scattering events at the edges compared to reactive ion etched samples, no significant improvement was seen. Concerning the lack of a collimated source of charge-carriers we plan to implement a pinhole collimator, based on the results which were just recently published, in our next devices.

It is worth mentioning that an alternative approach how to produce a source of collimated charge carriers is based on our earlier publication on Point-contacts [2], in combination with a *pn*-junction having a parabolic shape. The charge-carriers, which emerge isotropically from the point-source, will be collimated by the parabolic shaped *pn*-junction. However, at the current stage it seems that the experimental realization of this proposal is more challenging compared to the pinhole collimator.

Due to other priorities (see next section), this project was temporarily paused but will be continued in the near future.

Fabry-Pérot resonances in a graphene/hBN Moiré superlattice

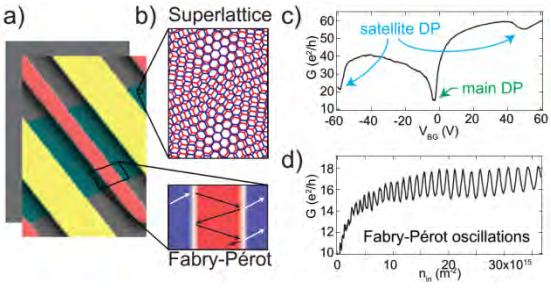

Fig. 1 Device geometry, superlattice and Fabry-Pérot signatures. a) False color SEM image of the 2-terminal pnp-device, where the leads are indicated with yellow, the top-gate with red and the graphene with cyan. b) The two key-ingrediences are the Moiré superlattice between graphene and hBN and the Fabry-Pérot resonances formed in the cavities. c) Conductance as a function of gate-voltage in the unipolar regime in the presence of a superlattice. d) Fabry-Pérot oscillations in the bipolar regime.

Similarly to the Michelson Morley Interferometer, Fabry-Pérot (FP) resonances are a phenomena well known from optics. Essential for the observation of FP resonances are two *pn*-junctions (semi-transparent interfaces), which are located perpendicular to the transport direction, as sketched in figure 1a and b. In this study we demonstrate confinement and appearance of FP resonances using band engineering. The semitransparent interfaces were defined either via the main or satellite DPs. Although several aspects of FP cavities have been investigated, such as the effect of the *pn*-junction smoothness on the visibility of the FP resonances,

the electronic enability of the cavity size has not been studied.

Even though the device dimensions (such as the width of the top-gate) are fixed, it turns out that the position of the *pn*-interface, which defines the effective width of the cavity, is tunable. We have shown that a given cavity length only depends on the ratio of the charge-carrier densities (n_{in}/n_{out}), by carefully tracking the exact position of the individual FP oscillation with varying charge-carrier densities. The latter requires a sample with very high FP visibility as shown in figure 1d. For the given device geometry and within the applied gate-range we found that each *pn*-interface can be shifted by roughly 100 nm. Our results are in good agreement with transport simulations, which were done by M.H. Liu.

Besides the tunable cavity length, we show within the same sample that the visibility of Fabry-Pérot (FP) resonances can be tuned, depending on the smoothness of the confining *pn*-interface. The smoothness of a *pn*-junction is defined as the ratio between the distance within which the charge-carrier density varies and the Fermi wavelength. In our system we can form two types of *pn*-interfaces. Either formed by using the electrostatic gates ("smooth" junction) or formed in the proximity of the n-doped contacts ("sharp" junction). The observed correlation between FP visibility and smoothness of the confining potential is in good agreement with what is expected from theory.

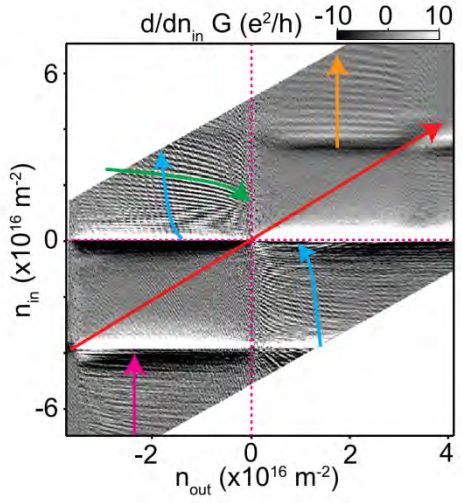

Fig. 2 Fabry-Pérot resonances in the presence of a Moiré superlattice. Numerical derivative of the conduction map as a function of inner and outer cavity densities. The various Fabry-Perot oscillations are indicated with the differently colored arrows.

So far we investigated FP resonances in the absence of a Moiré superlattice. However, by minimizing the angular mismatch between graphene and hBN to values below 1 degree, the band-reconstruction resulting from the superlattice becomes experimentally observable. At high doping the Fermi-energy is tuned beyond the satellite DP's, giving rise to a strong signal in the transport measurement. A direct proof that semitransparent interfaces can as well be formed via the satellite DP's is the observation of an additional set of FP resonances in the unipolar regime ($n_{in},n_{out}<0$ or $n_{in},n_{out}>0$), which is missing in the absence of a superlattice. This additional set of FP resonances is indicated with the purple and orange arrows in figure 2. For comparison, the FP resonances in the unipolar regime below the satellite DP are indicated with the red arrow, having a different behavior as a function of n_{in} and n_{out}. In addition, the FP resonances in the bipolar regime, where the semitransparent interface are defined via the main DPs, are indicated with the green and cyan arrows. By carefully analyzing the FP resonances defined via the satellite DP it is possible to extract information's on the band reconstruction, which is yet not fully known. Our observations are in good agreement with other experiments on the Moiré superlattice.

These results are published in Nano Letters [3].

We thank M. H. Liu and Klaus Richter from the University of Regensburg have supported us with tight-binding simulations for the Fabry-Pérot/Moiré experiment. High-quality hBN was provided by K. Watanabe, T. Taniguchi from the National Institute for Material Science at Tsukuba, Japan.

Outlook

The tunable *pn*-junctions can be used to probe local properties of the edges. By applying a strong magnetic field the charge-carriers are moving along the edges and the *pn*-interface in quantum Hall channels. Currently we are focusing our research towards this direction, where we have promising first results.

As mentioned previously, we will further try to realize the MMI interferometer with the improvements as described before.

References

[1] R. Maurand, P. Rickhaus, P. Makk, S. Hess, E. Tovari, C. Handschin, M. Weiss and C. Schönenberger, *Fabrication of ballistic suspended graphene with local-gating*, Carbon 79 486 (2014)

[2] C. Handschin, B. Fülöp, P. Makk, S. Blanter, M. Weiss, K. Watanabe, T. Taniguchi, S. Csonka, and C. Schönenberger, *Point contacts in encapsulated graphene*, APL 107, 183105 (2015)

[3] C. Handschin, P. Makk, P. Rickhaus, M-H. Liu, K. Watanabe, T. Taniguchi, K. Richter and C. Schönenberger, *Fabry-Pérot Resonances in a Graphene/hBN Moiré Superlattice*, Nano Lett. 17, 328 (2016)

A low-loss, broadband optical antenna for a single color center in diamond

Project P1212 Nano-photonics with diamond (comb.12)
Project Leader: R.J. Warburton and P. Maletinsky
Collaborators: D. Riedel (SNI PhD Student), E. Neu, and S. Starosielec

The nitrogen-vacancy (NV) center in diamond has a coherent spin and this feature is finding numerous applications in quantum sensing. These applications range from probing stray-fields close to the surface of integrated circuits to the detection of vortices in a high-T_c superconductor at low temperature. In these applications, the NV spin is both initialized and read-out optically. The optical transition is well suited to these two tasks but employing the NV for quantum photonics places more stringent demands on the optical properties. Ideally, the emitted photons should represent a high brightness source of indistinguishable photons. This is far from the case at present. We have already presented a powerful solution to the brightness problem [1] but other serious issues remain. Only a few percent of the emission goes into the useful zero-phonon-line (ZPL). Also, the frequency of the optical transition fluctuates in time. In fact, the green laser pulses required to reset the NV charge typically cause a shift of the optical frequency, probably by changing the occupation of defect states. Despite these difficulties, quantum optics techniques have been used to entangle two remote NV spins. The entanglement rate is however small and does not obviously represent a route to creating a viable technology.

We aim to solve these problems. There are two key concepts. The first is the creation of high quality NV centers in single crystal diamond membranes. The starting material is of the highest quality; the nano-fabrication is minimally invasive. Secondly, the membranes are embedded in a miniaturized cavity which should "funnel" the emission into the ZPL once the ZPL is tuned into resonance with the microcavity mode. We present here results on our on-going attempts to put these ideas into practice.

The fabrication of single crystal diamond membranes for photonics applications is now well established [1]. We have developed techniques to bond the membranes to highly-reflective dielectric Bragg mirrors: provided both surfaces are clean the bonding (via the van der Waals interaction) is effective. Additionally, post bonding, we have demonstrated that the membrane can be etched further allowing us to create membranes just a few hundred nanometers in thickness. These are ideal for the microcavity experiments. The microcavity consists of the bottom mirror and a curved top mirror [2, 3]. A finesse of several thousand could be achieved, limited largely by the reflections of the mirrors. This demonstrates that the diamond-dielectric interface does not scatter the light significantly. The high spin coherence of NVs close to the center of the membrane, the correct location for cavity enhancement of the optical properties, is maintained following the membrane fabrication [1].

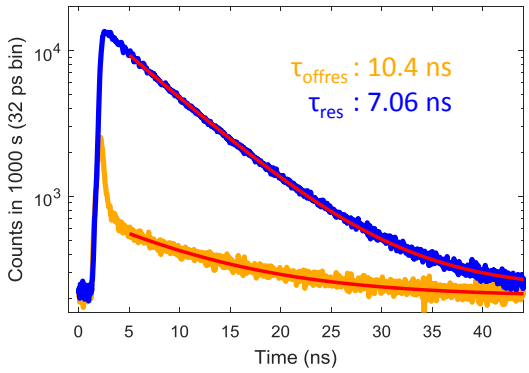

Fig. 1 Radiative lifetime of a single NV center in a microcavity. The NV is located at the anti-node of the microcavity. In one case, the frequency of the microcavity mode is tuned into resonance with the ZPL of the NV; in the other case, the frequency of the microcavity mode is detuned by 300 GHz.

The optical quality of NV centers in the fabricated membranes has been tested by comparing the properties to those in the original material. The brightness is roughly the same although there are fluctuations from one NV center to the next in the membrane. The low temperature line widths are around 1 GHz for NVs in the membrane, increased above 100 MHz for NVs in the bulk. The reason for this increase is not yet known. However, while these line widths are not ideal (the transform limit corresponds to ~10 MHz), they are much smaller than those of NVs in nano-diamond and they are also much smaller than the present microcavity mode line widths.

In the past year, we have successfully coupled single NV centers to a microcavity mode. The experiments were carried out at 4 K. The microcavity was tuned *in situ* into resonance with the ZPL of particular NV centers by adjusting a z-piezo (cavity frequency) and xy-piezos (anti-node position). Fluorescence emitted into the microcavity leaks out of the microcavity and is detected with single photon detectors. The radiative lifetime of an NV centre is 12 ns in the bulk diamond sample. On resonance in the microcavity, the radiative lifetime decreases to 7 ns (Fig. 1). The lifetime increases as the cavity is detuned, either spectrally (Fig. 1), or spatially. This is clear evidence for a Purcell enhancement of the radiative decay rate.

A quantitative analysis is presently ongoing. We stress that an increase in total decay rate of close to two corresponds to a large Purcell factor for the ZPL. Without the microcavity, radiative decay occurs predominantly into modes, which propagate laterally in the membrane itself. Emission into modes corresponding to vertical propagation is weak. For these reasons, without a microcavity the collection efficiency in a back-scattering geometry is small. With a resonant microcavity of the present type, emission into the lateral modes remains unchanged. In a microcavity tuned to the ZPL, the total decay rate can be reduced only by a massive enhancement of the ZPL decay rate into the vertical mode. The Purcell factor for the ZPL is at least ~25 in these experiments. Equivalently, close to 40% of the NV emission is funneled into the ZPL. This is a very positive result for quantum photonics as only ZPL emission is useful for generating spin-photon and spin-spin entanglements.

The experiment provides a number of pointers for further improvements. First, the ZPL emission out of the microcavity suffers from scattering loss. This can be much improved with better mirror coatings. Secondly, the Purcell factor can be increased further. Employment of thinner membranes is the most obvious way forward. Additionally, the mode volume of the microcavity can be reduced by using a smaller radius of curvature [4]. Thirdly, higher quality diamond membrane material will result in lower background emission and lower optical line widths.

References

[1] D. Riedel, D. Rohner, M. Ganzhorn, T. Kaldewey, P. Appel, E. Neu, R.J. Warburton, and P. Maletinsky, *Low-Loss Broadband Antenna for Efficient Photon Collection from a Coherent Spin in Diamond*, Phys. Rev. Appl. 2, 064011 (2014)

[2] L. Greuter, S. Starosielec, D. Najer, A. Ludwig, L. Duempelmann, D. Rohner, and R.J. Warburton, *A small mode volume tunable microcavity: Development and characteri-zation*, Appl. Phys. Lett. 105, 121105 (2014)

[3] L. Greuter, S. Starosielec, A.V. Kuhlmann, and R.J. Warburton, *Towards high-cooperativity strong coupling of a quantum dot in a tunable microcavity*, Phys. Rev. B 92, 045302 (2015)

[4] D. Najer, M. Renggli, D. Riedel, S. Starosielec, and R.J. Warburton, *Fabrication of mirror templates in silica with micron-sized radii of curvature*, Appl. Phys. Lett. 110, 011101 (2017)

Photo-driven hydrogen production based on molecular nanofactories

Project P1213 Artificial Metalloenzymes for Molecular Nanofactories
Project Leader: T.R. Ward and S. Panke
Collaborators: S. Keller (SNI PhD Student), A. Pannwitz, O. Wenger, and R. Alberto

Introduction

Hydrogen is an attractive, clean and renewable energy vector. It can be used as an energy carrier and be regarded as a potential transportation fuel. In the presence of dioxygen, dihydrogen donates both its electrons and water is the only waste product formed. Catalytic production of dihydrogen is an active area of research. Ideally, the reaction should proceed in both directions (oxidation and reduction) with high turnover numbers at ambient temperature and pressure ideally relying on the sun as an energy source (Fig. 1).

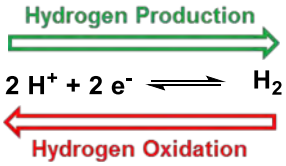

Fig. 1 Hydrogen production and hydrogen oxidation as an environmentally friendly means to store and release energy.

Hydrogenases are natural enzymes that catalyze these reactions with high turnover numbers. Yet the fragility of these enzymes renders their widespread use challenging. To circumvent these limitations, significant effort has been invested in developing robust artificial hydrogenases. There are different Co- and Ni-based small molecule catalysts that are promising for future use on a big scale. Yet their fine tuning is challenging as their second-coordination sphere is poorly defined. In a biomimetic spirit, we set out to incorporate the most efficient small molecule catalysts within a protein environment (streptavidin, Sav) to mimic the reactivity of naturally occurring hydrogenases in a more robust and easy to tune protein environment [1].

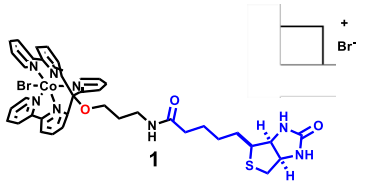

Fig. 2 Co-based artificial hydrogenase for hydrogen production with a biotin anchor (blue) for localization within streptavidin.

Photodriven hydrogenase based on the biotin-streptavidin technology

Within the last year, we linked a biotin anchor to a best-in-class small molecule hydrogenase: [Co pentapyridin] to afford catalyst **1** (Fig. 2)[2]. In collaboration with Prof. Roger Alberto (Uni ZH) we determined the photo-driven water reduction activity of catalyst **1** both inside and outside the Sav upon light irradiation at 453 nm. Initial experiments clearly demonstrate the production of dihydrogen in the presence of ascorbic acid as a sacrificial electron donor and $[Ru(bpy)_3Cl_2]$ as a photosensitizer. The artificial metalloenzyme **1**·WT Sav displays lower activity than the free catalyst **1**, thus highlighting the influence of the second coordination sphere on the catalyst activity. As amply demonstrated in the past, we anticipate that screening different streptavidin mutants will allow to rapidly and significantly improve the performance of the genetically optimized artificial hydrogenase.

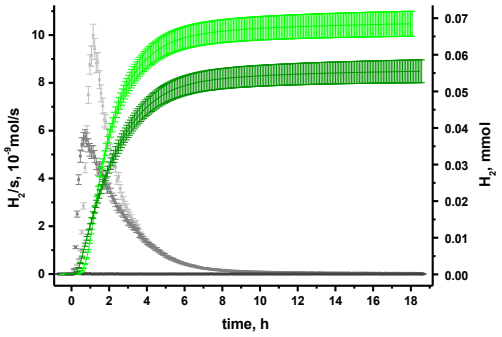

Fig. 3 Hydrogen evolution of the biotinylated catalyst in solution (light green) and inside the protein (dark green) as well as the rates for the catalyst in solution (light grey) and inside the protein (dark grey).

Towards a triad based on streptavidin as a scaffold

With the aim of designing a more efficient electron transfer triad, we set out to precisely localize the three components of the triad: the photosensitizer PS **2**, the biotinylated triarylamine TAA-Biot **3** and the methyl viologen MV. For this purpose, 4 different genetically engineered cysteine positions within Sav, were used to attach the photosensitizer **2** to Sav (Fig. 4 and 5)[3].

As a proof of concept, we could show that the biotinylated triarylamine **3** acts as an electron donor in the dyad TAA-Biot **3**·Sav–PS **2** (Fig. 6). In

collaboration with Prof. Wenger, we were able to detect the photo product of the oxidized triarylamine **2** using flash quench spectroscopy and an excess of MV^{2+} as an electron acceptor in solution.

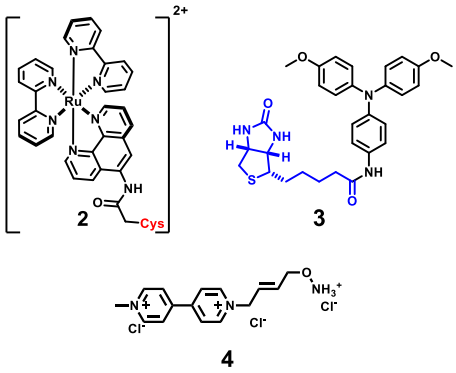

*Fig. 4 The $[Ru(bpy)_2(phen)]^{2+}$ PS **2** photosensitizer reacts with a cysteine residue engineered on the surface of Sav. In the presence of methyl viologen, the biotinylated triarylamine TAA-Biot **3** acts as a transient electron donor. At lower methyl viologen concentrations covalent tethering of a MV derivative **4** is beneficial.*

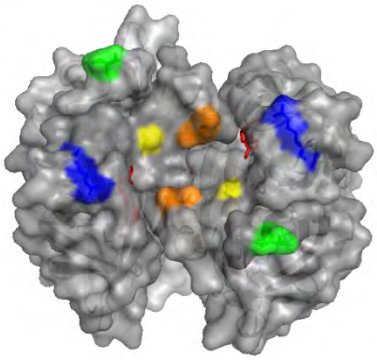

Fig. 5 Surface display representation of homotetrameric streptavidin, highlighting the symmetry related positions selected for introducing cysteine residues: K121 (orange), S112 (yellow), R84 (blue), T66 (green) and biotin (red stick representation); (pdb code: 3PK2).

Upon addition of an equimolar amount of an acetylated triarylamine instead of TAA-Biot **3**, the transient signal at 760 nm (diagnostic of a charge-separated species) could not be detected. Furthermore, a distance-dependence of the electron transfer rates from the triarylamine TAA-Biot **3** to the covalently bound photosensitizer PS **2** could be highlighted upon varying the position of the PS **2**.

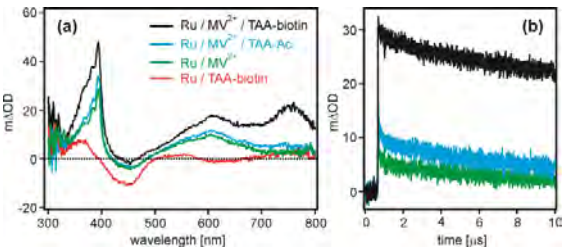

*Fig. 6 a) Transient absorption spectra measured after excitation at 532 nm with laser pulses of ~10 ns. The spectra were time-integrated over 200 ns immediately after excitation. Sample concentrations were: $5{\cdot}10^{-5}$ M Ru(II)-streptavidin, 120 mM MV^{2+}, $2.5{\cdot}10^{-5}$ M TAA-biotin **3** or TAA-Ac, where applicable. The solvent was MilliQ water at 25 °C. b) Temporal evolution of the transient absorption signal at 760 nm for 3 of the 4 samples from a).*

To further exploit streptavidin as a scaffold to precisely assemble a triad, we modified the *N*-terminus of the PS **2** derivatized Sav constructs [4]. For this purpose, a methyl viologen moiety was covalently linked to Sav's *N-terminus*. Initial experiments suggest that the *N-terminus* tethered MV **4** species does indeed interact with the bound PS **2**, as well as the bound triarylamine. In contrast, in the presence of unbound MV no significant interaction can be detected. This suggests that the MV **4** tethering is essential to favor electron transfer.

Outlook

Having demonstrated the feasibility of photo-driven hydrogen production using the Co-catalyst **1** inside streptavidin, our current efforts are aimed at improving the hydrogenase activity by screening a Sav mutant library.

To further extend the scope of complex molecular assemblies within protein scaffolds, we have demonstrated that it is possible to engineer Sav to harbor up to three components: i) biotinylation, ii) cysteine modification and iii) *N*-terminal modification. This allows precisely positioning and genetically optimizing the components of a catalytic triad (photosensitizer, e-donor and e-acceptor). This method can be used for a variety of catalytic applications requiring the precise positioning of multiple components.

References

[1] T.R. Ward, *Artificial metalloenzymes based on the biotin-avidin technology: enantio-selective catalysis and beyond*, Acc. Chem. Res. 44, 47 (2011)

[2] C. Bachmann, M. Guttentag, B. Spingler and R. Alberto, *3D element complexes of penta-dentate bipyridine-pyridine-based ligand scaffolds: structures and photocatalytic activities*, Inorg. Chem. 52, 6055 (2013)

[3] S.G. Keller, A. Pannwitz, F. Schwizer, J. Klehr, O.S. Wenger and T.R. Ward, *Light-driven electron injection from a biotinylated triaryl-amine donor to $[Ru(diimine)_3]^{2+}$- labeled streptavidin*, Org. Biomol. Chem. 14, 7197 (2016)

[4] L.S. Witus, T. Moore, B.W. Thuronyi, A.P. Esser-Kahn, R.A. Scheck, A.T. Iavarone and M. B. Francis, *Identification of highly reactive sequences for PLP-mediated bioconjugation using a combinatorial peptide library*, J. Am. Chem. Soc. 132, 16812 (2010)

Ultracold atoms and ions on a chip

Project P1214 An ion-atom hybrid trap on a chip
Project Leader: S. Willitsch and P. Treutlein
Collaborators: I. Rouse (SNI PhD Student), A. Mokhberi, and R. Schmied

Introduction

Quantum systems are highly susceptible to the effects of noise and so making the precision measurements required to accurately determine physical concepts such as the "shape" of the electron, or to follow the pathway taken by a chemical reaction, is impossible under standard conditions due to thermal fluctuations and their coupling to the surroundings. However, the development of "particle traps" enables holding a small sample of atoms in an ultra high vacuum (UHV), isolated from the outside world for periods of time from a few milliseconds to days. When combined with the technique of cooling atoms through the application of resonant laser light, this allows for an unprecedented ability to observe quantum effects without the interference of the environment.

In recent years, there has been a trend to scale down the particle traps from the bulky apparatus initially used to microscopic chips, capable of performing much more precisely controlled operations to the trapped particles. In particular, two types of chip have been the subject of a great deal of investigation – "atom chips" and "ion chips". Atom chips generate magnetic fields which cause small shifts in the energy of neutral atoms such that they are guided to a minimum in the magnetic field. Ion chips trap charged particles in a radiofrequency electric field, and with the aid of laser-cooling these particles form ordered structures known as Coulomb crystals. Since the ions are localized in these structures they can be easily individually addressed by lasers and hence are a prospect for quantum computing, or the loss of ions can be observed and used to monitor the progress of chemical reactions atom-by-atom. Here we report for the first time the implementation of an ion-atom chip capable of cooling and trapping both species simultaneously above a microstructured surface.

Design of the microscopic hybrid ion-atom system

Three components generate the trapping fields necessary for different species and stages of the experiment. Charged particles are confined through a variation of the macroscopic Paul trap by applying both static and time-dependent voltages to the ion chip, a gold-coated set of stainless steel electrodes designed to keep the ions at a distance of approximately 300 microns above the surface of the chip. These electrodes rest on a printed circuit board (PCB), which provides them with electrical connections and additionally contains a set of carefully designed wire traces to generate magnetic traps to contain pre-cooled neutral atoms. These atoms are initially collected and cooled to an initial temperature of 100 microKelvin from a background atomic vapour through the use of a mirror-MOT – a modification of the standard magneto-optical trap. This mirror MOT is formed by passing a high current through a U-shaped wire located underneath the atom chip in combination with cooling lasers reflected from the surface of the ion chip. The atoms may then be transferred to the magnetic trap generated through the atom chip and shuttled to a region where they can undergo Bose-Einstein condensation and interact with the ions.

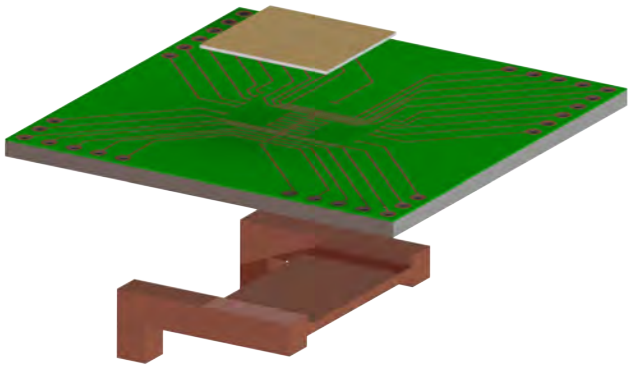

Fig. 1 Exploded view of the three layers of the hybrid chip trap showing the ion chip (top), atom chip (middle) and U-wire MOT (bottom). The long edges of the atom chip are 4 cm.

The chip itself forms one wall of a UHV chamber, with the remainder of the chamber consisting of a quartz cell allowing for optimal optical access. A pumping system attached to this cell then generates the vacuum necessary to allow experiments to be performed.

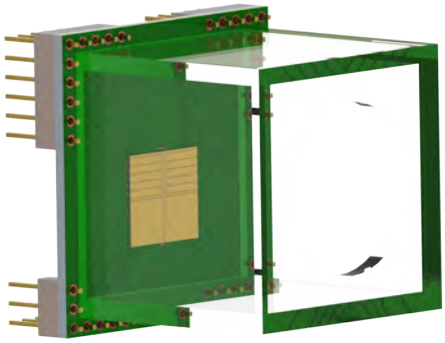

Fig. 2 The hybrid chip attached to a 3 cm x 3 cm fused silica cell to create a vacuum chamber such that trapped particles are isolated from the environment.

Simulations of trapped particles

Molecular dynamics simulations of the ion chip were performed in order to ensure that the ions could be stably trapped, and in order to predict the temperature of the resulting ion crystal. However, during the validation of the code against experimental results obtained using an existing ion chip, previously hidden properties of the trapped ions emerged [2]. It was found that due to the balance of heating and cooling forces, the behaviour of the ions could not be adequately described by a single temperature. Instead, a more accurate description is given by so-called "superstatistics" - an averaging of thermal functions such as the Maxwell-Boltzmann distribution over a range of temperatures.

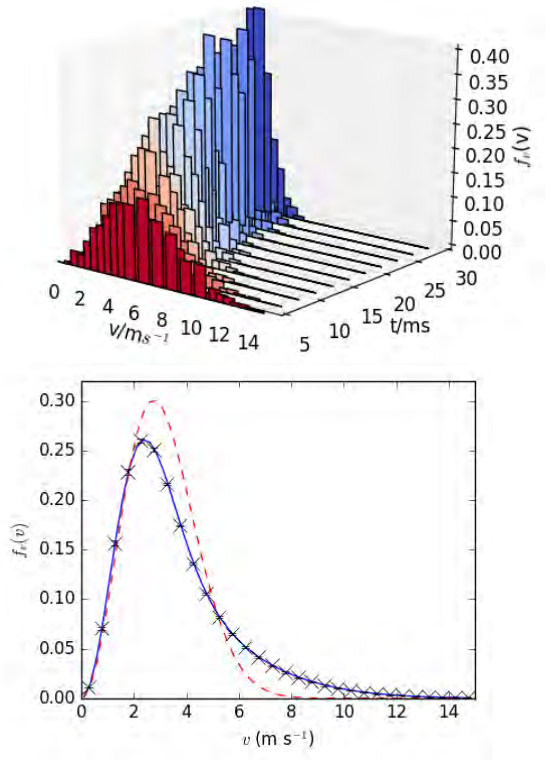

Fig. 3 Time-resolved (top) and time-averaged (bottom) velocity distributions in simulations of an ion trap. The instantaneous distributions are Maxwellian, while the distribution observed during experimental timescales is not. This can be seen in the lower figure comparing the simulated data (crosses) with a Maxwell-Boltzmann fit (red dashed line). A superstatistical treatment (blue solid line) gives a much improved fit.

This behaviour has been shown to have implications for reaction dynamics and precision spectroscopy, and the hybrid chip will allow for a further investigation of these effects.

Manufacturing process

Encouraging early results have shown that the prototype atom chip is compatible with the low pressures and high temperatures necessary for experiments with no loss of performance. A final version of the atom chip has now been designed and is ready for manufacture based on an "insulated metallic substrate" construction method, allowing a more efficient cooling of the chip than possible with traditional PCBs, which enables using higher currents and hence stronger trapping fields. The electrodes of the ion chip trap have been successfully fabricated and are awaiting transfer to the final atom chip. This will require precise alignment to ensure that at the end of the magnetic conveyor series the cloud of ultracold atoms is optimally overlapped with the trapped ion cloud. After this transfer, a fused silica cell will be glued to the chip to form a vapor cell capable of sustaining the low pressures of 10^{-10} mbar required to perform experiments.

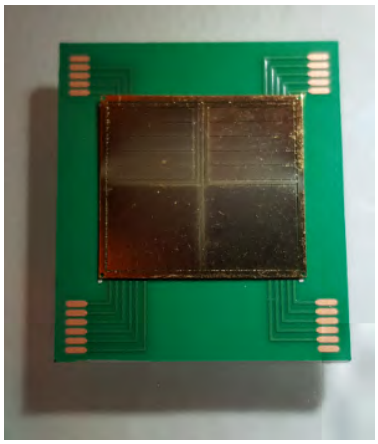

Fig. 4 Gold-plated ion chip on top of a prototype atom chip.

Outlook

The vacuum system is presently being assembled, and, following the construction and attachment of the vapour cell, alignment of the optics system can begin. The initial construction will allow for the generation of ion crystals and an atomic MOT, with a future upgrade after the arrival of precision current sources allowing the atom chip to be used to its full potential to generate a BEC. Initial studies will therefore focus on the reactive dynamics of ultracold ions and atoms, and future work will be able to investigate the behaviour of charged impurities in degenerate quantum systems.

References

[1] S. Willitsch, *Coulomb-crystallised molecular ions in traps: methods, applications, prospects*, Int. Rev. Phys. Chem. 31, 175 (2012)

[2] I. Rouse and S. Willitsch, *Superstatistical velocity distributions of cold trapped ions in molecular-dynamics simulations*, Phys Rev. A 92, 053420 (2015)

Nanoelectronics at ultra-low temperatures on a cryogen-free dilution refrigerator

Project P1215 Nanostructure quantum transport at microkelvin temperatures
Project Leader: D. Zumbühl and D. Loss
Collaborators: M. Palma (SNI PhD Student), D. Maradan, L. Casparis, A. Feschchenko, I. Khaymovich, M. Meschke, and J. Pekola

Introduction

Many quantum phenomena such as nuclear/ electron spin phase and fragile quantum Hall states cannot be observed because they occur at small energy scales. To access these phenomena, we need to lower the temperature in nanostructures below 1 mK. Therefore, we realized an advanced network of 16 Cu nuclear refrigerators for cooling of nanostructures. Building an on-chip thermometer capable of measuring temperatures below 1 mK is a challenging task. In order to be able to measure such low temperatures, we design and tested a normal-insulator-superconductor (NIS) junction that in theory should be able to measure 1 mK. The project about the NIS junction is in collaboration with the group of Jukka Pekola in Helsinki.

NIS on-chip thermometer

The NIS junction is formed by the overlap of superconducting layer (Al) with a normal metal layer (Cu). The tunnel barrier is provided by in-situ oxidation of the Al layer, resulting in less the 5 nm AlO_x. The overlap between the two layers occurs in an area of 400 x 400 µm². The NIS junction is a useful on-chip thermometer, which can be used in three different ways. We will describe these different methods to use the NIS junction as an on-chip thermometer.

The first method is based on the full-fit of the tunnel current through the junction as function of the voltage bias, where the temperature ($T_{full\text{-}fit}$) is the only fit parameter. The tunnel current is described as the convolution of the Fermi-Dirac distribution of the electrons inside the normal metal and the smeared superconductor density of states, which is described by the Dynes parameter γ [4]. This method assumes a constant superconducting gap (Δ) for temperatures much smaller than the critical temperature of the superconductor and a known tunneling resistance (R_T). The strength of this method is that $T_{full\text{-}fit}$ is independent of γ.

The second method is the semi-log method, which uses the exponential part of the I-V curve to extract the temperature $T_{semi\text{-}log}$. The temperature $T_{semi\text{-}log}$ is extracted by the semi-logarithmic slope $T_{semi\text{-}log} = dV/d(lnI)e/k_B$, with electron charge e and Boltzmann constant k_B. This method allows using the NIS as primary thermometer, meaning that the extracted temperature is independent of the device parameters, e.g R_T and Δ.

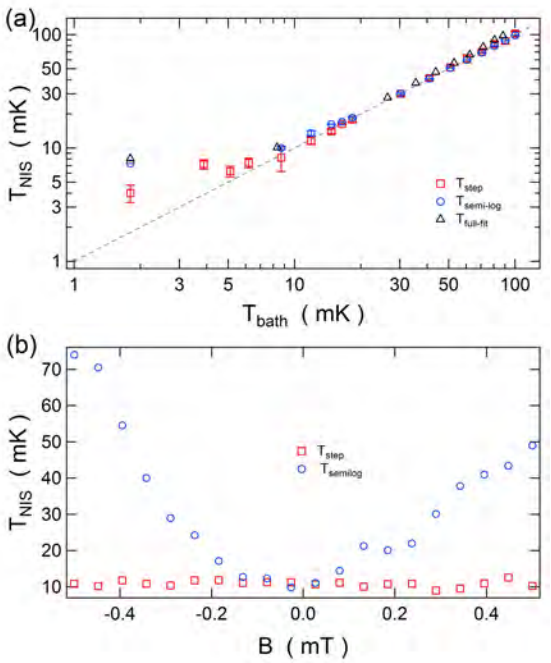

Fig. 1 Panel (a) shows the electron temperature of the NIS (T_{NIS}) extracted from full-fit (black triangles), semi-log (blue circles) and sub-gap steps (red squares) method. Panel (b) shows T_{step} and $T_{semi\text{-}log}$ as function of B-field.

However, the accuracy of the thermometer is strongly dependent on γ and only correct around zero *B*-field (Fig. 1b).

Nuclear demagnetization on a cryogen-free platform

In order to reach ultra-low temperatures in nanostructures we need to use Adiabatic Nuclear Demagnetization (AND) technique and to ensure a good coupling between the refrigerator and the sample. To fulfill the previous demands we implemented a parallel network of 16 nuclear refrigerators (NRs), where each lead has its own nuclear refrigerator, operating on a cryogen-free system. This offers a large experimental space and independence of liquid He. However, damping and isolating the vibrations generated by the pulse tube cooler is a challenging task.

We demonstrated cooling of NRs with high efficiency close to the completely adiabatic case down to 150 µK. The temperature is measured by a magnetic field fluctuation thermometer (MFFT) connected to a SQUID amplifier. This thermometer performs an inductive read-out of the thermal currents inside a high purity Ag-wire. The MFFT is

an ideal choice for ultra-low temperature since the overheating is reduced due to the inductive read-out and the lowest temperature achievable is set by the SQUID noise level.

The MFFT temperature shows an excellent agreement with the temperature of the NRs ($T_{e,Cu}$) from 4K down to 400 µK, below 400 µK the temperature of the MFFT is slight higher than $T_{e,Cu}$ due to the finite thermal link between MFFT and NRs (Fig. 2b). Below 10 mK heat leaks coming from heat release of various material might impede the reaching of temperatures below 1 mK. We measure heat leaks, which are independent of the magnetic field and they are about 1 nW/mol, allowing staying below 1 mK for roughly 50 hours of experimental time.

In order to quantify the performance of the NRs we use the efficiency $\xi = (T_i/T_f)/(B_i/B_f)$ of the AND process. We obtain an efficiency of about 100 % at high magnetic field down to 70% for the lowest field, as shown in figure 2a. The reduction of the efficiency is in agreement with reduction of the heat capacity of the NRs for smaller fields. We modeled the AND process assuming a constant heat leak and we are able to reproduce the data. Further, the model shows that the heat leak is independent of the sweep rate of the *B*-field. Therefore, we were able to enhance the performance of the AND process by decreasing the time of the demagnetization, as shown in figure 2a.

In conclusion, we successfully implemented an AND system on a cryogen-free system with high efficiency and good performance, indicating that the vibrations are not the limiting factor. Now the challenge is to transfer the cooling power from the NRs into the sample. Therefore, we tested a socket made of Ag-epoxy with embedded microwave filters and a socket made of sapphire and without any filter. The first kind of socket shows heat release and the temperature of the nanostructure is higher than the mixing chamber (MC) temperature. In the second socket we eliminated the heat release due to the Ag-epoxy. The temperature of the nanostructure was reduced compared to the previous socket but, however, still remains above the MC temperature. For the future, we are planning to use a sapphire socket with heavily filtered leads since electrical noise on the sample seems to be the bottleneck to go below 1 mK in nanostructures.

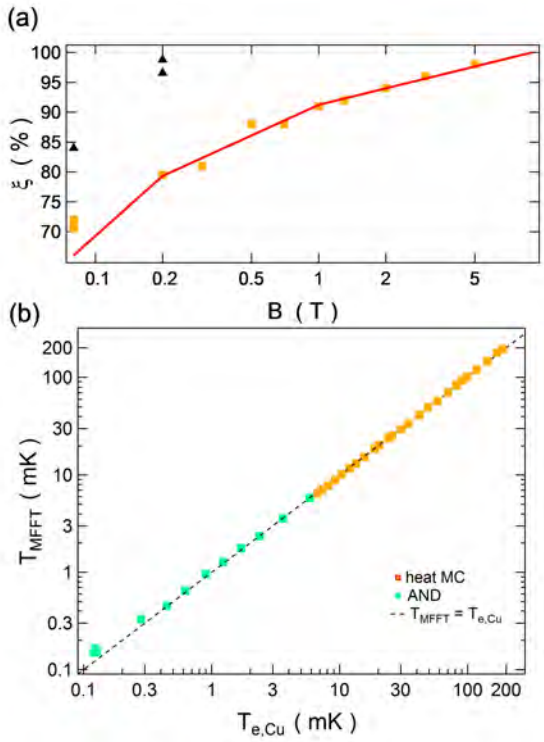

Fig. 2 Panel (a) shows the efficiency ξ as function of B-field. Panel (b) shows the Temperature measured by the MFFT (T_{MFFT}) versus the electronic temperature of the NRs ($T_{e,Cu}$).

References

[1] P. Simon and D. Loss, *Nuclear Spin Ferromagnetic Phase Transition in an Interacting Two Dimensional Electron Gas*, Phys. Rev. Lett. 98, 156401 (2007)

[2] A.V. Feshchenko, L. Casparis, I.M. Khaymovic, D. Maradan, O.-P. Saira, M. Palma, M. Meschke, J.P. Pekola and D.M. Zumbühl, *Tunnel junction thermometry down to millikelvin temperatures*, *Phys. Rev. Appl.* 4, 034001 (2015)

[3] R.C. Dynes, V. Narayanamurti, and J.P. Garno, *Direct Measurement of Quasiparticle-Lifetime Broadening in a Strong-Coupled Superconductor*, Phys. Rev. Lett. 41, 1509 (1978)

[4] D.I. Bradley, R.E. George, D. Gunnarsson, R.P. Haley, H. Heikkinen, Yu. A. Pashkin, J. Penttila, J.R. Prance, M. Prunnila, L. Roschier and M. Sarsby *Nanoelectronic primary thermometry below 4 mK*, *Nat. Comm.* 7, 10455 (2016)

Image states and energy dissipation on a topological insulator surface

Project P1301 Energy dissipation over structural and electronic phase transitions
Project Leader: E. Meyer and M. Poggio
Collaborators: D. Yildiz (SNI PhD Student), M. Kisiel, U. Gysin, and Th. Glatzel

Current status of the research

A tiny friction is caused due to the relative motion of bodies separated by few nanometers gap [1]. Non-contact friction can be measured by highly sensitive cantilever oscillating like a tiny pendulum over the surface. Within the initial part of project, we studied TaS2 and HOPG, which are known as layered crystals, showing very clear differences in their dissipation spectra. This observation might be counterintuitive regarding the fact that all these materials are thought to be good solid lubricants. Moreover mechanism of energy dissipation on TaS_2 depends on temperature driven phase transition of the crystal. Topological insulators (TIs) – again belonging into the family of intercalated compounds - have a bandgap in the bulk that makes the crystal insulator, whereas their surfaces (or edges) are conducting [2]. Protected topological states, offer promising playground to observe exotic physical phenomena like Majorana fermion bounded state or magnetic monopoles [3].

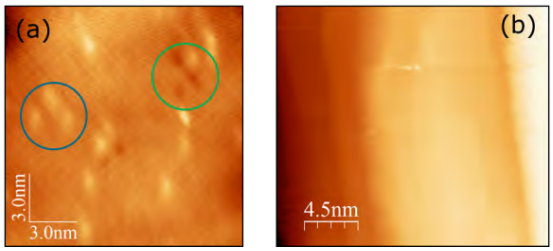

Fig. 1 STM images of two different Bi_2Te_3 crystals at 5K. Surface of native Bi_2Te_3 a) is characterized by large defects density while the Bi_2Te_3 b) is defect free. Tunneling parameters: a) I_t= 300pA, V_b= 330 mV, b) I_t= 440pA, V_b= 500 mV.

Here, we studied the TIs surface of Bi_2Te_3 by means of pendulum STM/AFM and we report on dissipation peaks occurring presumably due to charging of image potential states. Although electronic properties along with defect formation and TIs behavior of these systems have been studied [3], we are not close to having fully understood such systems. Our aim is to understand the frictional response of Bi_2Te_3 in deep TI phase as well as its frictional response when the TI phase is partially or fully suppressed. For that purpose, we probe surfaces with different defect density and under external magnetic field. Figure 1 shows STM images on a) defected and b) defect free crystals. All the measurements were done at 5K and the same ATEC-NcAu cantilever (k=58 N/m) was used for STM and AFM dissipation measurements.

Image states on Bi_2Te_3

Measurement of image states by means of STS was first reported in 1985 and they can help to understand the chemical nature of the surface [4]. Image states were measured on Bi_2Te_3 by using STS. We approached to surface in constant current STM mode and the tip was positioned on a point on the surface. STM feedback was kept active while performing the spectroscopy and sample bias was swept from 300mV to 10V. While sweeping the bias, the tip (cantilever) retracted away from the surface (from one image potential states to another) to keep the tunneling current constant.

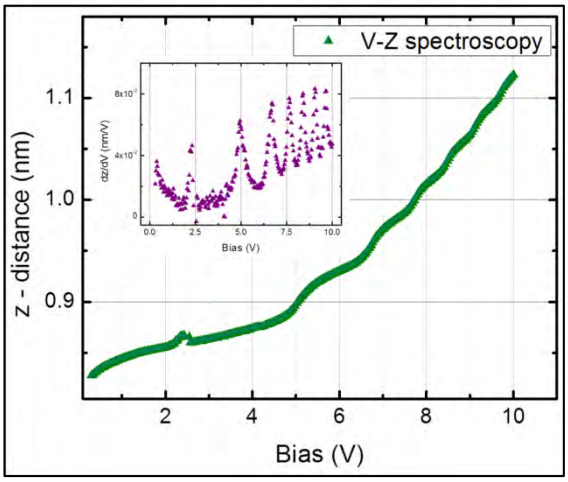

Fig. 2 z-V curve on Bi_2Te_3. Feature appeared close to 2 V may contain information from subsurface or interlayer states. Steps present after 5 V are the image potential states of the crystal that are measured above the surface. Tunneling parameters: It= 80 pA, Vb= 300 mV.

Figure 2 shows z-V curve obtained from STS. Steps are observed in z-V, which can be seen clearly identified as peaks in the inset curve, which is numerically derived z-V curve. The first step located at 5 V is in good correspondence to photo emission data [5] and is attributed to work function crystal. Each subsequent feature corresponds to another level of image state of the crystal. Feature at 2.4 V bias in the curve might be emerging from sub surface or quintuple interlayer states of the TI crystal.

Energy dissipation on Bi_2Te_3

Force spectroscopy was performed on defect free Bi_2Te_3 in order to understand the frictional response of the sample. Simultaneous energy dissipation was measured as a function of tip sample distance and

voltage. Figure 3a and b show the distance/voltage dependent dissipation map and dissipation curve at a constant distance z = 2 nm away from the surface, respectively. Dissipation map in figure 3a shows two plateaus up to 5V and several dissipation peaks for higher bias values when the tip is close to the surface (2-3 nm away from STM distance). These plateaus and peaks shift towards higher biases as the distance between tip and the sample increases due to change of tip-sample capacitance [6]. The first peak in the dissipation map located at 6 V bias on the curve (Fig. 3b) eventually converges very close to the values given by STS image states measurement as the tip approached the surface. Therefore we identify the observed dissipation peaks as related to charging/discharging the image potential states, similarly as was previously reported for quantum dots [6].

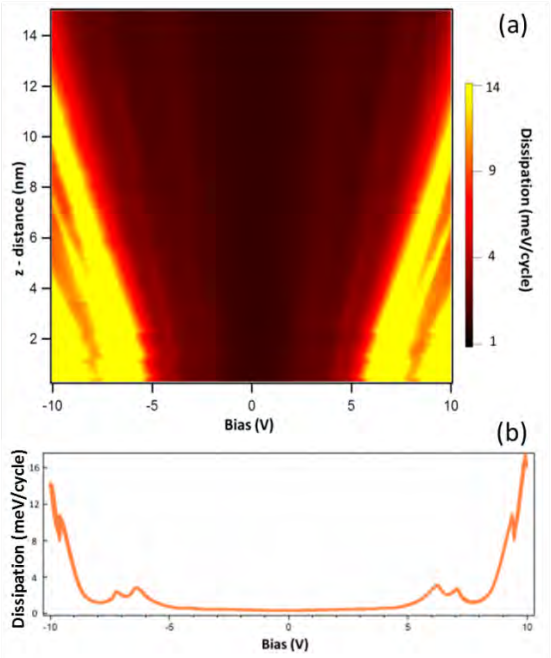

Fig. 3 a) Energy dissipation map plotted versus distance and tip-sample voltage (on defect free Bi_2Te_3). Bright contrast represents high dissipation. Series of dissipation spikes are visible on the map. Dissipation curve depending on bias at a constant distance z=3nm from the surface is plotted in b). A_{osc}= 400 pm, f_o=269 kHz, k=58 N/m.

We performed dissipation measurements under magnetic field. 100, 200, 400, 500, 600, 800 mT magnetic field applied respectively perpendicular to the sample surface.

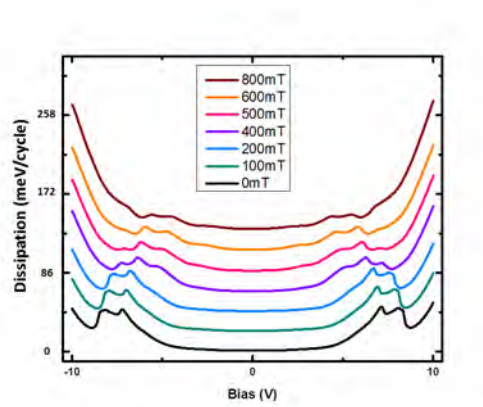

Fig. 4 Dissipation – bias curves for different external magnetic fields at a constant distance z = 5 nm from the surface. Constant shift is applied to curves in y-axis for visibility. Black curve is for 0 T magnetic field and there are two peaks visible on the curve. Peaks are observed to be suppressed and shifted towards zero bias as higher magnetic fields applied. For larger magnetic field new dissipation peak at lower voltages appear. A_{osc}= 300 pm, f_o=269 kHz, k=58 N/m.

In this study, we positioned the cantilever at constant distance 5 nm above the surface. Huge dissipation peaks were mapped with pendulum AFM and image potential states seem to be the reason of these giant dissipation peaks. The dissipation peaks observed to be shifted and suppressed as the magnetic field increases. The results show strong dependence of dissipation on magnetic field since the peaks are shifted to lower energies aas the magnetic field increases.

References

[1] M. Kisiel, E. Gnecco, U. Gysin, L. Marot, S. Rast, E. Meyer, *Suppression of electronic friction on Nb films in the superconducting state,* Nat. Mat. 10, 119-122 (2011)

[2] J.M. Kosterlitz D.J. Thouless, *Long-range order and metastability in two dimensional solids and superfluids.* J. Phys. C: Solid State Phys. 5, 124-126 (1972)

[3] M.Z. Hasan and C.L. Kane, *Topological insulators,* Rev. Mod. Phys. 82, 3045 (2010)

[4] G. Binnig, K.H. Frank, H. Fuchs, N. Garcia, B. Reihl, H. Rohrer, F. Salvain, and A.R. Williams, *Tunneling Spectroscopy and Inverse Photoemission: Image and Field States*, PRL, 55, 991 (1985)

[5] D. Haneman, *Photoelectric emission and work functions of InSb, GaAs, Bi2Te3 and ger-manium*, J. Phys. Chem. Solids, 3-4, 205-208 (1959)

[6] R. Stomp, Y. Miyahara, S. Schaer, Q. Sun, H. Guo, P. Grutter, S. Studenikin, P. Poole and A. Sachrajda, *Detection of Single-Electron Charging in an Individual InAs Quantum Dot by Noncontact Atomic-Force Microscopy*, PRL, 94, 056802 (2005)

Flagellum dynamics of predivisional daughter cells

Project P1302 Dynamic and molecular principles of surface-based cell motility and mechanosensation
Project Leader: T. Pfohl and U. Jenal
Collaborateurs: N. Sauter (SNI PhD Student), and M. Sangermani

Introduction

We use the asymmetric cell cycle of the gram-negative model bacteria *Caulobacter crescentus* to study the flagellum dynamics of predivisional daughter cells. The mother cell irreversibly attaches to a surface via a holdfast and a stalk. The attached cell then produces a daughter cell with a flagellum and pili. The flagellum is used for swimming and can rotate in both directions. When the flagellum rotates clockwise (CW), it forces the cell body to rotate counterclockwise (CCW) to balance torque and because of the cell shape the cell is propelled forward. When the rotation of the flagellum is reversed, the cell body also rotates in the other direction and the cell swims backwards [1]. It is believed that the reversal of the movement is necessary for the cell to achieve chemotaxis [2]. We found that the flagellum of the daughter cell is already rotating when the daughter cell is still attached to the mother cell. The rotation of the flagellum causes the daughter cell to swim away as soon as it is released from the mother cell. Moreover, we observed that the flagellum also rotates in both directions, CCW and CW, whilst still connected to the mother cell. Because we cannot image the movement of the unlabeled flagellum directly, we are observing the movement and rotations it causes on the daughter cell. The rotation directions are always determined for the daughter cell. To improve the sensitivity of our measurements, we attached cells irreversibly to colloidal beads instead of a solid surface and observed the movement of the bead over the cell cycle of the attached cell. Our aim is to analyze the generation of hydrodynamics forces during cell growth and division over the whole cell cycle.

Characterization of the behavior of predivisional daughter cells

We studied the behavior of the flagellum of the predivisional daughter cell via imaging the rotations of the daughter cell with high temporal resolution (Fig. 1). The analyzed CW rotations of the cell body have a higher frequency than for the CCW direction. In the shown example, an average CW frequency of (35 ± 1.9) Hz is found while the CCW frequency is slower with an average frequency of (28 ± 1.4) Hz. Moreover, the CCW rotations last longer on average than the CW ones. The average time for the CCW rotations is (1.2 ± 0.7) s and (0.5 ± 0.2) s for the CW direction. This data are similar to the data found for free-swimming swarmer cells [1]. The rotation of the daughter cell lasts on average several seconds until it is released from the mother cell. Most of the daughter cells are released from the mother cell when they are rotating CCW and hence the cell is pushed towards the mother (Fig. 2). It still needs to be determined whether shear forces facilitate the process of releasing the daughter cell or if this finding can purely be explained by the fact that the daughter cell spends more time in the CCW mode and it is therefore more likely to be released in this mode.

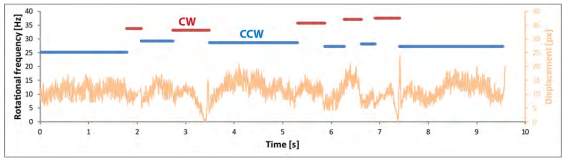

Fig. 1 Rotation spectrum of a typical predivisional daughter cell. The cell starts rotating in CCW direction (blue), then switches 10 x between CCW and CW directions until it is released from the mother after 9 s of rotation. The frequency in CW direction is always higher than in CCW direction. The cell spends more time in the CCW direction than CW and is released when in CCW direction

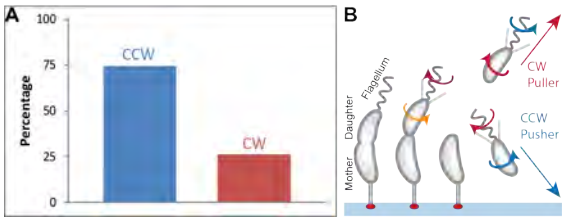

Fig. 2 a) Amount of daughter cells released from the mother cell when in the CCW mode and being pushed forward (blue) and amount of cells released from the mother in the CW mode and being pulled by the flagellum (red). b) Scheme of the release of daughter cells.

Characterization of predivisional daughter cells attached on beads

In our experiments, we let *C. crescentus* cells attach to polystyrene beads of different sizes. The cells were growing and generating daughter cells whilst being attached to the bead (Fig. 3c). The rotation of the flagellum generates a force on to the bead. The trajectories of different bead sizes and of beads with and without cells attached were tracked and compared. From the data, we are able to determine the moment the flagellum of the predivisional daughter cell starts to rotate.

1 µm diameter polystyrene bead: Predivisional daughter cells are able to swim with an attached 1 µm bead. We determined the average swimming speed to be around 10 µm/s. This swimming speed is a significant decrease of the average speed of a swarmer cell that is around 40 µm/s. The velocity of the bead is plotted against the time (Fig. 3a). The

onset of the movement of the flagellum can clearly be seen. The diffusive trajectory of the bead differs strongly from the trajectory of an actively driven bead. This can also be seen in figure 3b where the mean square displacement (MSD) is plotted for different segments of the trajectory. The trajectory of a bead without attached cell is added as a control.

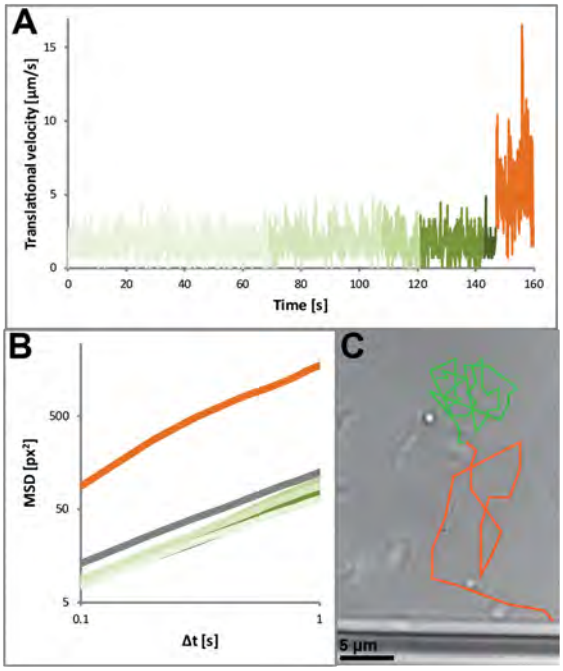

Fig. 3 a) Typical velocity of a cell attached to a bead. When the flagellum is not active, a diffusive movement is visible (green parts). When the flagellum is rotating, the speed of the bead increases (orange part). b) MSD of the different parts of the trajectory shown in A. Green parts indicate diffusive movement, the orange part represents the actively moved part. For a control, the data of a freely diffusing bead without a cell attached is shown in grey. c) Bright field image of a predivisional cell attached to a 1µm bead and schematic representation of the trajectory.

3 µm diameter polystyrene bead: Cells were also attached and grew on larger beads with a diameter of 3 µm. The cells are not able to swim anymore with an attached load of this size. Instead, the force generated by the flagellum causes the bead to rotate. Interestingly, the bead shows a rotation by a wiggling of the mother-daughter complex even before the rotation of the daughter body can be observed. It seems that the flagellum starts rotating even earlier than observed in the aforementioned experiments.

Model for the onset of flagellum movement

In our model, the flagellum starts working when the daughter body is still strongly connected to the mother cell (Fig. 4b). This effect of the onset of the flagellar movement cannot be observed in experiments where only the movement of the daughter cell is investigated (Fig. 4b, c). Only after the inner membrane (IM), containing mostly lipids, and the rigid cell wall consisting of peptidoglycan (P) went through the cell division process and the two cells are only connected by the outer membrane (OM), that is mostly lipids, the force of the rotating flagellum overcomes the forces connecting the two cells and the daughter cell is rotated by the flagellum (Fig. 4d). A few seconds later, the OM also completes division, the daughter cell is released from the mother cell and swims off.

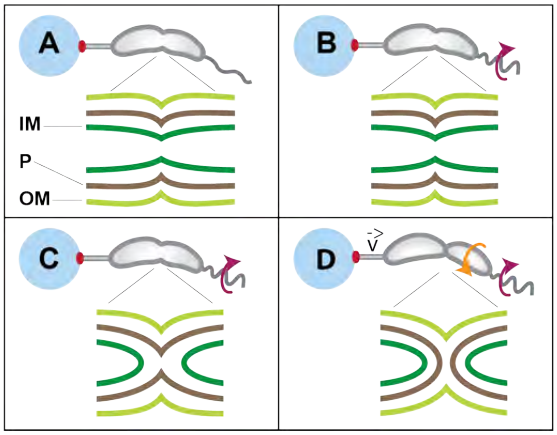

Fig. 4 a) Situation before the onset of flagellar rotation; IM, P and OM are still connected, the flagellum is not rotating. b) The flagellum starts to rotate, but no effect on the daughter cell (rotation) is visible, the connection between the two cells is still complete. c) The division process of IM is completed. Still no effect on the daughter cell is visible. d) The division of P is completed, the two cells are only connected by OM. The connection is soft enough and the daughter cell is rotated by the flagellum.

Conclusion

In this work, we observed that the flagellum of predivisional cells behaves very similar to the flagellum of free-swimming swarmer cells. The two rotation directions of the flagellum cause the daughter cell to counter rotate in CCW or in CW. In the CCW mode, the cell rotates generally longer, while in this direction the frequency of the daughter cell is lower. Most daughter cells were found to be released from the mother when they were rotating CCW. Moreover, the flagellum starts working before it has an impact onto the movement of the daughter cell. Rotation of the daughter cell is only possible when the force generated by the flagellum is stronger than the connection between the two cells.

References

[1] B. Liu, M. Gulino, M. Morse, J.X. Tang, T.R. Powers and K.S. Breuer, *Helical motion of the cell body enhances Caulobacter crescentus motility*, PNAS 111, 31 (2014)

[2] L. Xie, T. Altindal, S. Chattopadhyay and X.-L. Wu, *Bacterial flagellum as a propeller and as a rudder for efficient chemotaxis*, PNAS 108, 6 (2011)

Molecular muscles: a modular approach

Project P1303 Assembly and investigation of electrochemically triggered molecular muscles
Project Leader: M. Mayor and M. Calame
Collaborators: Y. Aeschi (SNI PhD Student), S. Drayss-Orth, and M. Mayor

Mechanically interlocked molecules in water

Assembly of molecular daisy chains by hydrophobic aggregation is a tempting option to exploit for the construction of supramolecular assemblies [1, 2]. Balancing hydrophobic and hydrophilic properties alongside with complementary topological features of receptor and guest components is essential to obtain well-defined aggregates. A modular assembly strategy is desirable as it enables the introduction of diverse functional subunits to obtain switchable, mechanically interlocked molecules. Additionally, synthesis of nanoscale objects from multiple supramolecular assemblies requires high-yielding and robust coupling chemistry. We therefore rely on Cu^{I}-catalyzed azide-alkyne click-chemistry [3] to obtain building blocks from fully functionalized subunits, which self-assemble to daisy chains under aqueous conditions. The same coupling chemistry allows trapping these daisy chains either as small aggregates (Fig. 1) or incorporated into larger, functional poly-/oligomeric superstructures. As a proof-of principle experiment for click-chemistry-based assembly/ interlocking strategy under aqueous conditions, we synthesized rotaxanes by a threading – followed by stoppering method.

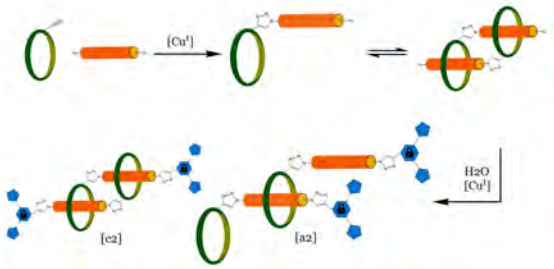

Fig. 1 Formation of interlocked cyclic [c2]- and acyclic [a2]-daisy chains by click stoppering reaction under aqueous conditions.

Rotaxane synthesis

Naphthalene axle **1** was designed as a simple, water-soluble model compound to investigate aggregation properties with Diederich-type-cyclophane [4] **2**, which revealed an association constant (K_a) of $1.4*10^5$ L mol^{-1}. The click-reaction with bulky stopper **3a** expectably allowed kinetic trapping of the cyclophane on the naphthalene axles, thus resulting in mechanically interlocked supermolecules. A yield of 59 % was obtained for rotaxane **4**. The rotaxane nature was confirmed by NMR and HRMS.

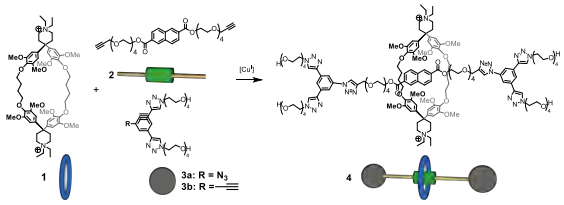

Fig. 2 Assembly of a rotaxane in water by Cu^{I}-catalyzed click chemistry. Counterions are omitted for clarity.

Assembly of a daisy chain precursor

Cyclophane **5** was synthesized in 10 steps in a high yield on multigram scale. Two quaternary ammonium centers provide solubility in water and a terminal acetylene serves as anchoring point for click chemistry. Oligophenyleneethynylene (OPE) rod **6** with two azide groups for click chemistry as well as two carboxylates to provide solubility in water was prepared. The negatively charged carboxylates are electrostatically complementary to the ammonium centers of the cyclophane, which increases binding affinity in addition to the hydrophobic effect [5]. A statistical coupling reaction led to daisy chain monomer **7** in 90 % yield, while it was necessary to employ only 2 eq. of the rod component to avoid twofold click reaction.

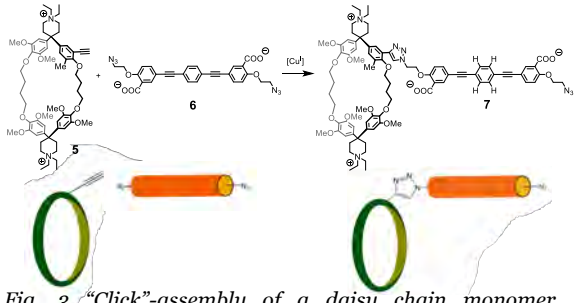

Fig. 3 "Click"-assembly of a daisy chain monomer. Counterions omitted for clarity. The phenylene protons marked with an asterisk exhibit the strongest chemical shifts in ^{1}H-NMR-spectroscopy upon complexation.

Aggregation studies

Dilution studies were undertaken by ^{1}H-NMR and fluorescence spectroscopy. It was found that a small amount of methanol is required render **7** soluble in millimolar concentrations. Concentration dependent ^{1}H-NMR shifts in D_2O/MeOD: 4/1 revealed complex formation down to concentrations of 50µM.

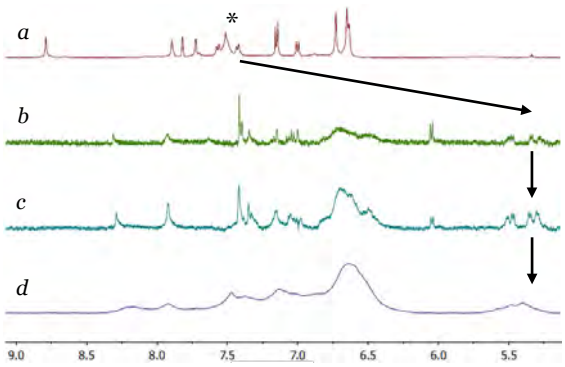

Fig. 4 Solvent and concentration dependent ^{1}H-NMR chemical shifts of 7. a: 1 mM in Acetone-d_6:MeOD 3:1. b,c, d: in D_2O/MeOD: 4/1, 0.1 mM, 0.9 mM, 10 mM.

The strongest indication of an inclusion phenomenon are the ^{1}H-resonances of the OPE-phenylene protons (see Fig. 4), which are shifted to the high field region 5.2-5.6 ppm upon complexation by the cyclophane [4]. If the hydrophobic effect and therefore aggregation is disrupted by choosing a solvent of low polarity/proticity, a downfield shift of approx. 2 ppm is expected [4, 5]. We found that indeed a spectrum recorded in Acetone-d_6/MeOD reveals the absence of signals at 5.2-5.6 ppm and reappearance of the OPE proton signals at 7.5 ppm. Furthermore, the OPE signals in a complexed state are split into multiple signals, reflecting the nonsymmetrical environment of the cyclophane cavity. In addition to the NMR results, concentration dependent fluorescence studies revealed a critical aggregation concentration in the order of ~10 µM (Fig. 5).

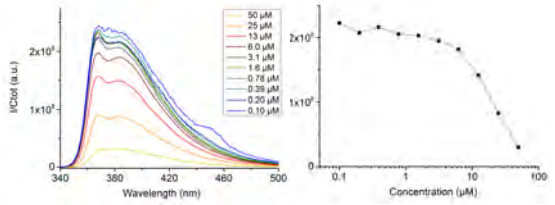

Fig. 5 Left: Fluorescence quenching at higher monomer concentration. Right: Emission intensity plotted vs. monomer concentration reveals a CAC of approx. 10 µM

Trapping daisy chains

Mechanically interlocked daisy chains were obtained by the click reaction with acetylene-functionalized stopper **3b** at 1.8 mM monomer concentration in H_2O/MeOH: 4/1. It was found that [c2]- as well as [a2]-daisy chains were formed, which was determined by ^{1}H-NMR and confirmed by high-resolution mass spectrometry. From HPLC-UV analysis, yields of 57 % [c2]-, 10 % [a2]-daisy chains and 33 % stoppered monomer were estimated. These results confirmed the formation daisy chains in aqueous solution, while the yields do however not necessarily reflect the supramolecular equilibrium.

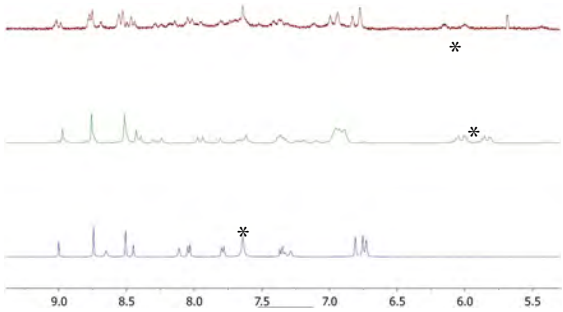

Fig. 6 ^{1}H-NMR spectra of interlocked [a2]- and [c2]-daisy chains and the stoppered monomer (top to bottom). OPE-proton resonances (asterisk) can be compared to figure 4.

Conclusion

[c2]- And [a2]-daisy chains were successfully synthesized. ^{1}H-NMR and fluorescence studies clearly underpin strong intracavitary complexation of the OPE rod, while it seems likely that several aggregation phenomena are superimposed. Currently we are investigating the concentration dependent aggregation properties of **7**, which is essential in our work towards the integration of this daisy chain motif into molecular machinery.

References

[1] J. Rotzler and M. Mayor, *Molecular daisy chains*, Chem. Soc. Rev, 42, 44 (2013)

[2] J. Rotzler, S. Drayss, D. Häussinger, O. Hampe and M. Mayor, *Molecular Daisy Chains: Syn-thesis and Aggregation Studies of an Amphiphilic Molecular rod*, Chem. Eur. J, 19, 2089 (2013)

[3] M. Meldal and C.W. Tornøe, *Cu-Catalyzed Azide-Alkyne Cycloaddition*, Chem. Rev. 108, 2952 (2008)

[4] S.B. Ferguson, E.M. Sanford, E.M. Seward and F. Diederich, *Cyclophane-arene inclusion complexation in protic solvents: solvent effects versus electron donor-acceptor interactions*, J. Am. Chem. Soc, 113, 5410 (1991)

[5] P.N. Taylor, A.J. Hagan, H.L. Anderson, *Hindered fluorescence quenching in an insulated molecular wire*. Organic and Biomolecular Chemistry, 1, 3851 (2003)

Monitoring β-barrel membrane protein folding

Project P1304 Folding mechanisms of β-barrel outer membrane proteins and their catalysis by natural holdases and foldases
Project Leader: S. Hiller and D.J. Müller
Collaborators: N. Ritzmann (SNI PhD Student), P. Rios Flores, T. Raschle, and J. Thoma

β-barrel membrane proteins are essential functional components of the outer membrane of Gram-negative bacteria, mitochondria and chloroplasts. Membrane proteins have highly interesting folding properties, since they fold in an external environment that comprises hydrophobic and hydrophilic phases. The biogenesis of these outer membrane proteins (Omps) poses a complex biophysical challenge to the pro- and eukaryotic cell, because the Omps are synthesized at locations distant from their target membrane. The overall essential biological function of Omp biogenesis is accomplished by molecular chaperones that pass the unfolded substrates from the ribosome to the destination membrane [1]. In the Gram-negative bacterium *E. coli*, the periplasmic chaperones SurA and Skp transport the substrate to the Bam complex, which folds and inserts them into the outer membrane [2]. The *in vitro* and the *in vivo* folding mechanisms of β-barrel Omps from mitochondria or Gram-negative bacteria are so far not understood at atomic resolution. The same polypeptide chains can refold *in vitro* in the absence of chaperones and other proteins, but resulting in the same three-dimensional β-barrel structures. In this project we employ structural biological and nanotechnological approaches to characterize the folding process of complex outer membrane proteins at atomic resolution. In the following we report two papers, which we published since starting our project and thereafter provide an overview of the following challenges in this project.

Monitoring backbone hydrogen bond formation

The three-dimensional structure of a β-barrel membrane protein is defined by backbone hydrogen bonds between adjacent strands. The biogenesis pathways of β-barrel membrane proteins are essential, but the underlying mechanism is still unclear. *In vitro*, β-barrel membrane proteins can be functionally refolded from a chaotrope-denatured state into detergent micelles or lipid bilayers, ending up in their native structure. Atomic resolution descriptions of *in vitro* folding thus provide important benchmark data for the folding biophysics and yield insight into structural determinants. *In vitro* folding of β-barrel membrane proteins has been characterized using biophysical and biochemical methods, including fluorescence spectroscopy, circular dichroism (CD) spectroscopy, SDS-PAGE migration shifts, and single-molecule force spectroscopy. However, despite the fundamental role for the protein structure, the formation of the hydrogen bond network during β-barrel membrane protein folding has so far not been observed at the atomic level. In this project we thus monitored the formation of interstrand hydrogen bonds during the folding process of a β-barrel membrane protein in detergent micelles by hydrogen–deuterium (H/D) exchange in combination with NMR spectroscopy and mass spectrometry [3]. We used the 8-stranded OmpX from *E. coli* as a model system. At the onset of the experiment, OmpX (148 aa) was solubilized in chaotropic denaturant solution, where the polypeptide was fully unfolded and adopted a random coil conformation without residual structure. Using a manually operated, custom-built setup, folding was triggered by rapid dilution with an aqueous folding buffer that contained the detergent micelles. This initial rapid dilution step was performed in deuterated solvent, leading to the incorporation of deuterons at all exchange-accessible backbone amide positions. The sample was then incubated for a variable folding time, after which a second rapid dilution step with hydrogen based folding buffer was performed, reducing the deuterium content in the solvent by about 80%. Finally, the sample was incubated until protein folding has progressed to completion.

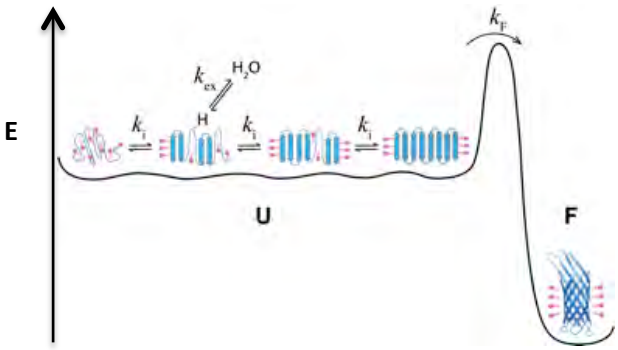

Fig. 1 Free energy E diagram for OmpX folding into detergent micelles. Upon rapid dilution from a denatured state, OmpX associates with detergent micelles to a dynamic conformational ensemble state (U). Four arbitrary conformations are shown in cartoon representation, as representatives for the dynamic ensemble. In this state, multiple conformations rapidly interconvert with kinetic rate constants k_i. No long-lived hydrogen bonds are formed, so that all backbone amides are effectively accessible to chemical exchange (k_{ex}) with the solvent. The folded state of OmpX (F) is separated from the conformational ensemble by a rate-limiting folding step with a kinetic rate constant k_F on the minutes time scale. Image taken from reference [3].

With this experimental setup we found that the residue-specific kinetics of interstrand hydrogen-bond formation are uniform in the entire β-barrel and synchronized to formation of the tertiary structure (Fig. 1). OmpX folding thus propagates *via*

a long-lived conformational ensemble state in which all backbone amide protons engage in hydrogen bonds only transiently. Stable formation of the entire OmpX hydrogen bond network occurs downhill of the rate-limiting transition state and thus appears cooperative on the overall folding time scale.

In summary, we have demonstrated the application of H/D-exchange experiments for the determination of hydrogen bond formation kinetics during folding of a β-barrel membrane protein into detergent micelles. Residue-specific kinetics of interstrand hydrogen-bond formation were found to be uniform along the amino acid sequence and synchronized to the formation of the protein tertiary structure. The H/D exchange setup is compatible with membrane mimetics other than detergents, including bicelles, liposomes, and lipid bilayer nanodiscs, as well as with other β-barrel membrane proteins, and it is also capable to detect partially folded intermediates. Its application will thus be of special interest in situations, where sequence-dependent intermediates may be expected, such as insertase-assisted folding of outer membrane proteins into lipid bilayers.

Chaperone assisted insertion and folding

The correct insertion and folding of membrane proteins is essential to function in living cells. Whereas in living cells molecular chaperones increase the folding yields of soluble proteins by suppressing misfolding and aggregation, it is not understood how they modulate the insertion and folding of integral membrane proteins into membranes. To study this process we used single-molecule force spectroscopy (SMFS) and NMR spectroscopy to characterize how periplasmic holdase chaperones SurA and Skp shape the folding trajectory of the large β-barrel Omp FhuA from *E. coli* [4]. After having unfolded and extracted a single FhuA from the lipid membrane by SMFS, we thus monitored how the unfolded polypeptide inserts and folds back into the membrane. It appeared that the unfolded FhuA polypeptide is prone to misfolding and cannot insert back into the membrane to adopt its native, functional structure (Fig. 2). However, this changed in the presence of either of the two periplasmic chaperones. It was observed that both chaperones SurA and Skp prevented the unfolded FhuA polypeptide from misfolding by stabilizing a dynamic, unfolded state. From this protected unfolded state the substrate could search for structural intermediates. During this conformational search the SurA chaperoned FhuA polypeptide refolded by stepwise inserting β-hairpins into the lipid membrane until the β-barrel entirely folded. Thereby the lipid membrane thus acted as a free energy sink for the insertion and folding of β-hairpins and physically separated transient folds from the chaperones. This trapping of folding intermediates funneled the unfolded FhuA polypeptide towards its native structure.

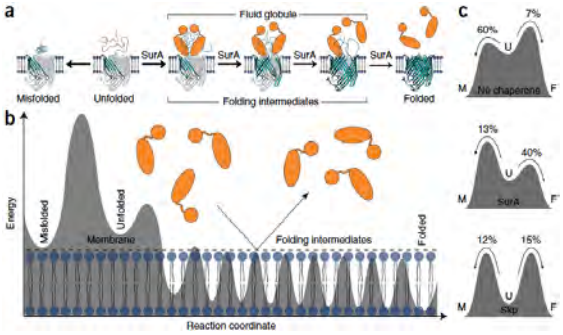

Fig. 2 Folding pathways and free-energy landscape of FhuA receptors. a) Insertion and folding pathways of FhuA in the absence of chaperones and in the presence of SurA (orange). Without chaperones, the majority of unfolded FhuA receptors misfold. SurA, when present, stabilizes the unfolded state of FhuA and promotes stepwise insertion and folding of β-hairpins in the lipid membrane. This stepwise insertion of secondary structures proceeds until the substrate completes the folding of the receptor. b) Hypothetical folding free-energy landscape of FhuA in the presence of SurA. SurA (orange) is spatially excluded from the lipid membrane (blue). Each β-hairpin inserted into the lipid membrane is stabilized by a free-energy well. The lipid membrane acts as a free-energy sink for the insertion of β-hairpins and physically separates transient folds from the chaperones. c) Modulation of the folding free-energy landscape by chaperones. The free-energy barriers separating the unfolded (U) from the misfolded (M) and folded (F) states, as determined from the observed folding probabilities, are shown. Image taken from reference [4].

Challenges ahead

The next challenges in this project are to study how the periplasmic chaperones SurA and Skp transport the Omp substrate to the Bam complex, and how they together fold and insert the substrates into functional Omp structure. We are in the progress of bringing these key players of Omp insertion and folding together to characterize how they function in detail by NMR spectroscopy and AFM.

References

[1] T.J. Knowles, A. Scott-Tucker, M. Overduin and I.R. Henderson, *Membrane protein architects: the role of the BAM complex in outer membrane protein assembly*, Nat Rev Microbiol 7, 206 (2009)

[2] J.G. Sklar, T. Wu, D. Kahne and T.J. Silhavy, *Defining the roles of the periplasmic chaperones SurA, Skp, and DegP in Escherichia coli*, Genes Dev 21, 2473 (2007)

[3] T. Raschle, P. Rios Flores, C. Opitz, D.J. Müller and S.Hiller, *Monitoring backbone hydrogen bond formation in β-barrel membrane protein folding*, Angew Chem Int Ed 55, 5952-5955 (2016)

[4] J. Thoma, B.M. Burmann, S. Hiller & D.J. Müller, *Impact of holdase chaperones Skp and SurA on the folding of β-barrel outer mem-brane proteins*, Nat Struct Mol Biol 22, 795-802 (2015)

Solid supports for protein crystallography at X-ray free electron lasers

Project P1305 X-FEL based dynamic studies on 2D and 3D nanocrystals of membrane proteins on solid supports
Project Leader: C. Padeste and H. Stahlberg
Collaborators: N. Opara (SNI PhD Student), T. Braun, S. Arnold, P. Ringler, K. Thodkar, M. Calame, X.-D. Li, B. Pedrini, I. Martiel, I. Mohácsi, and V. Guzenko

In December 2016, SwissFEL, the X-ray free electron laser (XFEL) at PSI, produced the first laser pulses in the soft X-ray regime. In the next year the machine will be completed and is expected to reach the full energy range in autumn. First experiments at the different end-stations are planned to start in late 2017. XFELs are very promising new analytical tools in many fields of research including protein crystallography. Thanks to their extreme brightness and femtosecond pulses, they allow collection of diffraction data from much smaller crystals than usually required for synchrotron-based experiments, and even 2-dimensional protein crystals have been demonstrated to produce well-defined diffraction patterns [1, 2]. Furthermore, the short pulse duration allows addressing very short time scales down to the femtosecond range. This lead to the vision that molecular movies can be compiled from time-resolved measurements carried out in pump-probe experiments, where a trigger such as an optical laser pulse induces a molecular event, which is then probed by the XFEL radiation at defined time intervals.

As a consequence of the high brightness of the beam the samples under investigation are locally destroyed when hit by an X-ray pulse. Therefore, data collection has to be done in a serial manner where new samples or un-probed areas within one sample have to be provided for each individual pulse. For protein crystallography, samples in the form of thousands of crystals can be delivered through a jet system which is operated either with liquid suspensions of crystals in buffer (liquid jet) or viscous media such as lipidic cubic phase (LCP injector). Alternatively, the samples are deposited on highly X-ray transparent supports which are scanned through the beam and probed by the individual X-ray pulses (fixed target approach).

At the SwissFEL serial protein crystallography experiments will be possible using liquid jets as well as using LCP injectors. In addition, a specialized automated set-up for fixed targets is being developed and will be available for serial diffraction data collection. In the current project we are investigating different aspects of the sample delivery using fixed targets, including materials with minimized X-ray absorption and systems for crystal pre-location in order to maximize the hit rate of the measurements. *In situ* crystallization of proteins on the supports avoids transfer of the sensitive crystalline materials and has been used for the production of large crystals for a specific X-ray-pump – X-ray-probe experiment.

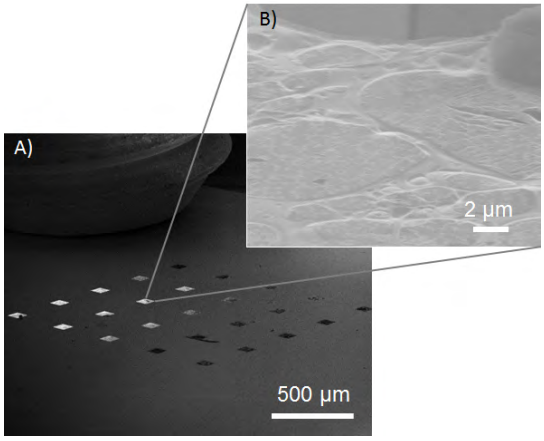

Fig. 1 SEM images of a silicon chip with holey carbon / graphene membranes. The close-up shows graphene spanning over the holey carbon network.

Single layer graphene (SLG) has been proposed as the ultimately thin material to support protein crystals. SLG may be grown on commercial copper foils using chemical vapor deposition. It may subsequently be transferred onto a material of interest: First, the grown SLG is coated with a thin layer of PMMA, which is supporting the SLG during copper etching at the surface of an etchant solution. The PMMA/SLG stack is then floated onto the substrate of choice and the polymer layer is dissolved in an organic solvent. However, to serve as a crystal support the SLG has to span freestanding over the considerable area matching the dimensions of the examined sample, which is challenging even though graphene shows remarkably high mechanical stability. In order to stabilize the very thin layers, a membrane-in-a-membrane approach was followed: A polymeric film (formvar) with holes in the micrometer size range was first formed on a glass slide and transferred to a silicon chip with 100 µm sized etched openings. The substrates were then coated with an evaporated carbon film. In the following step the polymer was washed away in solvents and finally the holey substrate was covered with the graphene sheet (Fig. 1). In the resulting graphene/carbon-bottomed wells *in situ* growth of lysozyme crystals was demonstrated (Fig. 2).

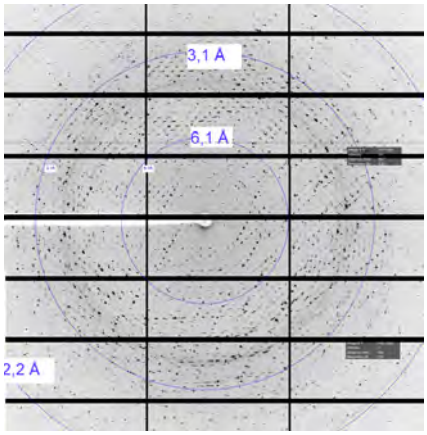

Fig. 2 X-ray diffraction image collected at the PX-III beamline at SLS from lysozyme crystallized in situ on graphene.

As an alternative to the polymeric interlayer, which provides a random arrangement of free-standing membrane parts, graphene sheets were also transferred onto 250 nm thick silicon nitride membranes with a periodic pattern of etched holes of 10 µm in diameter. In this approach the free-standing graphene areas are well located and could easily be addressed with the XFEL beam. In a test experiment 10 µm sized holes were covered with graphene in a yield of more than 50 % (Fig. 3).

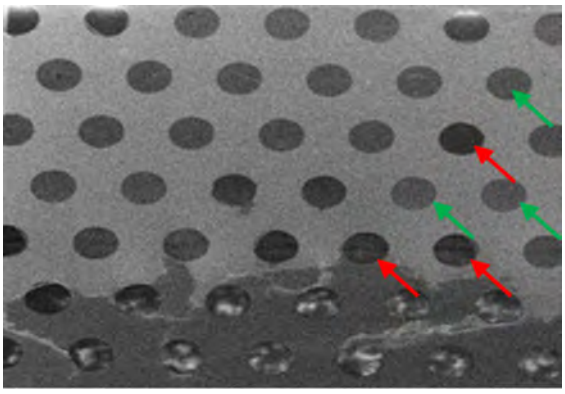

Fig. 3 Graphene suspended over a silicon nitride membrane (250 nm thick) with 10 µm holes on a silicon chip may serve as support for nano-crystalline samples. Regular spacing between the ultrathin membranes facilitates automated serial measurement of the deposited sample. Empty and graphene-covered holes are indicated with red and green arrows, respectively.

To optimize the hit rate in serial data collection at XFELs two different strategies are usually followed, namely crystal prepositioning and prelocation. During the deposition step, the crystals can be prepositioned inside small, periodically arranged wells in the chip, so that the wells are addressed with X-rays by a simple rastering motion at constant speed. For randomly positioned crystals, the crystals can be prelocated using an imaging technique before the XFEL data collection, so that the precise coordinates of the crystals on the support can be addressed directly with the X-ray beam at a high hit rate, without any prior manipulation of crystals. This requires the integration of specific reference marks on the sample for the crystal coordinates, which should preferentially be found not only with optical microscopy, but also by using the X-ray pulses directly.

In order to test the visibility of metal marks by X-ray fluorescence and to program and optimize addressing routines for the xy-stages, metal marks of different materials such as chromium, gold and nickel – 1 to 100 µm in size and 80 nm to 2 µm in thickness – were produced on silicon nitride membranes using e-beam lithography, metal deposition and lift-off processes. When scanned with the SLS PX-I microbeam, the micrometer-thick marks could be successfully identified within the accuracy of the beam size (Fig. 4). The signal-to-noise ratio of the fluorescence signal, detected either by using energy dispersive fluorescence spectra or non-energy dispersive total counts on a large area detector, were shown to be sufficient to foresee practical use of this method at SwissFEL.

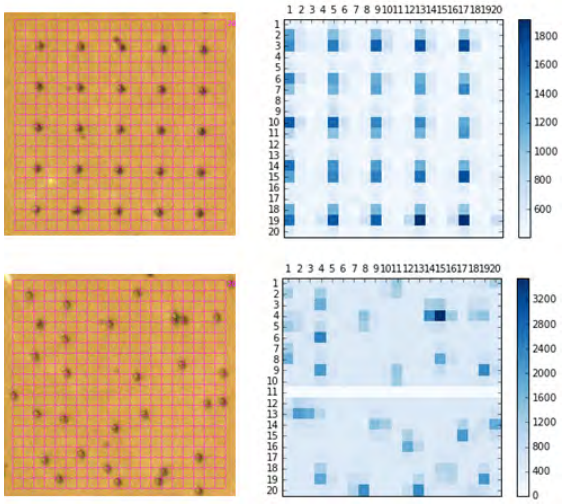

Fig. 4 Periodic arrays and random arrangements of nickel dots on silicon nitride membranes. Left: optical images, right: relative X-ray fluorescence signal recorded at the positions indicated by the grid.

References

[1] Schlichting I., *Serial femtosecond crystallography: the first five years,* IUCrJ. 2, 246–255 (2015)

[2] Pedrini, B. et al., *7 Å resolution in protein two-dimensional-crystal X-ray diffraction at Linac Coherent Light Source.* Phil. Trans. R. Soc. B 369 (2014) 20130500

Nano-pills for mosquitoes to interrupt malaria transmission

Project P1306 Slow-release nano-pills for mosquitoes for interrupting malaria transmission
Project Leader: P. Hunziker and R. Brun
Collaborators: D. Gonçalves (SNI PhD Student), X. Wang, K. Liu, P. Müller, and M. Rottmann

Introduction

In recent years an official research and development agenda for malaria eradication (malERA) was established. The goal is to completely eliminate and, if possible, eradicate the disease from as many areas as possible and control the others. To achieve this, and to complement the human stages tools in malaria portfolio, Transmission Blocking strategies (TBs) focusing on the mosquito stages of the parasite life cycle have been developed and some already implemented in the field. Some attractive targets are the stages in the mosquito midgut where a population choke point occurs, going to as few as 1-5 plasmodia per mosquito [1].

A new radical approach is being studied to use self-assembly polymers to form drug-carrier nanoparticles (NPs) [2], to design a setup to lure mosquitoes into ingestion [3], that would clear, or at least reduce, the parasite density to levels that would render it non-infective and interrupt the disease transmission and propagation. Aiming for a mosquito survival strategy, it is expected to avoid selective pressure towards drug-free mosquitoes and reduce likeness of resistance to appear as opposed with insecticide strategy. To achieve this, whole cycle models were established and different systems tested to optimize the design in terms of assembly, stability, targeting and release.

As proof-of-concept we propose to address a series of goals to validate this strategy:

- design a nanovector, non-toxic for the mosquitoes, that can easily encapsulate a drug of choice and be prepared *in situ* [4];
- tuning targeting and release system towards specific parasites stages and mosquito tissues;
- screen the best antimalarial candidates taking in to account efficacy, affordability, encapsulation compliance and environmental impact;
- design a highly stable setup, able to endure on the open in tropical settings and maintaining its critical properties;
- predict the impact in Malaria transmission by means of modulation and statistical tools based in laboratory collected data.

Here we report some of the key points of the last three milestones.

Results and Discussion

In situ NPs assembly system

A single-step in-line process based on nanoprecipitation of oxazoline-siloxane block copolymers in flow-focusing poly(dimethylsiloxane) microfluidics (Fig. 1) was designed to manufacture the nanosystem to be tested. Nanosystem characteristics could be controlled by copolymer concentration, block length and chemistry, microchannel geometry, flow rate, aqueous/organic flow rate ratio and payload concentration.

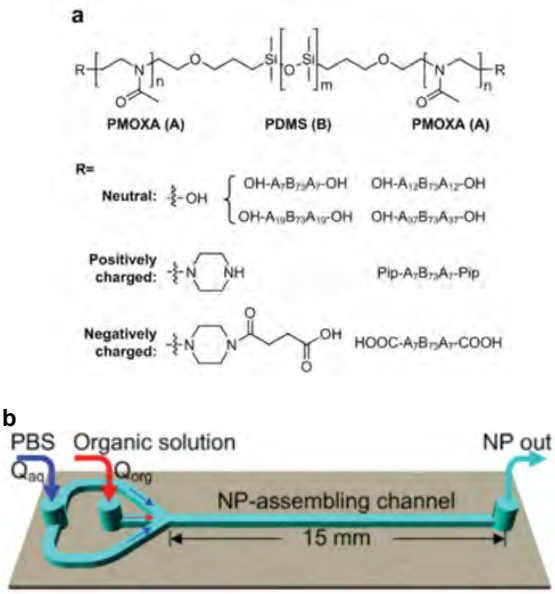

Fig. 1 Copolymers and microfluidic assembly of NPs. (a) Structure of block copolymers with different termini. (b) Topology of microchannels and fluidic interfacing.

NPs characterization

Purification of NPs is achieved with size exclusion cromatography and the help of a UV detector instrument to recover fraction with absorption peak at aprox 300 nm. Characterization of NPs systems was assessed by DLS measurements (size monodispersity) before feeding to mosquitoes. TEM and Cryo-TEM was also performed for certain samples.

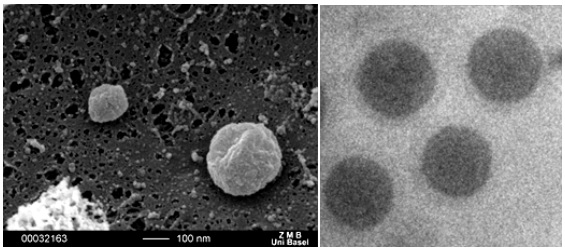

Fig. 2 Electronic Microscopy images of a triblock copolymer PDMS-PMOXA NPs.

Malaria mice/mosquito model

To accurately assess the impact of our nanosystem and in particular the efficacy of certain drugs inclearing parasites in the mosquito stages and avoid transmission to another host, a complete Malaria life-cycle model was established to follow parasites numbers at different stages and assess transmission rate. *P. berghei* parasites, an exclusive rodent infecting strain genetically modified to express a fluorescence protein (m-cherry) and luciferin when fed with the appropriate substrate was chosen and the mosquito vector Anopheles stephensi were chosen.

Drug screening in infected mosquitoes

New high troughput fluorescence screening method for NPs sytems in infected mosquitoes (soon to be published) has been implemented and validated to assess not only efficacy against malaria parasites with different drug candidates (Table 1), but also toxicity and general biodistribution and pharmacokinetics of such systems.

Table 1 Screening of antimalarials against mosquito-stage parasites and possible cargo candidates. Adapted from [1].

Drug	IC50 uM	Method
Primaquine	>10	ATP bioluminescence
	7.2 (1.5)	HTS confocal fluorescence
Mefloquine	100 (3.6)	HTS confocal fluorescence
	4.7 (2.10)	ATP bioluminescence
Pyronaridine	4.260 (0.240)	HTS confocal fluorescence
	3.2	ATP bioluminescence
	0.28	ATP bioluminescence
Pentamidine	0.404	ATP bioluminescence
	2.85 (0.540)	HTS confocal fluorescence
Methylene Blue	0.287	HTS confocal fluorescence
	0.49	ATP bioluminescence
	0.012	ATP bioluminescence
Diihydroartemisin	0.00217	HTS confocal fluorescence
	3.56	ATP bioluminescence
Artesunate	2.53	HTS confocal fluorescence
	2.3	ATP bioluminescence
	10.48	ATP bioluminescence
Epoximicin	0.00042	ATP bioluminescence
	0.0014	AlamarBlue
	0.00066	HTS confocal fluorescence

Impact of NPs and drug to infected mosquitoes

With this new method it was possible to gather data with the following implications:

- fluorescence dyes uptake in sugar meals can be detected at different time points after meal
- fluorescence tagged meals allow to quantify intake and amount ingested
- fluorescence meals allow to determine PKs
- co-block polymers allow to manipulate PKs
- repeated feading leads to accumulation plateau between 72 and 168 hours
- comparison of two fluorophores for dual-labeling of populations
- drug response curves have been obtained

Summary and outlook

The project is now transitioning to the final stages of the initial proposal. An optimized nano-vector system is now in place with a sensitive and quantitative high throughput screening method in a rodent/mosquito model. Large-scale efficacy data is being statistically treated to build models to extrapolate the transmission blocking efficiency to Malaria endemic regions, and then validated in a field study.

References

[1] Gonçalves D. and Hunziker P., *Transmission-blocking strategies: the roadmap from laboratory bench to the community*, Malaria Journal, **15**:95 (2016)

[2] Broz P. and Hunziker P., *Nanotechnologies for targeted delivery of drugs*, Wiley-VCH, 3731-3732 (2007)

[3] Knols BGJ, *Odour-mediated host-seeking behavior of the Afro-tropical malaria vector Anopheles gambiae Giles,* Parasitology Today, 159–161 (1996)

[4] Liu K. Z. Zhu, X. Weng, D. Gonçalves, B Zhang, A. Hierlemann and P. Hunziker, *Microfluidics-based single-step pre-paration of injection-ready polymeric nano-systems for medical imaging and drug deli-very,* Nanoscale, 16983-16993 (2015)

Optical and electronic measurements on mechanically controlled nanojunctions

Project P1307 Optoelectronic nanojunctions
Project Leader: M. Calame and M. Mayor
Collaborators: J. Overbeck (SNI PhD Student), L. Wang, P. Makk, C. Schönenberger, S. Neumann, and O.S. Wenger

Introduction

In this project we are working to combine optical methods with our existing expertise on electrical measurements of single molecule junctions [1] for characterizing junctions between different nano-structured materials and molecules.

Setup for optoelectronic measurements

In order to perform optoelectronic measurements, we built a compact setup that can be fitted to the available confocal microscopes and free-space optical setups. Lithographically fabricated samples can be strained and compressed by a three-point bending mechanism operated via mechanical gears or piezos.

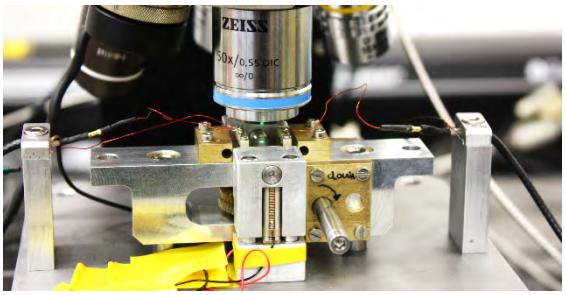

Fig. 1 Newly built optoelectronic break junction setup mounted to a WITec *Raman microscope.*

Suspended graphene nanojunctions

A major obstacle to optically addressing molecules and observe their electroluminescence in metallic break junctions is their proximity to the electrodes. Optoelectronic experiments on metallic point contacts in a break junction geometry have shown transmission of surface plasmons through such structures [2]. The comparatively strong absorption of metallic electrodes, however, leads to thermally-induced conductance changes that make the detection of a photocurrent signal from an individual molecule very challenging.

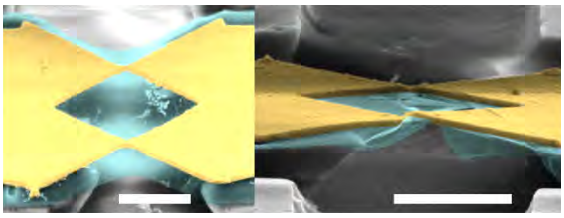

Fig. 2 Scanning electron micrographs of a twin-break junction (golden) on LOR supporting a layer of CVD-graphene (blue shading). Left: Before breaking. Right: The graphene ripped along the line connecting both Au-junctions and reconnected afterwards. Scale bar 2 µm.

Similarly, the high density of states in metallic electrodes results in a quenching of emission from radiative recombination of excitons in a molecular junction under bias [3]. By forming a junction with molecules between suspended graphene electrodes (Fig. 2) we will be able to perform Raman spectroscopy on molecules while simultaneously measuring their transport properties, detect electroluminescence and measure photocurrents.

Strain in suspended graphene nanojunctions

As a first necessary step to better understand the behaviour of our electrodes we are investigating the effects of strain in freely suspended graphene by Raman and transport measurements. Figure 3 shows a thin stripe of graphene suspended between two metal electrodes in a modified break junction geometry. By tuning the length of suspension under the electrodes we can vary the mechanical attenuation factor of our sample. We estimate that we are able to create several percent of controlled uniaxial strain while independently gating the graphene to characterise its transport properties.

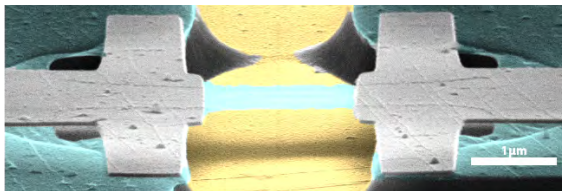

Fig. 3 Scanning electron micrograph of CVD-graphene (blue) freely suspended between two Pd-electrodes (gray). The local Au-bottom-gate is shaded in yellow.

Raman spectroscopy is a widely employed optical characterization of graphitic systems [4]. The most prominent signatures of uniaxial strain in graphene are the shift and splitting of the G and 2D and 2D' peaks [5, 6]. These effects have been investigated for exfoliated graphene, typically on a flexible poly-mer substrate. We have now observed these signa-tures in the above geometry (Fig. 4) where we are able to investigate the material properties decoupled from the substrate and design flexible electrode geometries. By fitting the position of the 2D peak as well as the split of the G peak we deduce that we can apply a strain of about 1% before damaging the graphene. We are currently investi-gating the polarization dependence to assess the crystallographic orientation of the graphene, which allows a more precise strain estimate. In collaboration with Lujun Wang (P1504) & Peter Makk from the group of Prof. Schönenberger we have started to investigate the effects of strain on transport.

This will allow us to disentangle the effects of strain and doping on the Raman spectra of graphene and to investigate artificial electromagnetic fields predicted for inhomogeneous strains [7].

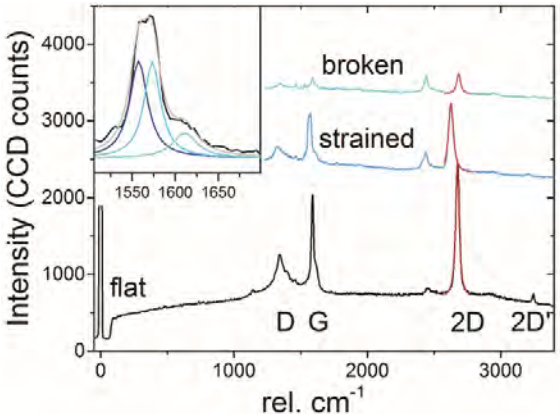

Fig. 4 Raman Spectra of freely suspended graphene under uniaxial strain. A strain-induced downshift of the G and 2D peaks with respect to the flat (slightly pre-strained) and broken (fully relaxed) configuration can be clearly seen even in this low resolution spectrum. The inset shows the G peak (black) fitted by 3 Lorentzians for the $G^{+/-}$ and D' modes, the sum of the fits is shown in grey.

Molecular systems for investigating charge transport

In parallel to characterising the graphene-based samples we are using our break junction setups to screen molecules for further measurements. In particular, we are investigating the relationship between electron transfer in donor-bridge-acceptor systems and conductivity in molecular junctions [8], together with Svenja Neumann from the group of Prof. Wenger (P1406).

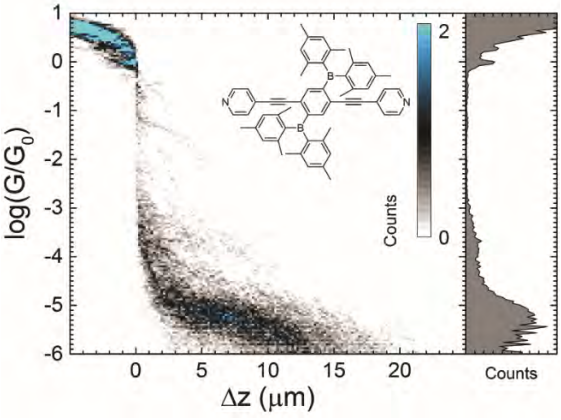

Fig. 5 Conductance-displacement histogram of the organoboron compound synthesized by S. Neumann, without the addition of fluorine. The slightly slanted plateau can also be seen as a peak in the conductance histogram displayed on the right.

Towards that end we are examining the conductivity of an organoboron-based molecule (Fig. 5) before and after the addition of fluoride ions in order to compare this response with the change in electron transfer rates across the same molecular motif, which has previously been measured by optical pump-probe experiments [9].

Initial measurements show a binding of the molecules to the electrodes, however with a low molecular conductance. We are currently trying to boost the conductance by employing different binding groups that allow us to quantify the effect upon fluoride binding.

To complement the optical characterization methods we are also adapting the well-established method of optical pump-probe measurements to an electrical measurement scheme to access time scales in the range of μs and down to a few tens of ns (Master Thesis by David Marti).

Outlook

The next step towards optoelectronic measurements is the full electrical characterization and gate control of the suspended graphene electrodes.

Acknowledgements

We thank Kishan Thodkar for help in growing graphene and Heinz Breitenstein & Yves Pellmont for support with the new setup.

References

[1] See for example: J. Brunner, M.T. González, C. Schönenberger and M. Calame, *Random telegraph signals in molecular junctions*. Journal of physics. Condensed matter, 26, 474202 (2014)

[2] D. Benner, J. Boneberg, P. Nürnberger, G. Ghafoori, P. Leiderer and E. Scheer, *Transmission of surface plasmon polaritons through atomic-size constrictions*. New J. Phys., 15, 113014 (2013)

[3] C.W. Marquardt, S. Grunder, A. Błaszczyk, S. Dehm, F. Hennrich, H. v. Löhneysen, M. Mayor and R. Krupke, *Electroluminescence from a single nanotube-molecule-nanotube junction*. Nature Nanotech, 5, 863–867 (2010)

[4] A.C. Ferrari & D.M. Basko, *Raman spectroscopy as a versatile tool for studying the properties of graphene*. Nature Nanotech. 8, 235-246 (2013)

[5] T.M.G. Mohiuddin et al., *Uniaxial strain in graphene by Raman spectroscopy*. Phys. Rev. B, 79, 205433 (2009)

[6] E. del Corro, L. Kavan, M. Kalbac and O. Frank, *Strain Assessment in Graphene Through the Raman 2D′ Mode*. J. Phys. Chem. C, 119, 25651–25656 (2015)

[7] M. Vozmediano, M. I. Katsnelson and F. Guinea, *Gauge fields in graphene*. Physics Reports, 496, 109–148 (2010)

[8] A. Nitzan, *A Relationship between Electron-Transfer Rates and Molecular Conduction*. J. Phys. Chem. A, 105, 2677–2679 (2001)

[9] J. Chen and O. S. Wenger, *Fluoride binding to an organoboron wire controls photoinduced electron transfer*. Chem. Sci., 6, 3582–3592 (2015)

Two-dimensional calixarene-based metal organic networks

Project P1308 Supramolecular charge and spin architectures produced by chemical clipping
Project Leader: P. Shahgaldian and T. Jung
Collaborators: M. Moradi (SNI PhD Student)

Introduction

The discovery of graphene and its unique physical properties combining outstanding mechanical, electronic and thermal properties has triggered a resurgence of interest from researchers in the design of two-dimensional and highly ordered monomolecular films [1]. In this context, metal organic networks (MONs), produced through the self-assembly of metal nodes and organic ligands, have gained significant attention [2].

The production of MONs requires confining the self-assembly reaction to two dimensions. In this respect, the air-water interface represents an excellent opportunity as it has been widely studied for the self-assembly of amphiphiles into two-dimensional monomolecular films. Additionally, the produced monolayers can be transferred onto solid substrates using Langmuir-Blodgett (LB) or Langmuir-Schaefer (LS) deposition techniques.

Calixarenes are cyclic organic synthons, which can serve as molecular backbones to design a range of amphiphilic molecules [3]. Recently, we demonstrated that calixarene-based monolayers can be stabilized using organic supramolecular clips [4] or metal ions [5]. Herein, we report the synthesis and self-assembly of 4 calix[4]arene-based amphiphiles (**1-4**) bearing different functional groups. The molecules are used as building blocks to form 2D self-assembled architectures at the air-water interface and on solid surfaces.

Results

We produced and fully characterized a series of amphiphilic calixarenes bearing carboxylic, methyl-cyano, methyl carboxylic, and methyl-pyrazolyl functions at the *para* position, and propyl chains on the phenolic rim (Fig. 1).

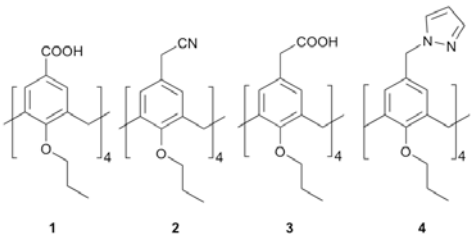

*Fig. 1 Chemical structures of carboxy- (**1**), methyl cyano- (**2**), methyl carboxy- (**3**) and methyl pyrazoly-l (**4**) propyloxy- calixarenes.*

The self-assembly of **1-4**, in the form of monomolecular layers, was studied using the Langmuir balance method on pure water and subphases containing $CuCl_2$ (Fig. 2).

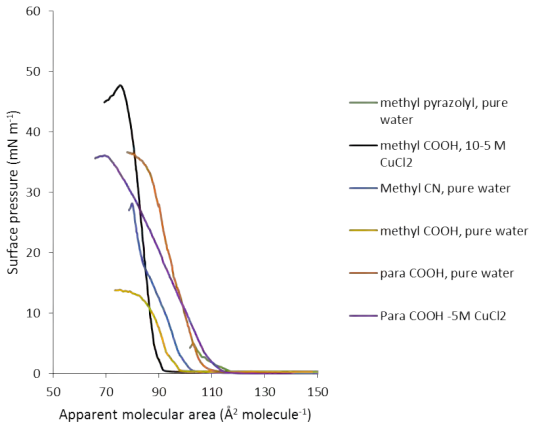

*Fig. 2 Π/A Langmuir isotherms measured on pure water (**1**—, **2**— and **3**— and on 10 μM $CuCl_2$ (**1**—, **3** —) subphases. **4** does not form stable monolayers both on pure water or on a $CuCl_2$ subphase. The isotherm of **2** did not show any relevant change in the presence of $CuCl_2$ and is omitted for clarity.*

The Langmuir compression isotherm studies show that **1** and **2** are able to form stable monolayers on pure water, with collapse pressure values of 34 and 28 mN m^{-1}, respectively. These values are fairly high for amphiphiles bearing only short propyl chains with limited capabilities for establishing van der Waals interaction. This strongly suggests that the monolayers are additionally stabilized through π-π interactions among neighboring calixarene molecules. Oppositely, **3** and **4** do not form stable monolayers on pure water. In the presence of a low concentration (10 μM) of $CuCl_2$ dissolved in the subphase, the isotherm of **1** shows a slight increase of collapse pressure to a value of 36 mN m^{-1} while the isotherm of **2** does not show any difference with regard to that measured on pure water. This suggests that no interactions occur between **2** and the studied ion. Remarkably however, in the presence of $CuCl_2$ (10 μM) in the subphase, **3** is shown to form a stable and well-defined monolayer with a collapse pressure as high as 47 mN m^{-1}. This stabilization effect is assigned to the coordination of the carboxylate functions of **3** with copper ions at the air-water interface. In the case of **4**, the presence of Cu^{2+} ions does not influence the self-assembly and no stable monolayer is produced.

The morphology of the monolayers of 1 at the air-water interface was studied by Brewster angle

microscopy (BAM)(Fig. 3). Form the micrographs, it can be seen that on pure water, the monolayer of 1 exhibits large crystalline domains of different contrast. This suggests the presence of organized anisotropic domains, which we attribute to a distinct molecular orientation in the layer. In the presence of 10 µM CuCl2, BAM images are significantly different as they reveal large dendritic domains of rotationally aligned molecules coexisting within an amorphous matrix. The 2D self-organization can be explained by the presence of deprotonated carboxylate functions in the calixarene structure that can form carboxylate-copper bridges, at the interface. By decreasing the aqueous phase temperature, the morphology of the monolayer significantly changes. The monomolecular film appears grainy on both pure water and $CuCl_2$ solution with an average grain size of ca. 5 µm.

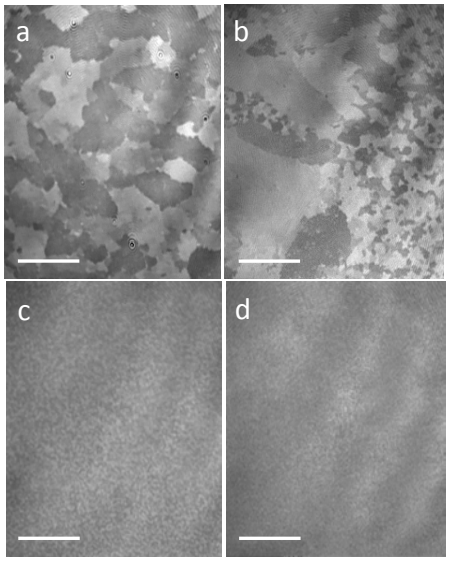

*Fig. 3 BAM micrographs of monolayers **1** measured at 23°C (a, b) and at 10°C (c, d) measured on pure water (a, c) and on 10 µM $CuCl_2$ (b, d). Scale bars represent 100µm.*

Monolayers of **1** were successfully transferred onto highly oriented pyrolytic graphite (HOPG) by the LS method and studied by *X*-ray photoelectron spectroscopy (XPS) and atomic force microscopy (AFM). XPS spectra, measured in absence of $CuCl_2$, reveal the characteristic peak of the carboxylate function at 288.4 eV (Fig. 4). In the presence of $CuCl_2$, this characteristic peak is significantly shifted at a binding energy of 288.8 eV. This result confirms the formation of coordination bonds between the carboxylate functions of the calixarene and copper ions.

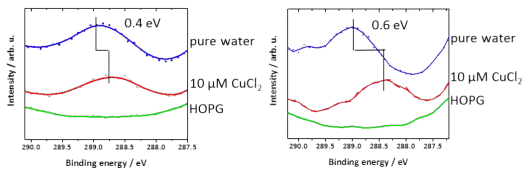

*Fig. 4 Identification of the carboxy peak shifts in the C1s spectra of the monolayer of **1** transferred from the air-water interface at 23°C (left) and at 10°C (right).*

AFM investigations carried out on LS monolayers allowed us to acquire molecular resolution images in the peak force mode. The micrographs revealed the presence of crystalline networks on the scale of up to 200 x 200 nm. The thickness determined by performing AFM after scratching the layer is 1 ± 0.4 nm; this value is consistent with the expected dimension of one monomolecular layer of **1** stabilized by Cu^{2+} ions.

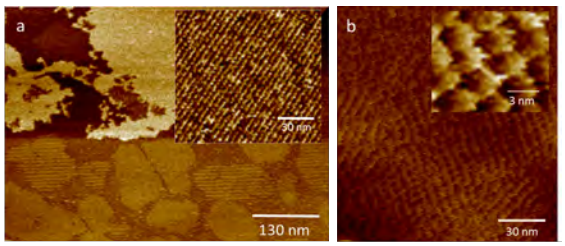

Fig. 5 AFM micrographs of monolayer of 1 produced on 10µM $CuCl_2$ transferred at 23°C a) and at 10°C b)

Conclusion

In summary, we have demonstrated that designer amphiphiles based on calixarenes can be used as organic synthons, in the presence of copper metal ions, to yield stable metal-organic networks at the air-water interface. When transferred onto solid substrates, the monomolecular layer retains the orientation of the building blocks across relatively large areas. The work is underway to expand the range of calixarenes macrocycles able to form MONs at the air-water interface and to exploit the produced layers as two-dimensional supramolecular systems.

References

[1] K. Ariga, *Organized Organic Ultrathin Films: Fundamentals and Applications*, Wiley (2012)
[2] O. M. Yaghi, *et al.*, *Synthetic Strategies, Structure Patterns, and Emerging Properties in the Chemistry of Modular Porous Solids*, Acc. Chem. Res., 31, 474, (1998)
[3] L. G. Tulli and P. Shahgaldian, *Calixarenes and Resorcinarenes at interfaces* in *Calixa-renes: Functionalization and Applications*, P. Neri, J. L. Sessler and M.-X. Wang, Springer, (2016)
[4] N. Moridi, *et al.*, *Langmuir–Blodgett mono-layer stabilization using supramolecular clips,* Chem. Commun. 49, 367 (2012)
[5] L. G. Tulli, *et al.*, *Interfacial binding of diva-lent cations to calixarene-based Langmuir monolayers,* Chem. Commun. 30, 3938 (2014)

Optomechanics with nanostructured silicon nitride membranes

Project P1309 Cooling and control of a nanomechanical membrane with cold atoms
Project Leader: P. Treutlein and P. Maletinsky
Collaborators: T. Karg (SNI PhD Student), and A. Jöckel

The field of nanomechanical oscillators has recently attracted great interest, as first experiments have succeeded in cooling the vibrations of such oscillators to the quantum ground state [1]. A current challenge in the field is to couple engineered mechanical oscillators to microscopic quantum systems with good coherence properties, such as ultracold atoms, solid-state spin systems or superconducting devices. The resulting hybrid mechanical systems offer new possibilities for quantum control of mechanical vibrations, precision sensing, and quantum-level signal transduction [2]. Our group reported the first experiments, where a nanomechanical oscillator was coupled to ultracold atoms in a trap using laser light [3]. In these experiments, the mechanical oscillator was still in the classical regime, mainly because it was placed in a room-temperature environment. To reach the quantum regime, we are currently setting up a new optomechanical system with improved parameters that is placed in a cryostat.

Novel types of membrane oscillators

In our new setup we employ specifically engineered silicon nitride membrane oscillators. In figure 1, two designs are shown: the first are "tether membranes" (Fig. 1a), consisting of a small membrane paddle suspended by ultrathin strings under tensile stress. They combine a very low effective mass with ultralow mechanical dissipation [4]. Moreover, a photonic crystal reflector can be fabricated at the centre in order to increase the optical reflectivity, resulting in increased optomechanical coupling. Our investigations revealed, however, that the photonic crystal reflector can distort the optical wavefront, thereby limiting the coupling efficiency to an optical cavity. In order to fully exploit their potential, more effort has to be put into the design and fabrication.

Another approach to reduce mechanical dissipation is to fabricate a phononic bandgap structure into the silicon chip hosting the membrane (Fig. 1b) [5]. In this way acoustic noise at the membrane frequency can be suppressed and high mechanical quality factors are obtained reliably. Compared to tether membranes, small square membranes have modes with higher mechanical frequencies, which is favorable for quantum-noise-limited operation. The design of our optomechanical cavity described in the following allows to easily switching between the two membrane designs.

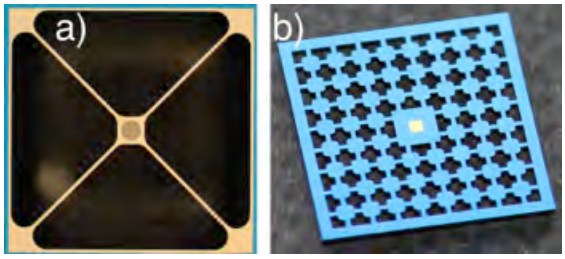

Fig. 1 a) Microscope image of a tether membrane with photonic crystal structure at the centre. The size of the full structure is 0.7×0.7 mm². b) Photograph of a phononic bandgap shielded silicon nitride membrane (yellow). The 270×270 μm² large membrane is surrounded by a periodic structure etched into the silicon chip that acts as a reflector for acoustic waves at the membrane frequency.

Membrane-in-the-middle cavity

Having good mechanical resonators at hand, the next step is to integrate them into an optical cavity in order to establish strong radiation pressure coupling. We have built a compact and monolithic cavity (Fig. 2) with two high-reflectivity mirrors mounted on piezoelectric transducers to independently control both the cavity length and the membrane position relative to the optical standing wave. The membrane chip is inserted between the mirrors, carefully aligned perpendicular to the optical mode and then glued to an exchangeable mounting piece. This allows switching between different membrane oscillators without having to rebuild the entire setup. The cavity has a finesse of 1600 at 780 nm. Together with a cavity length of 2.5 mm this results in a FWHM linewidth of 40 MHz.

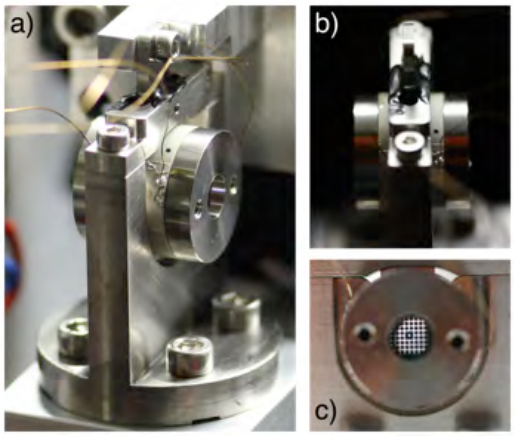

Fig. 2 a) Optical cavity with membrane inserted between the mirrors from the top b) such that the angle relative to the optical beam can be aligned precisely. c) View of the membrane chip through one of the cavity mirrors.

Optomechanical cooling experiments

To test our setup we demonstrate cavity optomechanical cooling of the vibrational modes of a phononic bandgap membrane. A cooling laser is injected into the cavity, red-detuned by half a cavity linewidth for maximum cooling efficiency. A second, weak detection beam on cavity resonance probes the cavity phase shift due to the membrane vibrations, which is detected in a balanced homodyne measurement. Optomechanical cooling of the (3,3) mode of a phononic bandgap membrane at 4.7 MHz is shown in figure 3. Upon increasing the cooling beam power from 60 µW to 10 mW, the mechanical resonance gets strongly damped and cooled from room temperature to about 500 mK.

Figure 4 shows simultaneous cooling of several mechanical modes, all coupled to the same optical mode. For all mechanical modes, the temperature decreases linearly with the applied cooling laser power, indicating that technical laser noise is negligible in these measurements. These measurements were done in a room temperature environment. Soon, we will be able to test the setup in a cryostat, which was recently purchased. Starting from about 4 K, we expect to see cooling to the few phonon regimes, which is an ideal starting point for coupling experiments with atoms.

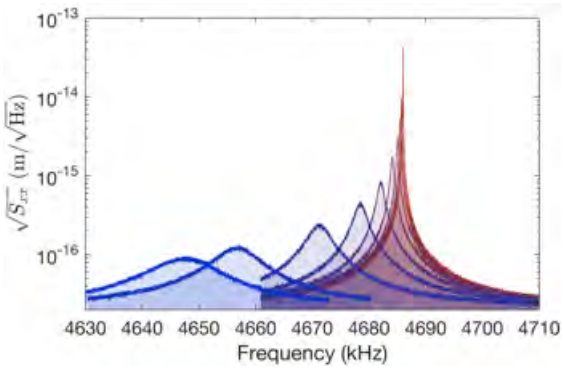

Fig. 3 Cavity optomechanical cooling of the membrane's (3,3)-mode. Displacement noise spectrum measured for a series of gradually increasing cooling laser power from 60 µW (red) to 10 mW (blue). One clearly observes strong broadening of the peak as well as a frequency shift due to the optomechanical coupling. The reduction of the peak area corresponds to a reduction of the temperature (Fig. 4).

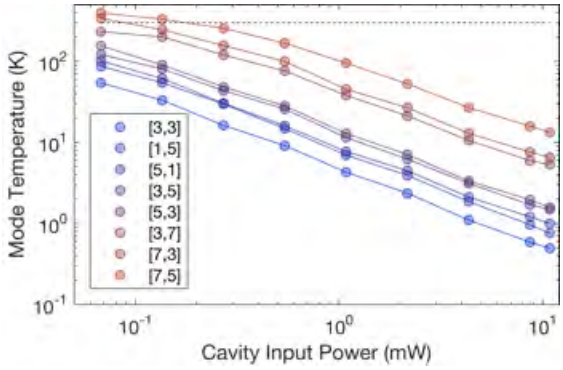

Fig. 4 Cavity optomechanical cooling of several mechanical modes, all coupled to the same optical mode of the cavity. The mechanical mode temperatures decrease linearly with the applied laser power, indicating that the cooling is unaffected by technical laser noise.

References

[1] M. Aspelmeyer, P. Meystre, and K. Schwab, *Quantum optomechanics*, Phys. Today 65, 29, 2012

[2] P. Treutlein, C. Genes, K. Hammerer, M. Poggio, and P. Rabl, *Hybrid Mechanical Systems, in Cavity Optomechanics* (eds M. Aspelmeyer, T. Kippenberg, and F. Marquardt) 327–351, Springer, 2014

[3] A. Jöckel, A. Faber, T. Kampschulte, M. Korppi, M. T. Rakher, and P. Treutlein, *Sympathetic cooling of a membrane oscillator in a hybrid mechanical–atomic system*, Nature Nanotechnology, 10, 55–59, 2015

[4] R. A. Norte, J. P. Moura, and S. Gröblacher, *Mechanical resonators for quantum optomechanics experiments at room temperature*, Phys. Rev. Lett., 116, 147202, 2016

[5] P.L. Yu, K. Cicak, N.S. Kampel, Y. Tsaturyan, T.P. Purdy, R.W. Simmonds, and C. Regal, *A phononic bandgap shield for high-Q membrane microresonators*, Appl. Phys. Lett. 104, 023510, 2014

Positive nanoparticle trapping in nano-fluidic systems

Project P1310 Plasmonic sensing in biomimetic nanopores
Project Leader: Y. Ekinci and R.Y.H. Lim
Collaborators: D. Sharma (SNI PhD Student)

Introduction

Single particle trapping and handling in a contact-free manner in a solution is of significant interest in the field of chemistry, biophysics, biotechnology, and medicine. There are several active and passive trapping techniques, one of which is geometry induced electrostatic (GIE) trapping that relies on the topography of a nanofluidic device surface and allows for single-particle trapping in an aqueous solution. In general, GIE-trapping nanofluidic devices are based on glass/silicon-substrates [1, 2], which acquire a net negative surface charge density in an aqueous environment (pH > 2) [3], thus applicable only for negatively charged nanoparticles. Due to a topographic modulation of the bounding surface of the device, electrostatic potential traps form at the locations of nanometric indentations (see Fig. 1) and allow for the confinement of single nanoparticles based on their charge, and independent of their size and other volumetric electrical and magnetic material properties. To widen the applicability of the method and use it for positively charged nano-objects, we have altered the surface charge to positive through surface functionalization. Here, we demonstrate the successful confinement of the positively charged 60 nm gold nanoparticle inside the functionalized device.

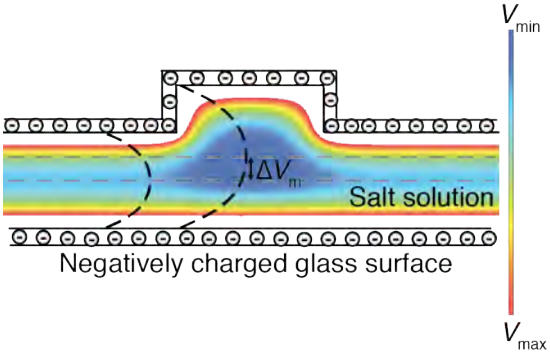

Fig. 1 Electrostatic potential trap inside a nanopockets embedded in the glass surface of the nanofluidic device. The color plot shows the spatial modulation of electrostatic potential due to geometric-modulation of the device surface. In the presence of a salt solution, electrostatic potential drops exponentially with distance from the charged glass surface.

Nanofluidic devices were fabricated using top-down lithography processes on a glass substrate and followed by thermal binding with cover glass as shown in figure 2. The prepared device was drilled for inlets and outlets, and connected to tubings by inlet/outlet ports (Fig. 3a) to allow the flow of a buffer solution. The obtained device can be used for negatively charged particle trapping. To achieve positively charged nanoparticle trapping, the device surface is functionalized using cationic poly-electrolyte, poly(ethylene imine) (PEI), solution that results in a positively charged surface as shown in figure 3b.

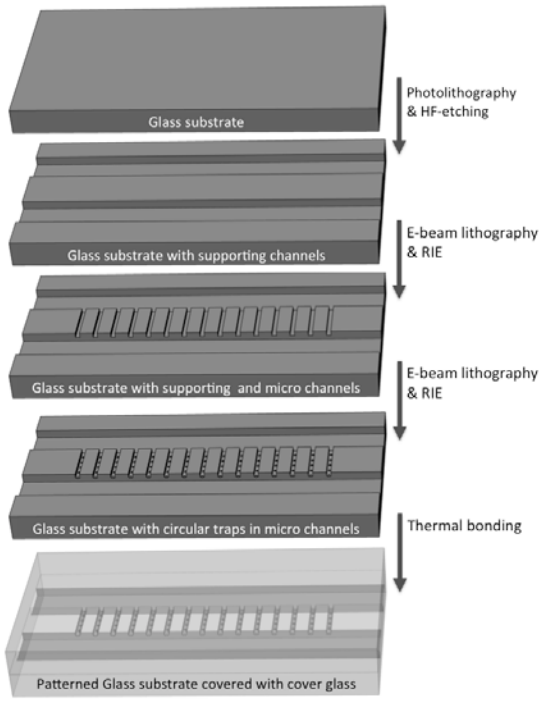

Fig. 2 Schematics of the nanofluidi device fabrication through top-down lithography processes on a glass substrate. Patterned glass substrate is bound to a cover glass to prepare GIE-trapping device.

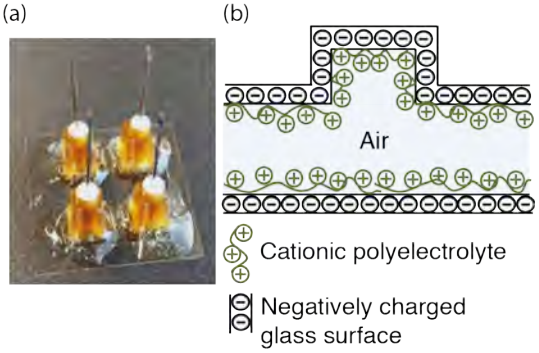

Fig. 3 a) Device after drilling holes and attaching inlet/outlet ports for buffer flow. b) Schematic of the modified glass surface after the surface functionalization using cationic polyelectrolyte solution.

Single positive nanoparticle trapping

A glass-based functionalized GIE trapping device is used for the trapping of positively charged 60 nm gold nanoparticles (AuNPs). Nanoparticle solution was prepared in dionized (DI) water (18.3 MΩ/cm^{-1}) and flushed through the device. Trapped nanoparticles were imaged using the interference scattering detection (iSCAT) technique. iSCAT allows for the detection of the trapped particles based on the interference of the scattered light from the particle and reflected light from the substrate surface. Each captured image was fitted with a Gaussian profile to get the center position of the trapped particle in each frame, which was further used for the particle trajectory. Mean square displacement (MSD), $< [\Delta r(\Delta t)]^2 >$, where $r = \sqrt{x^2 + y^2}$, is calculated as a function of lag time Δt for the confined particle, which reaches a plateau due to restricted motion of the particle trapped in the nanopocket. MSD value at plateau, $< [\Delta r]_P^2 >$, is directly correlated to the radial stiffness constant (k_r) for the electrostatic potential trap inside the nanopocket by $< [\Delta r]_P^2 > = 4k_B T/k_r$ [4], here, k_B is the Boltzmann constant and T the room temperature. Thus, the spread of the particle-scatter plot directly relates to the stiffness of the trap.

Successful trapping of a positively charged particle in 250 nm wide and 75 nm deep nanopockets is shown in figure 4, an associated scatter plot is presented in figure 4b. Stiffness constant of electrostatic potential traps in case of positively charged particle trapping is demonstrated in figure 4c, where the mean stiffness is 0.0266 ± 0.0160 pN/nm. The result was compared with the contact-free confinement of negatively charged 60 nm AuNPs in non-functionalized nanofluidic device, where the obtained mean stiffness for negative AuNPs is 0.0463 ± 0.0138 pN/nm. Observed average stiffness constant value for positively charged particle is lower than the negatively charged particle, which might be caused due to lower surface charge density of the functionalized device surface or differences in the net surface charge value for positive and negative AuNPs. It has been shown that in the case of poly(ethylene imine), surface charge density depends on many factors and can reach 20-25 microequivalents per gram [5], whereas a glass surface attains surface charge density of ~ 10^{17} e/m^2 [6].

The demonstrated feasibility of parallel contact-free trapping of positive nano-objects in the nanofluidic devices has broadened the applicability of the device for biomolecules, viruses, vesicles and proteins that have net positive surface charge.

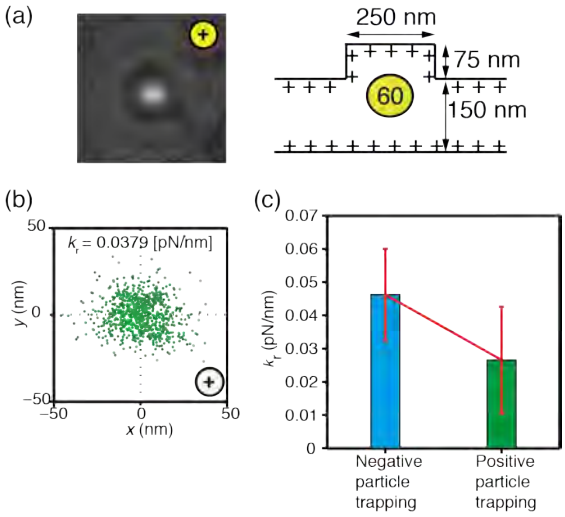

Fig. 4 a) Successful positive 60 nm diameter gold nanoparticle (AuNPs) trapping in 250 nm pocket with 75 nm pocket depth, and 150 nm channel height. b) Scattering plot from a trapped particle showing the motion of the particle inside the electrostatic trap. C) Comparison of trapping for negative and positive AuNPs in non-functionalized and functionalized nanofluidic device respectively. It shows higher trapping stiffness for negatively charged particle confinement than the same for positively charged particle.

References

[1] Krishnan, M., et al., *Geometry-induced electrostatic trapping of nanometric objects in a fluid.* Nature, 2010. 467 (7316): p. 692-5

[2] Gerspach, M.A., et al., *Glass-based geometry-induced electrostatic trapping devices for improved scattering contrast imaging of nano-objects.* Microelectronic Engineering, 2015. 145: p. 43-48

[3] Lowe, B.M., C.K. Skylaris, and N.G. Green, *Acid-base dissociation mechanisms and energetics at the silica-water interface: An activationless process.* J Colloid Interface Sci, 2015. 451: p. 231-44

[4] Mojarad, N. and M. Krishnan, *Measuring the size and charge of single nanoscale objects in solution using an electrostatic fluidic trap.* Nat Nanotechnol, 2012. 7 (7): p. 448-52

[5] Neu, M., D. Fischer, and T. Kissel, *Recent advances in rational gene transfer vector design based on poly(ethylene imine) and its derivatives.* Journal of Gene Medicine, 2005. 7 (8): p. 992-1009

[6] Behrens, S.H. and D.G. Grier, *The charge of glass and silica surfaces.* Journal of Chemical Physics, 2001. 115 (14): p. 6716-6721

Targeted proteomics to study spreading of protein aggregation

Project P1401 Targeted single cell proteomics using magnetic nanoparticles to study prion-like spreading of amyloid nanoparticles
Project Leader: T. Braun and H. Stahlberg
Collaborators: C. Schmidli (SNI PhD Student), A. Bieri, R. Sütterlin, A. Hierlemann, M. Leist, and S. Gutbier

Biomedical background

Stereotypic spreading of protein aggregation through the nervous system is a hallmark of many neurodegenerative diseases. This was shown for Alzheimer's disease (AD, amyloid-β & tau protein) and Parkinson's disease (PD, α-synuclein, or α-syn). A-syn is a natively unfolded, presynaptic protein of unknown function and unusual conformational plasticity. Evidence accumulates that progression of synucleinopathies not only involves transmission of simple "*protein misfolding*" but rather specific "*structural information*" from one cell to the next, leading to the progressive proliferation of "*structural α-syn strains*". It is suspected, that different forms of α-syn inclusions lead to different phenotypes of neurodegeneration, i.e., lead to different synucleinopathy diseases, such as PD, Dementia with Lewy bodies disease, or Multiple System Atrophy. How is such specific structural information transmitted? To date the mechanisms are unknown, but a prion-like transmission via an intrusion of protein nanoparticles imprinting their specific folding onto native host proteins is most likely.

Model system to study the prion like spreading

To study the prion like cell-intrusion and spreading of protein aggregate related to neurodegenerative diseases, we established the Lund human mesencephalic (LUHMES) cell line, which can be differentiated to dopaminergic-like neurons [1]. Upon differentiation, these cells can be seeded with fluorescence labeled amyloid nanoparticles in pulse chase experiments (Fig. 1). In order to study the spreading from one cell to the next, we are developing microfluidic chips, spatially separating "diseased" and healthy cells. In the microfluidic chip the two populations are connected by thin channels allowing the growth of dendrites between the two main compartments hosting the cell somas (Fig. 2).

The seeding and transmission experiments are analyzed by classical methods, e.g., electron microscopy (EM) and fluorescence light microscopy as shown in Fig. 1. However, today's biophysical and biochemical methods can trace the presence of proteins, but do not allow detecting *and* monitoring the structural arrangement of the involved proteins or structural strains. Visual proteomics [2] promises to overcome these limitations and complements classical analysis methods.

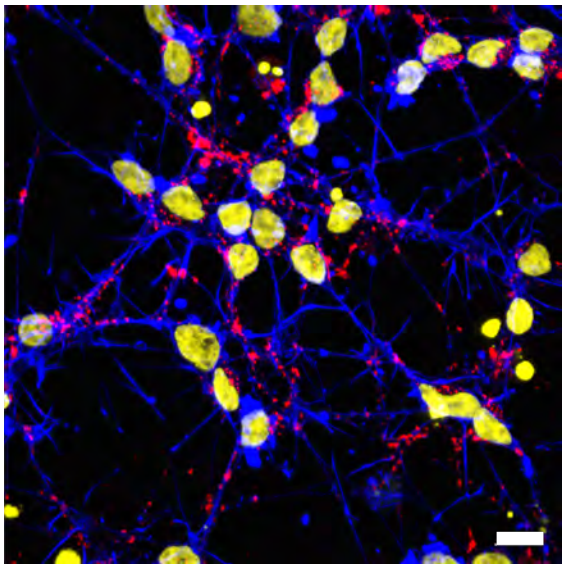

Fig. 1 LUHMES cell lines, differentiated for eight days to dopaminergic cell. Nuclei are stained yellow, actin filaments are labeled in blue. The α-syn protein nanoparticle seeds, which accumulated in the cells, are shown in red. Scale bar reads 10 µm.

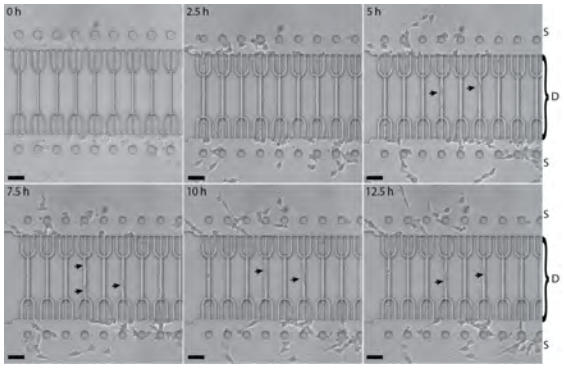

Fig. 2 Time-lapse light microscopy of LUHMES cell differentiation to dopaminergic neurons in a 1st generation microfluidic chip, separating "diseased" and "healthy" cells. Cell somas grow in two separated compartments (S). The channels in the middle should allow dendrite growth (D), but not the passage of complete cells. LUHMES cells were differentiated for two days in culture flasks, detached and infiltrated into the chip, where they were further differentiated. Time-lapse microscopy shows the attachment of the cells and ongoing differentiation, e.g., dendrite outgrowth, for the next 10 h. This experiments also reveals, that the channel structures are too high and cell somas can grow into the channels as indicated by arrows. This is now solved with a 2nd generation chip. Scale bar reads 20 µm.

Visual proteomics and targeted visual proteomics

We developed a simple but versatile method for the almost lossless sample conditioning and preparation of nanoliter volumes of biological samples for EM, keeping the sample under close to physiological condition [2]. A microcapillary is used to aspirate 3 to 5 nanoliters of sample. The microcapillary tip is immersed into a reservoir of negative stain, where the sample becomes conditioned by diffusive exchange of salt and heavy metal ions, before it is deposited as a small spot onto an EM grid. The minute sample volume required for this method enables alternative strategies for biological experiments, such as the analysis of the content of a single cell by visual proteomics, fully exploiting the single molecule detection limit of EM (see also report of project A9.12 SceNA). This new method is now employed to analyze the large protein assemblies of seeded LUHMES cells and corresponding control experiments. However, the complete cell proteome is very crowded and the visual identification can be difficult. Therefore, novel labeling methods and protein isolation strategies for minimal amounts of protein must be developed.

We are refining a fast and simple microfluidic method [3] for (i) the quantitative isolation of endogenous levels of untagged protein complexes from minute volumes of cell lysates and (ii) the labeling of specific components constituting these complexes. The method uses specific antibodies that are conjugated via a photo cleavable linker to super paramagnetic nanoparticles that are trapped in microcapillaries to immobilize the target proteins. Proteins are released by photocleavage, eluted and subsequently analyzed by quantitative transmission EM at the single molecule level. Alternatively, the proteins can be eluted by turning off the magnetic trap eluting the target protein bound to the nanoparticles. In this case, the nanoparticles are additionally employed as electrodense markers for labeling the target protein. Additionally, before elution (photoelution and co-elution with nanoparticles), immunogold can be employed to label proteins that interact with the primary target protein.

Figure 3 shows the graphical user interface controlling the "protein fishing" device for targeted visual proteomics. The software is programmed in LabView as openBEB plugin [4] and can be automatized by the openBEB macro language.

References

[1] D. Scholz, D. Poeltl, A. Genewsky, M. Weng, T. Waldmann, S. Schildknecht, and M. Leist, *Rapid, complete and large-scale generation of post-mitotic neurons from the human LUHMES cell line.* J. Neurochem., 2011, 119(5), 957–971

[2] S. A. Arnold, S. Albiez, N. Opara, M. Chami, C. Schmidli, A. Bieri, H. Stahlberg, C. Padeste and T. Braun, *Total sample conditioning and preparation of nanoliter volumes for electron microscopy*. ACS Nano, 2016, 10(5): 4981-4988

[3] D. Giss, S. Kemmerling, V. Dandey, S. Stahlberg and T. Braun, *Exploring the interactome: microfluidic isolation of proteins and interacting partners for quantitative analysis by electron microscopy*, Anal. Chem., 2014, 86, 4680–4687

[4] C. Ramakrishnan et al. *openBEB: open biological experiment browser for correlative measurements.* BMC Bioinformatics, 2014, 15:84

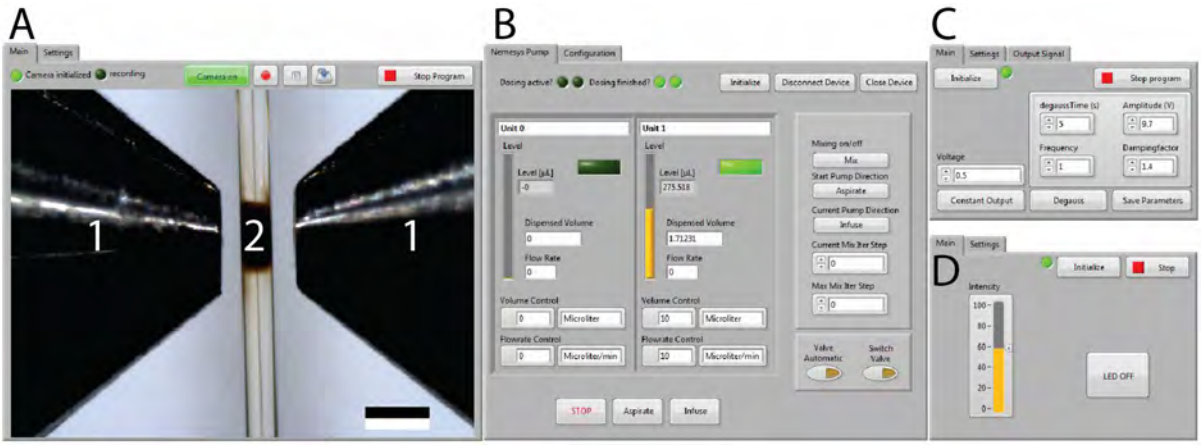

Fig. 3 Graphical user interface (GUI) to control protein fishing and interaction labeling of minute amounts of cell lysate. Four independent modules controlling different hardware parts are shown. A) Observation camera showing the poles (1) of the electromagnetic trap. (2) Plug of trapped composite super paramagnetic nanoparticles. Scale bar reads 500 µm. B) High-precision pump control. C) Control of electromagnet. D) LED control for photo-elution. Note, that these modules are running independently but are controlled and coordinated by the openBEB [4] software framework, also allowing automation by the openBEB macro language.

Pushing the limits of lightweight materials

Project P1402 Lightweight structures based on hierarchical composites
Project Leader: C. Dransfeld and C. Schönenberger
Collaborators: W. Szmyt (SNI PhD Student), S. Vogel, A. Diaz, M. Holler, J. Gobrecht, and M. Calame

Context

Composite materials based on carbon fibre (CF) are prone to failure at fiber-matrix interface upon compression or stress transverse to the fibre axis. Development of hierarchical composites constitutes a novel approach to enhance the mechanical properties of the interface [1]. Such materials are typically reinforced on microscale and nanoscale. In our study, we explore the approach of grafting of microscalecarbon fibre with nanoscale carbon nanotubes. In this approach however there is a challenge that during the carbon nanotube growth, tensile properties of the fibre are altered due to the dissolution of iron catalyst in the CF, leading to its degradation.

Results

There have been hypotheses that during the direct growth of carbon nanotubes on carbon fibre, the diffusion of iron nanoparticles into the fibre is a phenomenon significant to the creation of defects in the fibre [2, 3]. Our study verifies the hypotheses. We have carried out ptychographic X-ray computed tomography (PXCT) imaging of our samples in order to assess iron nanoparticle abundance within carbon fibre [4]. The PXCT examination has been carried out at the Coherent X-ray Scattering Beamline of the Swiss Light Source in Villigen, Switzerland. The sketch of the experimental setup is presented in figure 1.

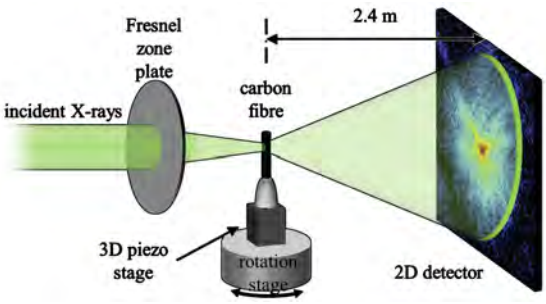

Fig. 1 Sketch of the experimental setup of the PXCT of a single fibre put in a glass capillary.

The imaging provided 50 nm - resolved 3D electron density maps of the examined samples (Fig. 2).

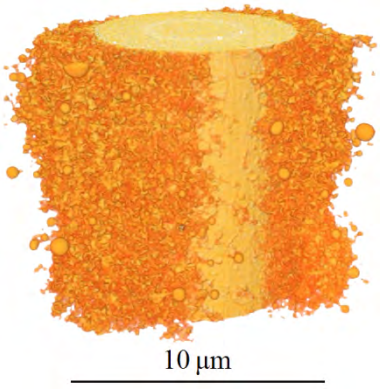

Fig. 2 3D render of a ptychographic X-ray computed tomography of carbon fiber without an alumina film grafted with carbon nanotubes.

We have introduced a novel methodology of 3D image analysis, which overcomes the resolution limitation of the method to a great extent. The results have been cross-checked by means of scanning transmission electron microscopy (STEM) and energy-dispersive X-ray spectroscopic (EDX) elemental analysis [5]. For the purpose of this examination, thin slices of carbon fibres were prepared by means of focused-ion beam (FIB) cutting. The procedure has been carried out in FEI Helios NanoLab™ 650 DualBeam™ at the Nano Imaging Lab at University of Basel, see summary in figure 3. The electron microscopy and elemental analysis constituted a validation of the novel approach to nanotomography data analysis. We have evidenced the protective effect of 11 nm-thick alumina film against the destructive iron infiltration effect. We believe that our method potentially allows for evaluation of efficiency of other approaches to minimization of the diffusion problem. The results provide a new insight into the mechanical performance of CFs and constitute valuable knowledge for the development of hierarchical composites.

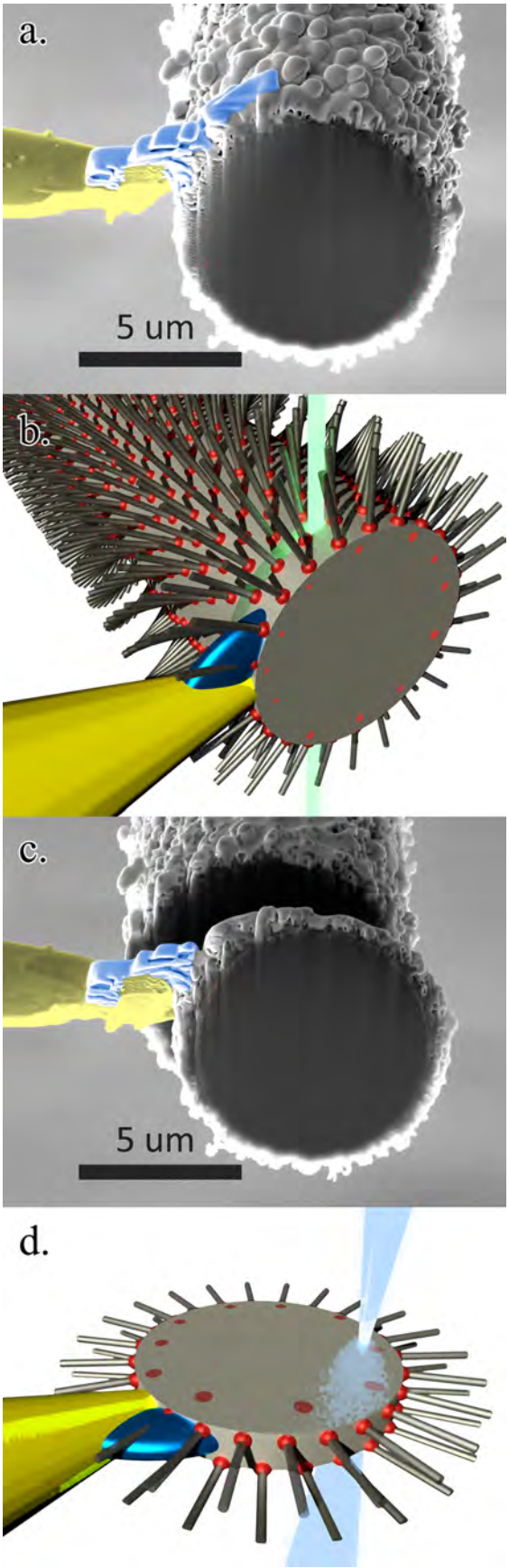

Fig. 3 Sequence of the FIB slicing followed by STEM/EDX examination presented at SEM images and 3D renders. a) carbon fibre without alumina film grafted with carbon nanotubes welded to a nanomanipulator needle (yellow) with ion-beam-deposited platinum (blue); b) FIB cutting of a slice of the sample; c) Slice detached and manipulated; d) STEM/EDX examination of the prepared slice.

References

[1] H. Qian, E.S. Greenhalgh, M.S.P. Shaffer, A. Bismarck, *Carbon nanotube-based hierarchical composites: a review,* J. Mater. Chem. 20 (23), p. 4751, 2010

[2] H. Qian, A. Bismarck, E.S. Greenhalgh, M.S.P. Shaffer, *Carbon nanotube grafted carbon fibres: a study of wetting and fibre fragmentation,* Compos. Part Appl. Sci. Manuf. 41 (9), pp. 1107–14, 2010

[3] S. Zhu, C.-H. Su, S.L. Lehoczky, I. Muntele, D. Ila, *Carbon nanotube growth on carbon fibers,* Diam. Relat. Mater. 12 (10–11), pp. 1825–1828, 2003

[4] W. Szmyt, S. Vogel, M. Holler, A. Diaz, J. Gobrecht, M. Calame, C. Dransfeld, *Proceeding of the 17th European Conference on Composite Materials,* June 26-30 2016, Munich, Germany

[5] W. Szmyt, S. Vogel, M. Holler, A. Diaz, J. Gobrecht, M. Calame, C. Dransfeld, *Protective effect of ultrathin alumina film against diffusion of iron into carbon fiber during growth of carbon nanotubes for hierarchical composites investigated by ptychographic X-ray computed tomography,* Carbon 115, pp. 347–62, 2017

Towards large peptides and small proteins for VUV-ionization

Project P1403 Tailor-made proteins and peptides for quantum interference experiments
Project Leader: V. Köhler and M. Mayor
Collaborators: J. Schaetti (SNI PhD Student), U. Sezer, S. Pedalino, J. P. Cotter, and M. Arndt

Large volatile peptides

The removal of internal charges and the introduction of a fluoroalkylchain at either the N-terminus or both the N- and C-terminus by amidation enabled thermal evaporation of overall charge-neutral tripeptides (Ala-Phe-Ala) which were subsequently ionized for mass detection by electron impact and enabled the recording of the first ever interference experiment of a peptide (annual report 2015). In subsequent designs tryptophan residues were incorporated to make the constructs amenable to photoionization at 157 nm [1]. In order to maintain a high fluoroalkyl to amino acid ratio tryptophan residues were alternated with lysine residues providing an additional nucleophilic amino group for every two peptide building blocks. Two alternative synthesis approaches were investigated: i) Fmoc-lysine was acylated at the side chain amino group with the N-hydroxysuccinimide ester (NHS-ester) of either *2H,2H,3H,3H*-perfluorooctanoic or undecanoic acid and the resulting amino acid building block employed in solid phase peptide synthesis (SPPS) ii) the core-peptide structure was assembled by SPPS with Boc-protected lysine side chain functionality and the resulting construct globally modified by perfluoroacylation with the respective NHS-ester in solution after cleavage from the resin. The first approach was successfully realized for constructs of up to 9 amino acids (**1** and **2**, 5 × Trp, 4 × Lys, 3082 and 3832 amu, respectively, Fig. 1) but failed for larger constructs.

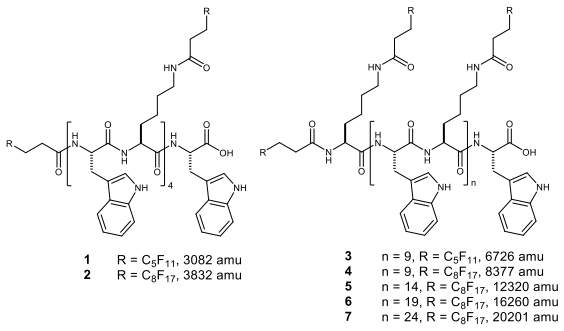

Fig. 1 Tryptophan-lysine constructs for photoionization with perfluoroalkylation for improved volatility.

The second approach enabled the synthesis of constructs with 20 amino acid building blocks (**3** and **4**, 6726 and 8377 amu), 30 amino acid building blocks (**5**, 12320 amu) and currently reaches its limitations with 40 to 50 amino acid building blocks (**6** and **7**, 16260 amu and 20201 amu, confirmed by MALDI). A noteworthy difficulty encountered is the low solubility of the perfluoroalkyl-decorated peptides. Thermal evaporation of constructs with up to 3832 amu under high vacuum was successful according to optical inspection and MALDI analysis of the condensate, but failed so far in the MS-coupled experiment with higher path-length.

VUV vs. EI ionization

Early constructs were ionized by electron impact (EI) after thermal evaporation leading to a high fragmentation ratio. EI was identified as a major cause of decomposition through comparison of spectra obtained by single photon ionization at 157 nm (vacuum ultraviolet, VUV). VUV-ionization resulted in a substantially reduced fragmentation ratio and only two major defined and expected fragments ([indole – H^-], [skatole – H^-]) thereby confirming the successful thermal launch of the perfluoroalkyl-decorated peptides (up to 1265 amu so far).

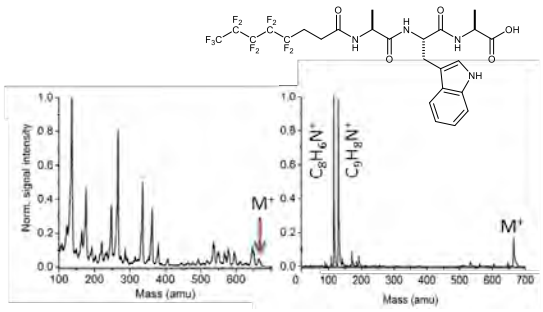

Fig. 2 Electron impact (QMS, left) vs. VUV-ionization (157 nm, TOF-MS, right) of a perfluoroalkyl decorated Ala-Trp-Ala (669 amu).

Laser desorption vs. thermal evaporation

For substantially larger perfluoroalkyl-decorated lysine tryptophan constructs such as **2**, however, to date no intact molecular ion could be detected after photoionization and thermal launch. This raised once again the question of the responsible experimental parameter: i) is successful photoionization under observation of the intact molecular ion limited to peptides of moderate molecular weight or ii) is the thermal evaporation of massive peptides despite extensive fluoroalkylation not possible with sufficient flux without decomposition [2]?

Laser desorption into an adiabatically expanding noble gas jet has been identified as an attractive and mild alternative for the generation of molecular beams [3]. Construct **1** was successfully launched and ionized. Further improvement was seen with modified launch methods. Purification, characterization, launch and ionization of higher mass constructs is currently under investigation.

Tryptophan tagged proteins

Tryptophan has the lowest ionization energy of the proteinogenic amino acids but is also the least abundant. Based on the successful photoionization of tryptophan rich large peptides [1] the attempt to increase the tryptophan content of small proteins by genetic encoding was undertaken. Tryptophan has higher abundance in membrane anchoring regions indicative of its hydrophobic nature [4]. To incorporate tryptophan-rich areas into proteins a simple extension strategy was chosen at the risk of low expression levels and insufficient solubility. As protein carriers of the tryptophan-rich genetically encoded tag, heat stable proteins were selected, which offer potentially the opportunity of simple purification by heat treatment. The expression of a range of C-terminal modified constructs was attempted in *E. coli*.

This simple strategy was successful and resulted in five soluble constructs so far counting the ones were additional solubility tags and linker regions were introduced. A construct, which carries five additional tryptophan residues, was investigated in more detail. Purification by heat treatment had only limited success since the construct tended to aggregate and precipitate. However, a sample with a high content of the protein construct was prepared and first laser desorption and photoionization experiments are in progress.

References

[1] M. Marksteiner, P. Hasslinger, M. Sclafani, H. Ulbricht and M. Arndt, *UV and VUV Ionization of Organic Molecules, Clusters and Complexes,* J. Phys. Chem. A 113, 9952 (2009)

[2] C.H. Becker, K.J. Wu, *On the photoionization of large molecules,* J. Am. Soc. Mass Spectrom. 6*, 883* (1995)

[3] F. Piuzzi, I. Dimicoli, M. Mons, B. Tardivel, Q. Zhao, *A simple laser vaporization source for thermally fragile molecules coupled to a supersonic expansion: application to the spectroscopy of tryptophan,* Chem. Phys. Lett. 320, 282 (2000)

[4] A.J. de Jesus, T.W. Allen, *The role of tryptophan side chains in membrane protein anchoring and hydrophobic mismatch,* Biochim. Biophys. Acta 1828, 864 (2013)

Targeting nanocarriers into the cell nucleus

Project P1404 Selective transport of functionalized nanocarriers into biomimetic and natural nuclear pore complexes
Project Leader: R.Y.H. Lim and C. Palivan
Collaborators: C. Zelmer (SNI PhD Student)

Introduction

Gene regulation in eukaryotic cells depends on the exchange of macromolecules between the nucleus and cytoplasm [1, 2]. This occurs through ~100 nm-diameter protein channels known as nuclear pore complexes (NPCs) [3]. Soluble transport receptors (e.g. importins and exportins) bind to cargoes tagged with a particular nuclear localization sequence (NLS) and shuffle them into the NPC. Nuclear import is terminated by the GTPase Ran in its GTP-bound form, which dissociates the import complex from the NPC and releases the cargo into the nucleus (Fig. 1) [4].

Numerous studies have resolved the molecular mechanism by which soluble proteins, dextrans and gold particles traverse the NPC. However, it is poorly understood how the nanomechanical properties of cargoes influence this process. In this project, we have engineered ~50 nm-sized synthetic cargoes based on polymersomes made of amphiphilic triblock copolymers. Indeed, these represent ideal candidates to study nuclear import as they can be engineered to exhibit a large variety of properties (size, stability, flexibility) [5]. Moreover, polymersomes functionalized with NLS can be used as nanocarriers for nuclear targeting [5, 6].

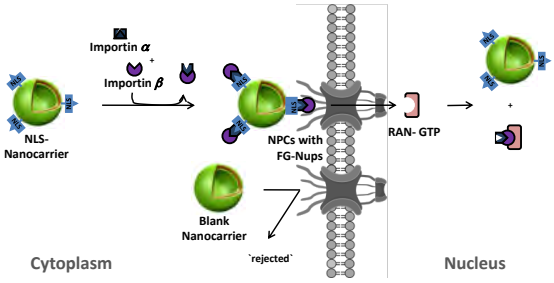

Fig. 1 Active nuclear import of NLS functionalized nanocarrier. Blank nanocarrier is rejected by the NPC.

Engineering NLS-nanocarriers for nucleocytoplasmic transport

Here, we have engineered synthetic polymersomes using an amphiphilic triblock copolymer $PMOXA_4$-*block*-$PDMS_{29}$-*block*-$PMOXA_4$. Importantly, the polymersomes exhibit excellent biocompatibility, as well as enhanced membrane stability and strength as compared to liposomes [5]. To facilitate the linkage of cysteine substituted NLS peptides to the polymersome surface, we mixed $PMOXA_4$-*block*-$PDMS_{29}$-block-$PMOXA_4$ copolymer with a maleimide end-group functionalized $PMOXA_4$-*block*-$PDMS_{29}$-*block*-$PMOXA_4$ (Fig. 2). NLS recognition by the nuclear import mechanism thereby authenticates the polymersomes as specific nanocarriers. Extrusion through 50 nm filters further yields NLS-nanocarriers that are 65 ± 27 nm large as determined by dynamic light scattering (DLS) and 66 ± 18 nm as confirmed by transmission electron microscopy (TEM).

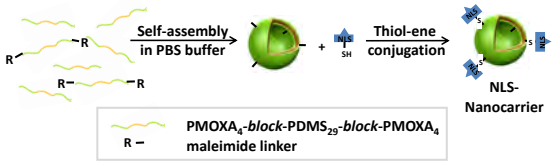

Fig. 2 Preparation route of NLS-nanocarriers.

NLS-nanocarriers are recognized by import receptors

Active nuclear import requires that importins recognize the NLS on the polymersome surface. To monitor this process *in vitro,* dual-colour fluorescence crosscorrelation spectroscopy (FCCS) allowed us to simultaneously record the auto-correlation curves of Bodipy 630/650 stained NLS-nanocarriers (blue) and Atto-488 labelled Importin α/β complexes (green) and to correlate the course of the two curves with one another (Fig. 3A). The high amplitude of the resulted cross-correlation curve (black) indicates substantial binding even in the subnanomolar working range. In contrast, the cross-correlation amplitude obtained by correlating the autocorrelation curves of blank nanocarriers to Importin α/β indicates that only very little unspecific binding takes place (Fig. 3B).

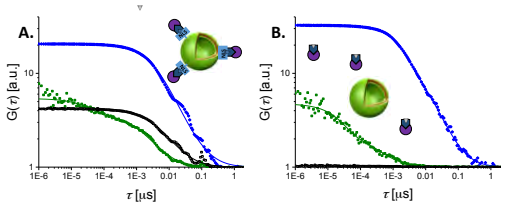

Fig. 3 FCCS binding studies between nanocarriers and Importin α/β: A) NLS-nanocarriers show high cross-correlation (black) and so, substantial binding to Importin α/β. B) Blank nanocarriers show almost no cross-correlation (black) and hence, very little unspecific binding to Importin α/β.

Nucleocytoplasmic transport of NLS-nanocarriers in permeabilized HeLa cells

Next, we tested for the transport viability of NLS-nanocarriers into the cell nucleus using digitonin permeabilized HeLa cells. Digitonin is a non-ionic detergent that selectively dissolves cholesterol from the plasma membrane while leaving the nuclear envelope intact. The perforated outer cell membrane

therefore allows for *in vitro* translocation into the cell nucleus using exogenously applied import factors including Importin α, fluorescently tagged recombinant Importin β (Atto-488) and RAN (Atto-565). Moreover, we stained the polymersomes with Bodipy 630/650 and used laser-scanning microscopy (LSM) for visualization. Under these conditions, we observe a partial uptake of NLS-nanocarriers into the cell nucleus. In comparison, blank nanocarriers are blocked out of the nucleus (Fig. 4).

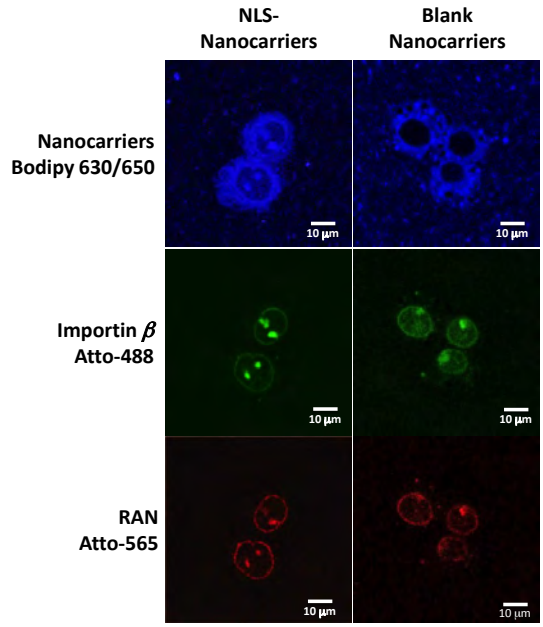

Fig. 4 Cellular uptake and distribution of NLS-nanocarriers (top left) and blank nanocarriers (top right) together with recombinant Importin β and RAN.

Summary

Together, the Lim and Palivan labs have successfully developed polymersomes that are selectively uptaken into cell nuclei. Next, we will manipulate the physico-chemical properties of the nanocarriers to evaluate and optimize nuclear transport. Our vision is to apply these bio-synthetic nanocarriers for use in drug and gene delivery.

References

[1] M. Stewart, *Molecular mechanism of the nuclear protein import cycle,* Nat Rev Mol Cell Biol 8.3, 195-208 (2007)

[2] S. Vujica, C. Zelmer, R. Panatala, R.Y.H. Lim, *Nucleocytoplasmic Transport: A Paradigm for Molecular Logistics in Artificial Systems,* CHIMIA *70*, 413-417, (2016)

[3] A. Hoelz, E.W. Debler, G. Blobel, *The structure of the nuclear pore complex,* Ann Rev Biochem 80, 613-643 (2011)

[4] L.E. Kapinos, R.L. Schoch, R.S. Wagner, K.D. Schleicher, R.Y.H. Lim, *Karyopherin-centric control of nuclear pores based on molecular occupancy and kinetic analysis of multivalent binding with FG nucleoporins,* Biophys. 106, 1751-1762 (2014)

[5] C.G. Palivan, R. Goers, A. Najer, X. Zhang, W. Meier, *Bioinspired polymer vesicles and membranes for biological and medical applications,* Chem. Soc. Rev, 45, 377-411 (2015)

[6] V. Mikhalevich, C. Zelmer, A. Car, C.G. Palivan, W. Meier, *Bio-inspired Polymer Membranes,* Bio-inspired Membranes, *RSC*, (2016)

Towards highly coherent, near-surface spins for nano-sensing in life-sciences and technology

Project P1405 Surface-Functionalization of diamond nano-magnetometers for applications in nano- and lifesciences
Project Leader: U. Pieles and P. Maletinsky
Collaborators: M. Batzer (SNI PhD Student), P. Appel, A. Barfuss, L Thiel, and S. Saxer

Introduction

Quantum sensing and nanoscale imaging using single electron spins in diamond has seen remarkable progress over the last years [1, 2]. In particular, nanoscale magnetometry using individual "scannable" electron spins has proven a highly fruitful avenue in the last years. It has offered unprecedented insights into materials as diverse as superconductors [3], ferro- or even anti-ferromagnets [4]. The quantum sensing group at the University of Basel is actively pursuing such single-spin, nanoscale magnetometry. On the one hand, we implement such novel nano-sensors in our lab and continue to push the frontiers of their sensitivity and spatial resolution. On the other hand, we apply these quantum sensors to outstanding problems in nanoscience and technology.

Our approach to nanoscale quantum sensing is based on all-diamond scanning probes, which contain single electronic spins in form of "Nitrogen-Vacancy" (NV) defect centers for sensing at their apex. We have originally developed this technology and systematically optimized performance and production-yield for our quantum sensors over the past years. Our main motivation is to apply the sensors to open problems in condensed matter physics. For example, this last year, we realized the first cryogenic scanning spin magnetometer [3], which was enabled by the robustness and efficiency of our quantum probes.

Key experimental results

Despite these significant advancements in this field of research, many open issues remain before nanoscale magnetometry can be conducted with near-optimal performance. In this project we are addressing some of the most pressing of these issues and have made significant progress in the last years.

The main topic that we are targeting here is that of shallow NV centers, which are located just a few nanometers below the diamond surface. Such centers are required to push NV magnetometry resolution into the single-digit nanometer range, as spatial resolution in this technique is solely given by the distance between the NV sensor and the sample under study. However, approaching the NV center to the diamond surface significantly degrades their spin and optical properties. It is commonly accepted that this degradation is a result of fluctuating spins and charges on the diamond surface [5]. Our approach to mitigate this problem is to gain control over the diamond surface chemistry by efficiently functionalizing it with proper chemical treatments. Such diamond surface functionalization will also form the basis for subsequent attachment of interesting bio-molecules, which may be studied using NV magnetometry.

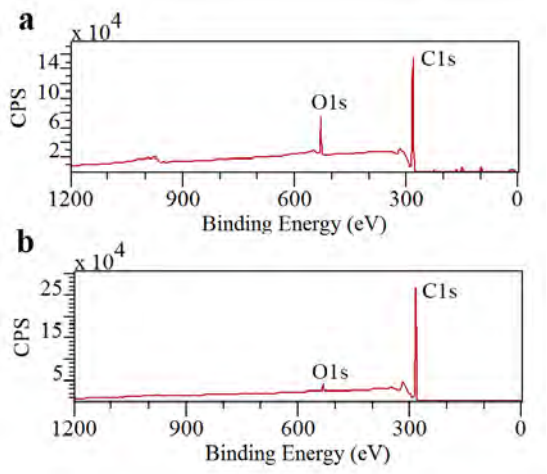

Fig. 1 a) representative XPS survey spectrum of the surface of an oxygen-terminated diamond single crystal. b) survey spectrum of the same diamond sample after hydrogen termination. The significantly reduces Oxygen 1s peak (O1s) is indicative for successful hydrogen termination of the diamond surface (note that hydrogen cannot be directly seen in XPS).

The focus of our activities this year was to achieve hydrogen surface termination of diamond. Hydrogen is expected to efficiently saturate dangling bonds on the diamond surface and thereby reduce the amount of spin- and charge-fluctuations occurring on the surface. To that end, we have established a collaboration with an external group (that of Prof. B. Abel at the University of Leipzig) to acquire techniques of efficient diamond hydrogen surface termination using exposure of our samples to Hydrogen gas at temperatures ~700°C. This surface termination was successful as evidenced by X-ray photoelectron spectroscopy (XPS) spectra (Fig. 1).

While our successful hydrogen termination may in principle mitigate the problem of spin and charge fluctuations on the diamond surface, a significant

problem remains. Hydrogen-terminated diamond surfaces are known to lead to significant (close to 1eV) band-bending of diamonds conduction and valence bands close to the surface. The result is complete de-ionization of near-surface NVs and loss of the desired NV spin properties [6]. To overcome these limitations, we are currently pursuing methods to overcome this band-bending by either working in high-vacuum conditions or by applying appropriate capping layers to the diamond samples. This work is ongoing but first experiments yielded promising, preliminary results.

Diamond scanning probe fabrication

The diamond surface-chemistry and nanofabrication methods developed within this SNI PhD project also had impact on the production of all-diamond scanning probe tips the quantum sensing group is fabricating for nanoscale NV magnetometry [7]. In particular, we developed methods to greatly simplify the fabrication process for such tips and to increase production yield and device performance. An example is illustrated in figure 2, which shows a newly developed method for scanning probe assembly, along with a finalized scanning probe device, which contains a single spin for magnetometry.

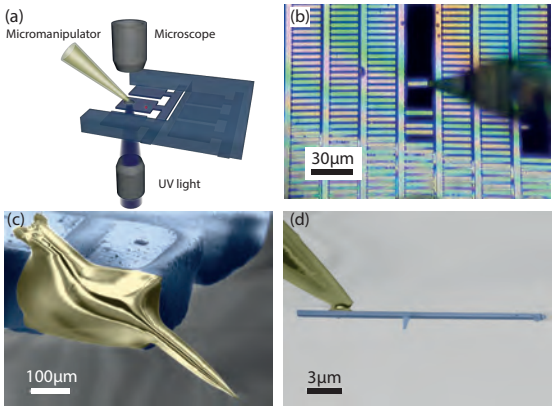

Fig. 2 a) Schematic of the setup for gluing the scanning probe to quartz tips. b) Optical microscope image during the transfer process. The scanning probe is glued to the apex of the quartz capillary tip using UV glue and the scanning probe is detached from the diamond chip by breaking. c) SEM image of the scanning probe attached to one prong of a tuning fork. d) SEM image of the nal scanning probe attached to the end of the quartz tip.

Outlook

In the current reporting period, we have laid a solid foundation for diamond surface functionalization by successfully demonstrating hydrogen termination of the diamond surface at high coverage. The central goal for the following year is to demonstrate the influence of our approach to diamond surface termination on the spin coherence properties (and thus the sensing performance) of near-surface NV centres in our diamond nano-devices. For this, we will pursue further our Hydrogen passivation approach, but also investigate alternative surface terminations, e.g. by realising Nitrogen-terminated diamond surfaces [8]. With a successful first demonstration on functionalized bulk diamond, we would then apply these techniques to diamond scanning probes to yield high sensitivity, nanoscale magnetometer. Ultimately, our properly functionalized diamond surface will also form an ideal basis to attach interesting bio-molecules or cells to the diamond surface for quantum sensing with single spins.

References

[1] J. Taylor J.M. Taylor, P. Cappellaro, L. Childress, L. Jiang, D. Budker, P.R. Hemmer, A. Yacoby, R. Walsworth, and M.D. Lukin, *High-sensitivity diamond magnetometer with nanoscale resolution*, Nature Physics **4**, 482 (2008)

[2] L. Rondin, J.-P. Tetienne, T. Hingant, J.-F. Roch, P. Maletinsky, V. Jacques, *Magnetometry with nitrogen-vacancy defects in diamond*, Rep. Prog. Phys. 77, 056503 (2014)

[3] L. Thiel, D. Rohner, M. Ganzhorn, P. Appel, E. Neu, B. Mueller, R. Kleiner, D. Koelle, P. Maletinsky, *Quantitative nanoscale vortex imaging using a cryogenic quantum mag-netometer*, Nature Nanotechnology 11, 677-681 (2016)

[4] T. Kosub, M. Kopte, R. Hühne, P. Appel, B. Shields, P. Maletinsky, R. Hübner, M.O. Liedke, J. Fassbender, O.G. Schmidt, D. Makarov, *Purely antiferromagnetic magneto-electric random access memory*, ArXiv: 1611.07027 (2016)

[5] B.A. Myers, A. Das, M.C. Dartiailh, K. Ohno, D.D. Awschalom, A.C. Bleszynski Jayich, *Probing surface noise with depth-calibrated spins in diamond*, Phys. Rev. Lett., 113, 027602 (2014)

[6] M.V. Hauf, B. Grotz, B. Naydenov, M. Dankerl, S. Pezzagna, J. Meijer, F. Jelezko, J. Wrachtrup, M. Stutzmann, F. Reinhard and J.A. Garrido, *Chemical control of the charge state of nitrogen-vacancy centers in diamond*, PRB 83, 081304 (2011)

[7] P. Appel, E. Neu, M. Ganzhorn, A. Barfuss, M. Batzer, M. Gratz, A. Tschoepe, P. Maletinsky, *Fabrication of all diamond scanning probes for nanoscale magnetometry*, Rev. Sci. Instrum. 87, 063703 (2016)

[8] M. Kaviani, P. Deák, B. Aradi, T. Frauenheim, J. Chou and A. Gali, *Proper surface termi-nation for luminescent near-surface NV centers in diamond,* Nano Letters 14, 4772 (2014)

Tuning of electron transfer and transport rates in molecular bridges

Project P1406 Charge transfer versus charge transport in molecular systems
Project Leader: O.S. Wenger and M. Calame
Collaborators: S. Neumann (SNI PhD Student) and J. Overbeck (SNI PhD Student)

Introduction

A controlled electron flow is very important for an efficient storage and conversion of energy and is also needed for successful integration of single molecules into electronic devices. We are interested in tuning the electron flow by manipulating molecular bridges either by intramolecular elongation of the system or by intermolecular interactions. The former is used to study the changes in the electron transfer rate in photoinduced electron transfer, whereas the intermolecular interactions are studied in mechanically controllable break junction (MCBJ) experiments for the determination of electron transport rates.

Molecular structures

For our studies, we developed and synthesized the systems **1** and **2**. System **1** (Fig. 1) is a donor-acceptor system consistent of a triarylamine (TAA) donor and a naphthalene diimide (NDI) acceptor, covalently linked via a bridge, which can be elongated by introduction of additional xylene units. With this system, photoinduced electron transfer and the change in the thermal electron transfer rate due to an elongation of the system can be studied.

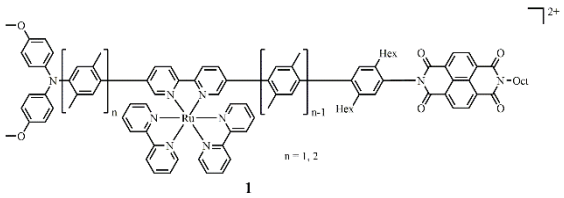

*Fig. 1 Molecular bridge **1** for electron transfer studies.*

System **2** (Fig. 2) is an organoboron wire in which the boron is stabilized by the introduction of mesitylene moieties. Due to the bulkiness of the mesitylenes, a pocket results where small anions like fluoride can bind to the boron atoms. The binding should result in a significant change of the HOMO/LUMO energies of the overall system, which should be observable by a change of the conductance of the system.

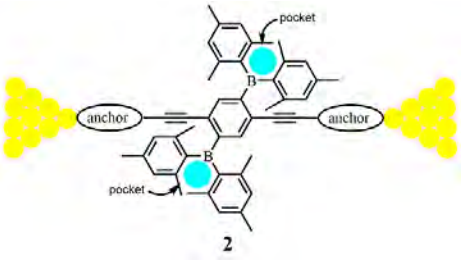

*Fig. 2 Molecular bridge **2** for electron transport studies.*

Since **2** is studied in MCBJ experiments, anchor groups are needed for the binding to the gold electrodes of the setup. We focus on pyridine and isonitrile anchor groups.

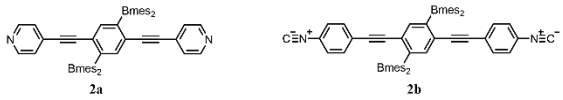

*Fig. 3 Molecular wire **2** with pyridine and isonitrile anchor groups.*

Distance dependence of the electron transfer rate

The electron transfer rate normally decreases if the distance between two reactants is increased [1, 2]. However, it was recently shown that an increasing distance in a covalently linked donor-acceptor system can also increase the transfer rate [3]. Our system **1** is structurally similar to the system with the unusual distance dependence but has a lower driving force for thermal charge recombination. This should allow us to observe the normally expected electron transfer behavior concerning the distance.

The photoproducts of system **1** were determined by transient absorption spectroscopy (Fig. 4). After excitation with light, an oxidized TAA and a reduced NDI species were obtained. The lifetimes of these species increased drastically by elongation of the system. Specifically, the electron transfer rate decreases from 10^6 to 10^5 s^{-1} in neat acetonitrile.

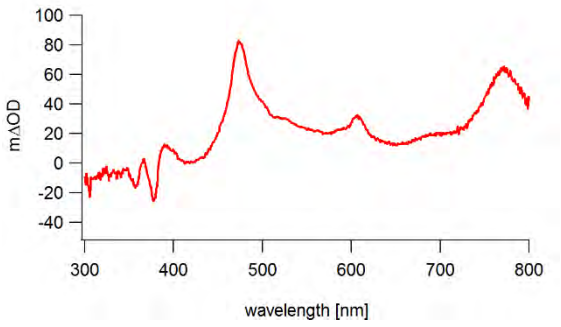

*Fig. 4 Transient absorption spectrum of **1**. The photoproducts are labeled.*

For the determination of the activation free energies of the thermal charge recombination, temperature dependent kinetics were performed. The electron transfer in the donor-acceptor system with n = 1 is activationless, whereas the system with n = 2 exhibits electron transfer in the so called normal region of Marcus theory.

Electron transport in organoboron wires

In light-induced electron transfer, the organoboron bridge **2** already showed a significant effect on the electron transfer rate after fluoride addition to a donor-bridge-acceptor system [4]. However, electron transport properties have not been studied previously.

We successfully synthesized wire **2a** and tested its electron transport properties using the MCBJ technique. The measurements were carried out at room temperature with a 100 µM solution of **2a** in chloroform (Fig. 5).

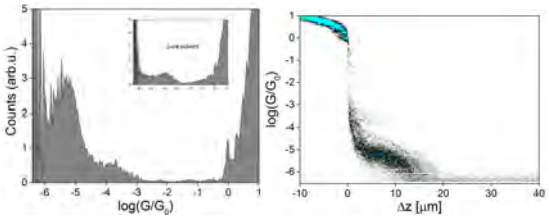

*Fig. 5 Left: 1D logarithmic conductance histogram for **2a** conducted from 100 individual traces and recorded with a bias voltage of 0.10 V. Right: 2D conductance histogram of **2a**.*

The 1-D conductance histogram indicated the formation of a molecular junction with a conductance around G = $10^{-5.4}$ G_0. The resulting conductance plateau for the measured traces is also indicated in the 2-D conductance-distance histogram. Fluoride addition to the MCBJ setup has not been tested yet, but UV/Vis titration in dry chloroform confirmed the binding of the fluorides to the system (Fig. 6).

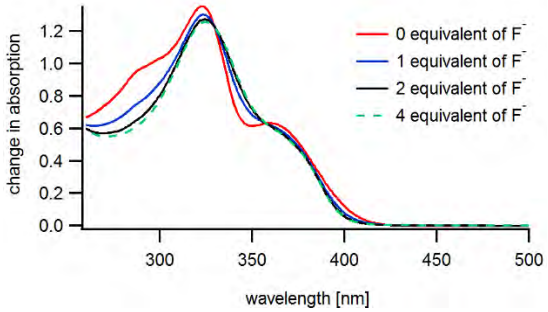

*Fig. 6 UV/Vis titration of **2a** in dry chloroform with successive addition of TBAF.*

Conclusion

The intramolecular elongation of system **1** resulted in a significant change in the electron transfer rate. Furthermore, we were able to show that the increase of the distance between the donor and the acceptor ensues the normal expected behavior for the electron transfer rate.

For system **2**, first MCBJ measurements of the organoboron wire **2a** indicate successful integration of the system into the setup and a measurable conductance. The resulting changes due to fluoride addition are going to be of interest in further studies. Moreover, the synthesis and MCBJ characterization of the wire **2b** are of interest.

References

[1] P.P. Edwards, H.B. Gray, M.T.J. Lodge, R.J.P. Williams, *Electron transfer and electronic conduction through an intervening medium*, Angew. Chem. Int. Ed. 47, 6758 (2008)

[2] M. Cordes, B. Giese, *Electron transfer in peptides and proteins*, Chem. Soc. Rev. 38, 892 (2009)

[3] M. Kuss-Petermann, O.S. Wenger, *Increasing Electron-Transfer Rates with Increasing Donor-Acceptor Distance*, Angew. Chem. Int. Ed. 55, 815 (2016)

[4] J. Chen, O.S. Wenger, *Fluoride binding to an organoboron wire controls photoinduced electron transfer*, Chem. Sci. 6, 3582 (2015)

Coupling an ultracold ion to a metallic nanowire

Project P1407 Coupling a single ion to a nanomechanical oscillator
Project Leader: S. Willitsch and M. Poggio
Collaborators: P. Fountas (SNI PhD Student)

Introduction

Numerous scientific approaches are aiming towards proper candidates for creating a hybrid system in the quest for developing quantum technologies. The motivation for a solid state-atomic interface emerges from the possibility to combine the advantages of these platforms. That being said, ultracold trapped atoms offer very good coherent properties, while a key benefit of nanomechanical systems is their coupling to electromagnetic radiation over a wide range of the spectrum, which facilitates interfacing with diverse quantum devices. One of the most promising candidates for the relevant atomic system is an ultracold ion, which can be isolated from the environment by being trapped via a radiofrequency electric field in ultra-high vacuum [1]. By laser cooling the ion to its motional ground state one can manipulate its motional and spin degrees of freedom with high accuracy. Moreover, a mechanical system is required that is highly scalable and integrable. For this, a nanomechanical oscillator has been chosen in the present implementation.

Currently, a great challenge is to couple mechanical oscillators to other quantum systems, while maintaining good coherent properties. In order to combine the aforementioned advantages one has to be able to transfer quantum states between these two systems. Here, we report progress towards the implementation of an ultracold ion-metallic nanowire interface in a miniaturized segmented layer ion trap (Fig. 1), to study the coupling mechanism between these two systems mediated by electric fields. We, also, propose a scheme towards the engineering of ion's motional quantum states after the direct mechanical drive of the coupled charge nanowire. Mainly, our aim is to study experimentally the coupling mechanism of this new interface. Ultimately, we envisage the possibility to realize the aforementioned state engineering scheme at a later stage of the project.

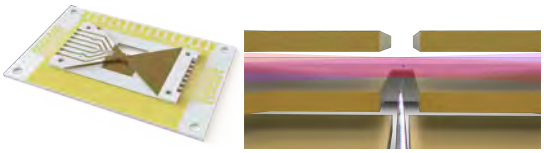

Fig. 1 Left: Miniaturized segmented layer ion trap consisting of a stack of gold coated alumina wafers clamped together on a printed circuit board. Right: Schematic representation of the experiment.

Numerical simulations of the segmented layer ion trap

A combination of finite elements calculations (FEM) -solving Laplace's equation- and molecular dynamics (MD) simulations -solving Newton's equations of motion classically- has already been performed, in order to optimize the geometry of the ion trap. In MD simulations we implemented the nanowire's effect as a force field acting on $^{40}Ca^{+}$ ion's motion, along with all the other forces that the ion is experiencing in a radiofrequency (RF) trap. We defined the parameters needed to realize the resonant excitation of a $^{40}Ca^{+}$ ion from the nanowire, e.g. the relative distance between these two systems, the nanowire's amplitude of oscillation and the applied DC voltage on the nanowire. Based on these parameters we optimized the geometry of the trap according to the stability parameters and the trap depth. As shown in figure 2 the trap perturbation caused by the nanowire does not destroy the confining trapping potential, which is crucial for the experiment. At the moment, the manufacturing of the trap is at its final stage and we have already started building the experimental set-up.

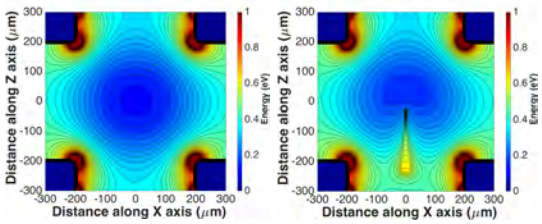

Fig. 2 Left: Total trapping potential for a single $^{40}Ca^{+}$ ion. Right: Distorted trapping potential including the effect of a charged nanowire and holder.

Quantum dynamics calculations

To study the evolution of ion's quantum state we solved numerically the Lindblad master equation,

$$\frac{d\hat{\rho}}{dt} = -\frac{i}{\hbar}[\hat{\mathcal{H}}_{tot}, \hat{\rho}] + \hat{\mathcal{L}}\hat{\rho} \qquad (1)$$

where we implemented the ion's motional decoherence based on realistic experimental parameters. We treat the nanowire as an oscillating electric field generated by a spherically charged particle located on its tip and we initialize the ion in its ground vibrational state, which can be achieved experimentally by resolved-sideband cooling. The total Hamiltonian in frequency units is

$$\hat{\mathcal{H}}_{tot} = \omega(\hat{b}^{\dagger}\hat{b} + \frac{1}{2}) - s\ (\hat{b}^{\dagger} + \hat{b})^2 + g\ (\hat{b}^{\dagger} + \hat{b})\ cos(\Omega t) \quad (2)$$

where s and g terms are the coupling parameters dependent on the ion's charge, the nanowire's voltage, the relative distance between the two systems and the $\hat{b}^{\dagger}$ and $\hat{b}$ are the ion's motional ladder operators. The g term has one additional dependence, which is the driving amplitude of oscillation of the nanowire. We assumed that we drive the nanowire continuously for a specific time interval (e.g. 30 μs), and we can neglect in this way the nanowire's dissipation. The end of our calculations corresponds to the discharge of the nanowire quasi-instantaneously, which is doable experimentally by switching off the nanowire's voltage with fast electronics. By properly tuning the s and g parameters we realized the creation of ion's coherent, squeezed and displaced squeezed states, as shown in figure 3 for a specific time step.

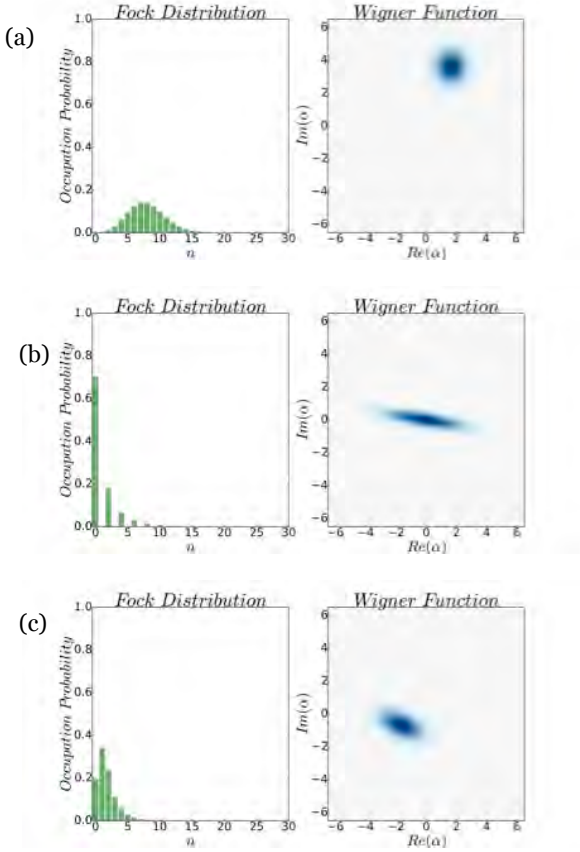

Fig. 3 Occupation probability distributions (left) and Wigner function (right) of $^{40}Ca^{+}$ ion's motional quantum states in a Fock basis for a) a coherent state, b) squeezed state and c) displaced squeezed state generated by a resonant drive with the nano-oscillator.

We, also, predict the creation of intermittent Schrödinger-cat states (Fig. 4) by creating a coherent state with large amplitude in a region of our trapping potential where it feels a Kerr non-linearity.

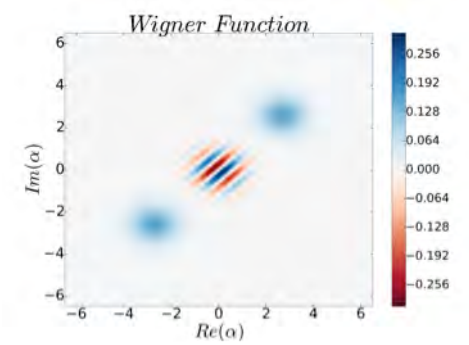

Fig. 4 Wigner function of a $^{40}Ca^{+}$ Schrödinger-cat state, which is a superposition of two coherent states with opposite phases.

In previous state engineering experiments [2, 3] the use of lasers for the creation of the motional quantum states was limiting the ion's excitations to <20 quanta, due to the interaction of the optical fields with the dipole and quadrupole moment of the atom. In our system, we expect to generate quasi-classical and non-classical states faster and with larger amplitudes, via the direct mechanical coupling of the ion with the nanowire. Furthermore, we will be free of laser fluctuations that cause motional and spin dephasing of the ion during the state creation stage.

Outlook

The fabrication of the trap is almost ready and the experimental setup is currently under construction. Based on the results obtained from our quantum dynamics calculations, we have explored the possibility to realize experimentally the on-demand ion's quantum state preparation after the direct mechanical coupling of the former with a charged nanowire. Specifically, the generation of ion's Schrödinger-cat and squeezed states by our classical resonator might prove very promising for fundamental studies towards insights on the borders of classical and quantum mechanics. Finally, our setup might prove fruitful for various possible applications as a probe of decoherence processes of quantum and macroscopic bodies, in quantum information processing or in quantum sensing and metrology.

References

[1] S. Willitsch, *Coulomb-crystallised molecular ions in traps: methods, applications, prospects*, Int. Rev. Chem. 31, 175 (2012)

[2] D. Kienzler, H.-Y. Lo, B. Keitch, L. de Clerq, F. Leupold, F. Lindenfelser, M. Marinelli, V. Negnevitsky, J.P. Home, *Quantum harmonic oscillator state synthesis by reservoir engineering*, Science 347, 53 (2015)

[3] H.-Y. Lo, *Spin-motion entanglement and state diagnosis with squeezed oscillator wavepackets*, Nature 521, 336 (2015)

Nanomagnets for artificial spin-orbit coupling in graphene nanoribbons

Project P1408 Clean zigzag and armchair graphene nanoribbons
Project Leader: D. Zumbühl and D. Loss
Collaborators: M. Rehmann (SNI PhD Student), Y.B. Kalyoncu, T. Camenzind, and C.P. Scheller

Introduction

Graphene has emerged as a material very rich in interesting physical phenomena and holds great promise for the discovery of new effects, which are potentially valuable for both fundamental research and applications. In our work, we investigate the electronic transport properties of narrow graphene channels, also called graphene nanoribbons (GNRs). It has been proposed by Klinovaja et al. [1] to use an array of nanomagnets, placed in close proximity to a GNR, to induce a giant spin-orbit coupling (SOC), which is otherwise absent in pristine graphene. By applying a magnetic field perpendicularly to the induced SOC field, an electronic band gap opens and allows the system to be tuned into a helical regime, where opposite spins are transported in opposite directions. Furthermore, a GNR in the helical regime which is brought into contact with an s-wave superconductor is expected to sustain a topological phase with localized Majorana fermions at the ribbon ends [1].

Fabrication and characterization of Permalloy nanomagnet arrays for the induction of SOC

To induce SOC in GNRs an oscillating magnetic field is required [1]. The strength of the induced SOC (Δ) is proportional to the wavelength (λ) of the magnetic field oscillation (λ = 400 nm gives Δ = 5 meV). By fabricating an array of rhomboid-shaped nano-magnets (Fig. 1a) it becomes possible to switch between a parallel (Fig. 1b) and an antiparallel (Fig. 1c) alignment of the magnetization by applying the external magnetic field either along the long axis or the short axis, respectively [2]. We plan to pattern such nanomagnets onto a hexagonal boron nitride (hBN) encapsulated GNR, which allows place-ment of the magnets close to the ribbon and, at the same time, ensures a high level of cleanliness of the GNR, which is important for observing the predicted physics.

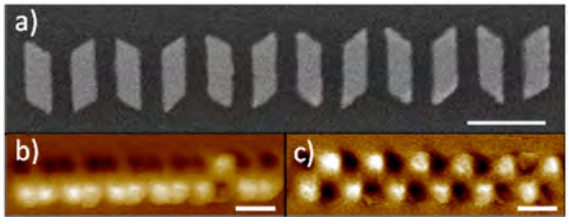

Fig. 1 a) SEM image of rhomboid-shaped permalloy nanomagnets. b) and c) MFM images of the nanomagnets shown in a) after applying an external magnetic field along the long axis b) and the short axis c) of the nanomagnets. All scale bars are 400 nm.

Encapsulation in hBN flakes for clean high quality graphene

In order to observe size quantization effects in GNRs it is crucial to maintain a high level of cleanliness of the graphene. More precisely, the mean free path (l_{mfp}) has to exceed the constriction length, giving rise to ballistic transport. A first step towards higher quality graphene devices was to place the graphene flakes on a hBN substrate, rather than on SiO2 which was shown to have a comparatively high amount of charge inhomogeneities which reduce the mobility of the devices. Although the hBN substrate led to an enhancement of the device quality, the fabrication of electrical contacts leaves resist residues (e.g. PMMA) from lithographic processing on the surface of graphene, which leads to a reduction of the electronic mobility. We have tried thermal annealing of the contacted graphene devices to obtain cleaner samples. However, thermal annealing led to a dramatic increase of the contact resistances, often hindering the execution of electronic transport measurements. Wang et al. have shown that graphene can be encapsulated between two hBN flakes and electrically contacted by one-dimensional side-contacts. By encapsulating graphene the device quality can be improved further, resulting in l_{mfp} ~ 1 um.

To establish the fabrication technique of hBN/graphene/hBN stacks, we fabricated a first encapsulated device in a Hall bar geometry, as shown in figure 2.

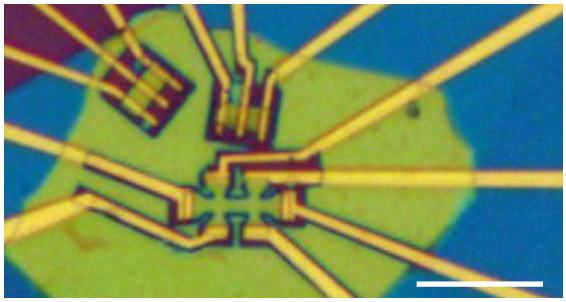

Fig. 2 Encapsulated graphene Hall bar and two 2-terminal devices. The yellowish region is where the bottom hBN flake is covered with the top hBN flake which is larger and exceeds the bottom flake (blueish regions). The Cr/Au-sidecontacts appear in yellow. Scale bar equals 10 um.

Indeed we measured mobilities of around 120'000 cm^2/Vs, corresponding to a l_{mfp} ~450 nm at a charge carrier density of 1e+11 cm^{-2}. This is a promising starting point for the fabrication of ballistic GNRs and the investigation of size quantization effects in these systems.

Weak localization in an ultra-clean hBN/G/hBN Hall bar

There is a large discrepancy between theoretically predicted spin lifetimes in graphene (~1 µs) and the experimental findings (~ps to ns). This suggests an extrinsic source of decoherence such as e.g. impurities or static ripples. Lara-Avila and coworkers have found that in SiC-supported graphene the decoherence stems at least partially from magnetic impurities which can be polarized in an in-plane magnetic field (Bip). Further it was shown [3] that information about the static ripple configuration of the graphene flake can be gained by investigating weak loacalizaion (WL) effects in dependence on Bip.

Motivated by these previous experiments, we performed WL measurements on an ultra-clean encapsulated Hall bar. Figure 3 shows the density averaged conductivity versus the out-of-plane magnetic field. The color code marks the difference in applied Bip. It is clearly visible that the WL curves taken at lower Bip exhibit a higher curvature (indicating a higher coherence time) compared to the curves measured at larger values of applied Bip. This is in qualitative agreement with the results found in [3]. However, a quantitative comparison of the extracted ripple size yields only a slightly lower amount of ripples in our encapsulated sample compared to the SiO2 supported sample investigated in [3]. Moreover, our extracted tau phi times are comparable or lower compared to the values found in [3]. Further evaluation of the data will be performed to gain insight into mechanisms, which possibly limit the coherence time in our encapsulated graphene Hall bar.

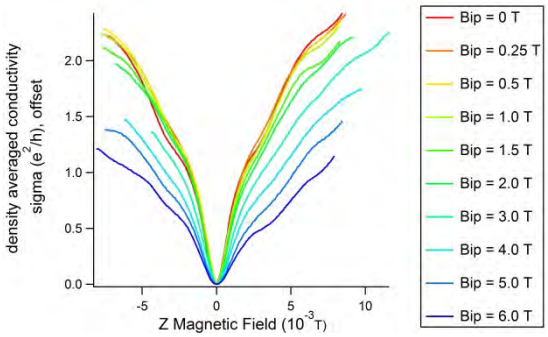

Fig. 3 Density averaged conductivity versus perpendicular magnetic field. The density is averaged in the range from n = 3.2 e-15 m⁻² to n = 1.2 e-16 m⁻². The color code indicates the applied Bip. The temperature of the mixing chamber was T = 30 mK.

Outlook

As mentioned above, encapsulating graphene between two hBN flakes leads to high electronic mobility and mean free paths which exceed possible constriction sizes of GNRs. Future experiments will focus on the investigation of narrow GNRs which are encapsulated and thus provide ballistic transport across the constriction. Besides bulk disorder (which is minimized by the encapsulation technique), edge disorder is presumably starting to play an important role for the electronic transport in narrow graphene nanostructures. To reduce the edge roughness we employ a cold remote Hydrogen plasma to anisotropically etch graphene into narrow channels with high edge quality and a low amount of chemical doping at the graphene boundaries [4]. We believe that such systems are promising to exhibit size quantization effects, which we will study in low temperature quantum transport experiments.

Furthermore, the top hBN flake can act as a gate dielectric, thus providing the possibility to fabricate local top gates which allow to locally tune the charge carrier density and therefore afford an additional experimental knob. In a first device we measured Fabry-Pérot oscillations in a 600nm narrow graphene channel over a distance of more than 300nm (Fig. 4). We plan to fabricate even narrower GNRs with top-gated constrictions to get insight into transport mechanisms inside the constriction.

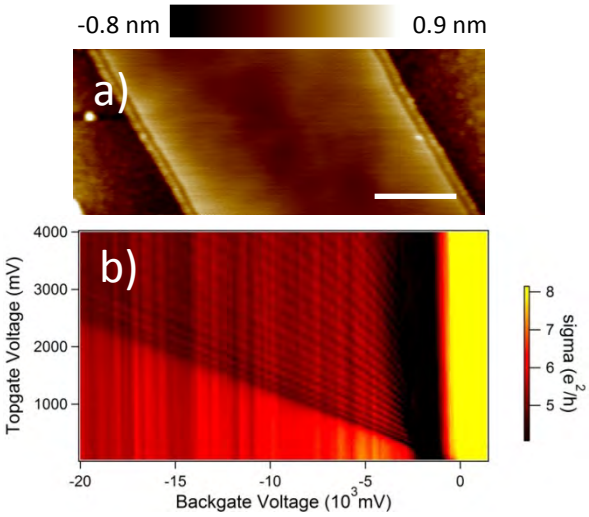

Fig. 4 a) AFM topography image of an H-plasma etched GNR. Due to the H-plasma exposure the graphene surface exhibits a very high level of cleanliness. Scale bar equals 200 nm. b) Conductivity as a function of backgate and topgate voltages. Due to the formation of pn-interfaces a cavity forms and leads to the observed Fabry-Pérot resonances.

References

[1] J. Klinovaja and D. Loss, *Giant Spin-Orbit Interaction Due to Rotating Magnetic Fields in Graphene Nanoribbons*, Phys. Rev. X 2013, 3, 011008

[2] A. Haldar and A.O. Adeyeye, *Deterministic Control of Magnetization Dynamics in Reconfigurable Nanomagnetic Networks for Logic Applications*, ACS Nano 2016, 10, 1690

[3] M.B. Lundeberg and J.A. Folk, *Rippled Graphene in an In-Plane Magnetic Field: Effects of a Random Vector Potential*, PRL 2010, 105, 146804

[4] G. Wang et al., *Patterning monolayer graphene with zigzag edges on hexagonal boron nitride by anisotropic etching*, APL 2016, 109, 053101

Nanomechanical sensors for fast viscosity and liquid density measurements

Project P1501 Nanomechanical mass and viscosity measurement-platform for cell imaging
Project Leader: T. Braun and E. Meyer
Collaborators: P. Oliva (SNI PhD Student), B. Bircher, C. Padeste, and N. Opara

Introduction

To date, most methods used to determine the viscosity and mass density of liquids have two drawbacks: Long measurement time (in the range of minutes) and high sample consumption (in the range of milliliters). Nanomechanical sensors promise to overcome these limitations.

We developed a method to decrease the time and sample volume required for such measurements. It features (i) a droplet-generating automatic sampler using fluorinated oil to separate microliter sample plugs, (ii) a PDMS-based microfluidic measurement cell containing the resonant microcantilever sensors driven by photothermal excitation, (iii) dual phase-locked loop frequency tracking of a higher-mode resonance to achieve millisecond time resolution, and (iv) signal processing to extract the resonance parameters, namely the eigenfrequency f_n and quality factor Q_n of mode n. From these two values, highly affected by the liquid characteristics surrounding the resonator, the liquid viscosity and the mass density can be calculated [1].

Instrument and measurement principle

The instrument is geared to measure viscosity and liquid values of small aqueous droplets in a two-phase microfluidic system. Figure 1 shows the fluid handling of the instrument and the measurement chamber.

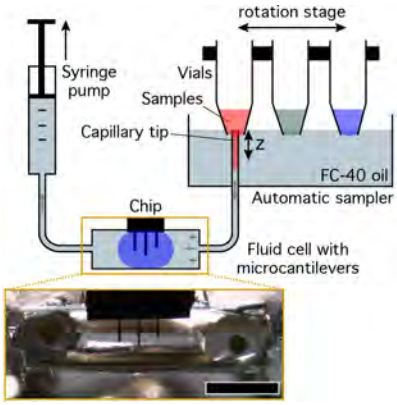

Fig. 1 Schematic of the fluidic setup (from [1]). The whole fluidic system is filled with fluorinated oil (FC-40). Samples float on the FC-40 oil and are confined by open-ended vials. 12 vials are mounted in a rotatable stage. Sample droplets are aspirated using a capillary that is controlled by a z-motor, and are separated by oil aspirated when the capillary is withdrawn (along z). Each vial is addressed by rotating the stage. The droplets are pumped through the fluid cell (bottom view) containing the resonant microcantilevers. A syringe pump maintains a constant flow rate of 1 µL/s. Inset: Micrograph of the fluid cell (scale bar: 1 mm).

A dual phase-locked loop (PLL) was employed to measure f_n and Q_n of a vibrational mode with a high time resolution (Fig. 2a). Two sideband frequencies adjacent to the eigenfrequency, were measured and converted into the corresponding eigenfrequency f_n and quality factor Q_n (Fig 2b).

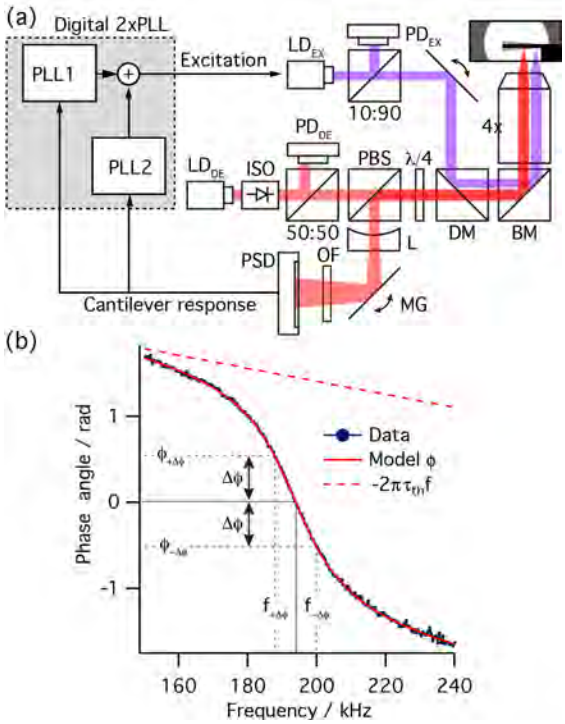

Fig. 2 Principles of eigenfrequency f_n and quality factor Q_n measurements of a given mode n using a nanomechanical microcantilever resonator (adapted from [1]). a) Schematic of the electronic and optical setup. Optical beam deflection system used to detect microcantilever vibration: The beam of a 780 nm diode laser (LD_{DE}; red) sequentially passes an optical isolator (ISO), a beam-splitter (50:50) to monitor the intensity on a photodiode (PD_{DE}), a polarizing beam-splitter (PBS), a quarter-wave retarder (λ/4) and a dichroic mirror (DM), and is reflected by a broadband mirror (BM). After focusing by passing through a microscope objective (4x), it is reflected from the microcantilever (in the fluid cell) and coupled onto a position-sensitive detector (PSD) using the polarizing beam-splitter (PBS). A concave lens (L) increases the displacement of the laser on the PSD. A mirror galvanometer (MG) automatically aligns the laser spot on the PSD and an optical filter (OF) blocks interfering light. Photothermal excitation used to drive the microcantilevers: An intensity-modulated 406 nm diode laser (LD_{EX}; violet) is coupled-in using the dichroic mirror (DM). A digital dual phase-locked loop (2 x PLL) is

used to detect the cantilever frequencies. The signal from the PSD is fed into the dual-PLL consisting of two parallel (PLL1 and PLL2) phase-detectors, PI controllers, and oscillators. The output of the oscillators is mixed and applied to LD_{EX}. b) Representative phase spectrum of the third mode of vibration of a 300x35x2 µm³ cantilever in water. The eigenfrequency f_3 = 194 kHz, the quality factor Q_3 = 8.4 and thermal time constant τ_{th} = 1.2 µs. The measured data (blue markers), model (solid red curve), and linear thermal lag included in the model (dashed red curve) are shown. The eigenfrequency and sideband frequencies and their corresponding phase angles are indicated by the solid and dashed grey lines, respectively. The phase is shifted to zero at the eigenfrequency.

Results

The measurement principle and the instrument were validated by screening series of 3 µL droplets of glycerol solutions separated by fluorinated oil at a rate of ~6 s per sample (Fig. 3a). Separation of sample droplets in a two-phase configuration with fluorinated oil was crucial to avoid dispersion. An analytical hydrodynamic model (HDM) [2] and a reduced order model (ROM) [3] were employed to calculate the viscosity and mass density of the sample liquids in a viscosity range of 1–10.5 mPa·s and a density range of 998–1154 kg/m³ (Fig. 3b). The time resolution of the detection system was in the range of milliseconds, whereas the sample droplet throughput was of the order of seconds per droplet. The ROM provided more accurate results, because it was calibrated with three reference fluids. In contrast, the HDM only requires a single calibration point and provides *ab initio* knowledge on the microcantilever behaviour.

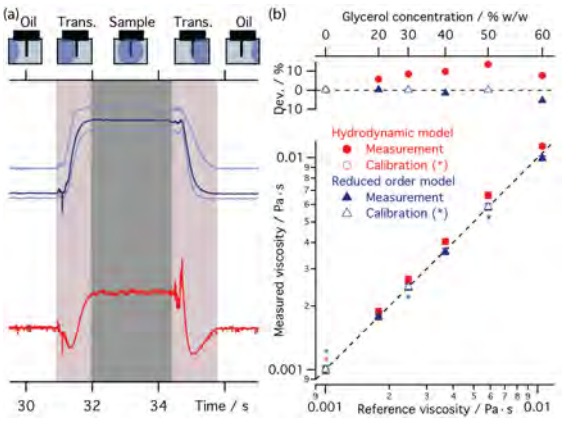

Fig. 3 Nanomechanical microviscometer for droplet screening in a two-phase microfluidics (adapted from [1]). a) Single droplet passage of a water sample (blue) encapsulated in an oil stream (gray) over the cantilever (black). When the oil-water interface passes the microcantilever, the laser beams are scattered and the PI and PLL controllers adjust to the new values, resulting in a transition region (Trans.) of several 100 ms. Immersed in sample, a new stable value is achieved, until the droplet is replaced by oil again. Light-blue: side band frequencies, dark blue: Eigenfrequency. Red: Q-factor. b) From the eigenfrequency and Q-factors viscosity values (and liquid densities, not shown) can be calculated using a three point calibration model [3] or by applying a hydrodynamic model [2].

Outlook

We are currently testing new nanomechanical resonators further reducing the sample volume below 100 nl and allowing multiplexing of the measurements. To this end, the optical actuation set-up had to be improved to allow more precise and flexible actuation of the arrayed resonators (Fig. 4).

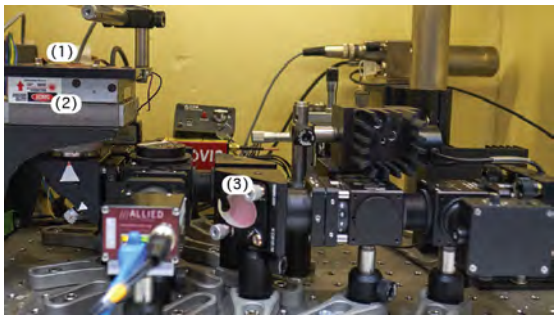

Fig. 4 Set-up modifications to support the new, arrayed nanomechanical sensors (November 2016). (1) New measurement chamber holder; (2) xy-stage; (3) beam shifter to displace detection laser (L_{DE}) relative to the excitation laser (L_{EX}).

References

[1] B. A. Bircher, R. Krenger and T. Braun. *Automated high-throughput viscosity and density sensor using nanomechanical resonators*, Sensor Actuat B-chem. 223(C): 784–90 (2016)

[2] C. A. Van Eysden and J. E. Sader, *Frequency response of cantilever beams immersed in viscous fluids with applications to the atomic force microscope: Arbitrary mode order,* J. Appl. Phys., 101(4), 044908 (2007)

[3] M. Heinisch, T. Voglhuber-Brunnmaier, E. K. Reichel, I. Dufour, and B. Jakoby, *Reduced order models for resonant viscosity and mass density sensors,* Sensors & Actuators: A-Chem, 220, 76–84 (2014)

Correlation of chemical, magnetic and morphological properties of goethite nanoparticles

Project P1502 Investigating individual multiferroic and oxidic nanoparticles
Project Leader: A. Kleibert and M. Poggio
Collaborators: D.M. Bracher (SNI PhD Student), T.M. Savchenko, M. Wyss, G. Olivieri, M.A. Brown, and F. Nolting

Introduction

Antiferromagnetic materials play an important role in modern spintronics devices such as spin valves and magnetic random access memories, and are further relevant for the development of novel ultra-hard magnetic materials [1, 2]. Also many multi-ferroic materials, which are of great interest for future spintronics applications, exhibit antiferro-magnetic order. However, to fully explore the potential of these materials it is necessary to study their properties at the nanoscale. The absence of a net magnetic moment in antiferromagnetically ordered matter makes a direct investigation of the magnetic properties difficult. In the present project we tackle this issue and develop a unique experimental approach, which does not only allow us to investigate the magnetic properties of individual, nanostructured antiferromagnets, but further to directly correlate the magnetism with chemical properties and morphology.

As a model system for these investigations we select synthethic goethite nanoparticles. In its bulk form goethite (α-FeOOH) is antiferromagnetically ordered at room temperature and has a Néel temperature of 400K. Goethite is a common mineral in the earth's crust and soils [3]. It plays an important role in many fields such as catalysis, corrosion, paleoclimatology, paleomagnetism, and for space exploration. However, in most cases goethite is found or is of interest in the form of nanoparticles. The latter usually possess a complex structure and morphology, which may lead to significant deviations from the known bulk properties and, thus, obtaining insight in their magnetism requires dedicated investigations. To correlate size, shape, chemical and magnetic properties of these nanoparticles we perform complementary microscopy and spectro-microscopy techniques on selected nanoparticles in addition to integral structural characterization.

Experimental

Magnetic and chemical characterization of the nanoparticles is achieved by means of spatially resolved X-ray absorption spectroscopy (XAS) using X-ray photo-emission electron microscopy (X-PEEM) at the Surface/Interface: Microscopy (SIM) beamline of the Swiss Light Source. Antiferro-magnetically and ferromagnetically ordered mo-ments are studied by means of the X-ray magnetic linear dichroism (XMLD) and the X-ray magnetic circular dichroism (XMCD) effect, respectively [4]. Local XMLD/XMCD spectra of individual nanoparticle structures are acquired by recording X-PEEM images as a function of photon energy and polarization, cf. Ref. [5]. The morphology is studied by means of scanning electron microscopy (SEM) and transmission electron microscopy (TEM). A solution of synthetic goethite nanoparticles in ethanol purchased from Sigma-Aldrich is spin coated on Si wafers with gold marker structures for the X-PEEM and SEM investigations. The spin-coating parameters are optimized for the (low) particle density as required for the X-PEEM investigations. For the TEM experiments the nanoparticles are dispersed on a TEM-compatible SiN-membrane substrate. The structure of the nanoparticles is investigated in solution by means of X-ray diffraction (XRD).

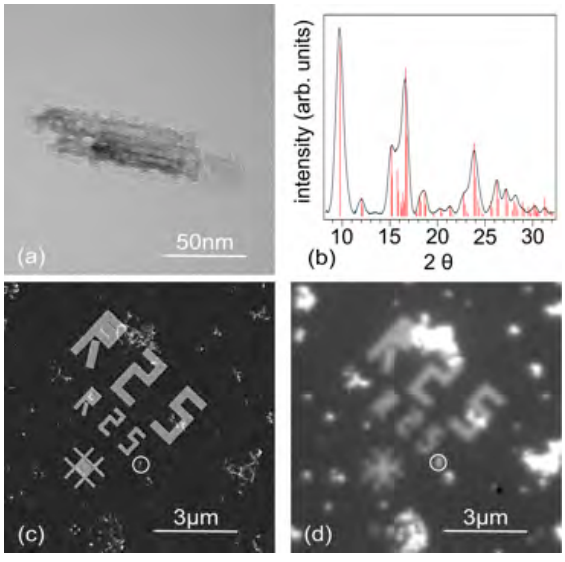

Fig. 1 a) TEM image of a goethite nanoparticle. b) X-ray diffraction pattern of goethite nanoparticles. c) SEM image of nanoparticles dispersed on a silicon substrate with litho-graphically made gold marker structures for particle identification. d) X-PEEM elemental contrast map of the same area recorded with the X-ray photon energy tuned to the Fe L_3 edge. The white circles in c) and d) highlight the very same particle as seen in both microscopes.

Results

TEM images as shown for example in figure 1a reveal defect-rich nanoparticles with an acicular morphology as often observed for goethite [3]. The length of the particles is approximately 100nm and the width about 20nm. The XRD pattern yields the goethite structure. Spin-coating on the Si wafers results in agglomerates of nanoparticles, which are randomly distributed over the surface. The agglomerates with variable size are visible as bright, irregular structures in the SEM image in figure 1c. The same sample area as seen in X-PEEM and with the photon energy set to the Fe L_3 edge is shown in figure 1d. At this photon energy the nanoparticles are resonantly excited and appear as bright features. The gold marker structures visible in figures 1c and d allow us to identify the very same nanoparticles in both microscopes. One nanoparticle structure is highlighted with a white circle in both images. Enlarged images of the same structure are shown in figures 2a and b. The SEM image in figure 2a reveals a complex morphology, likely due to two close-lying goethite needles. The spatial resolution of X-PEEM is about 50 – 100 nm and the needles are less well resolved.

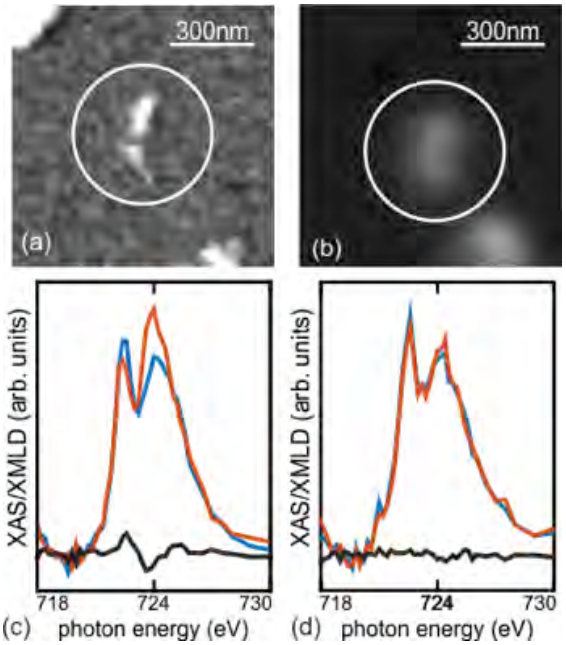

Fig. 2 a) SEM and b) X-PEEM elemental contrast image of the very same particle. The X-ray absorption spectrum recorded with linear horizontal (blue) and vertical (red) polarized light and the XMLD spectrum of this particle at room temperature and at 460K are shown in c) and d), respectively.

Local, polarization dependent XAS spectra taken in the marked circular spot are shown in figure 2c. The data cover the vicinity of the Fe L_3 absorption edge and are recorded at room temperature. Comparing spectra obtained with linearly horizontal (blue) and vertical (red) polarized radiation reveal a strong linear dichroism effect, which is separately plotted as the black line in figure 2c. The same spectra were also recorded at 460 K, i.e., above the known Néel temperature of bulk goethite, see figure 2d. At this temperature the dichroism effect vanishes, but it recovers after cooling back to room temperature. This reversible behavior is assigned to a transition between antiferromagnetic order below and paramagnetic properties above the Néel temperature, which according to additional measurements is above 380 K for the present particles. These data strongly suggest that the goethite nanoparticles exhibit antiferromagnetic order at room temperature. When rotating the sample azimuthally we further notice a pronounced anisotropy of the XMLD effect at room temperature, which confirms a preferred magnetization axis. Further experiments carried out with circularly polarized X-ray yield no indications of ferromag-netically ordered moments in these nanoparticles and further confirm a high degree of antiferro-magnetic order. Given the complex and defect-rich morphology of the particles (Fig. 1a), this is a surprising and important result.

Summary and Outlook

In conclusion, we demonstrate that nanoscale antiferromagnetism can be probed by means of spatially resolved, polarization-dependent X-ray absorption spectroscopy using X-PEEM. A correlation with morphology data is possible by means of marker structures and complementary microscopy, e.g., SEM. Specifically, our data suggest that synthetic goethite nanoparticles exhibit antiferromagnetic order irrespective of their complex and defective morphology. Next, the approach will be applied to nanoparticles of multiferroic materials such as BFO. At the same time we plan to use TEM compatible substrates, which will allow us to correlate the magnetic properties with the actual microstructure of the nanoparticles.

References

[1] S. Morup, D.E. Madsen, C. Frandsen, C.R.H. Bahl, M.F. Hansen, *Experimental and theoretical studies of nanoparticles of antiferromagnetic materials*, J. Phys.: Condens. Matter 19, 213202 (2007)

[2] N. Fontaíña-Troitiño, S. Liébana-Viñas, B. Rodriquez-Gonzàlez, Z.A. Li, M. Spasova, M. Farle, V. Salgueriño, *Room-temperature ferromagnetism in antiferromagnetic cobalt oxide nanooctahedra*, Nano Lett. 14, 640 (2014)

[3] R.M. Cornell and U. Schwertmann, The Iron Oxides: Structure, Properties, Reactions, Occurences and Uses 2nd edn, New York: Wiley-VCH (2003)

[4] J. Stöhr, *X-ray magnetic circular dichroism spectroscopy of transition metal thin films,* J. Electron. Spectrosc. 75, 253 (1995)

[5] C.A.F. Vaz, A. Balan, F. Nolting, and A. Kleibert, *In situ magnetic and electronic investigation of the early stage oxidation of Fe nanoparticles using x-ray photo-emission electron microscopy*, Phys. Chem. Chem. Phys. 48, 26393 (2014)

Valleytronics in strain-engineered graphene

Project P1504 Valleytronics in strain-engineered graphene
Project Leader: C. Schönenberger and M. Calame
Collaborators: L. Wang (SNI PhD Student), P. Makk, and J. Overbeck (SNI PhD Student)

Introduction

The valleys in graphene are the energetically degenerate but nonequivalent local minima (maxima) of the conduction (valence) band sitting at the corners of the Brillouin zone, called K and K'. Since the two valleys are far away from each other in momentum space, intervalley scattering is strongly suppressed, implying the potential use of the valley degree of freedom for electronic applications, referred to as valleytronics, in a way similar to the role of spin in spintronics.

In order to address valley, ultraclean disorder-free graphene is a prerequisite. With in-situ current annealing which cleans the resist residues from fabrication process, ultraclean suspended graphene has been developed, yielding very high mobilities and ballistic transport over micron distances [1]. Secondly, one needs a handle to control valley for generating and detecting the valley current. It has been predicted that non-uniform strains can generate pseudo-magnetic fields that act with opposite signs on the two different valleys in order to preserve time-reversal symmetry [2]. In this work, we aim to control the valley degree of freedom by strain engineering.

Strain configurations

Two possible strain configurations have been proposed. One is to apply stresses with triangular symmetry [2] (Fig. 1a) and the other is to bend the graphene ribbon into a circular arc [3] (Fig. 1d). For the triangular geometry, we can perform valley Hall effect measurements in analogy to spin Hall effect, in which a Hall voltage will be built up from a valley polarized current. For the arc geometry, deviations from the quantum Hall patterns due to valley effects can be studied when a tunable strain pattern is applied in addition to a constant magnetic field. However, both geometries are still experimentally challenging due to the complex fabrication process combined with non-trivial force patterns. Instead of applying stress perpendicular to the perimeter of the triangular geometry, we start with a simplified variation in which the three arms are fixed on the contacts (Fig. 1b) and the graphene is pulled down capacitively by using a back gate. In order to detect the valley Hall voltage, we connect a second triangular graphene as shown in Fig. 1c. If a current is injected from the bottom-left contact, for example, electrons from K valley will go to the up-left contact while electrons from K´ valley will bend to the right triangle. Then again in the second triangle, the K´ electrons will bend to the right and go to the bottom-right contact resulting in a potential difference between the right two contacts. This potential difference can be detected by voltage measurements. For the arc geometry, we design the contacts in a special shape so that an equivalent strain configuration can be achieved by pull the graphene uniaxially along the contact direction instead of bending it into a circular arc (Fig. 1e). The simplified bending can be realized by break junction technology if we fabricate the device on a flexible substrate.

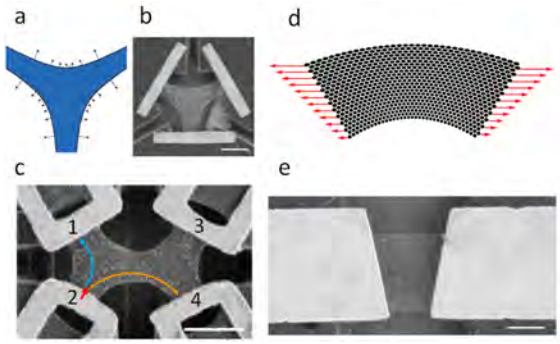

Fig. 1 a) Sketch of a triangular graphene sample with normal forces applied at the perimeter. The arrows indicate the required local stress [2]. b) SEM image of triangle shaped graphene suspended symmetrically by contacts. The graphene will be strained capacitively by using back gate voltages. c) SEM image of two of such triangular graphene connected together. d) Sketch of a rectangular graphene bended into a circular arc by normal forces applied at two opposite boundaries [3]. e) SEM image of rectangular graphene suspended with modified contacts. The strain can be generated by break junction technique. The scale bars correspond to 1 μm.

Local and non-local measurements

We have done a series of fabrication test of suspended four-terminal devices as shown in figure 1c. Two bilayer devices were successfully cleaned by current annealing. The local resistance R_L is defined by the voltage between contact 2 and contact 3 divided by the current injected between contact 1 and contact 4 while the non-local resistance R_{NL} is defined by the voltage between contact 3 and contact 4 divided by the current injected between contact 1 and contact 2.

The gate voltage dependence of R_L and R_{NL} were measured at cryogenic temperature. Interestingly, R_{NL} exhibits a much sharper peak than R_L at the charge neutrality point (CNP) as shown in figure 2a. The Ohmic contribution to the nonlocal resistance is described by the van der Pauw relation $R_{NL} \sim R_L(W/L)e^{-L/W}$, where W is the device width and L is the distance between the current path and voltage probes [4]. If the R_{NL} originates only from the Ohmic contribution, the shape of the R_{NL} curve should be the same as the R_L curve. This is obviously not the case in our measurement. According to ref [4], if the nonlocal resistance results from the VHE and the IVHE, the peak in R_{NL} can be described by a

power law relation $R_{NL} \sim R_L^3 \sigma_{xy}^2 e^{-L/\lambda_v}/\lambda_v$, where σ_{xy} is the valley Hall conductivity and λ_v is the valley diffusion length. We compared the R_{NL} curve with the R_L^3 curve of our data. The sharpness of the peak of the R_{NL} curve matches quite well with that of the peak of the R_L^3 curve after subtracting the contact resistance (Fig. 2b), which seems to imply the valley Hall origin of the non-local signal. However, the non-local signal maximizes at the CNP where no strain in graphene is generated by the back gate voltage capacitively. On the other hand, we cannot control the doping and the strain separately. So we can hardly attribute the signal to externally generated strain.

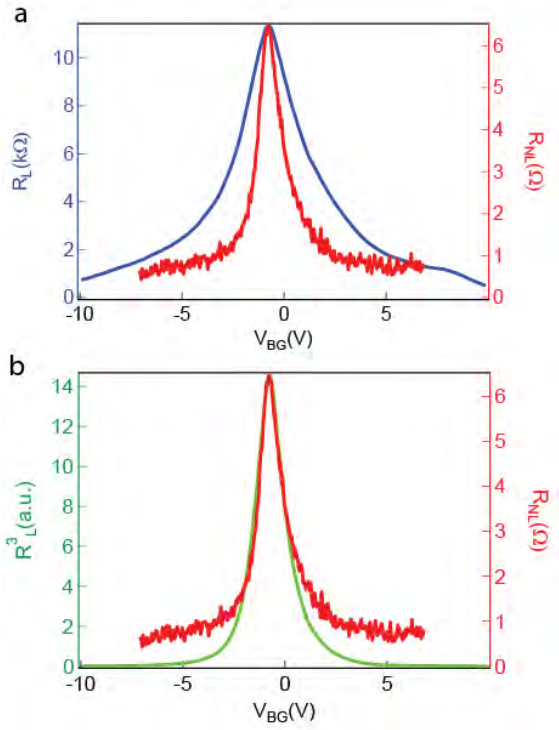

Fig. 2 a) Gate voltage dependence of R_L (blue) and R_{NL} (red). b) Shape comparison of the R_{NL} curve (red) with the R_L^3 curve (green).

Strain generation with break junction technique

We have successfully generated controllable strain in suspended graphene by break junction technique (Fig. 2) in collaboration with another SNI PhD student Jan Overbeck. Strain effects such as broadening and redshift of the G-peak and the 2D-peak in Ramen spectrum with increasing strain have been observed. We estimate that the strain achieved in our sample was approximately 1%. A built-in strain of roughly 0.1% after fabrication is extracted from the measurement data.

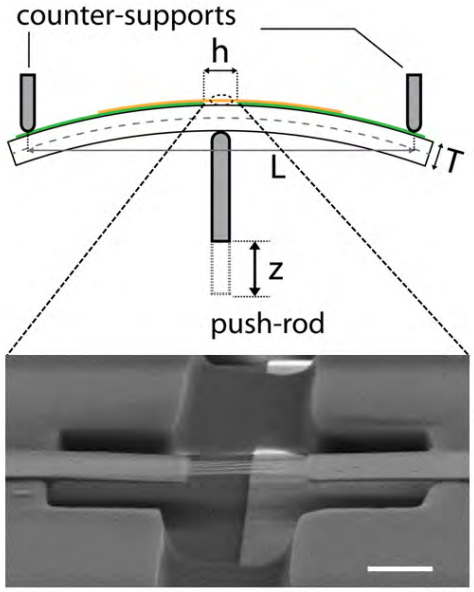

Fig. 3 A suspended graphene device is fabricated on a bendable substrate. The substrate is then bended in a controllable way so that a controllable strain can be generated in graphene. The scale bar is 1 μm.

Outlook

For the local and non-local measurements, we will further study temperature and magnetic field dependences of R_L and R_{NL}. In order to find out the origin of the non-local signal, same measurements on single layer devices are necessary. We are looking for methods to control the strain and the doping of graphene separately at low temperature. There are several options to try, such as NEMS, piezoelectric substrate, AFM tip, etc.

Since the break junction technique is not cryostat compatible, we will try to do current annealing and perform transport measurements at room temperature.

References

[1] P. Rickhaus, R. Maurand, M.-H. Liu, M. Weiss, Klaus Richter and C. Schönenberger, *Ballistic interferences in suspended graphene*, Nat. Comm. 4, 2342 (2013)

[2] F. Guinea, M.I. Katsnelson and A.K. Geim, *Energy gaps and a zero-field quantum Hall effect in graphene by strain engineering*, Nat. Phys. 6, 30 (2010)

[3] F. Guinea, A.K. Geim, M.I. Katsnelson and K.S. Novoselov, *Generating quantizing pseudo-magnetic fields by bending graphene ribbons*, Phys. Rev. B 81, 035408 (2010)

[4] R.V. Gorbachev, J.C.W. Song, G.L. Yu, A.V. Kretinin, F. Withers, Y. Cao, A. Mishchenko, I.V. Grigorieva, K. S. Novoselov, L.S. Levitov and A.K. Geim, *Detecting topological currents in graphene superlattices*, Science 346, 448 (2014)

*NANO*zyme: Nanobiocatalysts based on artificial metalloenzymes

Project A9.9 NANOzyme (FHNW, University of Basel, INOFEA AG, Basel)
Project Leader: P. Shahgaldian
Collaborators: P.F.-X. Corvini, T.R. Ward, M. Hestericová, B. Ricken, M.R. Correro, and Y. Dudal

Introduction

Enzymes are natural biomolecules endowed with the capability to catalyze a broad range of chemical reactions with exquisite selectivity and efficiency. Submitted since the origins of life to a series of selective pressures, enzymes have evolved to function efficiently in their "physiological" environment. However, when it comes to exploit enzymes for industrial synthetic processes in "non-physiological" conditions, these biocatalysts often suffer from stability issues. To overcome the gap left by natural evolution, strategies of enzymes resistance enhancement such as protection and structural modification have been developed. Additionally, cofactor recycling is another important hurdle for the use of certain enzymes such as oxidoreductases in industrial processes. The efficient chemical and electrochemical recycling of enzyme cofactors such as nicotinamide adenine dinucleotide (NAD^+) or flavin mononucleotide (FMN) is of high interest and has been intensively investigated as an alternative to enzymatic regeneration [1, 2].

The group of TRW has pioneered the field of artificial metalloenzymes and developed artificial catalytic systems for which no satisfactory homogeneous or enzymatic solution was available [3]. The groups of PFXC and PS have developed a chemical strategy to grow at the surface of silica nanoparticles an organosilica layer with a nanometer-precision [4]. This approach has been successfully applied to develop stable nanobiocatalysts consisting of enzymes covalently bound at the surface of silica nanoparticles (SNPs) and shielded with a protective organosilica layer [5, 6]. The present work aimed at combining both approaches to create novel nanobiocatalysts, which allow the *in situ* regeneration of redox coenzymes (*e.g.*, NADH, $FMNH_2$).

Results and discussion

In order to develop an enzymatic system possessing the ability to regenerate *in situ* $NADH,H^+$ from NAD^+, and $FMNH_2$ from FMN, it was decided to immobilize and confine two enzymatic systems (Fig. 1). The first one, an artificial ATHase, was introduced in order to allow the reduction of NAD^+ by consuming one formic acid molecule. The resulting $NADH,H^+$ would then serve as a coenzyme for the second enzyme of the cascade, namely a NADH-dependent FMN reductase, that was expected to reduce FMN into $FMNH_2$. It was postulated that confining this electron transfer chain within a thin organosilica layer would allow substrate/product channeling resulting in high catalytic efficiency.

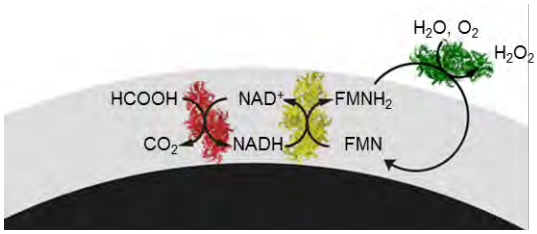

Fig. 1 Schematic representation of the nano-confined electron transfer chain reaction. ATHase (red protein) and RED (yellow protein) are co-immobilized and confined in an organosilica layer. Soluble luciferase (green protein) is added to the system in order to indirectly quantify the $FMNH_2$ production by measuring the production of H_2O_2.

Artificial transfer hydrogenases (ATHases) are created by the non-covalent incorporation of an organometallic cofactor within streptavidin mutants (Sav), which are genetically optimized by the introduction of point mutations on the Sav gene. Among the different SAV mutants, the [Cp*Ir(biot-p-L)Cl]·S112A-K121A (ATHase) revealed the highest catalytic activity toward NAD^+ reduction. It was chosen as artificial enzyme to produce the first intermediate ($NADH,H^+$) of the chain reaction. RED was heterologously expressed in *E. coli.* For ease of purification, a His_6 followed by a SUMO-tag was cloned to the 5' end of red gene. After IMAC purification the His_6-SUMO tag was cleaved by Ulp1 digestion before purification and immobilization.

In order to efficiently co-immobilize the selected ATHase and RED onto SNPs, a series of important parameters (temperature, pH and buffer composition) were carefully optimized (Fig. 2). Moreover, since RED has a greater turnover rate with regard to the ATHase, the adequate ratio of enzymes was assessed. A sequential co-immobilization of ATHase and RED was successfully achieved.

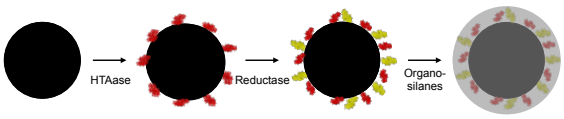

Fig. 2 Schematic representation of the cofactor recycling system. ATHase and RED are sequentially co-immobilized at the surface of SNP (black sphere). An organosilica layer (grey sphere) is produced through the controlled polycondensation of a silane mixture.

The controlled organosilica layer growth was achieved by incubation of the SNPs in a mixture of organosilanes; the SNPs produced were analyzed by field-emission scanning electron microscopy (Fig. 3). Optimization of the synthetic conditions allowed producing a protective layer of 10 nm fully shielding the immobilized enzymes.

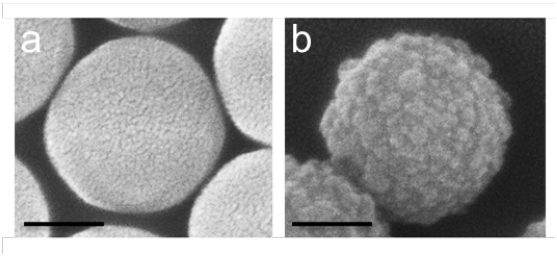

Fig. 3 SEM micrographs of SNPs before a) and after b) organosilica layer growth (scale bars represent 100 nm).

The immobilized and protected ATHase had a remarkably enhanced catalytic activity with regard to the soluble catalysts [7]. The turnover numbers were calculated based on the iridium content, which was quantified by means of inductively coupled plasma mass spectrometry. Importantly, the SNPs could be recycled at least twice, with only a slight decrease in conversion rates. Further experiments were performed in complex matrices including blood, urine, cell extract and solvent [7]. In all tested conditions, the protected catalyst was shown to be active.

In order to evaluate the NADH and $FMNH_2$ regeneration resulting from the cascade reaction, a soluble luciferase was added to the reaction mixture. The luciferase, in the presence of H_2O and O_2, oxidizes $FMNH_2$ into FMN and releases H_2O_2. Vanadium-(V)-oxide (V_2O_5) was used for H_2O_2 detection. V_2O_5 reacts with H_2O_2 to produce water and hydrogen diperoxodioxovanadate(III) which can be spectrophotometrically measured at 454 nm. In order to demonstrate the positive effect of enzymes confinement for cofactor recycling, additional catalysts were produced: *i)* ATHase and RED co-immobilized onto SNPs but not protected, *ii)* ATHase and RED immobilized separately onto SNPs with or without protective layer.

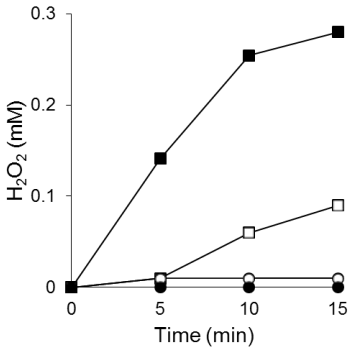

Fig. 4 Cascade reaction and cofactor recycling. H_2O_2 produced by: I) ATHase and RED co-immobilized and protected (black squares) or II) immobilized only (full spheres) and by a mixture of III) separately immobilized ATHase and RED protected (white squares) and IV) not protected (white spheres).

As shown in figure 4, the catalyst consisting of ATHase and RED co-immobilized and protected produced the highest amount of H_2O_2, 280 μM. The catalyst including ATHase and RED co-immobilized and not protected produced a negligible amount of H_2O_2. The system including a mixture of separately immobilized ATHase and RED protected and not produced 90 and 10 μM H_2O_2 respectively. This set of results represents a clear proof of the positive effect of the enzyme/substrate confinement in a cascade reaction.

Outlook

We have successfully developed a nanobiocatalyst that catalyzes a cascade reaction allowing *in situ* coenzyme regeneration. The cascade reaction is catalyzed by a) two different enzymes immobilized on SNPs and protected by an organosilica layer and b) a soluble enzyme, which uses as cofactor the product of the second enzyme. We have demonstrated that the cascade reaction catalyzed by the shielded/confined enzymes is remarkably improved with regard to the similar system but deprived of protection/confinement layer. Similarly, we have demonstrated that the "*vicinity*" of enzymes, working in tandem, promotes cofactor recycling.

References

[1] V. Kohler, Y.M. Wilson, M. Durrenberger, D. Ghislieri, E. Churakova, T. Quinto, L. Knorr, D. Haussinger, F. Hollmann, N.J. Turner, T.R. Ward, *Synthetic cascades are enabled by combining biocatalysts with artificial metallo-enzymes*, Nat. Chem. 5, 93 (2013)

[2] T. Heinisch, T.R. Ward, *Artificial metallo-enzymes based on the biotin–streptavidin tech-nology: challenges and opportunities*, Acc. Chem. Res. 49, 1711 (2016)

[3] T.R. Ward, *Artificial metalloenzymes based on the biotin-avidin technology: enantio-selective catalysis and beyond*, Acc. Chem. Res. 44, 47 (2011)

[4] A. Cumbo, B. Lorber, P.F. Corvini, W. Meier, P. Shahgaldian, *A synthetic nanomaterial for virus recognition produced by surface imprinting*, Nat. Commun. 4, 1503 (2013)

[5] M.R. Correro, N. Moridi, H. Schützinger, S. Sykora, E.M. Ammann, E. H. Peters, Y. Dudal, P.F.-X. Corvini, P. Shahgaldian, *Enzyme shielding in an enzyme-thin and soft organo-silica layer*, Angew. Chem., Int. Ed. 128, 6393 (2016)

[6] M.R. Correro, M. Takacs, S. Sykora, P.F.-X. Corvini, P. Shahgaldian, *Supramolecular enzyme engineering in complex nanometer-thin biome-metic organosilica layers*, RSC Adv. 6, 89966 (2016)

[7] M. Hestericova, M.R. Correro, M. Lenz, P.F.-X. Corvini, P. Shahgaldian and T.R. Ward, *Immobilization of an artificial imine reductase within silica nanoparticles improves its performance*, Chem. Commun. 52, 9462 (2016)

Single-cell nano analytics

Project A9.12 SCeNA (University of Basel, FHNW, Roche Basel)
Project Leader: T. Braun
Collaborators: H.-P. Lang, G. Schlotterbeck, G. Dernick, Ch. Berchtold, L. Rima, and S.A. Arnold

Introduction

The stochastic nature of biological systems inherently leads to heterogeneous cell populations. To date, most bioanalytical methods measure cell assembly averages, obscuring the cell heterogeneity and the biomolecular interaction networks. The aim of the SCeNA project is to combine cell culturing of adherent eukaryotic cells with different analysis methods characterizing different aspects of the cell. To this end, an in-house developed "cell picker" was combined with different hand-over and conditioning systems for subsequent analysis by visual proteomics (VP), reverse-phase protein arrays (RPPA) and liquid chromatography massspectrometry (LC-MS).

Live cell imaging and "cell picker"

We significantly improved our previous set-up for single-cell picking and lysis of adherent eukaryotic cells. The amended instrument allows live-cell imaging before cell lysis [1]. Figure 1 shows the principle of the cell picking: A platinum-coated microcapillary electrode (MCE) is used to target and lyse individual cells by electroporation. Following lysis, the ruptured cell is immediately aspirated into the tip of the MCE in a volume of 3 to 5 nl [1]. The whole process can be monitored by light-microscopy. The aspirated cell lysate can then be handed over for conditioning and analysis by various methods.

Fig. 1 Live cell imaging chamber, "cell picker" and condition station [1]. The essential components are placed on a work-platform mounted in a live-cell incubator stage (1). For single-cell experiments, miniaturized petri dishes are used to culture the cells (2). These poly-(dimethylsiloxane) (PDMS)-based wells are reversibly bonded to an ITO-coated microscopy slide (3). Cells are lysed by electroporation and the lysate is immediately aspirated (3–5 nl) by a microcapillary (4) [1]. The microcapillary is guided by a conductive sleeve (5) and connected by a press-fit mechanism (6) and a microcapillary (7) to a high precision pump system (not shown). For sample conditioning, the microcapillary tip is immersed in negative stain or trehalose solution contained in a 200 µl tube (8). Subsequently, the sample is deposited on a carbon coated EM grid held in place by a groove (9). (Figure and legend adapted from [1].)

Single cell visual proteomics (VP)

The cell lysate of the "cell picker" can be visualized by electron microscopy (EM) or atomic force microscopy (AFM). The aim of VP is to analyze the proteome contents by the visual appearance of the protein-complexes. This approach promises single molecule sensitivity for single-cell analysis. Before the analysis by AFM or EM, the sample must be conditioned to be suitable, *e.g.*, sample salts must be removed to prevent salt-crystal formation (AFM & EM), or to introduce heavy metal salts to increase the contrast (EM). To this end, we developed a sample-conditioning method for nanoliter-sized volumes (Fig. 2). The conditioning is driven by diffusion, utilizing the different diffusion constants of salt molecules and proteins.

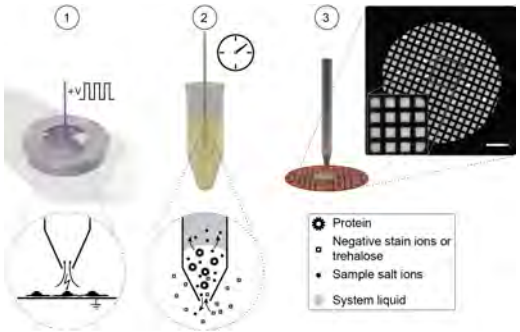

Fig. 2 The lossless sample preparation and conditioning process [1]. (1) Electroporation and aspiration (lysis) of a single cell from cell culture; (2) Immersion of loaded microcapillary tip into the conditioning liquid, here negative stain, for diffusion-driven desalting and staining of the sample; (3) Deposition of 5 nanoliter of sample on a glow-discharged EM grid and analysis by EM. Scale bar 500 µm. (Figure and legend adapted from [1].)

Figure 3A shows a typical image of single-cell lysate visualized by EM. Panel B shows an AFM image of synthetic amyloid fibril processed by diffusion-driven desalting.

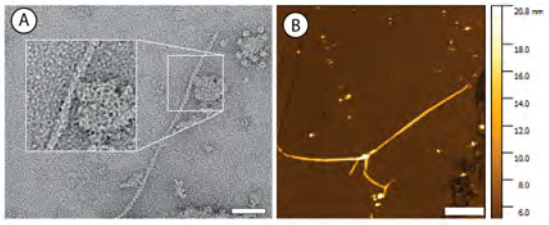

Fig. 3 Results of total sample conditioning and preparation tests. The method outlined in Fig. 2 was used [1]. A) TEM image of negatively stained single-cell lysate from a HEK 293 cell. Filamentous structures resembling F-actin are visible. Scale bar represent 50 nm. [1] B) AFM of synthetic amyloids conditioned using a volatile buffer (ammonium carbonate). Scale bar represents 2 µm [2].

Figure 4A shows a representative image of the negatively stained single-cell lysate from a heat-shocked cell, and panel B the corresponding negative control. The frequency of ring-shaped structures was significantly increased in the single-cell lysate of the heat-shocked cell. Visually, these structures resemble negatively stained heat-shock proteins (Fig. 4A, arrows) and are in good agreement with the reported structure of the Tric/CCT complex.

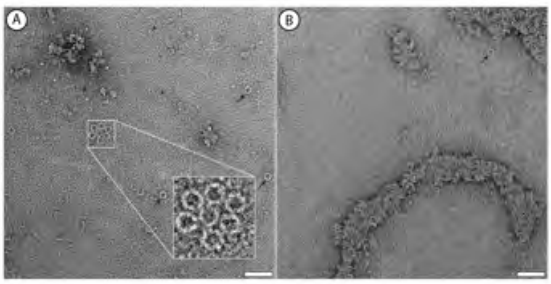

Fig. 4 The effect of heat-shock on HEK cells visualized by negative stain TEM of single-cell lysate [1]. A) Cell lysate from a single HEK cell after exposure to heat-shock. Multiple ring-shaped structures were found, and were related to heat-shock proteins (arrows) B) Representative negative-control image of single-cell lysate from a cell without prior heat-shock. Scale bars represent 50 nm.

Nanomechanical viscometry in two-phase microfluidic

We developed a top-down hand-over system that allows cell lysate to be directly fed into a two-phase microfluidics cartridge by a capillary gap handover (see last progress report). We optimized a nanomechanical microviscometer for high-throughput screening of liquid droplets in a two-phase microfluidics system [3] (see also report of project 1501), exhibiting few millisecond temporal resolutions for viscosity and liquid density measurements. We now produced sense and "antisense" RNA to measure the hybridisation of the two complementary strands as test. Such a sensor, combined with the developed hand-over system, can potentially be used to detect cellular RNA (transcriptomics).

Single cell reverse-phase protein arrays (RPPA)

In RPPA entire sets of complex biological samples, *e.g.*, cell lysates, are immobilized on a surface as spots and then probed by specific antibodies for particular proteins. Only a very small amount of sample is needed and we optimized the deposition by our single-cell lysis set-up (Fig. 1) for the analysis. For house-keeping proteins, we observed a roughly linear response to the number of cells lysed and dispensed. We automated cell picking and deposition using the openBEB platform [4] and 192 cells can now be spotted onto nitrocellulose or hydrogel coated slides within 90 min (Fig. 5).

We further developed assays to measure the expression of heat-shock protein (HSP60) and GAPDH, an enzyme involved in glycolysis (positive control). Currently, experiments are performed to assess biological experiments on single-cell level, such as the probing for heat-shock proteins and alpha synuclein, a protein involved in neurodegenerative diseases.

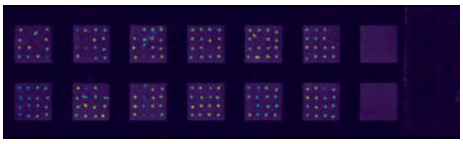

Fig. 5 Reverse phase protein array (RPPA) raw data. HEK 293 cells were grown confluent on ITO glass slides coated with poly-L-lysine. Individual cells were picked and deposited on nitrocellulose pads. Heat-shock proteins were detected using a primary antibody targeting HSP60. Detection was performed by a fluorescence labeled secondary antibody (read out wavelength: 785 nm).

Liquid-chromatography mass spectrometry (LC-MS) of single cell lysate

A newly developed hand-over system was used to transfer cell lysate from the picker directly into the LC-MS system (not shown). However, to get the necessary sensitivity for single cell analysis a highly optimized and sensitive setup is necessary. To achieve this, it is important to exactly know which metabolites might be found to develop the detection method accordingly. Therefore, a first survey by GC-MS using the Fhien method [5] was used to identify specific metabolites in batch lysate. Glutamate, Glutathione and Cholesterol have been identified as model compounds to develop and optimize the hand over system for single-cell sensitivity. These markers are now used for further optimization of our unique LC-MS approach for single-cell analysis. Currently, the sensitivity of the used systems allows for detection of the most abundant metabolites down to a level of about 10 cells (estimated on batch lysate). This developed hand-over system allows for separation and LC-MS detection of various metabolites in a new way. However, further optimization of the whole process is needed to access true single-cell sensitivity.

References

[1] S.A. Arnold, S. Albiez, N. Opara, M. Chami, C. Schmidli, A. Bieri, H. Stahlberg, C. Padeste and T. Braun, *Total sample conditioning and preparation of nanoliter volumes for electron microscopy*. ACS Nano 10 (5), pp. 4981-4988, 2016

[2] L. Rima. *Visual proteomics by AFM*. Master project work (Nanoscience curriculum), 2016

[3] B. A. Bircher, R. Krenger and T. Braun. *Automated high-throughput viscosity and density sensor using nanomechanical resonators*, Sensor Actuat B-chem. 223 (C), pp. 784–90, 2016

[4] C. Ramakrishnan et al. *openBEB: open biological experiment browser for correlative measurements*. BMC Bioinformatics, pp. 15-84, 2014

[5] O. Fiehn, *Mass-spectrometry-based meta-bolomics: limitations and recommendations for future progress with particular focus on nutrition research*. Metabolomics, 5, pp. 435–458, 2009

Towards biomimetic omniphobic polymer surfaces by combining hierarchical surface patterns and chemical surface modification

Project A10.07 RepAll (FHNW, PSI, Cellpack AG Packaging, Villmergen)
Project Leader: S. Neuhaus
Collaborators: M. Grob, P. M. Kristiansen, J. Schmidli, M. Voclova, R. Kirchner, C. Padeste, and A. Cousins

Introduction

Duck feathers, lotus leaves and the Salvinia plant serve as examples from nature for extremely hydrophobic surfaces. Their outstanding properties often arise from the combination of hierarchical surface structuring and optimized surface chemistry. Apart from water, omniphobic surfaces also repel numerous other liquids [1] and are of great interest for industrial applications. In this project we combine the possibilities of greyscale electron beam lithography (EBL) prototyping, roll-to-roll (R2R) replication and chemical surface modification strategies to mimic surfaces inspired by nature. Moreover, simple wire meshes were used as stamps to produce intricately structured surfaces with high water repellency.

Multilevel/hierarchical structures made by EBL

The reduction of the solid fraction in contact with a liquid leads to a contact angle (CA) increase due to the so-called Cassie-Baxter (CB) state (Fig. 1).

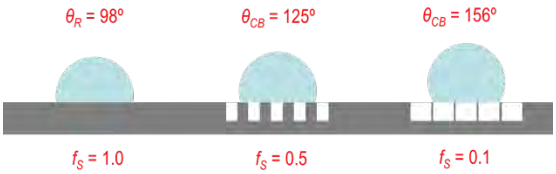

Fig. 1 Effect of reduction of the fraction of solid surface f_S on the water contact angle on a polyolefin surface. The contact angles θ_{CB} were calculated based on the contact angle θ_R of a smooth reference surface.

Patterns were realized by EBL in a hybrid organic-inorganic spin-on-glass. This material can be directly used as mold for hot embossing of polymer foils with high melting (polytetrafluoroethylene PTFE) or glass transition temperatures (polyetherimide PEI). These foils can subsequently be used as stamps for replication of the original patterns into polymer films with lower melting temperatures such as polyolefins by hot embossing. CA above 130° were achieved with multilevel patterns (Fig. 2, Tab. 1) [2]. The hydrophobicity of PTFE was increased by the same hierarchical pattern. Even higher CAs were obtained by further decreasing the solid surface fraction. To achieve a uniform distribution of solid and air regions, a hexagonal array of filled or hollow pillars was prepared (Fig. 3). Additional nano-patterns on top of the pillar were introduced to enhance liquid pinning [3, 4]. However, no significant differences were observed (Tab. 1).

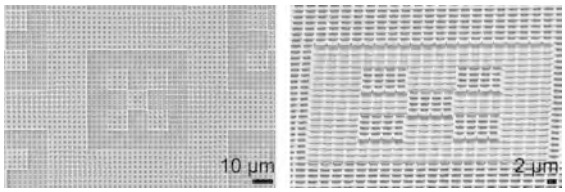

Fig. 2 Hierarchical grid pattern directly replicated from the spin-on-glass into an industrial packaging polyolefin by hot embossing.

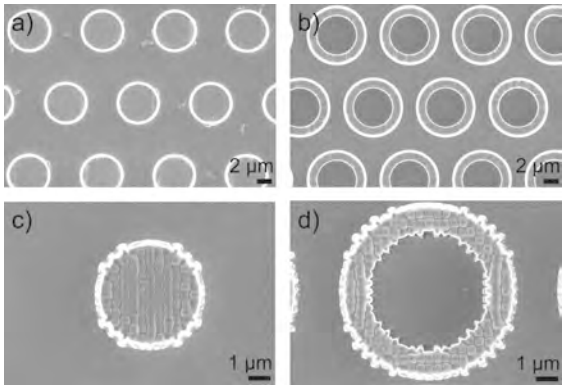

Fig. 3 Binary (a-b) and hierarchical (c-d) test patterns with f_s=0.2, replicated into polydimethylsiloxane (PDMS) used as pattern transfer material for further replication.

*Table 1 Comparison of CA of non-patterned surface (θ_R), patterned surface (θ_{CB}), theoretically expected value (θ_T) for hierarchical grid pattern and open pillars with (w) and without (wo) nano patterns. m = multilevel, p = pillar, *: at stability limit of CB state.*

Solid fraction f_s	Film material	θ_R[°]	θ_{CB}[°] wo	w	θ_T[°]
0.70 m	PTFE	105	128	-	119
0.70 m	Polyolefin	96	112	-	112
0.30 m	Polyolefin	96	132	-	137
0.20 p	PDMS	95	110	106	145
0.15 p	PDMS	95	122	110	150
0.10 p	PDMS	95	144	144	155
0.05 p	PDMS	95	149*	90	163

Using wire meshes as stamps for embossing

Interestingly, strongly repelling surfaces have also been achieved by hot embossing of LDPE with steel wire meshes [5]. We adapted this approach by using

special wire mesh grids for structuring of polyolefins. Strongly repelling topographies resulted in a CB wetting state with substantially augmented contact angles for various liquids [6-7]. An additional structure level was added to the wire meshes by nanosecond laser treatment, which resulted in regularly spaced corrugations on top of individual threads as illustrated in Fig. 4.

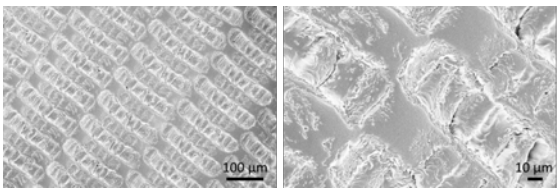

Fig. 4 SEM images of structured polyolefin films produced by R2R replication of laser treated wire mesh stamps. The additional corrugations on the threads were replicated as clearly seen in the close up.

R2R replication of EBL and wire mesh stamps

Wire meshes (both as received and modified by laser) and EBL replica stamps in PEI and PTFE (cf. Fig. 2) were replicated by R2R. The embossing temperature and pressure were varied in order to optimize the replicated structures with regard to high static CA and low roll off angles (ROA) (Fig. 5). Static CAs can be substantially increased by hot embossing, however, a smaller increase in CA was observed when using R2R. Interestingly, laser treatment of the wire mesh resulted in clearly improved CA in R2R. However, structuring of the foils invariably coincided with an increase in ROAs, and the highest static CAs were observed on samples with highest ROAs. A sufficient replication quality could not be obtained for the soft EBL stamps so far.

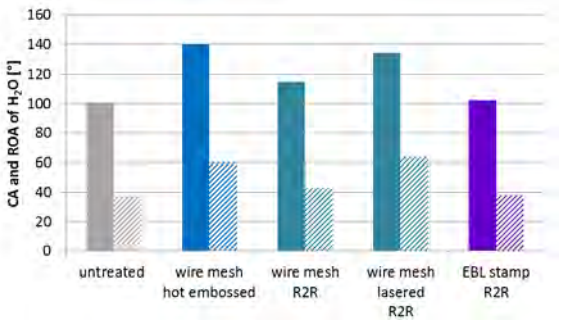

Fig. 5 Water CA (filled bars) and roll off angles (hatched bars) measured on flat (untreated) polyolefin foils and on structured foils prepared by hot embossing (90°C/200 bar) and roll embossing with wire meshes and EBL stamps (94°C/450 N and 94°C/300 N, respectively).

Chemical modification

Improvement of the dewetting characteristics of polyolefins proved to be difficult by means of e-grafting modification. In order to increase the hydrophobicity of the surface with an intrinsic CA of about 100°, grafting of silicones or aliphatic molecules was tested as fluoropolymers are undesirable in food packaging materials. However, the effects obtained did not lead to a significant improvement of the repelling and roll-off characteristics.
In an alternative approach, argon plasma treatment of polyolefin foils was followed by immersion of the samples in water in order to increase the yield of surface hydroxyl groups. These groups were used as anchor points for the polycondensation reaction of a silane in order to produce "liquid-like" surfaces as shown in [8] for glass substrates. Stable polysiloxane coatings were successfully obtained as proven by ATR-IR spectroscopy. The coating increased the water CA by 15°, but more importantly, it caused a very substantial increase of the oil CA. ROAs were 15° for water and 10° for oil, corresponding to a strong improvement of roll-off characteristics compared to the untreated foil (Fig. 6).

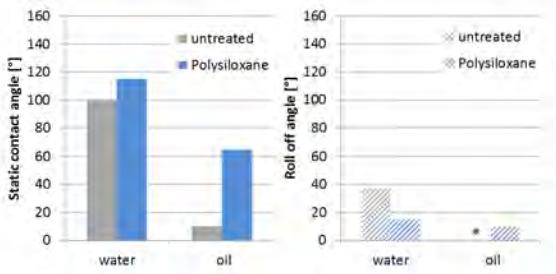

*Fig. 6 Static CAs and ROAs of water and oil on untreated and polysiloxane modified polyolefin surfaces. *Oil completely wets the untreated surface and the ROA could not be determined.*

Conclusions and outlook

It appears that the road towards industrial (super)omniphobic surfaces is a really difficult one. High CAs can be obtained by structuring, but are usually inseparable from high ROAs. An all-purpose solution is therefore probably not available on a (pre-)industrial scale, and truly superomniphobic surfaces (CA > 150°, ROA < 5°) seem to be out of reach for industrial products.
The EBL structures investigated are very promising but pose significant challenges for replication due to their delicacy. Improved results are expected if the R2R setup is optimized and the process is pushed to its limits. On the other hand, replication of simple wire meshes by hot or R2R embossing resulted in very good water repellency. A lot of effort also went into the demanding development of a suitable chemical surface modification strategy. Using our novel modification protocol, improved CAs and in particular, substantially lowered ROAs were obtained. Combination of R2R replication of wire meshes with surface chemical modification will be carried out in the near future to wrap up the project.

References

[1] A.K. Kota et al., *MRS Bulletin* 38 (2013), 383
[2] R. Kirchner, S. Neuhaus, P.M. Kristiansen, H. Schift, *Proc. 42nd Int. Conf. on Micro and Nano Engineering*, Wien, Sept 19.-23., 2016
[3] H.S. Grewal et al., *Soft Matter* (2016), 12, 859
[4] R. Hensel et al., *Langmuir* 29 (2013), 1100
[5] E. Bormashenko et al., *Appl. Surf. Sci.* 270 (2013), 98
[6] J. Schmidli, M. Grob, A. Stumpp, P.M. Kristiansen, S. Neuhaus, *3rd Polymer Repliation on Nanoscale*, Windisch, May 19-20, 2016
[7] P.M. Kristiansen, J. Köser, J. Schmidli, C. Rytka, S. Neuhaus, H. Schift, J. Gobrecht, i-*net Innovation Landscape Nano Event*, Muttenz, Sept. 9, 2015
[8] L.M. Wang et al., *Ang. Chem.- Int. Ed.* (2016), 55 (1), 244

Atomic-scale analysis of the SiC/Oxide interface to improve high-power MOSFET devices

Project A10.08 Atolys (University of Basel, PSI, ABB Switzerland Ltd, Baden-Dättwil)
Project Leader: S. Goedecker
Collaborators: S. Gerstl, E. Mueller, T. Jung, J. Lehmann, H. Bartolf, and G. Alfieri

Introduction

SiC provides a well-suited material for high-energy efficiency, high power and high temperature device applications compared to Si. SiC power-MOSFETs, however, are so far compromised by low channel mobilities and threshold voltage instabilities due to the inferior quality of the SiC in proximity to the semiconductor/oxide interface [1]. In the thermal oxidation of SiC, higher defect densities occur near the gate insulator/semiconductor interface and also in the oxide region. These defects originate from the more complex nature of the oxidation process which requires diffusive removal of carbon atoms in the form of CO and CO_2 from the crystalline SiC bottom substrate. Each defect contributes differently to the interface state densities (D_{IT}). Dangling bonds contribute in the magnitude of ~10^{11} eV^{-1} cm^{-2}, carbon clusters around ~10^{12} eV^{-1} cm^{-2} [2]. This sums up the interface state density to 10^{12}-10^{13} eV^{-1} cm^{-2} near the conduction band edge (E_C), roughly two orders of magnitude larger than for Si. Several origins for NITs have been suggested. Carbon clusters, such as carbon dimers, or graphitic microcrystals can also act as NITs [3]. Independent of the nature of the defects, these act as traps for carriers with a certain lifetime and thereby affect the electronic property of the semiconductor [4]. Alternative processes / materials like hybrid oxides or high k dielectrics may reduce the density of traps at the SiC/SiO_2 interface. This project, however, aims at improving the affordable thermal oxidation process and later also at comparing it to the deposition of oxides, e.g., by ALD. Post-oxidation annealing in nitric oxide significantly improves the SiC MOS performance [5] but the reason is still unknown. It remains a pestering issue to avoid the defects and to identify the most relevant defects for degrading the performance of the SiC MOS.
In this project, our region of interest (ROI) is the 3 to 5 nm thick region above the SiC/oxide interface which affects the channel mobility the most. The defects here shall be simulated 'in silico' and compared to our experimental results. For this purpose, thin specimens (30 nm thick) were produced by Focused Ion Beam (FIB) with specific dimensions for Transmission Electron Microscopy (TEM) and Local Electrode Atom Probe (LEAP) analysis. In order to gain knowledge about the chemical bonding of the atoms in the interface region Raman spectroscopy was used.

Interface defect – Simulations

Theoretical studies of the SiC-SiO2 interface containing defects and its structural evolution during the oxidation process were performed using minima hopping method (MHM) simulations. The framework involves a fast method for calculating the energy, force, stress etc. (Density Functional Tight Binding scheme), density functional schemes like modified Becke-Johnson exchange potential in combination with L(S)DA correlation, conformational and transition path sampling methods. Here we have explored different configurations of 4H-SiC in different environments such as oxygen, nitric oxide (NO) and nitrous oxide (N2O). During oxidation, we have observed that carbon silicon chains, which consist of carbon rings and carbon silicon rings appear at the interface of SiO2/4H-SiC (Fig. 1). It is also observed that these chains are stable only near the interface. By simulating the N2O and NO passivation, we have observed that N2, CO, C-N compounds, SiO2 and carbon clusters form at the interface (Fig. 1b, c). These findings provide novel insight into the structural and electronic properties of the realistic SiO2/SiC interface.

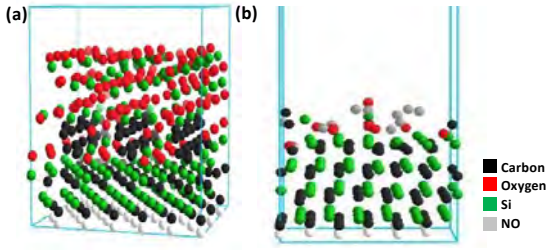

Fig. 1 a) low energy intermediate structures formed by oxidation of SiC; 5C and 6C-chains can be identified at the interface b) During NO passivation C-N compounds form at the interface.

Experimental study: Microscopic analysis

We compare SiC/SiO_2 interfaces of 'TGO' (N_2O based gate-oxide formation [6]) and 'DRY' (dry O_2 based) oxidation processes. First LEAP pillars were prepared and investigated: The interface is wide, ~4 nm thick and the stoichiometry is gradual, not changing abruptly. Thereby defects in the channel region are expected.
In parallel to the first successful LEAP results, we also investigated the morphology of the interface using Atomic Force Microscopy (AFM), after stripping the 50 nm thick oxides by HF etching to

uncover the SiC underneath. The AFM investigations (Fig.2a to 2d) show that the TGO process creates a smoother interface (Roughness R_{max} =1.3 nm) as compared to the DRY (R_{max} = 7 nm) (Fig. 1a). The lower interface-roughness might be the reason for the improved MOS performance of the TGO devices as confirmed by our electrical (C-V) measurements. The process of removing the oxide was explored with time dependent etching and its influence on the interface morphology has been discussed in figure 2.

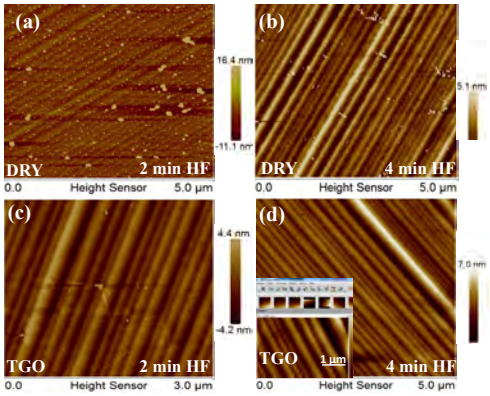

Fig. 2 a), b) The morphology of the dry sample changes by the exposure to HF. After 2 minutes etch residues line up at steps like a necklace, after 4 minutes significantly fewer residues, some of them clustered in regions persist. c), d) The morphology of the TGO sample does not show a significant modification by HF etching, either after 2 min as well as after 4 min of exposure.

The AFM results made us more curious about the chemical bonds at the interface and their modification by the oxide etch. Raman spectroscopy, a well-established technique, is capable of discerning even slight changes in the bonding structure making it a valuable tool in the characterization of, also carbon, defects. Our initial results provide conforming evidence about the presence of non-SiC, i.e. defective carbon in the interfacial region. By in-depth analysis we found for the first time that the binding state of the carbon atoms in the near-oxide region and as minor inclusions in the oxide is different from the 'bulk' (Fig. 2). These unprecedented results agree well with both AFM/etching and theory.

Carbon-related Raman peaks were observed for both TGO and DRY samples but with different intensity. The latter contain more detectable carbon defects than the former as indicated by the intensity difference. An explanation might be provided by the TGO/passivation process diffusively penetrating the oxide and the below interface region with N. By this exposure N or NO species either bind to or substitute with some of the C defects. This chemical passivation mechanism leads to a significant reduction of the electronically active defect sites as reported in the literature and confirmed by our own transport data. We plan more direct structural investigations by STEM.

Our most recent STEM results of DRY samples revealed the presence of nanocrystals in the amorphous oxide, possibly related to C clusters as evidenced above. Further LEAP analysis is currently in progress i) to improve the data acquisition in view of the difficult-to-map SiC/SiO2 interface and ii) in order to improve the reconstruction parameter sets. Visible Raman has been taken up as it is 50-230 times more sensitive to sp_2 sites. Visible photons preferentially excite C related Π-states, which exhibit a strong spectroscopic signature due to their polarizability and delocalization. Hence Raman, in particular tip enhanced Raman (TERS) potentially provide unique evidence for the undesired carbon at and in the interface. It is a major achievement that LEAP data and theory are now complemented and confirmed by Raman and initial STEM data. All experiments agree well with the numerical simulations.

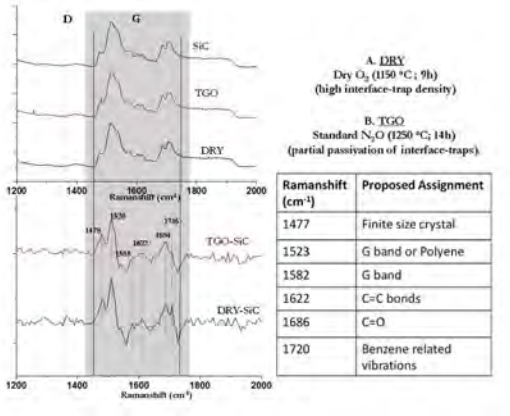

Ramanshift (cm^{-1})	Proposed Assignment
1477	Finite size crystal
1523	G band or Polyene
1582	G band
1622	C=C bonds
1686	C=O
1720	Benzene related vibrations

Fig. 3 Second order Raman spectra of oxide stripped SiO2/SiC interfaces grown by the two investigated processes (TGO and DRY). The secondary peaks of SiC tend to mask the unwanted carbon peaks: D (defect peak) and G (graphitic peak) are shown in top panel; Identification of the carbon peaks based on literature values (table). Remarkably, and characteristic differences occur in the Raman spectra of near oxide carbon. For visibility and quantification, difference spectra after subtracting the SiC reference have been calculated and analyzed (table in fig. 3).

Following up on the successful initial results we aim at providing an unprecedented in-depth analysis using Raman and STEM along with LEAP to prove the presence of unwanted and here theoretically evidenced carbon clusters at the interface for different oxides (thermally and deposited). Along with the theoretical input we expect to reach further in depth conclusions on the defect types, as well as their relative occurrence and impact on the electronic MOS-interface performance, in particular relation to the reduced carrier mobility as observed in also our transport measurements.

References

[1] Liu et al., *Applied Physics Reviews*, 2 (2015)
[2] Chang et al., *Applied Physics Letters*, 77 (2000)
[3] Constant et al., *Applied Physics Letters*, 94 (2009)
[4] Lohrmann et. al., *Applied Physics Letters*, 108 (2016)
[5] Gavrikov et al., *Journal of Applied Physics*, 104 (2008)
[6] A. I. Mikhaylov et al., *Materials Science Forum*, 821-823 (2015) 508-511

Antibacterial nanostructures mimicking cicada wings for consumer products (Nano-Cicada Wing)

Project A10.10 Nano-Cicada-Wing (University of Basel, FHNW, DMS Nutritional Products Ltd., Kaiseraugst)
Project Leader: E. Meyer
Collaborators: M. Kisiel, Th. Glatzel, M. Waser, J. Köser, Y. Grether, and H. Hug

Project overview

Recently the antimicrobial activity of biological and biomimetic nanostructured surfaces has gained large interest [1]. Such surfaces are of great interest since due to the absence of chemical biocides their application currently does not require special regulatory steps. While structured surfaces of certain insect wings and structured nanomaterials like graphene or black silicone exhibit bactericidal activity other mimicking surfaces lack this effect but show reduced adhesion of different bacterial strains [2, 3]. Within the Nano Cicada Wing project, we try to mimic antibacterial insect wing surfaces by means of nanostructured and chemically modified polymer surfaces. We combine plasma exposure polymer surface (PEEK, polystyrene (PS), polycarbonate (PC)) structuration, chemical functionalization and antimicrobial activity assays with Fluorescence Microscopy, Scanning Electron Microscopy (SEM) and Atomic Force Microscopy (AFM).

Generation of nanostructured polymer surfaces and quantification of bacterial adhesion

Nanostructured polycarbonate and PEEK surfaces were generated by low energy plasma etching. Typical structures obtained by this procedure are shown in figure 1. The height of the produced pillars and distance between them strongly depend on plasma power, exposure time and plasma composition. The effect of plasma condition was investigated to obtain optimally structured polymers. We have found that the increase of the exposure time results in increased length of the pillars, which as the plasma exposure goes on, stick together due to pillars softening and electrostatic attraction between them.

When bacteria in liquid came in contact with nanostructured PC surfaces they survived to a similar extend like on unstructured reference polymer surfaces. However, the number of adhering bacteria was reduced and was investigated quantitatively by the alamar blue assay, which quantifies cells by detecting their metabolic activity.

The adhesion of *E.coli* on nanostructured polycarbonate was reduced by 60% as compared to unstructured polymer (Fig. 2, left). Future studies will have to investigate the generality of this adhesion reducing effect for other nanostructured polymer surfaces.

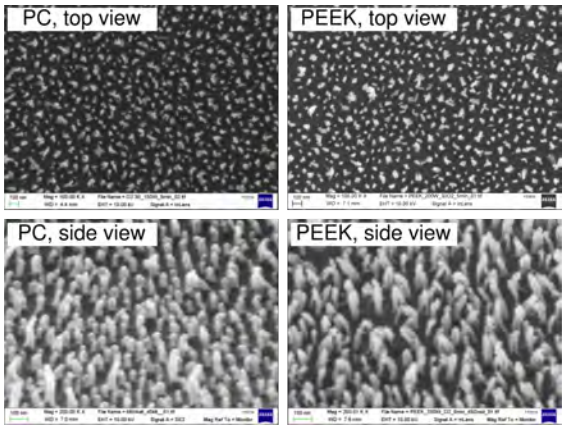

Fig. 1 Comparison of nanostructured PC and PEEK. Please note the different magnifications of top view images and side view images.

In the next step nanostructured polycarbonate surfaces were chemically modified to investigate a possible cooperative biocidal effect between the nanostructured surfaces and chemical surface properties. First, structured PC was modified with hydrophobic octadecyltriethoxysilane to mimick the hydrophobic insect wings. No increased bacterial death could be detected and the number of adherent bacteria on silanized structured samples exceeded the numbers on silanized flat PC surfaces (Fig. 2, left). Finally, structured PC surfaces were modified with 0.1 % polyethyleneimine (PEI) since certain cationic polyelectrolytes have been reported to weaken and/or destroy the bacterial cell membrane. Dead/live staining could not detect an increased ratio of dead:live cells. The adhesion was the same on PEI modified structured and flat surfaces (Fig. 2, left), however the overall bacterial adhesion on all PEI coated surfaces was drastically increased (Fig. 2, right) due to the interaction of the PEI-modified surface with the negatively charged bacteria.

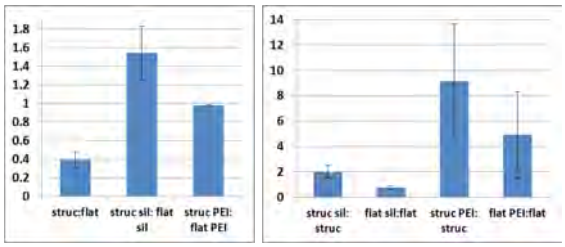

Fig. 2 Relative bacterial adhesion on different chemical modified and/or structured surfaces as quantified by the metabolic alamar blue assay.

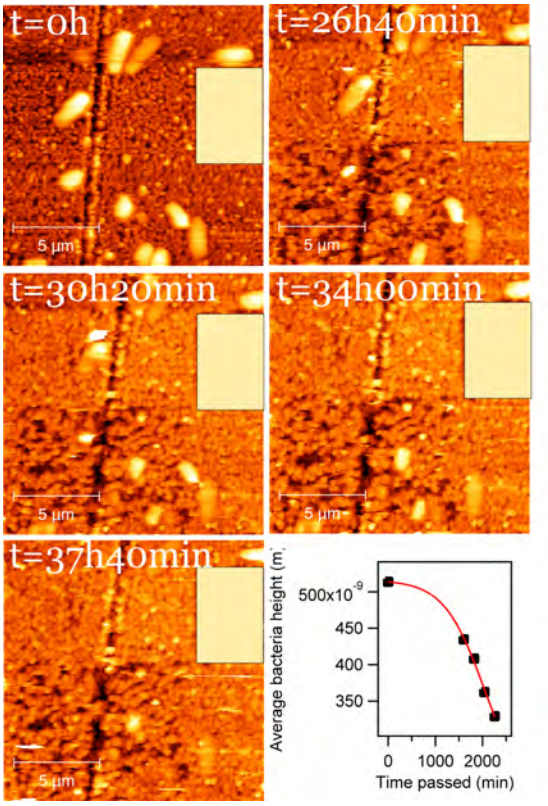

Fig. 3 Time sequenced AFM images of E. coli bacteria situated onto gold-coated PEEK surface. Scan area equals 15µm-15µm. The yellow rectangle marks the same position on the sample surface. The apparent bacterial height decreased by a factor of 2 after 2500 minutes of measurement.

AFM-based biomechanical characterization of *E. coli* bacteria under liquid environment

While most of the experiments reported in literature, operate under ex-situ conditions we perform AFM measurements in aqueous environment in order to observe the mechanical rapture or the reduced adhesion of the living cells. The liquid AFM results showed that only a small fraction (about 5%) of bacteria are killed by a native structured polymer PEEK surface. The killing rate is enhanced on gold-coated PEEK surface. Figure 3 shows that bacterial membranes are getting destroyed by the structure. The whole process, however, is relatively long and we relate it to bacteria starvation due to lack of resources.

In order to perform the adhesion measurements, we have used CytoSurge Fluid-AFM from Nanosurf furnished with microfluidic cantilever. This solution allows measuring adhesion forces between single *E. coli* bacteria positioned at the tip apex and the flat and structured polycarbonate surface (Fig. 4).

In full agreement with fluorescent microscopy results (Fig. 2, left), the AFM measurements reported 60% adhesion reduction on structured polycarbonate as compared to flat surface. Due to surface roughness the force curve obtained on the structured polycarbonate is extended over the tip-sample distance, as shown in figure 4.

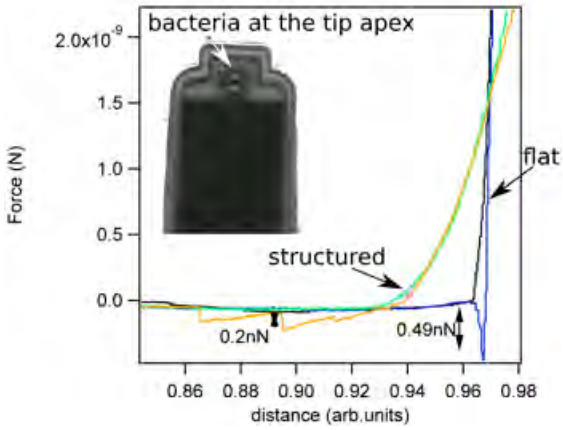

Fig. 4 Adhesion forces for E. coli cell envelope measured on flat and plasma structured polycarbonate surface. Adhesion forces are reduced by factor 2.5 on structured areas. Inset shows cantilever with microfluidic channel and single, intact E. coli bacteria attached to the very end of the tip.

References

[1] Ivanova, E.P., Hasan, J., Webb, H.K., Truong, V.K., Watson, G.S., Watson, J.A., Baulin, V.A., Pogodin, S., Wang, J.Y., Tobin, M.J., Löbbe, C., Crawford, R.J., *Natural bactericidal surfaces: mechanical rupture of Pseudomonas aeru-ginosa cells by cicada wings.* Small 2012, 8, 2489-94

[2] Ivanova, E.P., Hasan, J., Webb, H.K., Gervinskas, G., Juodkazis, S., Truong, V.K., Wu, A.H., Lamb, R.N., Baulin, V.A., Watson, G. S., Watson, J.A., Mainwaring, D.E., Crawford, R.J., *Bactericidal activity of black silicon.* Nat Commun 2013, 4, 28

[3] L. Jin, W. Guo, P. Xue, H. Gao, M. Zhao, C. Zheng, Y. Zhang and D. Han, *Quantitative assay for the colonization ability of heterogeneous bacteria on controlled nanopillar structures.* Nanotechnology 2015, 26, 055702

Micro-optics with ultra-smooth surfaces

Project A10.13 SurfFlow (PSI, FHNW, Heptagon Advanced Micro Optics, Rüschlikon)
Project Leader: H. Schift
Collaborators: S. Neuhaus, M. Altana, N. Chidambaram, and R. Kirchner

The challenges of 3D lithography

Polymer microlenses are used in various devices, including smartphones. Since they are so small (from a few mm to 50 µm diameter) they have to be processed using novel 3D lithographic methods that build the lenses out of thin layers (e.g. grayscale electron or laser writing). These structures are then used as master structures for further replication, i.e., a generation of many identical copies by molding. For refractive micro-optical elements direct write laser-lithography (DWL) with single photon absorption (1PP) (Fig. 1a) is the preferred choice for mastering. By modulation of the dose, different levels can be fabricated in a photosensitive polymer film. However, this process is not applicable for microlenses with high structures and deep central sags surrounded by high aspect ratio tips between adjacent lenses in array configuration (Fig. 2). We have therefore used two-photon polymerization (2PP) DWL (Fig. 1b), a novel technique with a high degree of freedom for complex designs. During this process, the focus (so-called voxel) with 200 × 200 × 600 nm³ is moved through the viscous material called IpDip, a negative resist. The trajectories and layering during the direct writing process often results in roughness in the range of the writing increment (i.e., 100 - 200 nm), which has adverse effects for optical applications. Typically, sub-20 nm roughness is needed for transmission with low stray light.

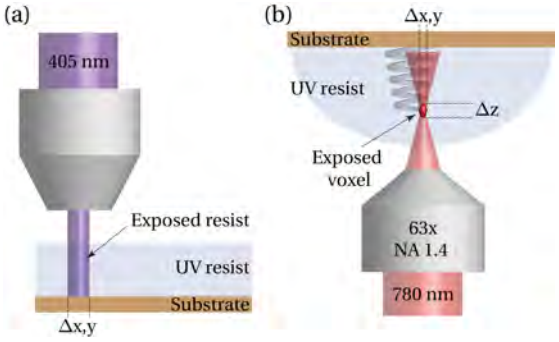

Fig. 1 Direct write laser lithography (DWL) with a) single-photon (1PP) and b) two-photon polymerization (2PP). While in 1PP the laser light is absorbed in the entire film, in 2PP the laser intensity is only high enough to cause polymerization in a voxel which is scanned through the photosensitive material.

Optically smooth surfaces

In the SurfFlow project, we addressed the problem of surface roughness in micro-optical components produced with 3D lithography. We decided to develop a novel technique, which smoothens out surface roughness without losing the shape and structural details of the master structure. Such a post-processing method enables us to write the master structures without employing time-consuming writing strategies for smaller surface roughness; and we chose instead a technique which modifies the polymer only in the top skin layer and thus increases its ability to flow during heating.

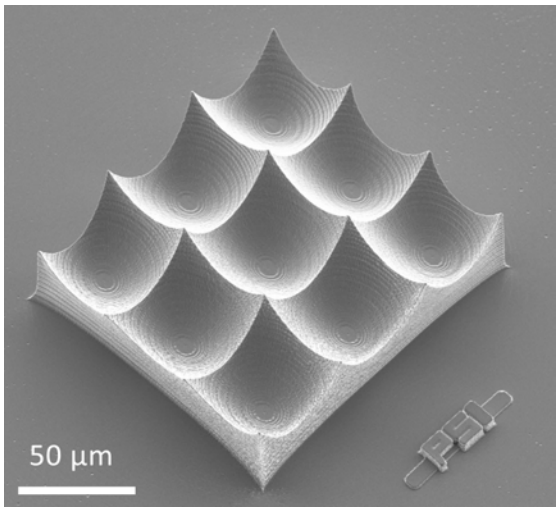

Fig. 2 SEM micrograph of a 3×3 microlens array (50 µm × 50 µm each) with 40 µm deep sag: Master structures were fabricated using 2PP-DWL in IpDip.

Other methods to smoothen out this unacceptable roughness often result in either loss of structural fidelity or in extreme writing times.

Tuning material contrast by UV-exposure

Exposure to electrons, photons of different wavelength and ions is well known to modify polymers by cutting polymer chains and thus reducing their molecular weight M_w. This is for example used for grayscale electron beam lithography, to obtain 3D topographies by direct writing depending on the applied irradiation dose, because a polymer with different M_w can be dissolved at different rates. Such exposed polymers have proven to enable selective thermal reflow as well, because not only the M_w, but also the glass transition temperature T_g is reduced upon exposure. The process works particularly well for thermoplastic polymers such as PMMA (poly methyl methacrylate) [1]. At T_g, which is typically around 100 to 120 °C, the polymer changes from a solid state to a viscous-elastic and finally viscous liquid. The reduced T_g of exposed polymers allows for reflow at temperatures below the original T_g. Therefore, the exposed polymer can selectively be affected by thermal treatment. A selective, locally confined reflow is the basis of surface smoothening of the so-called TASTE process. This self-optimizing process is governed by surface tension and

generates smooth 3D shapes with nanometer roughness. The specific novelty of the method is not only the coincidence of reducing T_g by exposure and surface confined selective thermal reflow but also the ability to tune it towards the equilibration of surface undulations typically obtained with 2PP-DWL. For surface confined absorption 172 nm Vacuum UV light proved to be ideally suited because large areas can be exposed in ambient. Through in-depth analysis of the polymer absorption and reduction in M_w upon exposure we were able to reduce the T_g of PMMA within a small, confined region on the material surface of around 400 nm.

Hot embossing with soft stamps

The smoothing process, however, is not directly applicable to the UV-cured IpDip material. A two-step replication process chain was developed for a micro-lens array structure with deep 3D reliefs and sharp features enabling the transfer of the photo-cured acrylic resist patterns into PMMA with the same structural polarity via an intermediate stamp (Fig. 3). By using UV-curable PDMS (poly dimethyl siloxane), high fidelity negatives were cast from the original microstructures made by 2PP and subsequently replicated into PMMA using thermal imprint. The mechanical properties of the new UV-PDMS (X-34-4184, Shin-Etsu Chemical Company Ltd.), along with its nearly zero process shrinkage proved to be highly suitable to replicate both 50 µm high concave features and sharp tips with an apex diameter of 500 nm. The results prove that silicone rubber, despite its elasticity, has specific advantages in thermal imprint in structures where both tall microstructures and sub-micron surface structures have to be replicated. This way, high fidelity PMMA structures with low defects could be prepared by the optimized processing found in this work to have a replication of 3D masters for further up-scaling [2].

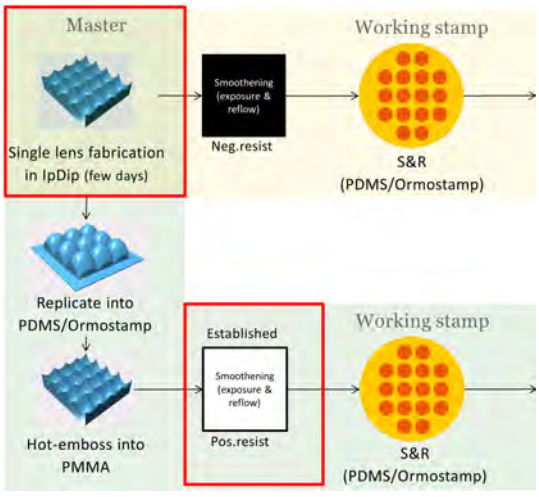

Fig. 3 Process routes for replication of micro-lenses, fabricated by 2PP-DWL in negative resist (IpDip). Only the copying into a thermoplastic material enables the use of the TASTE process in a post-exposure thermal reflow. The optical elements can then be used for further up-scaling into a working tool by step&repeat imprint.

Smoothening of lenses with 3D topographies

By selecting the appropriate annealing temperature only slightly lower than the original T_g (at around 90°C) we achieved an exclusive softening of the confinement region. Thus the roughness of the original structure (Fig. 4a) could be entirely removed while structural details were preserved (Fig. 4b). This was proven by optical measure-ment of a large area microlens array, too.

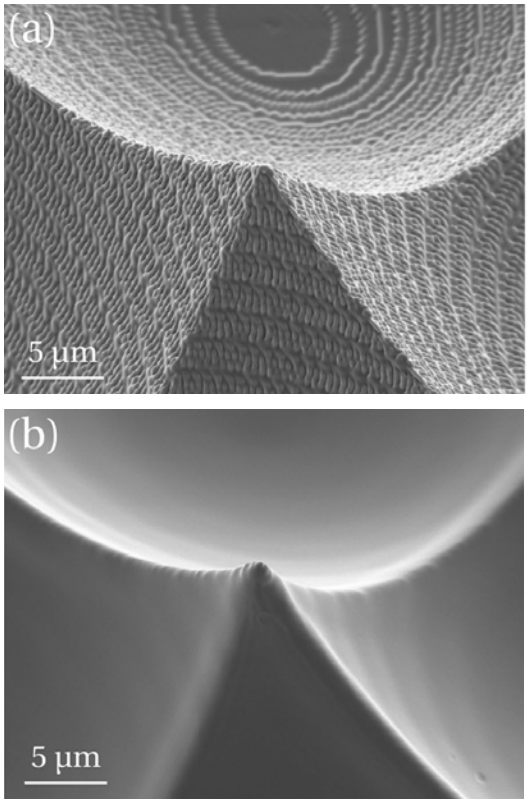

Fig. 4 SEM micrograph of a high aspect ratio tip constituting the intersection between adjacent lenses. Only with surface selective modification of the polymer, roughness of the master structure (top) in the range of 100 nm can be smoothed out while structural details in the sub-µm range are preserved (bottom).

Within the SurfFlow project, we transformed the original TASTE process with its lithographically controlled modification to complex structures which had an intrinsic roughness over the entire surface, including concave sags and high aspect ratio tips. Using selective post-processing is therefore a good way to significantly reduce the roughness of micro-optics below typical values proposed by optical industry, i.e. 20 nm.

References

[1] A. Schleunitz, V.A. Guzenko, M. Messer-schmidt, H. Atasoy, R. Kirchner, and H. Schift, *Novel 3D micro- and nanofabrication method using thermally activated selective topography equilibration (TASTE) of polymers*, Nano Convergence 1:7 (2014)

[2] N. Chidambaram, R. Kirchner, M. Altana, and H. Schift, *High fidelity 3D thermal nano-imprint with UV curable polydimethyl siloxane stamps*, J. Vac. Sci. Technol. B 34, 06K401 (2016)

CerInk: Biomimetic ceramic scaffolds with density gradient fabricated by Binder-into-Bed 3D-printing and ceramic NanoInk

Project A11.01 CerInk (FHNW, PSI, Medicoat AG, Mägenwil)
Project Leader: A.M. Rohner
Collaborators: R. Schumacher, N. Matter, A. Testino, A. Carino, and P. Gruner

Introduction

3D printing of bioceramics as artificial bone and as patient specific substitute for hard tissue has been a challenge throughout the last years. Although much scientific work was invested towards commercial products of these highly bioactive materials, only a few ended up in market readiness, mainly due to concerns of sufficient mechanical stability.

A substantial know-how for powder-bed based 3D-printing of calcium phosphate bioceramics was established at the FHNW during the past several years and throughout several industrial and public funded projects. The ability to build up biomimetic hydroxyapatite scaffolds by 3D-printing was first shown in 2008 along with an industry founded project. Mechanical properties were further improved by either biopolymeric infiltration or throughout modifying sinter properties of the bulk material [1, 2]. In the same year, we could demonstrate that the presence of a small amount of locally added nano hydroxyapatite (HA) particles increases the sinter activity of bulk HA in each layer, resulting in a local significantly higher density as shown in figure 1.

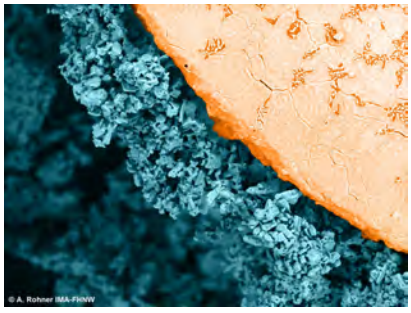

Fig. 1 Interface between standard 3D-printed HA bulk material resulting in porous structures (gray) and a section with additional nano HA particles leading to a massive densification (orange).

The CerInk project addresses this challenge with a modified Binder-into-Bed (BiB) 3D-printing system which allows a straight forward fabrication of both, mechanical stable and bioactive ceramic scaffolds. In collaboration with nanoparticles experts at PSI, we investigate and develop a novel HA ceramic NanoInk to be used within a binder-into-bed 3D-printing system, which will lead to significantly increased densification of 'green' parts due to drastic improved sintering conditions (Fig. 2). Both, the 3D-printing system as well as this NanoInk are designed to enable a selective deposition of nano HA particles within each HA build layer, allowing a direct control of density gradient in the final product. This new printing approach offers unprecedented opportunities for miming natural bone structures by adding more NanoInk in areas with cortical bone properties, causing a local densification of the material, or less NanoInk for cancellous and less dense areas.

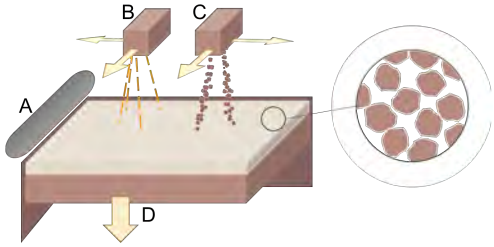

Fig. 2 Binder-into-Bed (BiB) 3D-printing using NanoInk. (A) Bulk ceramic HA powder layer deposition unit; (B) Printhead with binder; (C) Printhead with ceramic NanoInk; (D) steadily lowering building platform with bioceramic HA bulk powder-bed (particle size 25 µm)

Ink preparation and testing

Nano powders were produced either by milling down HA powder from Medicoat or by synthesise HA combined with the segmented flow tubular reactor (SFTR) [3] at the PSI. The produced nano particles (in the range 20-100 nm) were then mixed with different water and organic based solvents. To develop printable inks some specific rheological parameters [4] (Ohnesorge number & Reynolds number) should be achieved. High viscous inks or inks with low surface tension end up in insufficient drop formation and therefore in unsuccessful printing results. The NanoInks contain a nano HA solid load of 10-39 %, a viscosity of 8.13-102 mPa*s and a surface tension in the range from 46.0-57.2 mN/m. Some of the produced inks could not be printed because of a high sedimentation rate. This is partially related to a high solid load or the thixotropic flow characteristic, which could not be handled with the printhead used on our system. The sedimentation led to clogging of the printhead membrane (Fig. 3, left). However, an ink with a solid load of 20 wt.% could be used for printing of up to 70 layers until the membrane was clogged.

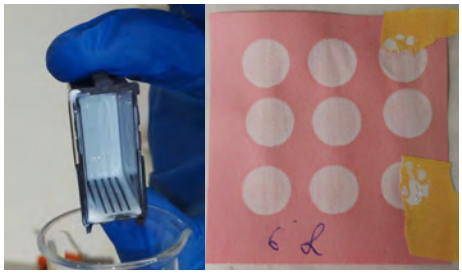

Fig. 3 HP printhead with sedimented nano HA particles on top of the printhead membrane (left). Printed NanoInk no. 1 on paper after 6 layers (right).

Since ink jet printing droplets are produced in a relatively short timeframe, the ink dynamic surface tension – measured with a bubble pressure tensiometer – needs to be evaluated with respect to the surface age (Fig. 4). The surface tension is rather high in the very beginning (<0.2 s) and it reaches a plateau value after about 2 s. This dynamic behaviour can be strongly influenced by adding surfactants. All formulated inks show a higher surface tension compared to the ink produced by Hewlett Packard. Nevertheless, some of the NanoInks show good printability.

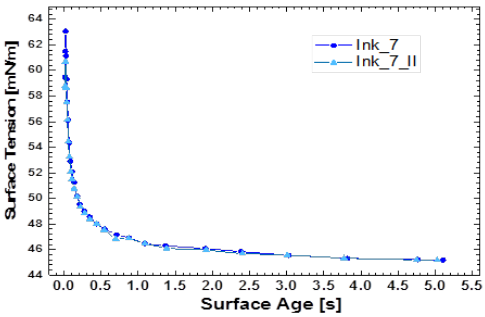

Fig. 4 Dynamic surface tension measurement of ink 7.

Surface interaction between bulk and ink

Preliminary tests on the surface interaction between the evaluated bulk material and various NanoInks was initially tested at PSI by using HA pellets. HA powders were mixed with an appropriate amount of cellulose and pressed with 5 tons to get a solid non-breakable 10 mm pellet. A volume of 100 µL NanoInk was deposited in a defined area of the pellets. Ceramic bodies with porosity and mechanical properties similar to the BiB printed samples were obtained after burnout of the cellulose in a static oven at different temperatures.

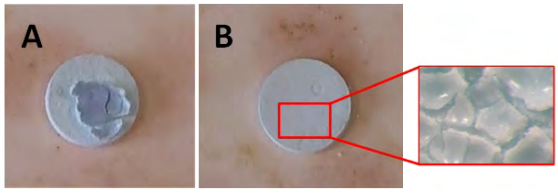

*Fig. 5 100 µL of HA inks were deposited on HA pellets and sintered at 1350 °C for 1 h on green part. **A)** Micro-sized ink (~25 µm) and **B)** Nano-sized ink (~50 nm)*

This procedure was required in order to easily produce several pellets for compatibility tests. Then, these pellets were sintered at 1350 °C for 1 hour (Fig. 5). Optical microscope pictures showed that the micro-sized (<25 µm) particles on top of the surface had only a partial surface interaction after sintering (Fig. 5a), whereas nano-sized (~50 nm) particles were absorbed into the body and able to consolidate by sintering a layer of porous HA (Fig. 5b).

Progress on material

At this stage of the project, several parameters have to be evaluated to fulfil the project requirements. For instance, the amount of nano HA which has to be printed into each layer in order to promote the localized densification effect. Moreover, the correlation between the body density and the mechanical properties has to be investigated. To these aims, a new series of samples have been produced, containing different amount of nano HA, as well as additional sintering aids, such as colloidal silica and bioglass. The optimal sintering profile for each formulation is under investigation by measuring the thermomechanical properties of the green bodies upon heating up to 1500 °C. Several sintered bodies with the appropriate shape will then be produced for mechanical testing.

Discussion and Outlook

Although all of our inks lay within the given Ohnesorge and Reynolds values, not all of them could be used for printing. We could demonstrate that the sedimentation rate and the solid load are factors which significantly influence the printability. The higher the solid load the higher the chance to get agglomerates of nanoparticles and therefore increased sedimentation rate. Consequently, the printing membrane gets clogged. The ink development is ongoing. On one hand, we aim to avoid the sedimentation, either by varying the solid load, the viscosity or the surface tension. On the other hand, we have the strategy to increase the amount of solid HA nanoparticles in the ink or to combine NanoInks with additional sintering aids in order to optimize the localized sintering capability of the ink.

References

[1] Stevanovic S., Chavanne P., Braissant O., Pieles U., Gruner P., and Schumacher R., *Improvement of mechanical properties of 3D printed hydroxyapatite scaffolds by polymeric infiltration*. Bioceram Dev Appl., 2013, S1:012

[2] Rohner A.M., *Postprocessing of 3D printed ceramic scaffolds for bone replace-ment*. RT eJournal , 2014, Vol 11

[3] Testino A., F. Pilger, M.A. Lucchini, J.E.Q. Quinsaat, C. Stähli, and P. Bowen, *Continuous Polyol Synthesis of Metal and Metal Oxide Nano-particles Using a Segmented Flow Tubula Reactor (SFTR)*, 2015, Molecules, 20, 10566-10581

[4] Güngör, G.L., et al. (2016) *Dyes and Pigments 2016*, 127-148

Hybrid pixel detectors for electron diffraction of nano-samples

Project A11.04 HPD4FED (University of Basel, PSI, Dectris Ltd., Baden)
Project Leader: J.P. Abrahams
Collaborators: T. Gruene, H. Stahlberg, B. Schmitt, and C. Schulze-Briese

The use of light to see the smallest

The use of light and its interaction with matter is one of the best-developed technologies how researchers investigate our environment. One well-known example is the light microscope that shows us the world of things smaller than the eye can see. Another example is the use of X-rays, which are used in medicine to look at our body (e.g. bones and teeth). Most likely the use of light is so widely used because sight is our strongest sense. When it comes to the world of the very small, however, light meets limitations, and at some point even light microscopes cannot be used anymore. Where light meets its limits, one can use electrons to look at a higher level of detail – down to individual atoms. Many of us will be familiar with beautiful images from the world of the small, e.g. the close-up view of ants and other insects. Such images have been generated with electron microscopes. The production of such images is much more complicated than taking a picture through the lenses of light microscopes. One of the many reasons: the smaller the objects we look at, the more sensitive they become to the damaging nature of radiation. When we spent too much time in the sun, we burn our skin or in the worst case develop skin cancer. Similarly, small samples get easily destroyed as soon as we use special radiation to look at them – be it with electrons on a microscope, or with the strong X-ray light source, the SwissFEL. At the level of small molecules like proteins, destruction is happening so quickly that we hardly have enough time to take an image of sufficient quality and other tricks are necessary.

A new trick

One of the youngest groups at the PSI, under supervision of group leader Prof. Jan Pieter Abrahams, has recently shown we can overcome this limit. The trick is to take an indirect image of the sample, a so-called diffraction image. This trick gives us more time by a factor of a thousand than with standard imaging to record images. In order to explore this trick, the group is developing an electron diffraction instrument. The Kanton Aargau funds one of its most important components: the construction of a dedicated camera that records the image by selecting exactly that radiation which contains the valuable information. The group has developed two prototypes, based on the Timepix chip (CERN), which are operational and has shown the superiority of this new type of detector technology, a *hybrid pixel detector* [1].

The project

In parallel the PSI detector group has developed a number of hybrid pixel camera chips. They are named after mountain peaks of the Jura. Pilatus has been established for X-ray diffraction about a decade ago. EIGER [2] is the next generation of the PILATUS detector with smaller pixels and higher frame rate. Frame rates up to 2 kHz are possible in continuous data streaming. This year, the HPD4FED group recorded the very first diffraction pattern with an EIGER camera mounted on an Electron Microscope. An example pattern can be seen in figure 1. This first experiment was only meant as pilot test before taking the next steps in developing even a better detector. However, considering that the EIGER chip is designed for X-rays, and thought to be not ideal for electrons, the clarity and sharpness of the peak pattern (which is typical for diffraction data) was a very good result and the experiment a great success.

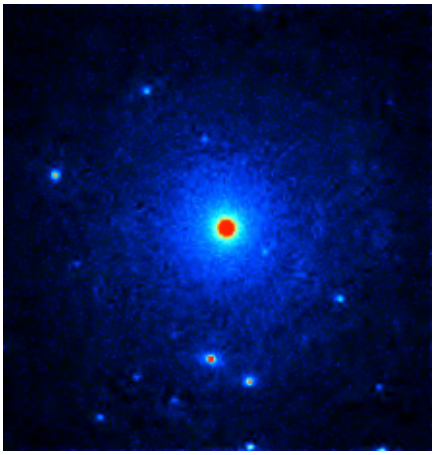

Fig. 1 First electron diffraction image recorded with an EIGER chip. The individual spots and their intensity are the scientifically relevant data. The noise free EIGER chip makes spots all the way to its edge visible.

"Real world" results

The object used during the experiment is a so-called zeolite. Zeolites are «scaffold» molecules and form a diverse class of microporous minerals. The nano-meter sized grains find wide applications in the refinery and chemical industry. The Swiss global player Clariant produces zeolite powder for the reduction of toxic by-products in industrial processes. The powder grains are too small for any other visualizing application than electron diffraction, especially when someone is interested in single grains of the bulk material. Figure 2 shows the chemical interpretation of the diffraction data

from zeolite recorded with the EIGER camera. The blue «clouds» show the scaffold built from the individual zeolite atoms at an unprecedented level of detail. The project members were very excited with the green «clouds» in the figure: for one of the first times the material between the scaffold could be visualized.

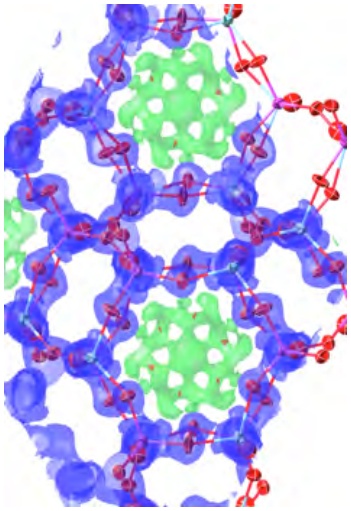

Fig. 2 The chemical result after interpretation of the diffraction data from figure 1. Red and blue small spheres are atoms of a zeolite mineral. They interpret the blue "cloud", which is the actual data. The green clouds have not yet been modeled. They demonstrate the sensitivity of the data collected as part of this project.

Future prospects

The results showed that there is still a lot to gain on the visualization of electrons, especially when diffraction of the biological smallest is involved. The first step on a road of applying known and new technologies has been made. We expect that with applying the even newer detectors, already in development by the PSI detector group, a new step can be made. Just like the PILATUS and EIGER, these detectors have been developed with X-ray radiation in mind. Testing these detectors early 2017 will give extra insights. Combined with lessons learned from other sources, this research will be the spark to set the specifications of the best, for high-energy electron diffraction, Electron Microscope detector.

References

[1] E. van Genderen, M.T.B. Clabbers, P.P. Das, A. Stewart, I. Nederlof, K.C. Barentsen, Q. Portillo, N.S. Pannu, S. Nicolopoulos, T. Gruene and J.P. Abrahams, *Ab initio structure determination of nanocrystals of organic pharmaceutical compounds by electron diffraction at room temperature using a Timepix quantum area direct electron detector,* Acta Crystallogr. A72, 236 (2016)

[2] R. Dinapoli, A. Bergamaschi, B. Henrich, R. Horisberger, I. Johnson, A. Mozzanica, E. Schmid, B. Schmitt, A. Schreiber, X.T. Shi, G. Theidel, *EIGER: Next generation single photon counting detector for X-ray applications*, Nuclear Instruments & Methods in physics research A, 650 (1), 79 (2011)

Development of an immunoglobulin detecting biosensor

Project A11.05 IgG AptaNP (FHNW, D-BSSE ETHZ Basel, FGen GmbH, Basel)
Project Leader: G. Lipps
Collaborators: M. Held, R. Pellaux, C. Puorger, C. Meyer, and O. Revelles

Sensing particles

Particles with a sensing function are of great interest for bioanalytic and diagnostic applications due to their ease of handling, separation, and immobilization. In this project we are developing an aptamer-based nanosensor to detect human immunoglobulins (IgG). The signal originating from the particles upon activation by the analyte can be directly quantified with any fluorescence-sensitive device including standard microtiter plate readers, microfluidic configurations or flow-cytometry.

IgG binding aptamer

Our nanosensor is based on a mixed RNA/DNA aptamer developed by Nakamura and colleagues [1]. The aptamer binds with high specificity and affinity (K_D ~ 100 nM) to human IgG. This aptamer is rather well characterized and the structure of the complex between aptamer and IgG [2] clearly shows the folding of the aptamer into a hairpin and the contribution of eight nucleotides to the binding (Fig. 1). Based on these investigations we could design a series of structure switching aptamers to sense IgG.

Fig. 1 Complex between human IgG (grey surface) and aptamer Apt8-2 [2]. The aptamer adopts a hairpin conformation. Nucleotides are colored according to base: G (green), A (red), U (magenta) and C (yellow).

Structure switching aptamers

Aptamers may have a high conformational flexibility. This property can be used to engineer aptamers which specifically undergo a conformational change upon binding to its ligand [3]. These so called "switching" aptamers can be combined with fluorophore/quencher pairs, which then enable a fluorescent readout of the binding reaction (Fig. 2).

A

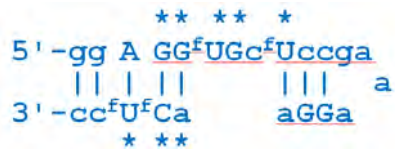

B

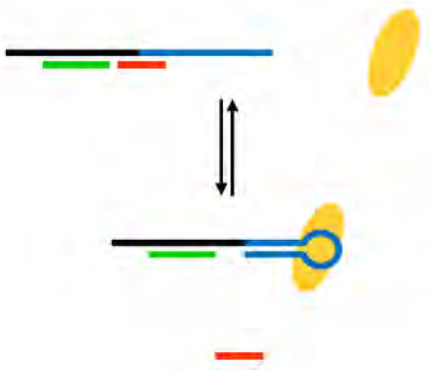

Fig. 2 A: Conformation of the IgG bound aptamer. Asterisks denote nucleotides important for IgG binding. Vertical lines show base pairing between both arms of the hairpin. B: Molecular mechanism of structure switching. The 5' end of the aptamer (blue) is extended by a DNA stretch (black) complementary to short oligonucleotides bearing a fluorophore (green) or quencher (red), respectively. Upon binding of IgG (orange eclipse) the aptamer adopts the hairpin conformation and displaces the oligonucleotide carrying the quencher. As a result, the fluorescence increases.

We tested a number of different quencher oligonucleotides, which interfere with the hairpin conformation of the aptamer but differ in length and position. As indicated by an increase of the fluorescence of the aptamer in solution, some of these probes (e.g. Q5BH, Q5D and Q1D) were indeed efficiently removed from the aptamer by IgG (Fig. 3).

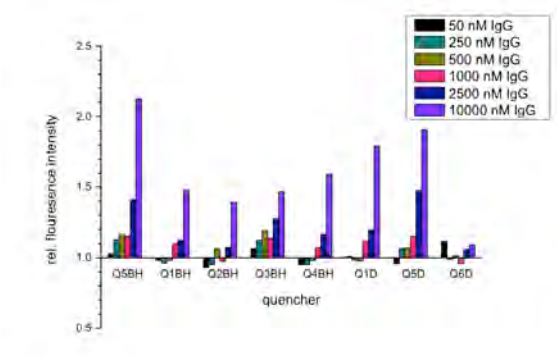

Fig. 3 Comparison of switching aptamers with different quenchers. The biosensors were tested between 0 and 10 μM human IgG.

Next we immobilized the biosensors onto magnetic beads (diameter 1 μm, ~0.5 Mio biosensors/bead) and monitored the fluorescence using flow cytometry. In the presence of 10 μM IgG the fluorescence intensity is about twice as high as in the absence of IgG. Thus the in solution measurements are in good agreement with the results of the immobilized biosensor.

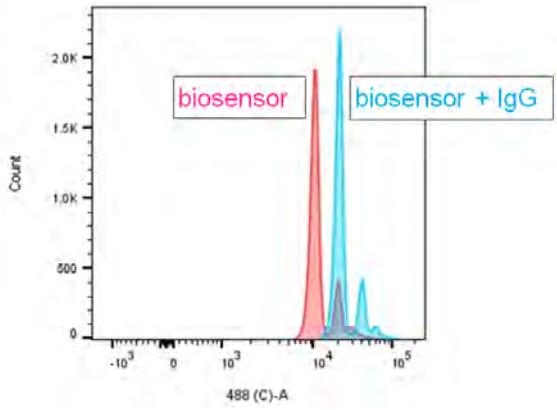

Fig. 4 Performance of the immobilized biosensor. The fluorescence is approximately doubled in the presence of IgG.

References

[1] S. Miyakawa, Y. Nomura, T. Sakamoto, Y. Yamaguchi, K. Kato, S. Yamazaki, Y. Nakamura, *Structural and molecular basis for hyperspecificity of RNA aptamer to human immunoglobulin G*. RNA, 2008, 14 [6], 1154-1163.

[2] Y. Nomura, S. Sugiyama, T. Sakamoto, S. Miyakawa, H. Adachi, K. Takano, S. Murakami, T. Inoue, Y. Mori, Y. Nakamura, H. Matsumura, *Conformational plasticity of RNA for target recognition as revealed by the 2.15 A crystal structure of a human IgG-aptamer complex*. Nucleic Acids Res., 2010, 38 [21], 7822-7829

[3] Nutiu, R. & Li, Y., *Structure-switching signalling aptamers*. J. Am. Chem. Soc., 2003, 125 [16], 4771-4778.

Development of nanostructured silk fibroin-synthetic textile composites

Project A11.10 NanoSilkTex (FHNW, University of Basel, HeiQ Materials AG, Bad Zurzach)
Project Leader: O. Germershaus
Collaborators: D. Buser, J. Sahlin, R. Razo, U. Pieles, M. Schönenberger, W. Bender, and M. Height

Introduction

Silk is a natural material, which is used since centuries for textiles and numerous other purposes. Silk yarn is traditionally reeled from cocoons of *Bombyx mori* and is known for its luster, wearing comfort, hydrophilicity and exceptional mechanical strength. However, textiles made from natural silk yarns are expensive to produce and lack the functional versatility provided by modern synthetic textiles.

The aim of the NanoSilkTex project is to open entirely new opportunities for the use of silk in modern textiles. Pure silk fibroin (SF), the main structural protein of the silk thread (Fig. 1), is extracted from silk cocoons, yielding a concentrated aqueous protein solution. This transformation of solid silk fibers into an aqueous silk fibroin solution allows reprocessing of silk fibroin and transformation of synthetic fibers on the nanometer scale.

Fig. 1 Hierarchical structure of threads from Bombyx mori composed of two filaments of silk fibroin coated with silk sericin. Silk fibroin itself is composed of hydrophilic domains and hydrophobic repetitive domains. Hydrophobic domains arrange into antiparallel beta sheeted crystallites [1].

Concept

Within NanoSilkTex, synthetic fibers made from polyester are coated with silk fibroin with the aim to impart silks advantageous material properties to synthetic textiles, e.g. improving mechanical strength, wear comfort and hydrophilicity. To achieve this goal, the nanoscale structure of the silk coating as well as its attachment to the polyester surface is optimized. Towards this end, characterization and control over silk fibroin properties after extraction, during coating and after potential curing of the coating as well as proper selection of coating process conditions are crucial.

Four coating strategies are investigated. The simplest coating strategy consists of direct multiple dip coating of polyester using diluted silk fibroin solution (strategy 1). The second strategy uses layer-by-layer coating based on electrostatic interaction between negatively charged silk fibroin and polycations (strategy 2) [2]. In addition to these two strategies, which are based on physical interactions between silk fibroin and the fiber surface, two alternative strategies based on chemical conjugation are evaluated (strategy 3 and 4). Finally, properties of the silk fibroin coated synthetic textile such as yield strength, bending stiffness, feel to the touch, wicking properties and UV transmission are evaluated.

Coating of synthetic textile samples with silk fibroin

Silk fibroin extraction was optimized regarding extraction efficiency and removal of silk sericin. Size exclusion chromatography and SDS-PAGE was used to characterize silk fibroin after extraction. Hydrolysis of silk sericin (degumming) using sodium carbonate solution at elevated temperature was found to significantly affect silk fibroin molecular weight distribution. Extended incubation for sericin hydrolysis resulted in increased formation of low molecular weight fragments of silk fibroin. Based on the analytical characterization, it is assumed that hydrolysis of silk fibroin occurs mainly in the hydrophilic and charged domains of the protein, potentially detrimentally affecting fibroin micelle formation. However, based on FTIR analysis, the capacity to form crystalline beta sheets is unaffected. In addition, it was observed that the storage stability of silk fibroin increased with increasing degumming time, representing a favorable property for industrial processing.

Regenerated silk fibroin solution was used for coating of polyester fibers. In addition to variation of the coating strategy, silk fibroin concentration as well as the number of dip coating cycles was varied. In general, dip coating was found to be efficient and straightforward (Fig. 2). Multiple coating cycles in all cases resulted in deposition of increasing amounts of silk fibroin on the fiber surface. However, use of silk fibroin at high concentrations resulted in inhomogeneous coating and formation of silk fibroin lamellae between individual polyester fibers (Fig. 2D). Film coating homogeneity was evaluated using fluorescently labeled silk fibroin and confocal laser scanning microscopy. Using silk fibroin at 0.5% and 2 coating cycles, the coating appeared to be homogenous throughout the investigated piece of fabric and the coating

surrounded the individual fibers without extensive lamellae formation.

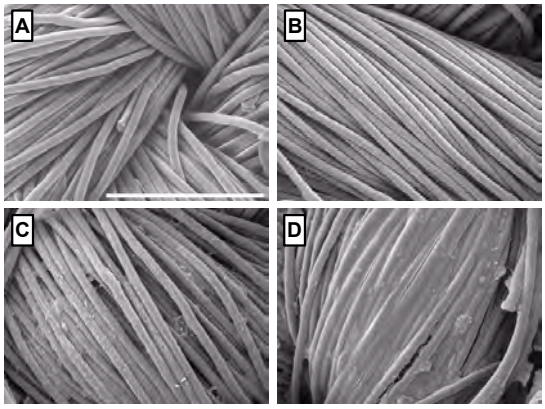

Fig. 2 Scanning electron micrographs showing blank polyester fabric (A), and silk fibroin coated polyester fabric using strategy 2 with 0.05%, 2 cycles (B), 0.3%, 5 cycles (C) and 0.5%, 10 cycles (D). Scale bar represents 200 µm.

Wash fastness and bending stiffness of silk fibroin coated polyester textile

An important prerequisite for commercial application of silk fibroin coating on polyester fabrics is its resistance to washing. Wash fastness was tested using 3 and 10 standard machine washing cycles, quantifying the amount of silk fibroin before and after washing. It was found that wash fastness varied between the different coating strategies. Direct coating of polyester (strategy 1) showed inferior wash fastness with approx. 70% loss of silk fibroin after 3 washing cycles. Electrostatically bound silk fibroin (strategy 2) showed only 42% loss after 3 cycles and 53% loss after 10 cycles. Coating strategies employing chemical conjugation to the fiber surface (strategy 3 and 4) further improved wash fastness, resulting in only up to 22% loss of silk fibroin after 10 washing cycles.

Besides wash fastness, mechanical properties of the textile are of major relevance. It was observed that coated textile samples became stiffer with increasing coating thickness. Therefore, 3-point bending tests were performed to quantify bending stiffness (Fig. 3).

It was found that silk fibroin coating resulted in 1.5 to 12-fold increase of bending stiffness compared to untreated polyester. Increase of bending stiffness is regarded as unfavorable for functional textiles. Therefore, optimization of the coating process regarding maximum wash fastness and minimum increase of bending stiffness is of paramount importance.

Functional characterization of silk fibroin coated polyester textile

Coated textiles were characterized regarding water uptake (wicking), water transmission, UV absorption, optical appearance and feel to the touch.

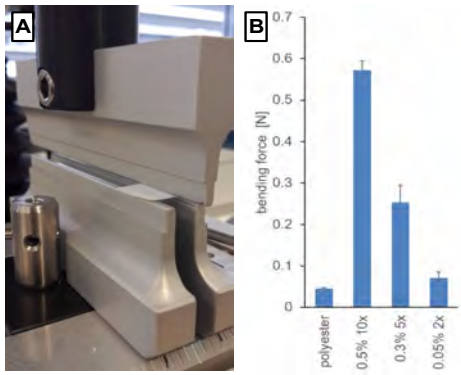

Fig. 3 Evaluation of bending stiffness of coated textile samples. (A) Experimental setup of 3-point bending test. (B) Bending stiffness of samples with different silk fibroin layer thickness prepared using coating strategy 2.

Wicking properties were evaluated to assess the ability of the different samples to efficiently distribute moisture, which is an important aspect of textiles resulting in improved wear comfort due to distribution and evaporation of sweat. Untreated polyester showed negligible water uptake, in line with results reported in the literature. Polyester lacks polar groups on its surface and therefore shows a moderate hydrophilic character. Furthermore, hydrophobic seizes are frequently used during production of the textile, resulting in low surface energy and poor wettability of polyester. However, silk fibroin coating significantly improved the wettability of polyester, especially at the high coating level (0.5%, 10 cycles). It is also interesting to note that strategies 3 and 4 resulted in coating amount-independent improvement of wettability, most likely related to the chemical modification of polyester surface.

Transmission of textile samples in the UVA (315-400 nm) and UVB (280-315 nm) range was determined to assess the sun protection effect of untreated polyester versus silk fibroin coated polyester. UV transmission measurements showed that coating of polyester with increasing amounts of silk fibroin resulted in increased absorption of textiles in the UVA and UVB range. This effect was observed at the high coating level (0.5%/10x) in the case of all coating strategies, whereas coating at the low level (0.05%/2x) was only efficient in the case of coating strategies 3 and 4.

Finally, the optical appearance of uncoated and SF coated polyester was assessed. Silk fibroin coated polyester fabrics had a smoother appearance and were less shiny than untreated polyester. Furthermore, SF coated textiles appeared to have higher luster, especially at the highest coating level.

References

[1] N. Du, Z. Yang, X.Y. Liu, Y. Li, H.Y. Xu, *Structural origin of the strain-hardening of spider silk*, Advanced Functional Materials 21, 772 (2011)

[2] L. Li, S. Puhl, L. Meinel, O. Germershaus, *Silk fibroin layer-by-layer microcapsules for localized gene delivery*, Biomaterials 35, 7929 (2014)

Uniaxilly oriented anisotropic electrospun nano-fibrous layers for optical applications

Project A11.12 NF-Optics (CSEM, FHNW, BASF Schweiz AG, Basel)
Project Leader: M. Stalder
Collaborators: A. Hafner, R. Oehrlein, C. T. Bormann, Y. Grether, P.A. Lassi, M. Waser, U. Pieles, and R. Ferrini

Introduction

Today most optical instrumentation is based on thin optical films which act as interference filters, color beam splitters etc. The majority of these components are manufactured by vacuum processes like magnetron sputtering or physical vapor deposition. Because of their large technical demands, vacuum free methods are very much anticipated. Electrospinning is a method to deposit nano-fibrous materials originating from the production of non woven fabrics for applications in filtration, textile, and medtech industries. The goal of this project is to use electrospinning for depositing highly oriented nano-fibrous layers of dielectric materials on planar substrates like glass or thin polymer sheets as optical components.

Manufacturing of sub-micron fibers and nano-fibers by electrospinning has attracted a lot of interest in the past years, as it is simple and cheap [1]. With nano-fibers, a variety of applications are available such as tissue engineering, bioassays, sensing, textiles and more. The deposition of highly oriented nano-fibrous layers of optical materials with high refractive indices is a new approach for the production of optical anisotropic films such as waveplates. These are used to modify the state of polarization of light e.g. in liquid crystal displays, projectors or novel brand protection devices.

Development of uniaxially aligned nano-fibrous layers with a high fill factor by electrospinning

Various commercially available polymers as well as novel synthesized high-refractive index polymers were used for electrospinning and two methods for aligning electrospun fibers were evaluated. A first selection of materials was based on commercially available polymers as shown in Table 1 including the index of refraction n and the color of the polymers.

Table 1 commercially available polymers used for electrospinning.

polymer	index of refraction n	color
P84	1.68	yellow
PVP	1.52	colorless
PEO	1.45	white

All of the polymers in Table 1 are well suitable for electrospinning. With regard to spinning, nano-fibers PEO and PVP are preferred materials. P84 seemed to result in fibers diameters in the range of 200nm, while spinning smaller fibers lead to bead formation (see scanning electron microscope (SEM) images in Fig. 1).

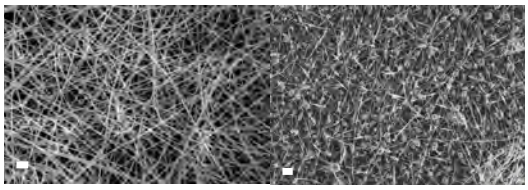

Fig. 1 Electrospun P84 free of bead defects (left) and with bead defects (right). Scale bar: 2 µm

A first generation of polymers with very high-refractive index (n~1.7) was specially synthesized by the industrial partner BASF. The colors of the polymers were colorless in one case, but mostly resulted in light yellow or brown. All polymers were tested for electrospinning. However, it turned out that the average molecular weight of the polymers was too low for direct electrospinning. These polymers were therefore also co-spun as mixtures with PVP or P84. By adding PVP/P84 some of the BASF polymers gave high quality fibers. A second generation of polymers with a higher average molecular weight was synthesized recently. They are colorless, n ~ 1.7 and will be tested soon.

In order to obtain an optical birefringent layer the nano-fibers need to be uniaxially aligned. The alignment has also a direct influence on the fill factor; the higher the alignment, the higher the fill factor (unaligned fiber mats < 0.1, target fill factor range for aligned fibers 0.5 – 0.6).

To orient fibers, two methods were used: electrospinning on conductive collectors separated by an insulating gap [2], and by collection on a rotating cylinder collector (Fig. 2).

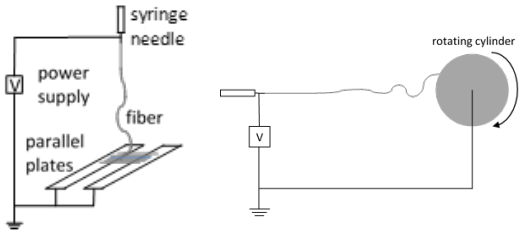

Fig. 2 Two methods for aligning electrospun fibers: parallel conductive collectors separated by an insulating gap (left) and rotating cylinder collector (right)

In the first approach, an electrode design of various parallel plates was studied with respect parallel orientation of the spun fibers. Polyimide P84 was

investigated because of its high refractive index of 1.68. After optimizing the spin parameters and set-up the achieved alignment was encouraging, as displayed in figure 3. For more details see [3].

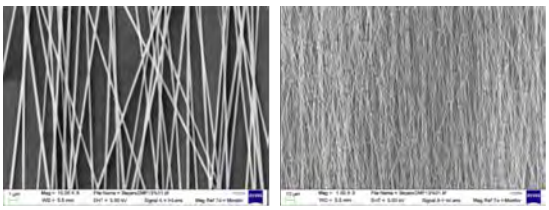

Fig. 3 Uniaxially electrospun fibers produced by the parallel plate method

Collecting electrospun fibers on a rotating cylinder allows coverage of comparatively large surface areas. Obtaining highly aligned fibers on rotating cylinders can however be challenging. To obtain straight aligned fibers by this method, it is necessary to have correct rotating cylinder speed. When the speed is too low, fibers will not align, if it is too high, air turbulences cause misalignment of the fibers. Furthermore the inherent random motion, the whipping instability of the electrospinning jet can cause misalignment to a point where no orientation can be observed despite collection on a rotating cylinder. These parameters can vary strongly from polymer to polymer and have to be evaluated for each polymer.

Based on those requirements, PEO and PVP were chosen as polymers. PVP can be spun directly on the rotating cylinder to obtain aligned fibers. For PEO it is known that whipping instabilities can be vastly reduced by placing an electrode plate behind the needle, which creates a more uniform electrical field. Using this setup, we were able to produce the highly aligned fibers (Fig. 4).

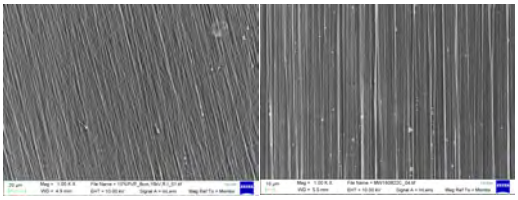

Fig. 4 Highly aligned electrospun fibers from PVP (left) and PEO (right)

Figure 4 shows that the polymer PEO resulted in the best fiber layers so far.

Optical characterization of unidirectional nano-fibrous layers

Nano-fiber samples were prepared by the parallel electrode method and by wrapping up the fiber on a drum. The fibers were then transferred onto glass substrates of a few mm² for optical inspection. A typical nanofiber sample (based on polyimide P84) is shown in figure 5.

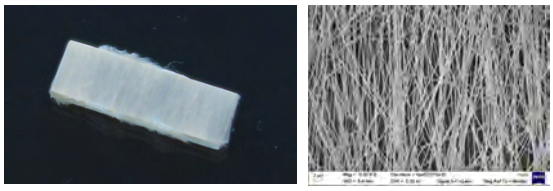

Fig. 5 Image of a polyimide P84 nano-fiber coated glass substrate with a size of approx. 4 x 15 mm² (left) and an SEM image of such fibers (right)

The image shown in figure 5 (left) shows that the nanofiber sample acts as strong scattering device and figure 5 (right) shows that the nanofiber sample hold a fiber diameter of 150 – 300 nm. The fabricated samples were inspected with a polarization microscope in transmission and reflection. Figure 6 shows the reflection of a polyimide P84 sample between crossed polarizers.

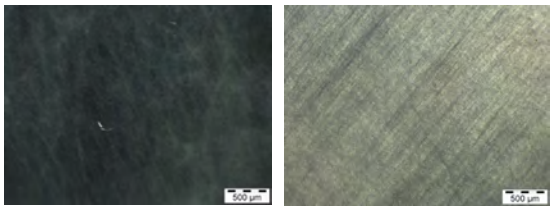

Fig. 6 Reflection image of a polyimide P84 based nanofiber sample between crossed polarizers, fibers aligned parallel to polarizer (left) and fibers aligned at 45° to polarizer (right)

Figure 6 shows that the reflection image of the nanofibers oriented at 45° to the polarizer is brighter than the image of the nanofibers oriented parallel to the polarizer. This is an indication for birefringence. It is however very weak in this case. Note that in reflection, the light passes twice through the nanofiber layer, the birefringence is therefore higher and brighter image is observed than in transmission.

We are confident that with next generation nano-fiber layers with a higher fill factor, fiber diameters < 100 nm and suppressed fiber bundling, first waveplates can be built and characterized.

References

[1] A. Greiner und J.H. Wendorff, *Elektrospinnen - eine faszinierende Methode zur Präparation ultradünner Fasern*, Angew. Chem. **119** 5770 (2007)

[2] D. Li, Y. Wang and Y. Xia, *Electrospinning Nanofibers as Uniaxially Aligned Arrays and Layer-by-Layer Stacked Films*, Adv. Mater. **16** 361 (2004)

[3] P.A. Lassi, *Uniaxially oriented anisotropic electrospun Nano-Fibrous Layers for Optical Applications*, Bachelor Thesis, Linköping University (2016)


KANTON AARGAU


SNI
SWISS
NANOSCIENCE
INSTITUTE
EINE INITIATIVE DER UNIVERSITÄT BASEL
UND DES KANTONS AARGAU


Universität
Basel


n w
Fachhochschule
Nordwestschweiz


PAUL SCHERRER INSTITUT
PSI


D-BSSE
Department of Biosystems
Science and Engineering


csem


Universitätsspital
Basel


Swiss TPH
Swiss Tropical and Public Health Institute
Schweizerisches Tropen- und Public Health-Institut
Institut Tropical et de Santé Publique Suisse

Educating
Talents
since 1460.

University of Basel
Petersplatz 1
P.O. Box 2148
4001 Basel
Switzerland

www.unibas.ch